AFM automation for mechanically characterizing biological samples at different scales

Javier Lopez Alonso

Université de Lille

Thèse de doctorat

AFM automation for mechanically characterizing biological samples at different scales

Automatisation de l'AFM pour la caractérisation mécanique des échantillons biologiques à différentes échelles

Thèse de doctorat de l'Université de Lille
préparée à CMPI

Ecole doctorale n°632 Sciences de l'Ingénierie et des Systèmes (ENGSYS)

Thèse présentée et soutenue par :

JAVIER LOPEZ ALONSO
le 20 septembre 2023 à Lille
en vue de l'obtention du grade de
Docteur de l'Université de Lille
Spécialité Micro-Nano systèmes et Capteurs

Composition du Jury :

Dr Etienne Dague (Directeur de Recherche CNRS) LAAS (Toulouse)	Rapporteur
Dr Grégory Francius (Directeur de Recherche CNRS) Université de Lorraine	Rapporteur
Dr Patricia Losada-Pérez (Associate Professor) EST – Université Libre de Bruxelles	Examinatrice
Dr Kislon Voitchovsky (Associate Professor) Université de Durham	Examinateur
Dr Bruno Grandidier (Professeur) IEMN – Lille	Président du jury
Dr Vincent Dupres (Maitre de conférence) CMPI-Université de Lille	Directeur de thèse
Dr Nuria Gavara (Assistant Professor) Université de Barcelone	Membre invité
Dr Frank Lafont (Directeur de Recherche CNRS) CMPI-CIIL (Lille)	Membre invité

Abstract

In recent years, there has been a significant rise in the study of cellular and extracellular matrix (ECM) mechanics, driven by the recognition of its crucial role in physiological and pathological processes such as cell division, migration, differentiation, and malignancy. Atomic force microscopy (AFM) has emerged as a powerful technique for investigating the mechanical properties of living cells and ECM, offering measurements of stiffness, elasticity, adhesion, and viscoelasticity. However, AFM's effectiveness in biological research is limited by its reliance on skilled users and its low throughput. To overcome these challenges, researchers have been working on enhancing AFM's throughput to improve efficiency and enable the acquisition of larger data sets.

In this work, we propose an automated system based on object detection that incorporates algorithms to ensure the quality of the acquired data. To demonstrate the viability of our developed automated AFM system, we conducted tests on three samples commonly studied using AFM, each at a different size scale.

First, we conducted experiments on artificial nanovesicles (NVs) with three different lipid mixtures and three different extrusion sizes. In our results we observed that the Thin Shell theory is less affected by the NVs size and provides a better description of the NVs' mechanical properties than the Hertz Model. The development of automated data acquisition and data analysis protocols, pave the way for establishing a methodology that can be applied to cell-derived extracellular vesicles under both pathological and non-pathological conditions.

Additionally, we treated Telomerase Reverse Transcriptase immortalized Retinal Pigment Epithelial (hTERT-RPE-1) cells with Latrunculin-A, confirming a decrease in the apparent Young's modulus (E) compared to non-treated cells. This validates the application of our system to mammalian cells.

By integrating a tracking algorithm, we monitored the mechanical properties of migrating NIH3T3 fibroblasts on glass over time. We observed that the front-to-back E ratio and the leading edge/following edge E ratio of migrating NIH3T3 cells are weakly correlated with the migration speed but not with the migration angle or changes in the migration angle of the cell. Suggesting that even when cells are moving in a particular direction, they are constantly probing alternative paths.

Furthermore, we successfully adapted the system to measure the mechanical fingerprint of rat bladder tissue. Our automated experiments successfully captured the mechanical fingerprint of the tissue samples, revealing the three distinct mechanical regions and obtaining values consistent with previous studies.

In addition to the automated AFM system, we developed an open-source software package for measuring elastic and viscoelastic properties from AFM data. The software was validated against MATLAB scripts and commercial software.

This work contributes to the advancement of biophysical research by introducing a novel automated AFM system capable of characterizing the mechanical properties of diverse biological samples and an open-source software package for extracting elastic and viscoelastic properties from AFM data.

Résumé

Ces dernières années, l'étude de la mécanique des cellules et de la matrice extracellulaire (MEC) a connu un essor considérable, en raison de la reconnaissance de son rôle crucial dans les processus physiologiques et pathologiques tels que la division cellulaire, la migration, la différenciation et la malignité. La microscopie à force atomique (AFM) s'est imposée comme une technique puissante pour étudier les propriétés mécaniques des cellules vivantes et de la matrice extracellulaire, offrant des mesures de rigidité, d'élasticité, d'adhésion et de viscoélasticité. Toutefois, l'efficacité de l'AFM dans la recherche biologique est limitée par sa dépendance à l'égard d'utilisateurs qualifiés et par son faible rendement. Pour surmonter ces difficultés, les chercheurs se sont efforcés d'améliorer le débit de l'AFM afin d'accroître l'efficacité et de permettre l'acquisition d'ensembles de données plus importants.

Dans ce travail, nous proposons un système automatisé basé sur la détection d'objets qui incorpore des algorithmes pour garantir la qualité des données acquises. Pour démontrer la viabilité du système AFM automatisé que nous avons mis au point, nous avons effectué des tests sur trois échantillons couramment étudiés à l'aide de l'AFM, chacun à une échelle de taille différente.

Tout d'abord, nous avons mené des expériences sur des nanovésicules artificielles avec trois mélanges de lipides différents et trois tailles d'extrusion différentes. Dans nos résultats, nous avons observé que la théorie de l'enveloppe mince est moins affectée par la taille des NVs et fournit une meilleure description des propriétés mécaniques des NVs que le modèle de Hertz. Le développement de protocoles automatisés d'acquisition et d'analyse des données ouvre la voie à l'établissement d'une méthodologie pouvant être appliquée aux vésicules extracellulaires dérivées de cellules dans des conditions pathologiques et non pathologiques.

En outre, nous avons traité des cellules épithéliales de pigment rétinien immortalisées par la télomérase inverse (hTERT-RPE-1) avec de la latrunculine-A, confirmant une diminution du module de Young apparent (E) par rapport aux cellules non traitées. Ceci valide l'application de notre système aux cellules de mammifères.

En intégrant un algorithme de suivi, nous avons surveillé les propriétés mécaniques des fibroblastes NIH3T3 en migration sur le verre au fil du temps. Nous avons observé que le rapport E avant-arrière et le rapport E bord d'attaque/bord suivant des cellules NIH3T3 en migration sont faiblement corrélés à la vitesse de migration, mais pas à l'angle de migration ni aux changements de l'angle de migration de la cellule. Cela suggère que même lorsque les cellules se déplacent dans une direction particulière, elles explorent constamment d'autres chemins.

En outre, nous avons adapté avec succès le système pour mesurer l'empreinte mécanique des tissus de la vessie de rat. Nos expériences automatisées ont capturé avec succès l'empreinte mécanique des échantillons de tissus, révélant les trois régions mécaniques distinctes et obtenant des valeurs cohérentes avec les études précédentes.

En plus du système AFM automatisé, nous avons développé un logiciel libre pour mesurer les propriétés élastiques et viscoélastiques à partir des données AFM. Le logiciel a été validé par rapport à des scripts MATLAB et à des logiciels commerciaux.

Ce travail contribue à l'avancement de la recherche biophysique en introduisant un nouveau système AFM automatisé capable de caractériser les propriétés mécaniques de divers échantillons biologiques et un logiciel libre pour extraire les propriétés élastiques et viscoélastiques des données AFM.

Table of contents

1. Introduction

Biophysics is an interdisciplinary research field that combines biology, physics and engineering. Biological systems that play a role in the mechanics or structure of an organism are identified and modelled following soft matter physics. By applying these theoretical developments, instruments and methodologies are then developed to acquire data that allows to better describe and quantify the mechanical properties of these systems. Bringing new insights into their mechanisms, which enable to refine the theoretical models and gain a deeper understanding of how these systems work. The diagram below provides a visual representation of this process, highlighting the iterative nature of biophysical research and the close interplay between theory and experimentation.

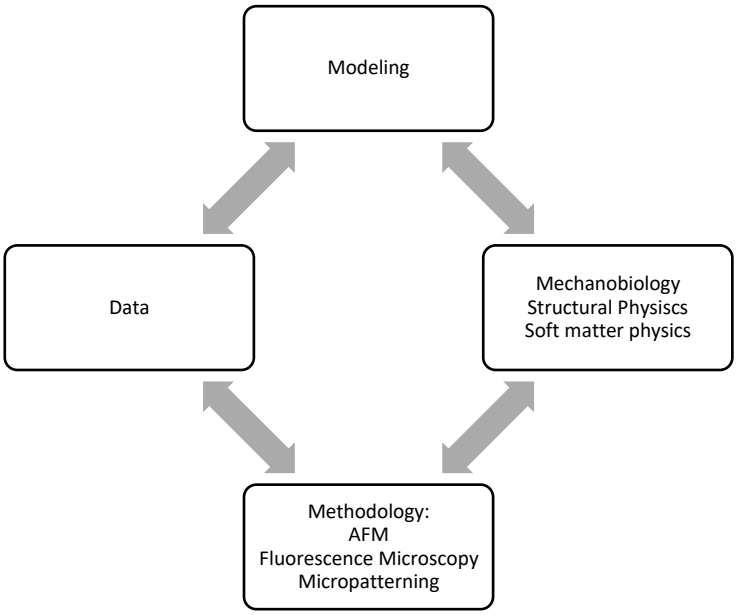

Figure 1: Diagram depicting the relationship between the different building blocks of biophysics.

The work of this thesis focuses on the development of automation for Atomic Force Microscopy (AFM), with the goal of increasing its throughput and tackling one of the main limitations that prevents its wide application in biology (Darling & Di Carlo, 2015). To demonstrate the viability of the developed automated AFM system, three samples commonly studied by AFM at different size scales have been selected for testing: artificial nanovesicles measuring 30nm, 50nm, and 100nm in diameter, Telomerase Reverse Transcriptase immortalized Retinal Pigment Epithelial (hTERT-RPE-1) / NIH3T3 cells with

diameters between 30µm and 100µm, and 50µm thick rat bladder tissue sections, as the smallest, intermediate, and largest samples, respectively.

This introduction is structured into four main chapters, each of which represents a fundamental pillar of this work. Chapter 1 presents an overview of the key structural components that significantly contribute to the mechanical properties of each sample type selected for our study. The purpose of this chapter is to help the reader to understand the factors that impact the mechanical properties of these samples.

In Chapter 2, we examine the relevance of mechanical phenotyping by discussing the major applications and landmarks of investigating the mechanical properties of biological samples. While our study focuses on the Atomic Force Microscopy (AFM) technique, we acknowledge the availability of other methods to characterize the mechanical properties of biological samples. These alternative techniques together with their strong points and limitations are briefly summarized in Chapter 3.

Finally, Chapter 4 provides an in-depth analysis of the working principle of AFM, including its classic operation modes, strengths, limitations, and how this technique is currently utilized to measure the mechanical properties of biological samples. Additionally, the chapter presents a rigorous evaluation of the previous developments with the aim of increasing AFM throughput, focusing especially on automation.

1.1. The structure of eukaryotic cells, epithelial tissue and nanovesicles

1.1.1. Eukaryotic cell

Cells are heterogeneous systems, with a typical diameter between 10 µm and 100 µm (Ashrafuzzaman & Tuszynski, 2013a, 2013c), formed by different components with unique mechanical properties. As a result, cells behave both as an elastic solid over short time scales and as a viscous fluid over longer time scales. To understand the overall mechanical properties of the cell, it is essential to understand the mechanical properties of its main components (Figure 2) and how they interact with each other.

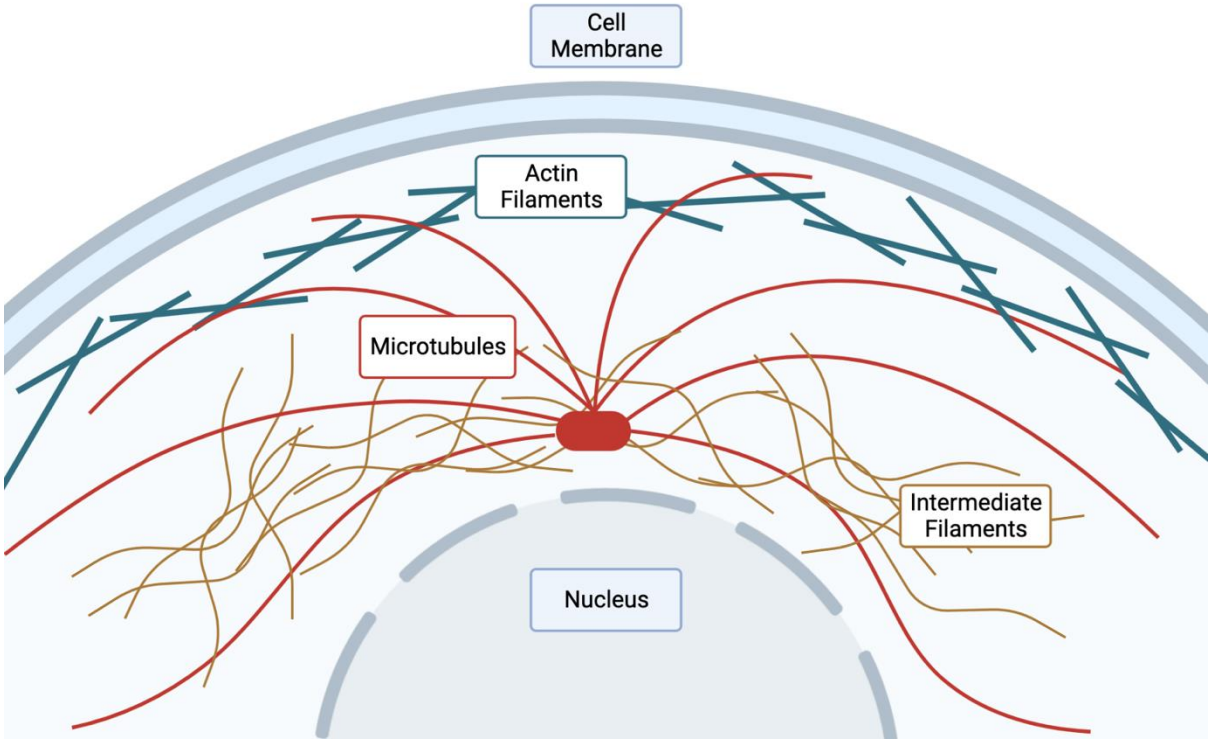

Figure 2: Schematic depicting the intracellular components contributing to the mechanical properties of the cell.

1.1.1.1. Cell membrane

The cell membrane is a viscoelastic semipermeable barrier that separates the inner part of the cell from its environment. The barrier itself mostly consists of a phospholipid bilayer including embedded proteins. However, the

composition of the cell membrane is not homogeneous and varies between cell types and among its microdomains. The main functions of the cell membrane are adhesion, signalling, transport and homeostatic regulation (Ashrafuzzaman & Tuszynski, 2013b).

Only small molecules like CO_2 and O_2 can permeate through the cell membrane without the input of cellular energy. Larger molecules require an active transport via transmembrane channels, transporters or through the endo and exocytosis of vesicles. For all active methods, energy input from the cell is needed.

Together with transporters, other proteins like adhesion complexes, receptors, enzymes and channels are found in the cell membrane. Depending on their role, some of these proteins are anchored to the cytoskeleton or the extracellular matrix (ECM), whereas other proteins, as well as some lipids from the bilayer, can laterally diffuse freely through the membrane (Ashrafuzzaman & Tuszynski, 2013c).

Due to its numerous connections to the cytoskeleton, extracellular matrix and other cells, the cell membrane is an integral contributor to the cellular mechanical behaviour. Either by propagating extracellular stresses and strains into the intracellular components of the cell (mechanosensing) or by transforming these mechanical signals into biochemical signals (mechanotransduction). A clear example of this role are focal adhesion points (FA), dynamic macromolecular assemblies located on the cell membrane consisting of ECM molecules, integrin receptors and focal adhesion-associated proteins. FAs physically connect the cytoskeleton with the ECM, allowing the cell to directly sense mechanical stresses and undergo modifications to respond to them. A more in detail explanation of these processes is given in section 1.1.2.1.

1.1.1.2. Cytoskeleton

The cytoskeleton is a dynamic three-dimensional network consisting of microfilaments, microtubules and intermediate filaments (Figure 3), which expands through the whole cell and constitutes its major mechanical structure.

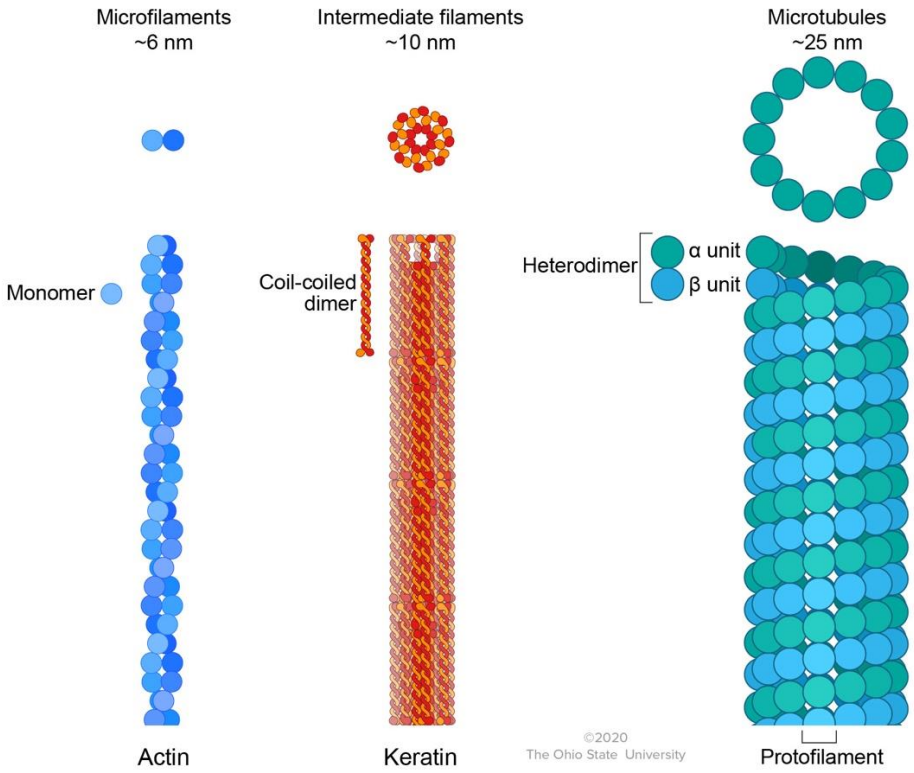

Figure 3: Diagram depicting the sizes of three main components of the cell cytoskeleton: microfilaments (~6 nm diameter), intermediate filaments (~10 nm diameter) (Premanandan, 2017)

Microfilaments are made from linear polymers of G-actin (monomeric globular actin), known as actin filaments (F-actin), coiled around each other in a helical orientation (Figure 3). They help maintaining the position of the different organelles, while providing both tensile strength and resistance to deformation to the cell. Moreover, their ability to polymerize and depolymerize within minutes makes them crucial in the formation of filopodia, lamellipodia and pseudopodia, structures required for cell locomotion (Bearer, 1993; Trepat et al., 2012). Microfilaments can be found forming stress fibres, where multiple microfilaments are cross-linked together, and in many cases, include myosin motor proteins. These structures are commonly found connected to FAs, making them key in the mechanosensing and mechanotransduction processes.

Microtubules are polarized polymers of tubulin (Figure 2). These dynamic structures are constantly assembling and disassembling at the plus and minus ends respectively. Structures formed by microtubules can be both permanent, like in the case of cilia and flagella, or temporary, like the spindle formed during cell division. Microtubules provide compressive strength to the cell while serving as "railways" for intracellular cargos.

The category or intermediate filaments includes more than 70 different types of filaments. The proteins forming intermediate filaments have been grouped into five types (Herrmann et al., 2007):

- Type 1-2: Includes acidic and basic keratins. Mostly found in epithelial tissues.

- Type 3: Includes Vimentin, Desmin and GFAP. Mostly found in connective tissues.

- Type 4: Including neurofilaments.

- Type 5: Includes Lamins. Filaments found forming the nuclear lamina of all tissue cells.

The role of intermediate filaments is to provide structural integrity to the cell by linking the cytoskeleton components, organelles and the cell membrane together. Although most of the filaments in this group share a common structure and dimensions, due to the high heterogenicity in their chemistry and polymerization, this group presents filaments with different physical properties and functions. As an example, Desmin and Keratin filaments together with neurofilaments have been shown to have a high extension capability, allowing them to sustain high tension forces (Kreplak et al., 2005). Vimentin filaments, on their side, have been shown to serve an important role on protecting the cell nucleus mechanical integrity and cell against compressive stress (Pogoda et al., 2022).

1.1.1.3. Nucleus and other organelles

The nucleus is the largest compartment inside the cell. Its main function is to contain the genetic information of the cell and the molecules needed for DNA/RNA synthesis, transcription and processing. It consists of an envelope, formed by the nuclear lamina and the nuclear membranes; and the nuclear lumen, where the nuclear matrix and the chromosomes with their associated proteins are located.

The nuclear matrix and the nuclear lamina are the main components in the nucleus that help sustaining the shape and mechanical stability of the nucleus.

The nuclear matrix is a filamentous structure, composed mostly of actin and myosin (Lammerding, 2011), that serves as a scaffold for other nuclear components. The nuclear lamina has a similar structure, but composed of Lamins, nucleus specific proteins from the group of intermediate filaments, implied in biochemical processes, such as: signalling, chromatin remodelling and nucleic acid processing (Butin-Israeli et al., 2012; Dechat et al., 2008).

As the physical size of each organelle greatly determines their contribution to the mechanical properties of the cell, the nucleus is the inner compartment of the cell with the most influence in the overall mechanical properties of the cell (Caille et al., 2002). However, its influence will vary depending on the morphology and nuclear-cytoplasmic ratio of each cell.

Although it is known that mechanical tension can regulate gene expression, it is still not known which is the mechanism that connects sensing these extracellular stresses with the transcriptional machinery inside the nucleus.

1.1.2. Tissue

Tissues are groups of cells that are specialized in performing specific functions in the body. There are four main types of tissues: epithelial, connective, muscle, and nervous (Ross & Pawlina, 2016a).

Epithelial tissue is composed of a layer of closely packed cells that line surfaces and organs throughout the body. The cells are arranged in sheets and can be classified based on their shape and arrangement. Simple epithelium is a single layer of cells, while stratified epithelium has multiple layers. Squamous epithelium is composed of flat, scale-like cells, while cuboidal epithelium is composed of cube-shaped cells, and columnar epithelium is composed of tall, column-shaped cells. The basement membrane separates the epithelial tissue from the underlying connective tissue and provides support and anchorage (Ross & Pawlina, 2016b).

Connective tissue is characterized by a matrix of extracellular material (ECM) that surrounds and supports the cells. The matrix is composed of fibers such as collagen and elastin, as well as a ground substance of proteoglycans and glycoproteins. There are several types of connective tissue, including loose connective tissue, dense connective tissue, adipose tissue, and bone tissue. Each

type has a unique structure and function, ranging from providing support and protection to storing energy and producing blood cells (Ross & Pawlina, 2016c).

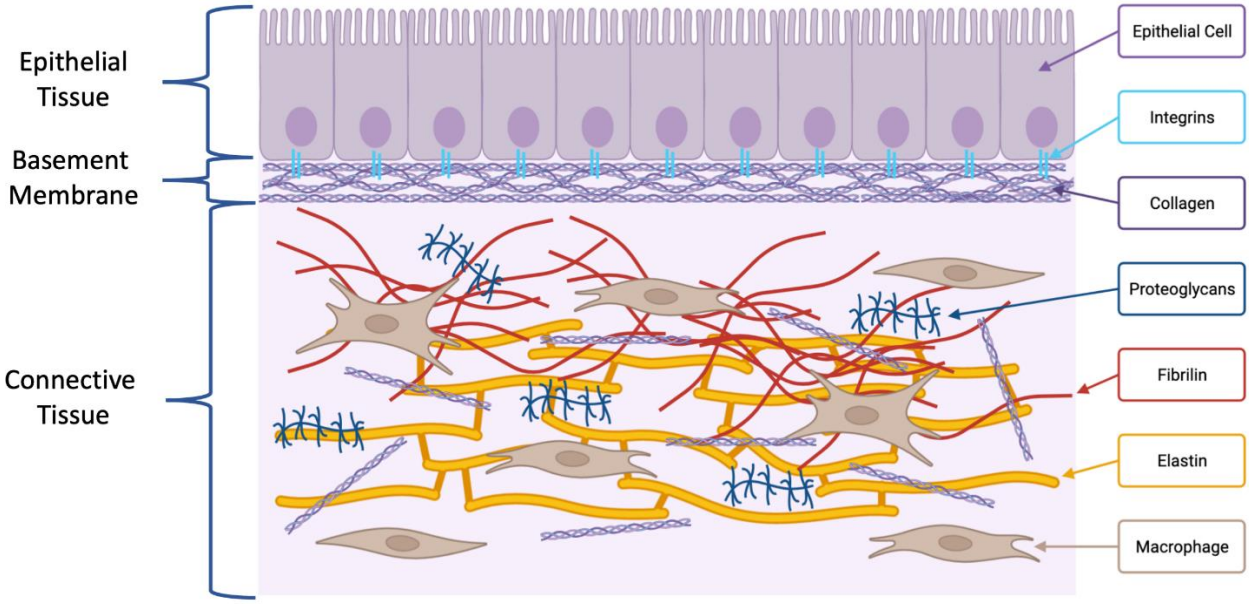

Figure 4: Simplified schematic showing the main components of epithelial and connective tissue.

Muscle tissue is composed of specialized cells called muscle fibers that can contract and generate force. There are three types of muscle tissue: skeletal, cardiac, and smooth. Skeletal muscle is attached to bones and is responsible for movement, while cardiac muscle forms the walls of the heart and is responsible for pumping blood. Smooth muscle is found in the walls of organs and blood vessels and is responsible for contraction and relaxation (Ross & Pawlina, 2016d).

Nervous tissue is composed of specialized cells called neurons that transmit signals throughout the body. Neurons are characterized by a cell body, dendrites that receive signals, and an axon that transmits signals to other neurons or to muscles or glands. Glial cells provide support and insulation for the neurons (Ross & Pawlina, 2016e).

Due to the heterogeneous composition of tissues (Figure 4), their mechanical properties are the result of the cells and the ECM interacting with each other (Figure 5). The ECM is a highly controlled and regulated environment that surrounds the cells. The main component of ECM is the extracellular fluid (EF), composed by water and soluble components. In the EF cells secrete a wide variety of insoluble bioactive macromolecules, like fibrous proteins, that determine physical and mechanical properties of the ECM. As its composition

is influenced by the cells it surrounds, ECM has different properties based on the organism and tissue type. For example, bone tissue ECM is strongly mineralized and dense, while in blood, the liquid plasma is the ECM.

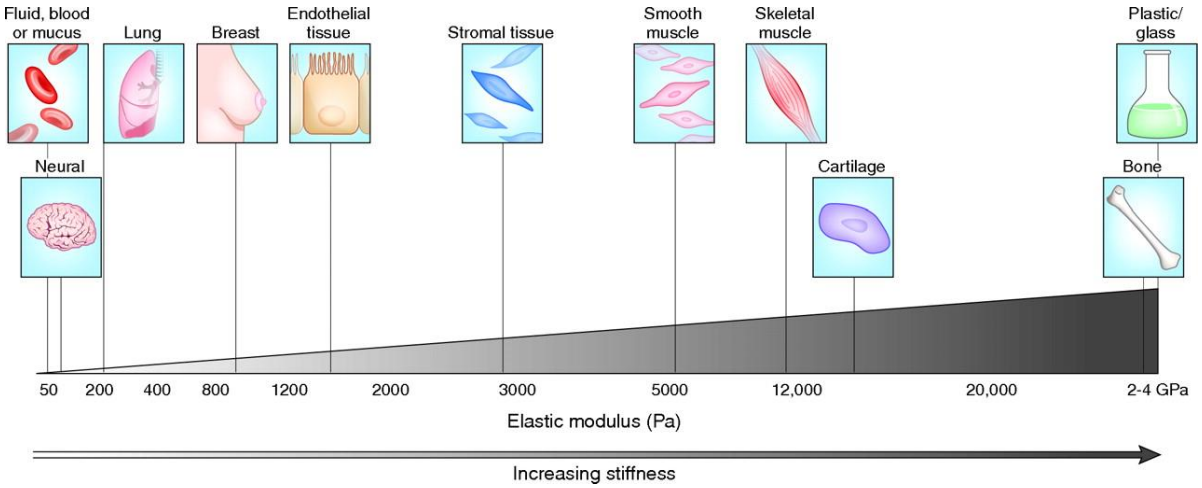

Figure 5: Diagram depicting the Young's modulus, measured in Pascals (Pa), of different tissues. Reproduced from (T. R. Cox & Erler, 2011)

The ECM does not only serve as a scaffold for the cells. In the same way the cells influence the composition and properties of the ECM, the ECM influences the cells it surrounds. Moreover, the dynamics of ECM control the fundamental behaviours and characteristics of the cell, such as proliferation, adhesion, migration, polarity, differentiation and apoptosis (T. R. Cox & Erler, 2011).

The ECM is primarily composed of fibrous proteins, glycoproteins, and proteoglycans (Kular et al., 2014; McKee et al., 2019). Collagen is a fibrous protein which constitutes the basic structure of most tissues. It provides the ECM with tensile strength and stretch resistance. Most collagen molecules form a triple-stranded helix that then they can assemble into supramolecular complexes. 28 types of collagen molecules have been identified to date, each one with different properties and expression levels in tissues (Ricard-Blum, 2011). Collagen fibbers are composed by a heterogeneous mix of collagen types, with one type of collagen being predominant for each type of fibber. In the human body Type I collagen is the most abundant (Von der mark, 2006).

Glycoproteins are proteins containing oligosaccharide chains. Oligosaccharide chains are short, branched, and may or may not be negatively charged. The three most important proteins in the ECM are elastin, fibronectin and laminin. Elastin provides stretch resistance to the ECM. Laminin is an important component of the basal lamina, a barrier that prevents cells from one type of tissue infiltrating into another, allowing the layering of dissimilar types of

tissue (Aumailley, 2013). Fibronectin (FN) is a group of proteins crucial for cell-ECM communication that are found in the ECM assembled as a fibrillar matrix in all tissues and throughout all stages of life. FN are modular proteins composed of types I, II and III repeating units, which exist in multiple isoforms generated by alternative splicing (Pearlstein et al., 1980).

Finally, proteoglycans are composed by glycosaminoglycan (GAG) chains attached to a polypeptide side chain. Glycosaminoglycan chains are long, linearized, and negatively charged as a result of the presence of sulphate and uronic acid functional groups. Their main role in the ECM is mechanical. Together with fibrous proteins they are the main determinants of the mechanical properties of the ECM (Silver et al., 2021).

1.1.2.1. Cell-Extracellular matrix interaction

Although there are multiple ways the cell and ECM communicate, the interactions mediated by integrins are the most prevalent and better characterized. Integrins are transmembrane proteins only found in multicellular organism (metazoan), constituted by an alpha chain and a beta chain with an extracellular domain that interacts with the ECM and an intracellular domain that interacts with the intracellular constituents of the cell (Takada et al., 2007). The extracellular domain of integrins is the largest and includes both chains. Integrin can exist in two main conformations: active and inactive. In the inactive conformation both chains of the integrin are bent and neither the extracellular and intracellular domains are linked to any ligands or intracellular components. When the integrin is fully activated, either by inside-out or outside-in signalling, both chains become fully extended in the extracellular domain and they separate in the intracellular domain, forming a shape reminiscent of an arch.

Once activated, integrins tend to migrate through the cell membrane and form dynamic clusters that gradually mature into FAs. These FAs are essential for maintaining cell morphology and facilitating cell locomotion by anchoring the cell to the surrounding ECM (Trepat et al., 2012). Mature FAs include hundreds of proteins which can be divided into four categories based on their contribution to the following four processes:

1.1.2.1.1. ECM-receptor binding

In the tissue cells interact both with the ECM and other cells. To trigger the correct response, the cell has different mechanisms that allow it to sense different stimuli. As an example, unlike cell-ECM interactions, cell-cell interactions are mediated by cadherins and not by integrins (Maître & Heisenberg, 2013).

Biochemical information about the cell surroundings is crucial. Ligands bind to cell receptors that then activate biochemical cascades inside the cell which trigger multiple responses, such as the production of certain proteins (i.e., Insulin, Fibrin...). However, the cell also requires access to mechanical information of its surroundings, like changes in the stiffness of the ECM or sensing external forces being applied to the ECM. Receptors like integrin, bind to molecules in the ECM, like fibronectin, and trigger the formation of FAs. These receptors serve as hubs for the transmission of mechanical information between the cell and the ECM (Teckchandani & Cooper, 2022).

1.1.2.1.2. Linkage to actin cytoskeleton

Integrin molecules are not directly connected to the cell's cytoskeleton, they connect through collection of proteins that form a structure known as the integrin adhesome. Talin is the main protein responsible of mediating the connection between the intracellular domain of the integrin beta chain, to the cytoskeleton's actin filaments (Klapholz & Brown, 2017). It is then one of the most important proteins capable of sensing mechanical forces.

In the initial stage of FA activation, talin dimers are in the cytoplasm in a closed conformation. Through mechanisms that are not fully understood, a signal triggers the opening and activation of the talin dimers. Four steps are required to form the ECM–integrin–talin–actin link. The activated talin dimers then bind to the intracellular region of the beta chain for up to four integrins. Talin dimers can be oriented both in parallel and perpendicular to the cell membrane. Talin then binds to as many actin filaments as possible through its actin binding sites. The mechanical forces on the integrins and/or actin fibers are transmitted to talin, causing it to unfold and expose interaction sites for other key integrin associated proteins such as vinculin, RIAM, FAK and paxillin (Das et al., 2014; Klapholz & Brown, 2017). At this point, the adhesome and the connections

between the ECM and the cell cytoskeleton are fully formed. However, as FAs are highly dynamic structures, these connections are not permanent and can be disassembled.

1.1.2.1.3. Mechanosensing

Mechanosensing consists in the perception of mechanical information from the environment surrounding the cell (Y. Chen et al., 2017). Currently the exact mechanism of this process is not fully understood. Once a connection has been formed between the ECM and the cell's cytoskeleton, forces are transmitted from the ECM to the cell and vice versa. The cell can then translate these mechanical stimuli into biochemical signals through mechanotransduction.

1.1.2.1.4. Mechanotransduction

Mechanical stimuli influence and play a key role in multiple cellular processes. Like in the case of mechanosensing, the exact mechanism of how mechanical stimuli are transformed into biochemical signals is not fully understood. However, recent studies have described direct links between the mechanical properties of the ECM, mesenchymal stem cell differentiation (Engler et al., 2006), axonal growth (Barros et al., 2011; Myers et al., 2011) and cell migration (Mechanotaxis) (Cortese et al., 2009; Gray et al., 2003).

1.1.3. Nanovesicles

Vesicles are membrane-enclosed compartments (Figure 6) that can be found inside and outside of bacteria, Archaea, plant cells and animal cells. Membrane rigidity and luminal pressure are the two main contributors to the mechanical properties of vesicles, with the luminal pressure playing a dominant role in vesicles with a fluid phase membrane. Based on their origin, composition and size, vesicles play key roles in multiple processes of the cell, such as: intracellular trafficking, protein recycling, signal transmission and intercellular communication (Camussi et al., 2010). Although their structure is less complex than for cells and tissues, they are a fundamental tool in biology for fundamental research, where they are commonly used as model systems to study the properties and dynamics of cell membranes.

One class of vesicles that has gained a growing interest in recent years, is extracellular vesicles (EVs). Previously, it was thought that EVs were used by the cell to dispose of cellular material no longer needed by the cell. However, recent studies have shown that EVs play a key role in cell-to-cell communication (Camussi et al., 2010). EVs are nanoparticles (30 nm–10 µm) (S. M. Johnson et al., 2020) secreted by the cell delimited by a lipid membrane derived from the cell membrane which encapsulates bioactive material, including micro-RNA, messenger-RNA and proteins. Through EVs this cargo can be delivered to receptor cells, where it can be utilized and result in changes in the cell's phenotype. Upon contact with the microenvironment of the recipient cell, EVs can signal through surface receptors or enter the cell through various endocytic pathways (Gurung et al., 2021; Mulcahy et al., 2014).

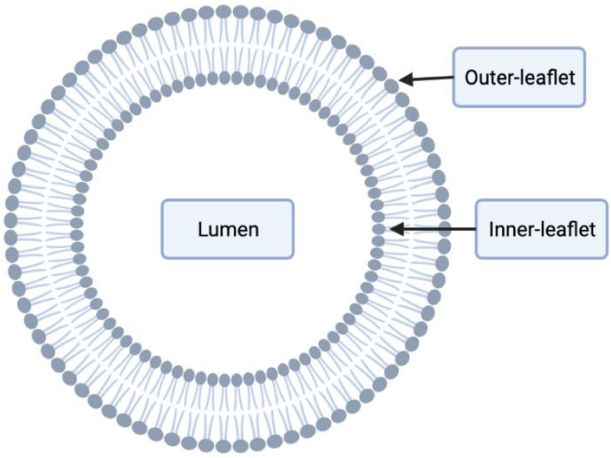

Figure 6: Schematic showing the general structure of vesicles.

Although several types of extracellular vesicles exist, microvesicles and exosomes are the best characterized. Exosomes are homogeneous bioparticles formed from multivesicular bodies (MVBs), intracellular endosomal organelles formed by multiple intraluminal vesicles enclosed within a single outer membrane, with a diameter between 40-100nm. Microvesicles are heterogeneous EVs with different shapes and a diameter between 100-1000nm, formed by the regulated release of outward budding of the plasma membrane (Ståhl et al., 2019).

As the number of EVs and their composition changes based on their biogenesis and cell state, several studies have focused on describing how EVs are implied in biological processes and characterizing their physical-chemical properties. These studies have led to the discovery of the implication of EVS in the

propagations of diseases like cancer (Chang et al., 2021), HIV (Dias et al., 2018) and Alzheimer (Aharon et al., 2020). Moreover, as EVs can cross biological membranes and are readily available in body fluids (i.e., urine, blood, saliva...), they show great potential for being used in the clinic as disease biomarkers.

1.2. Applications of mechanical phenotyping

1.2.1. Single cells

Mechanical properties are crucial for regulating biological functions of the cell, such as: cell movement, cell growth, cell differentiation and fate. One of the most relevant examples of the influence of the mechanical stimuli in the function of the cell, are the findings reported by Engler and co-workers (Engler et al., 2006). In this study, the authors have showed that mesenchymal stem cells (MSC) grown on gels with an elasticity corresponding to different solid tissue types (0.1–1 kPa for brain, 11 kPa for muscle and 34 kPa for collagenous bone), would commit to the lineage specified by the gel matrix elasticity. Although the mechanism is not fully understood, these experiments clearly showed how the mechanical properties of cells and their surroundings are able to trigger different biochemical and genetic responses in the cell.

Cell locomotion is another process that has been shown to be influenced by the mechanical properties of the cell environment. Cells do not migrate in a random manner, they follow trajectories to reach specific positions, depending on their cell type and function. To perform this guided process, the cell must adopt the correct polarity, initiate the propulsion and then maintain/correct the propulsion through the whole path. The specific mechanisms that guide cell migration are not fully understood. However, there are three main factors known to influence cell migration: chemical stimuli (Chemotaxis) (Bussmann & Raz, 2015), adhesion gradient (Haptotaxis) (Wen et al., 2015) and mechanical stimuli (Mechanotaxis) (Cortese et al., 2009; Gray et al., 2003).

Together with cell differentiation and migration, mechanical properties have been related to cell aging. In the work of Zhan and collaborators (Zahn et al., 2011) they observed that the average apparent young modulus of fibroblasts from young donors (<25 years) were stiffer than the ones from older donors (>30 years). It thus demonstrates that the mechanical properties of human fibroblasts depend on the donor's age.

Apart from helping to better understand fundamental processes like cell differentiation, migration and aging, the mechanical phenotyping of cells has also been identified as a potential label-free method to discriminate between normal and abnormal cells. Cancer is one of the principle causes of death in developed countries like France (*Causes de Décès - Inserm-CépiDc*, 2020). In the same manner as physicians use palpation to detect stiff masses in the patient's body that could correspond to tumours, several authors have explored the possibility to use mechanical phenotyping to detect tumoral cells or provide information about cancer prognosis. Several authors have shown that cancerous cells are softer than their healthy counterparts when seeded on rigid surfaces like glass or plastic. However, clinical application as a diagnosis method still requires systematic studies (Lekka & Laidler, 2009). As the most widely used technique to measure the mechanical properties of cells, AFM measurements have been used to discriminate between cancerous and non-cancerous cells in multiple types of cancers (Deng et al., 2018; Gnanachandran et al., 2022; Lekka, 2016; Lekka et al., 2012; Lekka & Laidler, 2009; Li et al., 2021).

Additionally, mechanical phenotyping has been shown to allow to distinguish between cancerous cells with different malignant levels. As an example, on 2012 Xu and collaborators (Xu et al., 2012) measured the apparent young's modulus with AFM of highly invasive ovarian cancer human cells (HEY A8) compared to their less invasive parental cells (HEY), and observed that cells with a higher malignant potential showed a lower mean apparent young's modulus than their less malignant counterparts. Moreover, on 2020, Riana and collaborators (Rianna et al., 2020) showed that tumour cells soften when navigating confined spaces, suggesting the existence of a mechano-adaptive mechanism which facilitates the migration of metastatic tumour cells through narrow spaces.

As a result of these findings, mechanical phenotyping has gathered a lot of interest and is seen as an alternative means for diverse biomedical applications, such as: early-stage diagnosis, immune status analysis, drug screening or cell separation (Darling & Di Carlo, 2015). However, this approach has some limitations:

- When measuring the mechanical properties of cells in vitro, the cell is a different environment to the one it would experience in vivo. Normally measurements are acquired on cells seeded in petri dishes, where the cell is not confined in a three-dimensional structure like it would in the tissue.

- The mechanical properties of the substrate (Brandl et al., 2007; Leipzig & Shoichet, 2009; Yeung et al., 2005), cell morphology and the region measured in the cell have an effect in the measured mechanical properties.

- One of the most used samples for diagnosing diseases in patients are solid tissue biopsies. However, if clinicians want to use single cell mechanical phenotyping in the clinic, they first need to extract single cells from the tissue sample. This means that an additional step is required in the sample preparation protocol, making the process more complex and time-consuming.

1.2.2. Tissue

Mechanical phenotyping of tissues has emerged as a promising diagnostic tool, as the mechanical properties of tissues play a crucial role in tissue function and health. Alterations in the mechanical properties of tissues can reflect underlying changes in tissue composition or structure, which may be associated with various diseases or conditions (Júnior et al., 2023; Martinez-Vidal et al., 2023). Consequently, characterizing the mechanical properties of tissues has the potential to identify changes indicative of disease or injury and reveal new biomarkers for diagnosis and treatment.

The most notable example of bringing this technology closer to the clinic has been the work of Plodinec and collaborators (Plodinec et al., 2012) where they used indentation-type atomic force microscopy (IT-AFM) to study the stiffness profiles of human breast biopsies (Figure 7). In this study they observed that benign tissues show uniform stiffness profiles characterized by a single distinct peak, whereas malignant tissues present a broader stiffness distribution, representative of higher tissue heterogenicity, with a prominent low-stiffness peak. This study showed the potential to include the nanomechanical characterization of biopsies into the clinic.

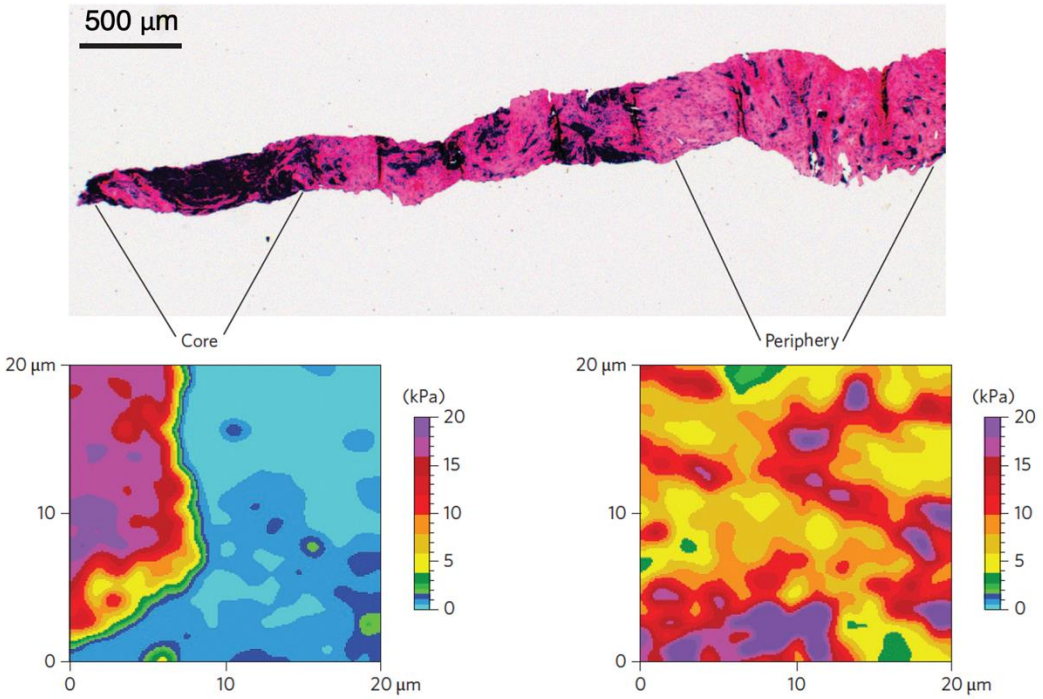

Figure 7: The Young Modulus (E) varies from core to periphery in human breast cancer biopsies. The representative E map (24 x 24 pixels) of the fibrotic periphery tissue presents higher E values than the tumour core, mostly composed of cancerous cells. (Reproduced from Plodinec et al. 2012)

Although diagnosis has been one of the key applications explored for nanomechanical fingerprinting, understanding the mechanical properties of tissue has been crucial for other applications like the development of implants (Prat-Vidal et al., 2020), by better mimicking the mechanical properties of the targeted tissue, or to understand how the mechanical properties of the tissue change as we age (Sicard et al., 2018).

1.2.3. Extracellular vesicles

While performing their functions extracellular vehicles (EVs) are exposed to several mechanical stresses that lead to changes in their shape. As an example, endo/exocytosis, fusion and transport are all processes that involve deformations of the EV's membrane.

Experimentally, it has been observed that changes in the global stiffness of EVs alter their endocytic pathways (Banquy et al., 2009), efficiency of uptake (Anselmo et al., 2015; Kol et al., 2007) and circulation time in the blood (Anselmo et al., 2015). Therefore, the mechanical characterization of EVs is seen as a key factor to understand the physiological and pathophysiological role that EVs

play in various diseases or to optimize their function when used as drug delivery vehicles.

1.3. Techniques for mechanical phenotyping

Several methods have been developed to measure the mechanical properties of biological samples. In this section we will go over the most prevalent techniques used in the field.

1.3.1. Micropipette aspiration

Micropipette aspiration is one of the most used techniques thanks to the simplicity of the setup. The sample is positioned at the end of a micropipette and a negative pressure is applied (Figure 8). By observing how the sample deforms as the pressure increases via an optical microscope the mechanical properties of the sample can be extracted.

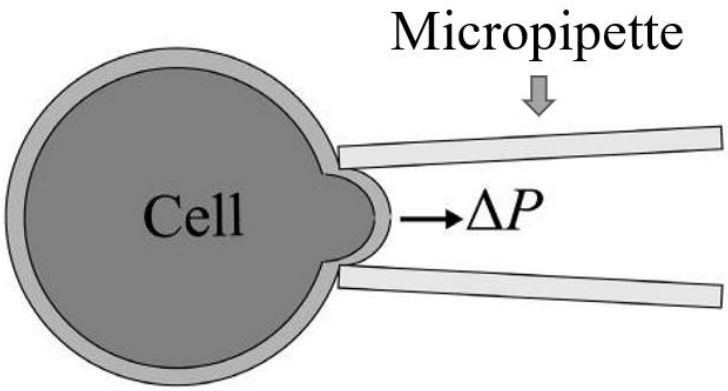

Figure 8: Diagram depicting the measurement on a cell by micropipette aspiration, where a negative pressure is applied (ΔP) to deform the cell.

Although it is simple, this method has several limitations:

- Spatial resolution: The spatial resolution is determined by the size of the opening of the micropipette. Specialized glass pulling methods can produce pipettes with an inner diameter in the range of tens of nanometres. However, these nanopipettes are in general custom made, very fragile and susceptible to clogging.

- Drift: The lack of parallelism in the contact region between the micropipette and the sample makes it practically impossible to measure small deformations. This highly limits the application of this technique to large bodies.

- Computationally demanding: To measure the deformation, each frame of the video acquired during the measurement must be processed. Depending on the duration of the experiment and the frame rate of the video this process can significantly contribute to the length of a single experiment.

- Low throughput: The classic setup for this technique is composed of a single micropipette measuring one sample for a fixed amount of time. In most cases the sample consists of bodies suspended in a liquid medium, therefore a period is required to position the opening of the micropipette close to the body to be measured, and aspirate medium till the sample is secured on the tip of the micropipette. Together with the postprocessing, these factors make the throughput of this setup low.

To overcome the limitations previously described, several approaches have been explored. For improving the throughput of this technique, microfluidic systems have been developed based on the principle of micropipette aspiration that allow for the parallel testing of multiple samples. Using a different approach, authors like Liu and collaborators (Liu et al., 2019) have incorporated a robotic sample feeder tube into the setup to eliminate the manual step of securing the sample on the micropipette's tip. With the goal of eliminating the time-consuming image postprocessing step of this technique, Berardi and collaborators (Berardi et al., 2021) have incorporated interferometry readouts to this setup, allowing for the direct measurement of displacement and pressure in real time with sub-nanometre resolution.

1.3.2. Optical Tweezers

This instrument uses a laser to create a potential well, capable of trapping objects within a specific region. As these systems are only capable of generating forces in the range of hundreds of piconewtons, they are normally used to manipulate particles attached to the cell membrane. Moreover, these systems can only work with small cells and the heating of the lasers can damage the cell, making it challenging to study cell mechanics.

Recent developments by Guk and collaborators (Guck et al., 2001), consisting on combining two divergent diametrically aligned laser beams to generate a two-dimensional potential well (Figure 9), have tackled some of the limitations of optical tweezers. This system allows for the confinement of larger cells (6 µm-30 µm diameter) and can generate enough force to apply small deformations (2-5%) to BALB 3T3 fibroblasts. However, when integrating more powerful lasers to achieve higher deformation forces, special consideration must be taken to assess and minimize the effect of the localized heating in the viability and the mechanical properties of the sample.

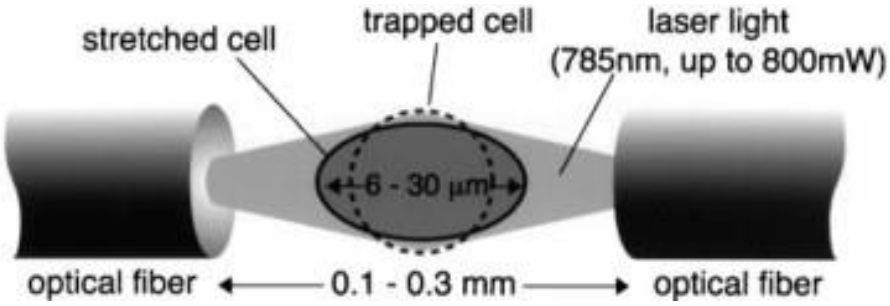

Figure 9: Diagram depicting the optical stretcher developed by (Guck et al., 2001)

As these techniques do not require direct contact with the sample and can measure cells in suspension, they can be integrated into microfluidic systems as the main mechanical characterization technique. Thus, it makes them viable for high throughput mechanical characterization of cells in suspension.

1.3.3. Magnetic Tweezers

This technique relies on placing magnetic beads inside or attaching them outside of the sample and optically observing how these beads move when a magnetic field is applied. By monitoring the displacement of the beads, the mechanical properties of the sample can be characterized. Magnetic bead twisting cytometry (MBTC) and magnetic bead microrheology (MBM) are the most used approaches to investigate the mechanical properties of cells using magnetic tweezers. MBTC uses the external magnetic field to apply torque to the beads, while MBM uses the magnetic field to translate them.

The major advantages of this technique are that it can easily be used to monitor the mechanical properties of the interior of the cell and that it can provide a reading of the mechanical properties of different parts of the cell all at once.

However, this technique relies on being able to reliably optically track the beads while being limited to only applying forces in the range of piconewtons and not allowing to choose where the stress is exerted on the cell.

1.3.4. Microfluidics-Based systems

One of the most promising approaches to develop a high throughput single cell mechanical screening technique suitable for the clinic is microfluidic-based systems, as they yield the highest throughputs of any current available technique (up to 20,000 cells/s) (Dudani et al., 2013). In these setups there are two main approaches to deforming the cells:

- Fluid-Based deformation: These techniques rely on using microfluidics to deform the cell, either by applying a known shear stress, generating a pinching flow or passing them through microchannels. By analysing the optical images acquired during the experiment and monitoring the deformation behaviour of the cell, the mechanical properties can be measured. An example of this approach is the chip developed by Belotti and collaborators (Belotti et al., 2019) which forms a single stream of evenly spaced cells and directs them to a region where a pinching flow capable of deforming cells has been generated (Figure 10).
-

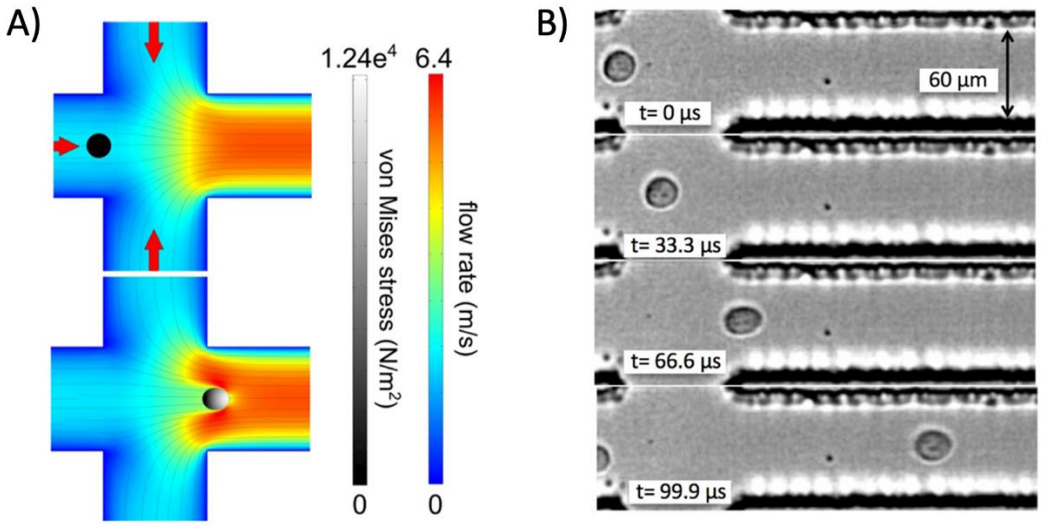

Figure 10: Microfluidic-based system developed by Belotti et al. 2019. The cells are directed into a region in the chip where a pinching flow deforms the cell. A) Diagram depicting the pinching flow and how the stress is applied on the cell. B) Optical image sequence of a cell being deformed by the pinching flow. Reproduced from (Belotti et al., 2019)

- Microelectromechanical Systems (MEMS)-Based deformation: Another approach to using the flow of the medium is to use MEMs to deform the cells. In 2018 Takayama and collaborators (Takayama et al., 2018) developed a system capable of detecting, capturing and compressing cells flowing through a microchannel by combining two systems capable of performing compression and sensing separately (Figure 11). By combining electrical and mechanical measurements at different compression levels this system allows for the multiparameter characterization of non-adherent single cells.

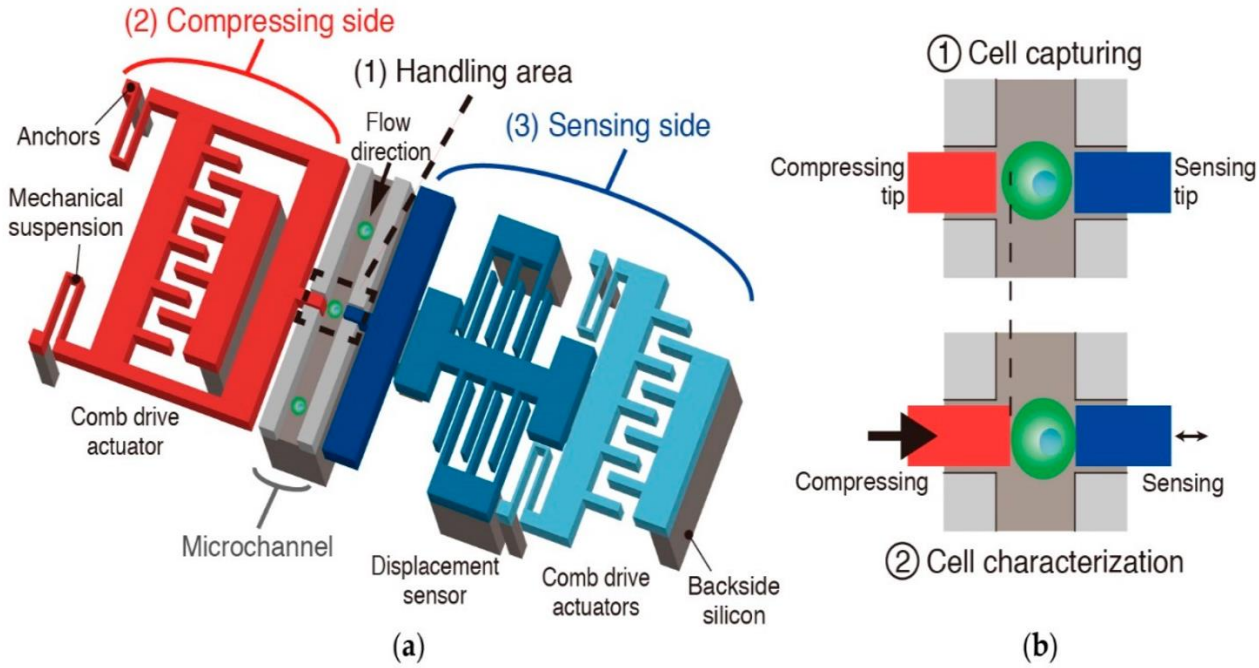

Figure 11:Diagram depicting the mechanism of the MEMS device developed by Takayama et al. 2018. This device consists of a microfluidic channel with two opposing tips to handle the cells, a series of comb drive actuators to perform compression and a differential capacitive sensor for displacement measurement. By adjusting the flow rate inside of the microchannel single cells can be captured between the sensing and compressing tip. (Takayama et al. 2018)

Although these systems present a higher throughput than any other mechanical phenotyping technique, they are limited to cells in suspension and can only provide a global measurement of the sample. This bulk measurement can be sufficient for certain applications, but as seen in chapter 1.1, cells are highly heterogeneous and valuable information about the distribution of the mechanical properties within the cell cannot be captured using these approaches.

1.3.5. Scanning Ion-Conductance Microscopy

The Scanning Ion-Conductance Microscope (SICM) consists of a micropipette with an electrode in its interior used to monitor the ion current (I) through the pipette. The value of I registered by the electrode depends on the position of the tip of the pipette relative to the sample. Therefore, by continuously monitoring I and incorporating this value within the z feedback loop, the tip of the micropipette can be moved across the surface of the sample to obtain its detailed topography without directly touching it (Hansma et al., 1989; Korchev et al., 1997).

Although this technique is traditionally used for imaging, developments like in the work of Rheinlaender and Schäffer (Rheinlaender & Schäffer, 2013) allow to use this approach for deforming the sample without mechanical contact using a pressure-induced microfluidic flow within the pipette (Figure 12), thus making it possible to map the sample's stiffness together with its detailed topography.

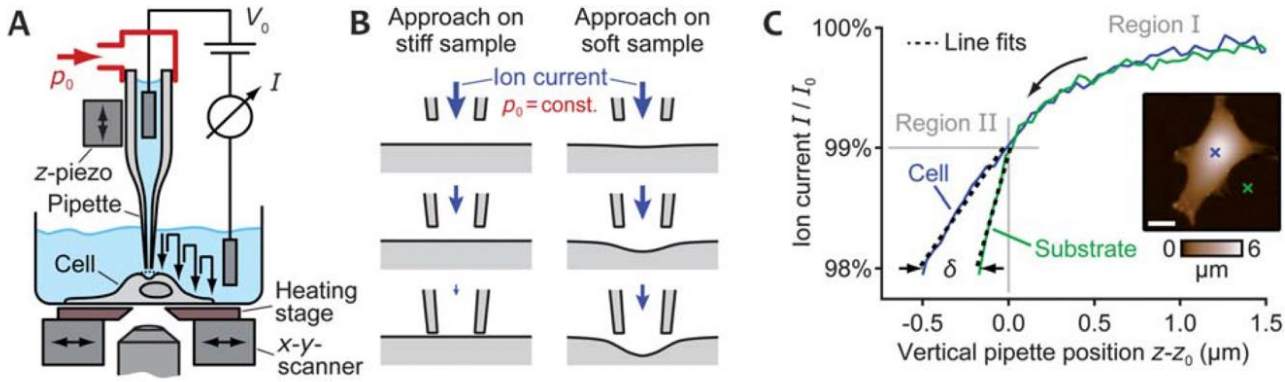

Figure 12:Figure depicting a SICM setup capable of acquiring mechanical measurements on cells by generating a flow to deform the cell. A) Schematic of the system components. B) By applying a constant pressure inside the micropipette, a microfluidic flow capable of deforming the sample is generated. If the sample is deformed with the pressure applied, the ion current will be larger at the same vertical pipette position. Making it possible to acquire ion current vs vertical pipette position curves and measure the stiffness of the sample. C) Example of ion current vs vertical pipette position curves on the substrate and on top of a cell. (Rheinlaender & Schäffer, 2013)

Advantages of SICM include its high-resolution imaging capabilities, non-invasive imaging that is suitable for delicate samples, live imaging of biological processes, versatility to image a wide range of samples, and its ability to provide topographic imaging of the sample surface.

However, SICM also has some disadvantages, such as its slow imaging speed, the need for a complex setup that can be difficult to operate, the possibility to

apply only small deformations to the sample, the susceptibility of the nanopipette to clogging, and its sensitivity to external interference, such as electrical noise. Nevertheless, this technique has been developing rapidly in the recent years to mitigate some of the negative aspects mentioned.

1.3.6. Atomic Force Microscopy

Currently atomic force microscopy (AFM) is the most widely spread method to characterize the mechanical properties of biological samples, thanks to its high versatility and it being a well stablished technique, with multiple groups specialized in this technique.

Since this work focuses on the development of AFM automation, chapter 1.4 offers a detailed explanation of the working principle of AFM together with its strong points and current limitations.

1.3.7. Summary table

Technique	Sample Restrictions	Mechanical Properties	High Throughput	Commercially Available
Micropipette Aspiration	In suspension	Elastic and viscoelastic properties of a region or the whole body	Potentially	No
Microfluidic-Based Systems	In suspension	Deformability of the whole body	Yes	No
Optical Tweezers	Adhered to substrate or in suspension	Elastic and viscoelastic properties of a region or the whole body	Potentially	Yes
Magnetic Tweezers	Adhered to substrate	Elastic and viscoelastic properties of a region	No	No
Scanning Ion-Conductance Microscopy	Adhered to substrate	Elastic properties of a region or the whole body	Potentially	Yes
Atomic Force Microscopy	Adhered to substrate	Elastic and viscoelastic properties of a region or the whole body	Potentially	Yes

Table 1:Summary table of the main techniques used for the mechanical phenotyping of biological sample.

1.4. Atomic force microscopy on biological samples

1.4.1. Working principle

The AFM is a near field scanning probe microscopy (SPM) technique based on the Scanning Tunnelling Microscope (STM), developed by Binning and Rohrer in 1981(Binnig & Rohrer, 1983), who were awarded the Nobel prize in 1986 for their design. By not relying on an optical imaging system the resolution of SPM is not limited by the diffraction limit of light, making it possible to study the interactions of molecules or single atoms. The clearest example of the value of this technique is how in 1982 STM was used to solve the mechanism of reconstruction of the Si (111) 7x7 unit cell, one of the most intriguing problems in surface science at the time. In a few days, using the STM Binning and Rohrer were able to experimentally observe the relief of Si (111) 7x7 unit cells bounded by minima (empty atom positions) and maxima (presence of adatoms) (Binnig et al., 1983). It thus provides the first real space determination of the Si (111) 7x7 unit cell reconstruction (Figure 13) and solving the mysteries of its mechanism.

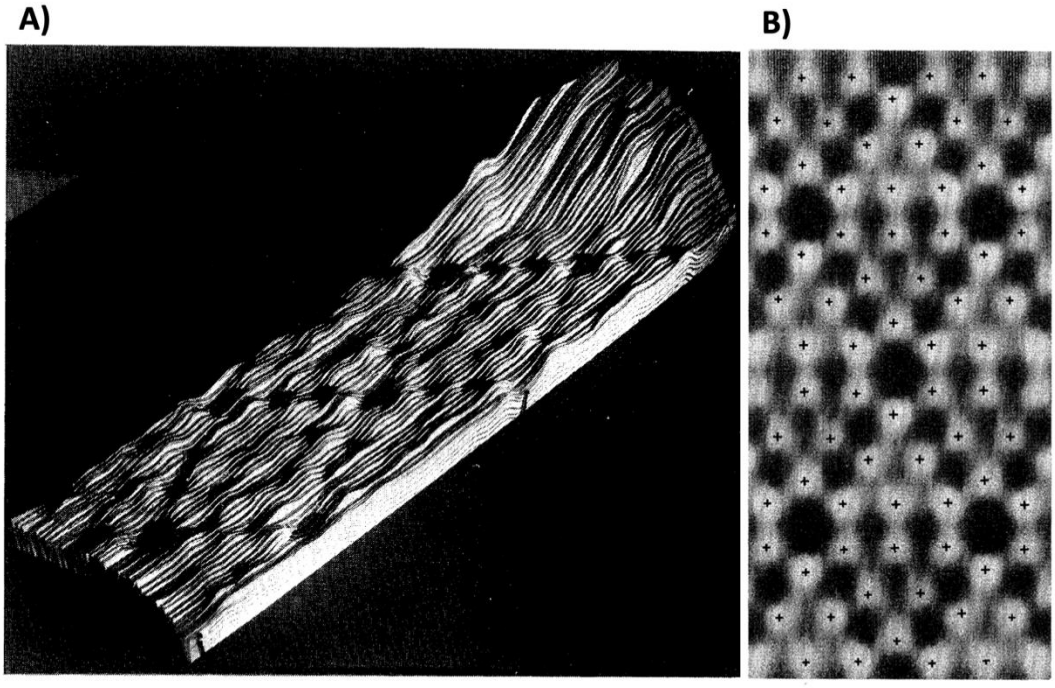

Figure 13:STM images acquired on Si (111). A) Relief of two complete Si (111) 7x7 unit cells. B) Top view of the relief shown in A (The hill at the right is not included). (Reproduced from Binning et al. 1983) (Binnig et al., 1983)

The major limitation of STM is that it can only be used on conductive materials, since current is being tunnelled from the tip to the substrate, both have to be conductors of electricity (Binnig & Rohrer, 1983). To overcome this challenge and extend the technique to non-conducting materials in 1986 Binning, Quate and Gerber (Binnig et al., 1986) developed AFM by proposing to use the sensitivity of STM to measure the forces between the front atom of the tip and the sample while it was being rastered under the tip. To monitor the position of the AFM tip, they incorporated a feedback system to measure the tunnelling current between an STM tip mounted on top of the gold foil cantilever where the AFM tip was mounted (Figure 14). This setup allowed them to monitor the position of the AFM tip with sub-Angstrom resolution while the sample was rastered under it and obtain the first topographic scans by AFM on an Al_2O_3 sample.

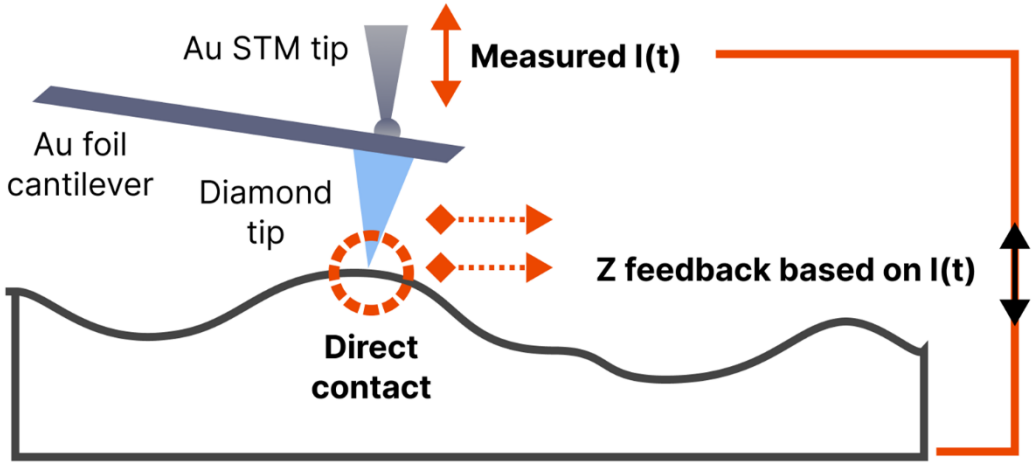

Figure 14:Experimental setup of the first AFM. An STM is used to monitor the deflection of a gold lever rastered on top of the sample surface. The tunnelling current between the gold cantilever and the STM tip (It) is used as feedback to control the sample z position.

Maintaining the tunnelling current between he STM tip and the gold foil cantilever was the main challenge of the early AFMs, making these instruments very delicate and unstable. To overcome this issue, several approaches were developed through the years to monitor the deflection of the cantilever. Most modern AFMs rely on a laser and a four-quadrant photodiode to monitor the deflection of the cantilever. By reflecting a laser on the back of the cantilever and aligning the reflected laser where the voltage of the four quadrants is identical, a subtraction circuit can be used as a null detector to measure the displacement of the cantilever in real time both in the up-down motion, based on how the voltage values change on the top and bottom quadrants, and the left-right motion, based on how the voltage values change on the left and right quadrants. It is then possible to measure both normal and lateral forces. The

development of the optical lever system revolutionized AFM (Figure 15), allowing it to be performed in liquid and enabling the study of living cells in the 1990s.

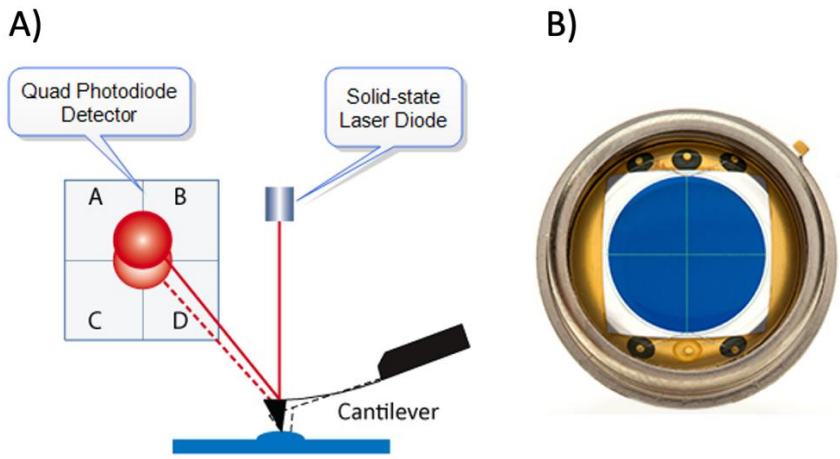

Figure 15:A) AFM Optical lever system (® Bruker). B) Quadrant pin photodiode (® First Sensor)

Similarly to STM, the AFM maintains a constant force as the tip is rastered across the sample surface by comparing the voltage output of the photodiode with a reference voltage by using a feedback circuit that adjusts the Z position of the sample or the cantilever, depending on the AFM setup.

To move in the x, y and z axis with the sensitivity that AFM requires to obtain high-resolution scans, piezoelectric actuators are commonly used (Figure 16). Piezoelectric materials have an atomic structure that allows them to change their shape when a voltage is applied to them. Modern piezoelectric actuators consist of a piece of piezoelectric material with two electrodes on opposite sides. By shifting the voltage difference the material can expand or contract on a given axis. Depending on the instrument design, all the piezoelectric actuators may be used to control the sample holder, the tip, or a combination of both (i.e., X and Y actuators controlling the sample holder and Z actuator controlling the tip position).

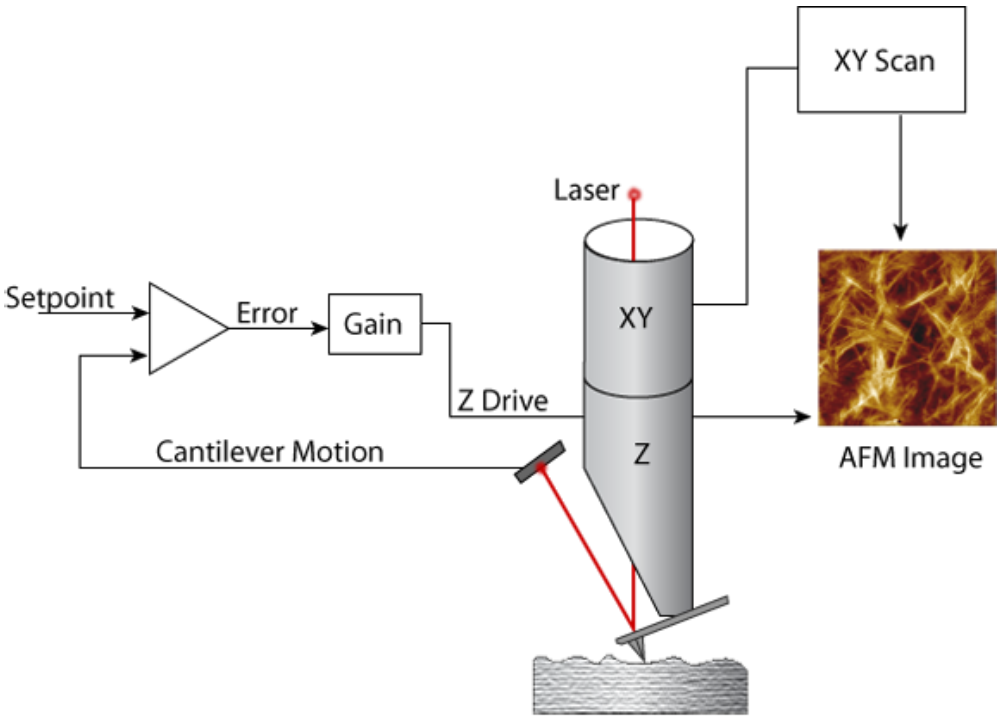

Figure 16:Schematic of AFM setup where the X, Y and Z piezoactuators are used to drive the probe and feedback-loop (Bruker®).

The relationship between the voltage applied and displacement of piezoelectric materials is non-linear, making it necessary to calibrate the piezoelectric actuators of the system. Piezoelectric actuators can also generate a voltage difference from displacement, making them suitable as sensors. Initially, piezoelectric sensors were incorporated to record the actual z displacement. However, by integrating these sensors into the feedback circuit they can be used to correct the voltage applied to the z actuator. This mode is commonly referred as 'z closed-loop', which greatly improves the accuracy and diminishes the distortion of the topographical images acquired.

1.4.2. AFM probes

The AFM probe is the sensor that interacts with the sample. It is typically made of silicon or silicon nitride and can be coated by different materials. Probes are composed by a cantilever with a tip on one of its ends mounted on a chip. Multiple cantilevers can be mounted on the same chip like in the MLCT-Bio probes manufactured by Bruker.

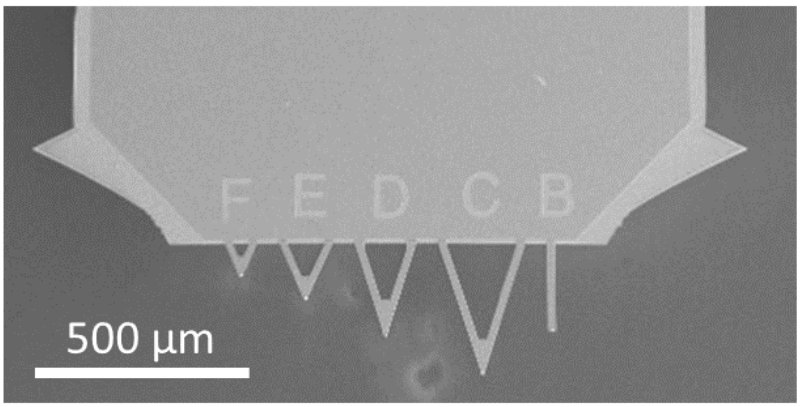

Figure 17:Scanning electron microscope image of a multi-cantilever MLCT-Bio probe. (Courtesy of N. Barois)

The cantilever behaves like a Hookean spring, making it possible to convert its deflection into force by applying Hooke's Law. The force exerted by a spring is then directly proportional to the amount of deformation or displacement from its equilibrium position. Mathematically, this can be expressed as:

$$F = k_{cant} \, x \, d$$

where F is the force applied to the spring, d is the displacement from the equilibrium position, and k_{cant} is the spring constant, which measures the stiffness of the spring and is typically measured in Newtons per meter (N/m).

Different cantilever lengths, materials and shapes result on multiple spring constants and resonant frequencies, making them suitable for different applications. Probes may also be coated with different materials to minimize artifacts, like optical interference, or to allow other applications, like magnetic force microscopy (MFM) in the case of nickel-coated probes or force spectroscopy measurements in the case of gold-coated probes.

The key parameters when selecting an AFM probe are:

- Spring constant (k): This parameter will limit the imaging force that can be applied. If the k of the sample is way larger than the one of the cantilever, the cantilever will bend, and the sample will not deform. In the same way, if the k of the sample is significantly smaller than the k of the cantilever, the tip will penetrate the sample without any detectable bending of the cantilever. For this reason, it is important to select a cantilever with a k that will allow the sample to deform as well as cause

the cantilever to deflect. Although this is critical for mechanical measurements, selecting a probe within the right k range is also important for imaging applications. If a sample is imaged with a stiff cantilever, the AFM tip will deform too much or damage the sample, resulting in images with artifacts or the destruction of the sample.

- Tip sharpness (r): This value determines the measurements lateral resolution. If r is too small, the tip can easily damage soft biological samples.

- Resonance Frequency (f): This value determined the duration it takes the cantilever to reach its equilibrium oscillation. Therefore, its value limits the maximum scanning speed.

- Quality factor (Q): This value determines the number of cycles it takes to reach equilibrium oscillation. Together with the resonance frequency, this value limits the maximum scanning speed.

Multiple tip geometries are available for scanning probe microscopy (Figure 18), each designed for specific applications. For imaging purposes, narrow needle-like sharp tips are preferred to achieve maximum resolution. However, when studying the mechanical properties of a sample, larger colloids of several micrometres in radius or blunted pyramids may be more suitable.

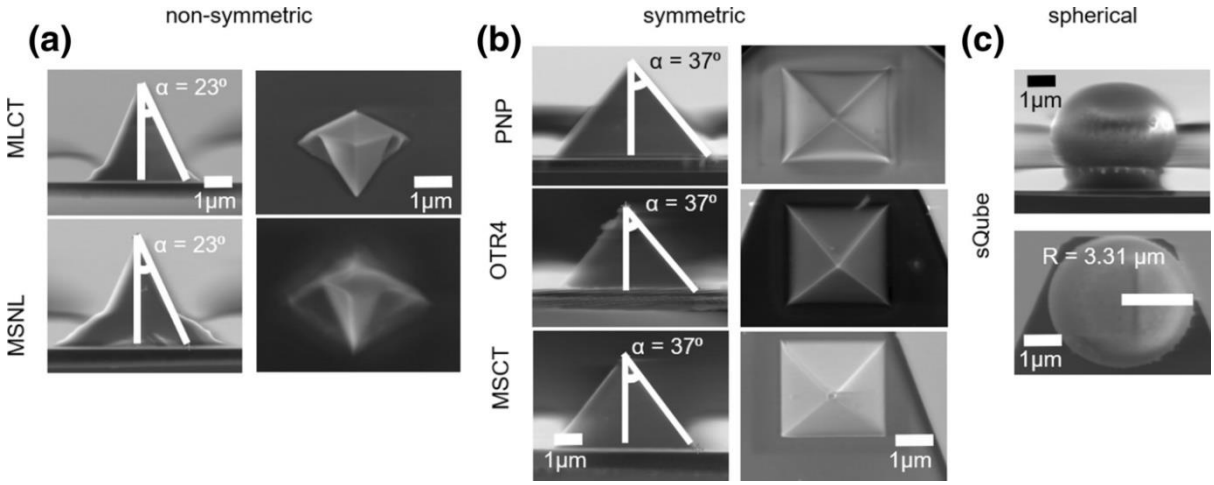

Figure 18:Examples of different AFM tip geometries. A) Non-symmetric pyramids. B) Symmetric pyramids. C) Spherical tips. Reproduced from (Zemła et al., 2020)

For biological samples, low spring constants and blunted tips are required to measure small forces (pN – μN) without damaging the sample. High-resolution images can be obtained by using sharp tips in combination with oscillating modes to minimize sample damage.

1.4.3. Imaging modes

To obtain a topographical image of the sample, the tip is raster-scanned on the sample surface while the feedback loop is used to adapt the tip position to the height of the sample and prevent the tip from crashing. There are three main imaging modes in AFM depending on the tip and sample interaction:

- Contact AFM (<0.5nm probe-surface separation): Being the first developed mode for AFM, in this mode the AFM tip and the sample remain in contact through all the scans. However, this approach can easily displace and deform the sample as a result of the normal and lateral forces applied by the tip. This makes it sometimes unsuitable for soft delicate samples, limiting its applications in biology.

- Oscillating Mode / Tapping Mode® (0.5nm – 2nm probe-surface separation): To minimize the damage of the sample, the tip is oscillated so it enters in intermittent contact with the sample. This approach is critical for applications like High-Speed AFM where delicate molecules like DNA are imaged at speeds up to 500 μm/s to obtain movies displaying their dynamics.

- Non-Contact (0.1nm – 10nm probe-surface separation): During the measurement the tip is oscillated over the sample. The shifts in the amplitude of the oscillation or the changes in resonant frequency can be monitored at constant height or used as reference channel to drive a feedback loop to generate a scan of the sample surface. However, the applications of this mode in biology are very rare due to its difficult use in liquid medium.

1.4.4. Force modes

On a classical AFM experiment to characterize the mechanical properties of a sample, tip-sample force versus tip-sample distance curves are acquired by a cyclic z-movement of the cantilever in and out of contact with the sample.

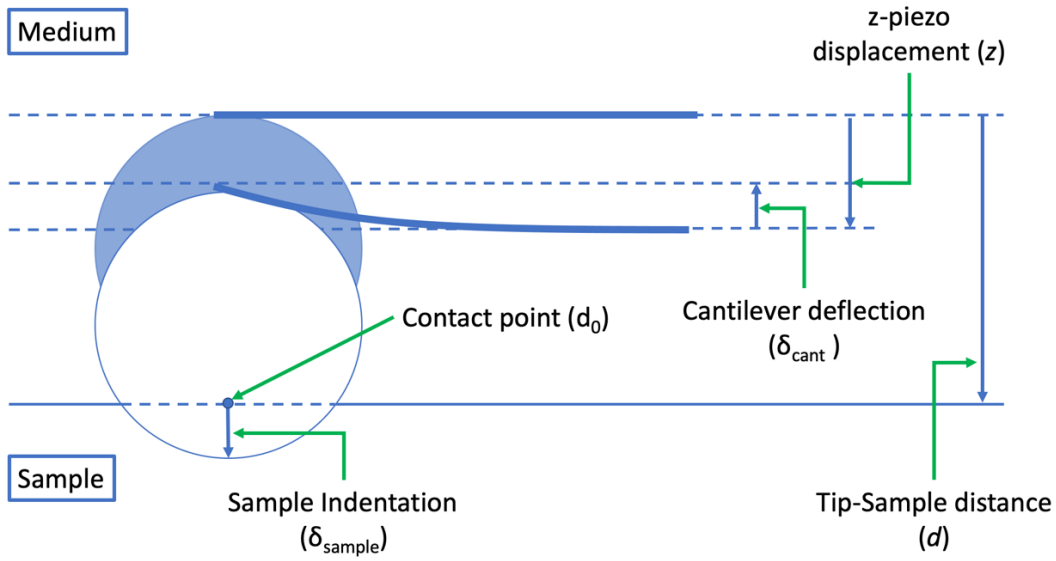

Figure 19:Diagram depicting an AFM tip indenting the sample with the nomenclature normally used to describe the physical variables involved in the process.

However, the AFM does not measure tip-sample force (F) versus tip-sample distance (d) but rather cantilever deflection (δ) versus z-piezo displacement (z) (Figure 19). To convert δ vs z curves into F vs d curves, first cantilever deflection – z data is collected for each cantilever deflection value. To obtain F, Hooke's law is applied:

$$F = k_{cant} \, x \, \delta_{cant}$$

For obtaining d from z, the length of the tip is ignored and d_0 (distance at which the tip and the sample are in contact) is considered as an arbitrary value. With these assumptions we obtain:

$$d = z + \delta_{cant}$$

The dominant interactions between the AFM tip and the sample at non-contact short probe-sample distances are Van der Waals interactions. However, long-range interactions like capillary or electrostatic forces are significant further away from the surface. When the tip and the sample enter in contact, the probe

experiences predominately repulsive Van der Waals forces. Once the force setpoint is reached and the tip starts to retract from the sample, the tip mainly experiences attractive Van der Waals forces. Figure 20 presents a visual representation of the effect of these forces while acquiring a force-distance curve.

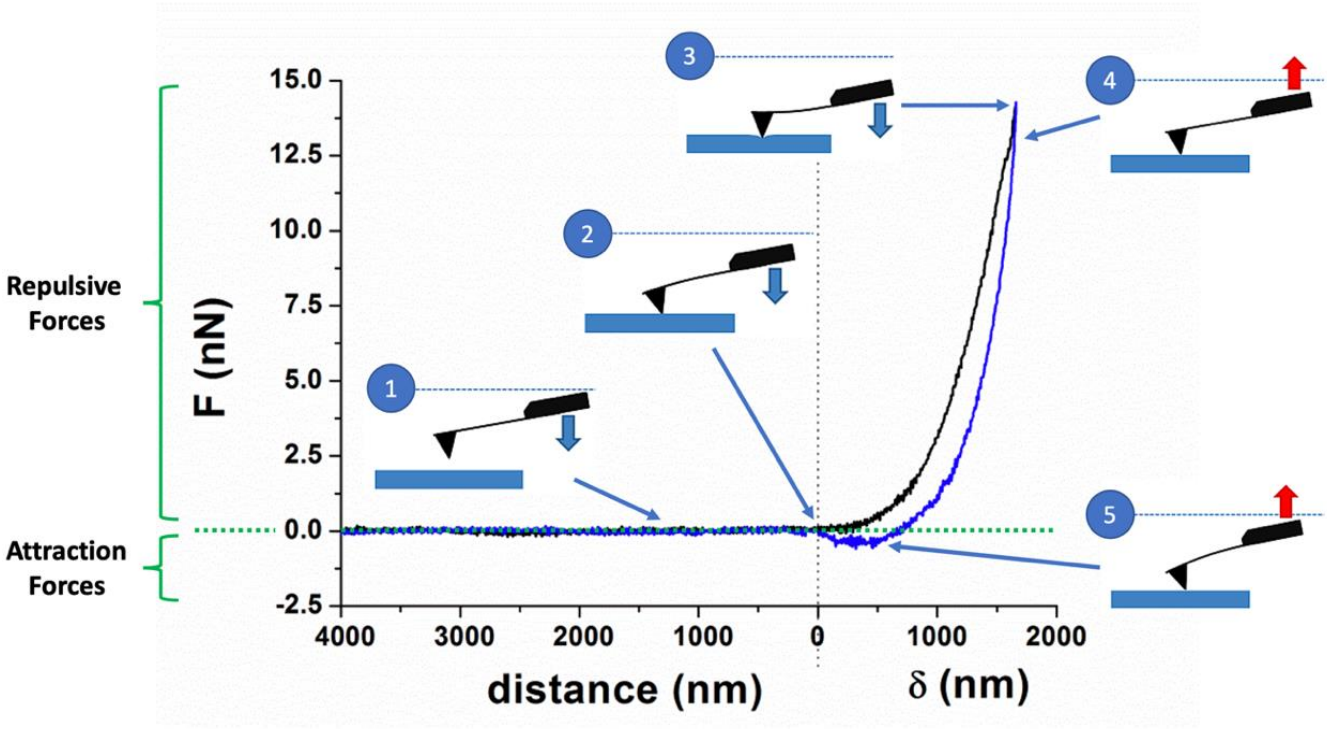

Figure 20:Summary of tip-sample force vs tip-sample distance curve acquisition by AFM. 1) The cantilever approaches the sample surface. 2) The AFM-tip contacts the sample surface. 3) The force (F) / indentation (δ) setpoint is reached. 4) The cantilever starts to retract from the sample surface. 5) The maximum attraction force is sensed by the cantilever before detaching the sample. Image modified from (Gavara, 2017).

There are two main approaches when modelling the repulsive interaction when the tip contacts the sample (Figure 21). One option is to consider the tip and the sample as a collection of atoms and their interaction as a collection of atom-atom interactions or molecule-atom interactions depending on the composition of the substrate. However, this is a very fundamental and complex approach to describe the system, which requires complex calculations and to know where the atoms of the system are located. Considering that this interaction involves a macroscopic number atoms, a simpler approach is to use continuous models to describe this interaction. The probe can be modelled as a sphere, cone or pyramid, depending on the geometry of the tip, while the sample is modelled as a plane and continuum elasticity can be used to describe the interaction between the tip and the substrate. When working with

biological samples like liposomes, cells and tissues the second approach is the most used in the AFM community (Carl & Schillers, 2008).

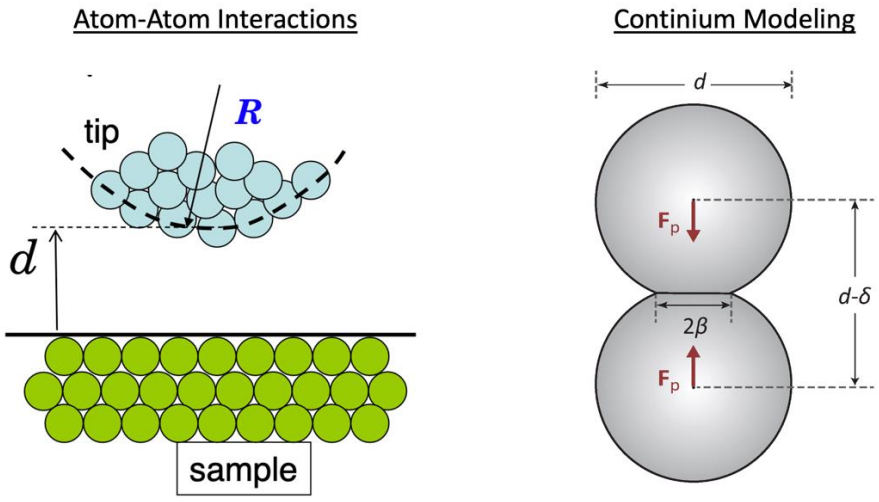

Figure 21:Diagram depicting the two main approaches to model the tip-sample interactions during an AFM measurement. Reproduced from (Raman et al. 2002 & Leduc et al. 2016)

1.4.5. Contact models

When studying contact mechanics, the aim is to define:

- The nature of the contact: know if its reversible (elastic material) or if there is hysteresis (viscous material).
- The contact area as a function of the force applied.
- The presence of deformation or adhesion.
- Analytical models that relate these properties and allow us to quantify them.

The origin of the contact mechanics field can be traced back to 1881, when Heinrich Hertz published his manuscript 'On the contact of elastic solids' (Hertz, 1882). In his work, Hertz aimed at understanding how the optical properties of lenses stacked together would be influenced by the force keeping

them together. He modelled this system as two spheres that deform under the imposed loads when they enter in contact. By half-space approximation this model can be extended to a sphere in contact with an infinite half space. The deformation of the material under load is dependent on its elastic modulus, which describes the resistance of a material to being deformed elastically when a stress is applied to it. However, the Hertz model considers a contact between homogeneous and isotropic materials, with no adhesion, infinite thickness of the bodies, under small stresses (i.e., linear regime) and with purely elastic deformation (no viscosity considered).

Bradley, in 1932, modelled this system as contact between two rigid spheres only considering atom-atom interactions according to the Lennard-Jones potential. Later in 1965 Sneddon extended the model by considering a rigid shape (i.e., sphere, cone, pyramid, ...) contacting a linearly elastic half-space. Nevertheless, neither Hertz, Bradley nor Sneddon considered the effect of the long-range Van der Waals surface forces in the interaction.

Two main models emerged during the 1970s that included the effect of Van der Waals forces when the atoms are close but not in contact. The Johnson-Kendall-Roberts (JKR) model (K. L. Johnson et al., 1971) describes a soft tip contacting a soft substrate and includes the short-range forces in the contact region as the tip approaches, contacts and retreats from the substrate.

On the other hand, the Derjaguin-Müller-Toporov (DMT) model (Derjaguin et al., 1975), considers an elastic sphere contacting a rigid substrate, while taking into consideration the Van der Waals forces outside of the contact region. In 1992 Maugis proposed a generalized multiparametric model bridging the gap between the limits of the JKR and DMT theories (Maugis, 1992).

Currently, the most widespread method to study the mechanical properties of biological samples by AFM is to fit a contact model to the approach segment of each force-distance curve for obtaining the Elastic Modulus (Carl & Schillers, 2008). The model is chosen based on the tip geometry used during the experiment, such as Hertz (Hertz, 1882) for a paraboloidal tip, Sneddon (Sneddon, 1965) for a conical tip, or Bilodeau (Bilodeau, 1992) for a pyramidal tip. For stiff samples with low adhesion, the DMT model is typically used. While for soft samples with high adhesion, the JKR model is applied (Figure 22).

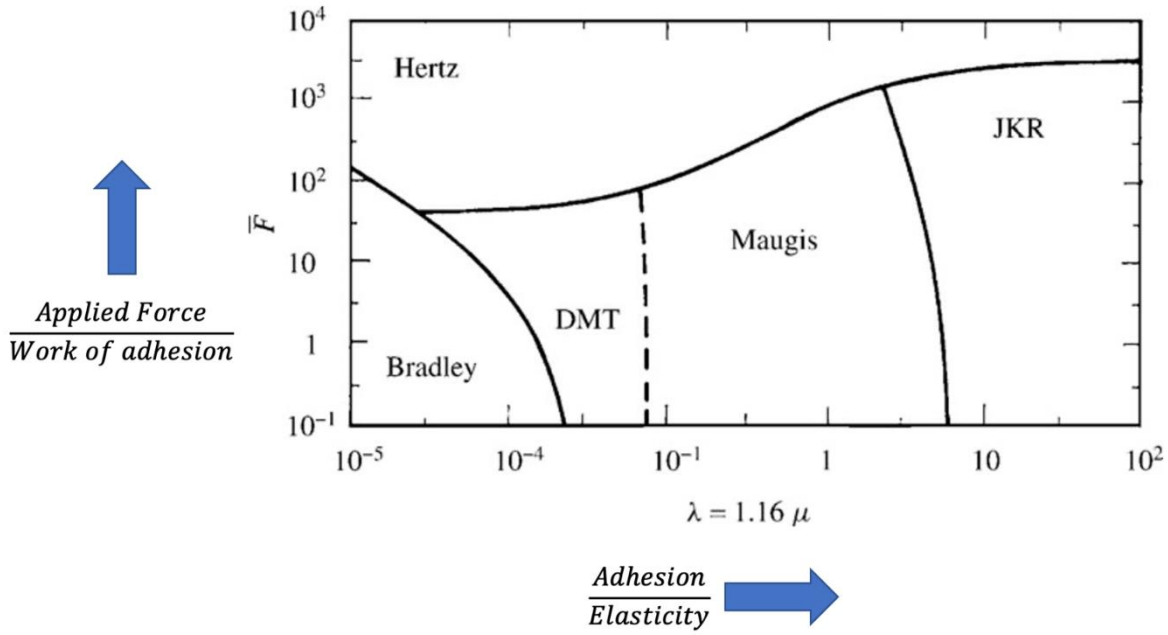

Figure 22:Diagram depicting which model to use based on the reduced load ($\bar{F}$) and the elasticity parameter (λ). Reproduced from (Leite and Herman 2005).

All models mentioned above describe a non-deformable probe of a known geometry indenting an infinite purely elastic, isotropic, linear half space of known Young´s modulus and Poisson ratio, conditions that are not met in an experimental setting. Therefore, the absolute values obtained from this analysis can only be considered as an approximation. Nevertheless, this approach allows to compare the values obtained in different samples, under the same experimental conditions, and gather insights of how the mechanical properties change.

Although biological samples are commonly modelled as purely elastic materials, cells and tissues exhibit a viscoelastic behaviour. For this reason, alternative AFM acquisition modes and contact models have been developed to characterize the viscoelastic properties of biological samples (Figure 23):

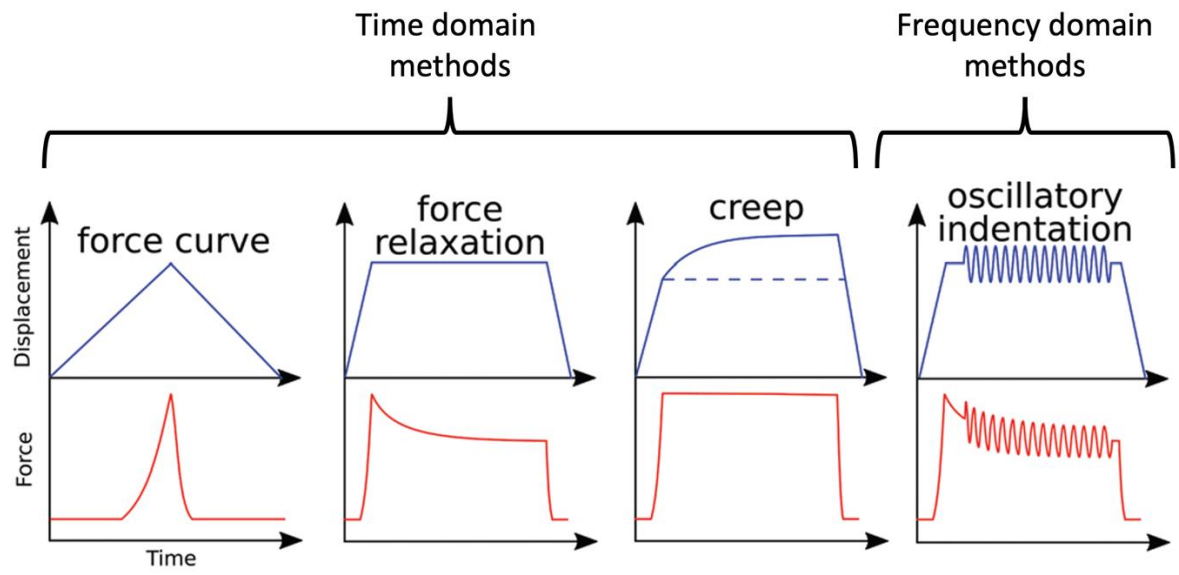

Figure 23:Schematic showing the main AFM protocols to measure the viscoelastic properties of biological samples (Efremov et al. 2019).

Time domain methods:

The force relaxation and creep methods are the classical approaches to measure viscoelastic properties with AFM. In these experiments the sample is loaded and then either the indentation depth (force relaxation) or the force is kept constant. The data acquired can be modelled after classical viscoelastic models, like the Kelvin–Voigt model, to describe stress-relaxation behaviour, or the Maxwell model, to describe creep behaviour (Efremov et al., 2019).

Force curves consisting of an approach-retract cycle are the most simple and ubiquitous measurements obtained by AFM. In 2013 Rebelo and collaborators (Rebelo et al., 2013) proposed a method to obtain qualitative information about the local apparent viscoelastic properties of the cell by computing the area of the gap between the approach and retract segments which is proportional to the apparent viscosity. Several models have been proposed to quantify the viscoelastic behaviour of cells from classical force-distance curves (Figure 24), based in the works by Lee and Radock, Graham and Ting (Graham, 1967; Lee & Radok, 1960; Ting, 1966, 1968). Although the data required for this approach can be acquired in most AFM setups, the models to quantify viscoelasticity from these measurements are complex and are not widely available neither in commercial nor in open-source software.

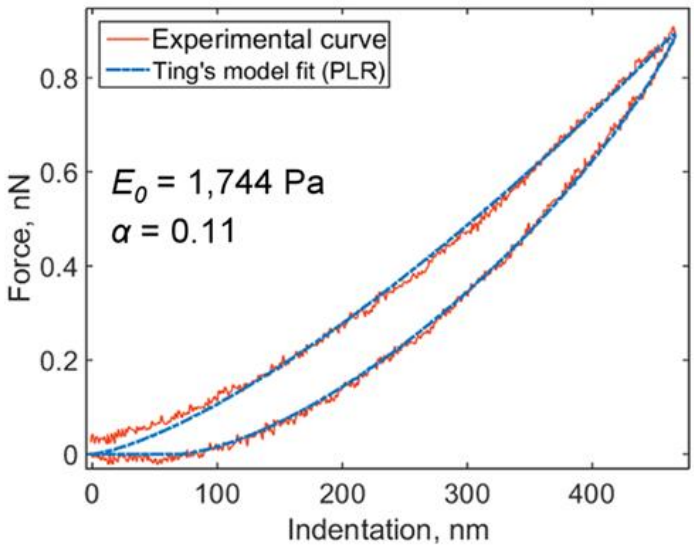

Figure 24:Example of how the instantaneous elastic modulus (E_0) and the power law exponent (α) can be obtained by fitting the viscoelastic model developed by Efremov et al. 2017. Values of α are in the range of 0-1. Values close to 0 represent solid like behaviour, while values close 1 represent fluid like behaviour. Reproduced from (Efremov et al. 2017)

Frequency domain methods:

In 2003 Alcaraz and collaborators (Alcaraz et al., 2003) proposed an AFM-based method to measure the storage and loss modulus of the sample at the nanoscale, by oscillating the cantilever at different frequencies while indenting the sample. Although this technique allows to work with a wide range of frequencies, it requires a specialized setup and additional instrument calibrations (i.e., piezo lag, viscous drag correction).

The classical approach to perform these experiments is to indent the sample and apply cyclical forces at different frequencies. Although, the z-piezo movement is normally used to oscillate the cantilever, other methods have been developed to excite directly the cantilever and achieve higher operational frequencies. Additionally, with the goal of increasing the rheological properties on a wider frequency range and increasing the acquisition speed of these measurements, other approaches have been developed consisting on oscillating the cantilever using a multi-frequency signal (Roca-Cusachs et al., 2006) or performing a sweep of frequencies (Schächtele et al., 2018).

1.4.6. Calibrations

The AFM is an instrument that inputs voltage into piezoelectric actuators and outputs voltage values measured by a photodiode. To convert these voltage values into physical properties like sample deformation or force, that can be used to measure the mechanical properties of a sample, three main calibrations are needed:

- Piezo calibration: This step allows to obtain the factor to convert voltage applied to the piezo actuator into displacement. This procedure must be done for each X, Y and Z piezo. By scanning standard gratings of known dimensions in contact mode, the calibration factor to convert measured volts into piezo displacement is obtained. Many modern instruments now incorporate a Z-sensor that detects how much the Z-piezo is moving, requiring to perform these calibrations less often.

- Cantilever deflection calibration: To record the tip-sample interaction forces the deflection angle of the cantilever is measured through the photodiode. According to beam theory the deflection of the cantilever is linearly proportional to the up-down tip displacement. Therefore, by measuring the voltage output of the photodiode the tip position can be obtained. The classical approach for this calibration, called contact-based approach, consists in obtaining a force-distance curve on a non-deformable stiff substrate (i.e., mica, glass, silicon, sapphire, depending on the sample to be characterized). This can be challenging in cell samples, because even the bare regions of the glass will be covered by extracellular matrix secreted by the cells. The slope on the contact region of the curve corresponds to the deflection sensitivity, which is the factor that relates z-piezo displacement to cantilever deflection in volts. In 2017, Schillers and collaborators (Schillers et al., 2017) reported the results of their AFM calibration standardization study. In this work, they observed that the deflection sensitivity determined by this method will be wrong by between 5% and 20%. This error will then be carried on when determining the spring constant, which will be offset by roughly twice the error in the deflection signal.

  The major disadvantage of contact-based methods is that sharp tips can be damaged when indenting stiff substrates. For this reason, calibration is often performed at the end of the experiments, especially in force

spectroscopy, to avoid destroying the grafting on the tip. In 2006 Higgins et al. (Higgins et al., 2006) proposed a non-contact method to obtain the deflection sensitivity from the thermal spectrum of the cantilever, assuming that the spring constant remains unchanged in air and liquid. This approach requires a previous calibration of the spring constant in air with the Sader method. As this method yields a deflection sensitivity different to the one obtained by contact-based methods, the result is then multiplied by a correction factor to obtain the correct value.

- Cantilever stiffness calibration: Together with the cantilever deflection calibration, cantilever stiffness calibration must be done for every cantilever. The determination of the cantilever's spring constant (k_{cant}) is extremely important for any quantitative application of AFM. Knowing the force that is being applied to the sample, it allows to understand the physic regime of the experiment. Volts do not provide intuition of the stress being applied to the sample, whereas by knowing the force being applied in the contact region, the stress applied can be easily determined. Moreover, voltage is not a magnitude that can be compared between systems, since it heavily relies on the components of the instrument and the positioning of the laser on the photodiode.

  Although the length and width values of the cantilever provided by the probe manufacturer tend to be exact, the precise thickness of the cantilever is often not known due to the great difficulty of controlling the chemical etching processes used during manufacturing; thus, the spring constant of the cantilever cannot be directly obtained by applying $k_{cant} = Eb t^3/4L^3$, where E is the elastic modulus, b the width, L the length and t the thickness of the cantilever. Scanning electron microscopy (SEM) could be used to determine the thickness of the cantilever. However, it requires access to a SEM and would have to be performed after every experiment. Instead, vibrometers can be used to calibrate the spring constant of AFM cantilevers with high accuracy. However, these devices are expensive and not widely available. Manufacturers like Bruker and Olympus sell pre-calibrated probes using this method commercially.

  To address this issue, many indirect methods have been developed, with the Sader method being the most widely used, thanks to its ease of use and applicability to different cantilever geometries (rectangular, V-shaped).

The Sader method relies on measuring the Q factor and resonant frequency from the thermal spectrum of the cantilever to estimate k using hydrodynamic theory. This approach considers that as the cantilever oscillates the surrounding fluid applies force on the cantilever in two ways: by adding resistance to the motion (hydrodynamic drag) and by adding mass to the cantilever. By relating the measured resonant frequency and Q factor of the cantilever oscillating in a fluid to the values in a vacuum, the analytical formula to determine the spring constant of the cantilever for the first eigenmode (k_1) can be derived, taking into consideration density and viscosity of the fluid (Figure 25).

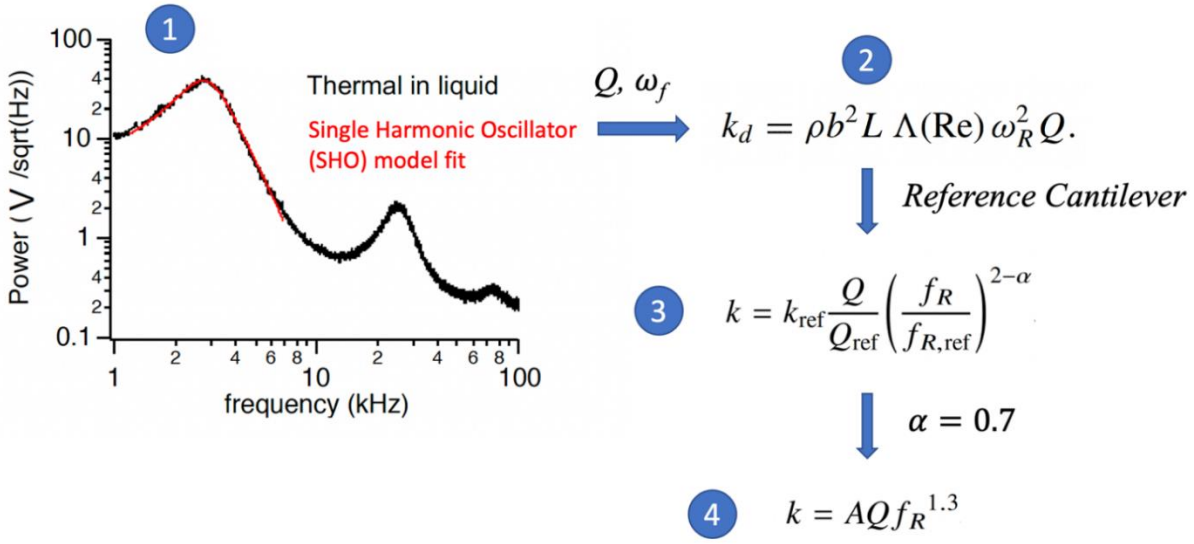

Figure 25 Diagram representing the Sader method cantilever calibration. 1) The first eigenmode is fitted using the SHO to obtain the experimental cantilever's amplitude (A), Quality factor (Q) and resonance frequency (ωf). 2) Using the experimental parameters an initial value of k1 is obtained. 3) The computed k1 in step 2 is refined by comparing the experimental values of the quality factor (Q) and the resonance frequency (fR) to the reference values of a cantilever with the same geometry, Q, k1 and fR. 4) Through appropriate averaging expression on step 3 can be generalized to accommodate multiple reference cantilevers. This results on the expression on step 4, where A is a universal coefficient for a particular cantilever geometry. (Sader et al., 2012, 2016)

1.4.7. AFM Strong points and limitations

This section includes a summary of the strong points and current limitations of AFM for studying biological samples.

- Strong points:

    - As a type of SPM, AFM does not rely on optics to generate an image and is not limited by the diffraction limit of light. Therefore, high resolution images can be acquired by AFM, making it possible to study single molecules like DNA.

    - Since, the AFM generates an image by rastering a tip over the surface of the sample, no labelling is required, allowing for high sample versatility.

    - AFMs can operate both in-air and in-liquid. Allowing the measurement of a wide range of samples, from Silicon wafers in-air to cancerous cells in-liquid.

    - To study the mechanical properties of materials, in AFM the sample is indented with a tip mounted at the end of a cantilever until a certain deformation or force setpoint is reached. As the deflection of the cantilever can be precisely monitored, the AFM is able to apply a wide range of forces, ranging from pN-μN.

    - AFM is a highly versatile technique. Several force measurement modes and mechanical models have been developed, allowing to characterize multiple physical properties of the sample (elasticity, adhesion, viscoelasticity) in 2D and 3D (Gnanachandran et al., 2022). Moreover, since the AFM probe can directly interact with the sample, by functionalizing the AFM probe, chemical and biological properties (molecule recognition, cell activity) of the sample can also be determined (Bueno et al., 2017). Whole cells can be attached to the functionalized AFM tip or tip-less cantilever to measure the forces involved in intercellular (Sancho et al., 2017),

host-pathogen (Ciczora et al., 2019) or cell-extracellular matrix (Chighizola et al., 2022; Holuigue et al., 2023) interactions.

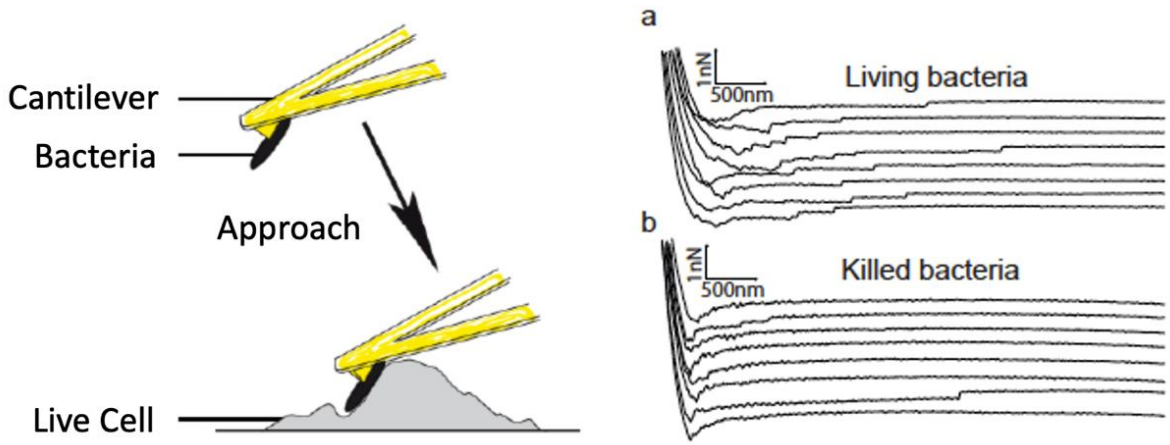

Figure 26: Diagram summarizing the work of Ciczora et al. 2019. A live or dead bacteria is attached to the AFM cantilever tip and brought into contact with a living cell (left). Force-distance curves are acquired (right). Force-distance curves acquired with living bacteria (a) present more adhesion events than the curves acquired with dead bacteria (b). A part of the number of adhesion events, the adhesion forces between the bacteria and the cell can be measured. Image reproduced from (Ciczora et al., 2019)

Nanomanipulation of the sample is also possible with AFM. As an example, FluidFM (Meister et al., 2009), consisting of a hollow cantilever incorporating a nanofluidic channel in its interior, have enabled developments like Live-seq, which allows the sequential profiling of single-cell transcriptomes in live cells (Figure 27).

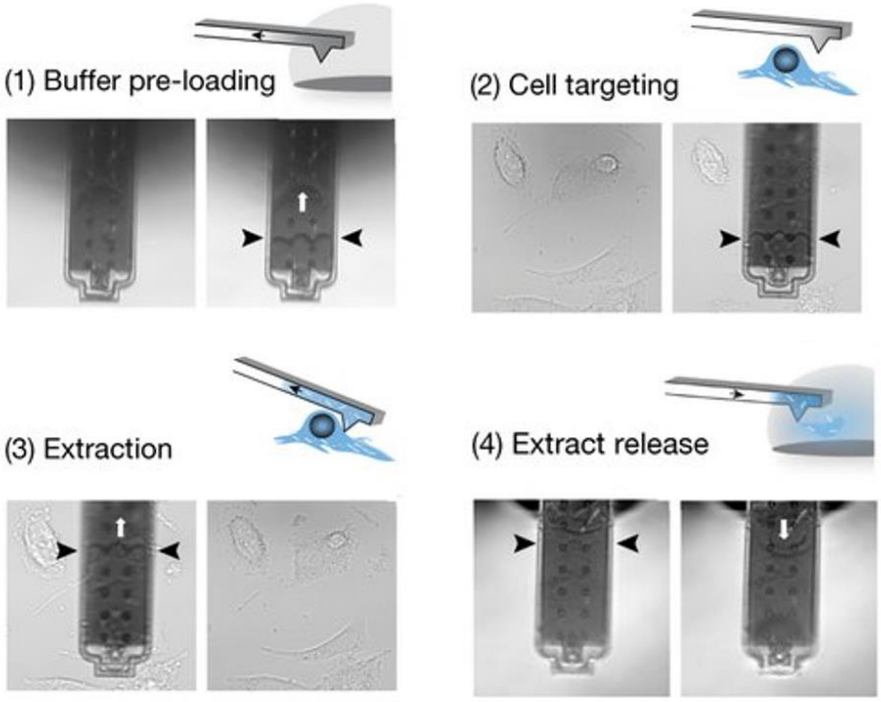

Figure 27: Diagram summarizing the principle of Live-seq using FluidFM. 1) The microchannel inside of the cantilever is loaded with buffer. 2) The user selects the cell from the sample. 3) The sample is extracted from the cell. 4) The extract from the cell is released. Reproduced from (W. Chen et al., 2022)

- Limitations for Imaging:

    - Many biological samples are extremely delicate, making it impossible to image them by AFM in contact mode. Oscillating and non-contact imaging modes have helped to minimize this issue and have extended the application of AFM.

    - AFM remains a "surface" technique that can only be used to image the cell surface, unlike other microscopy techniques like fluorescence or transmission electron microscopy.

    - Measurements acquired by AFM correspond to the topography of the sample plus a convolution of the tip shape, deformation of the sample and instabilities in the feedback system. Damage to the tip or contamination getting adhered to the tip can result in the effect of these artifacts on the image getting amplified.

    - A major limitation of conventional AFM imaging is its low time resolution when compared with other techniques like confocal

microscopy. Advances like miniaturizing the system's piezoactuators and the AFM probe, allow High-Speed AFM to image at speeds ~1000 times faster, making it one of the few techniques available that allows the monitoring of dynamic molecular biological processes in real time (Figure 28) (~100 ms) (Dufrêne et al., 2017). However, most current HS-AFM setups cannot be used on mammalian cells or tissue samples, due to their rough topographical profile.

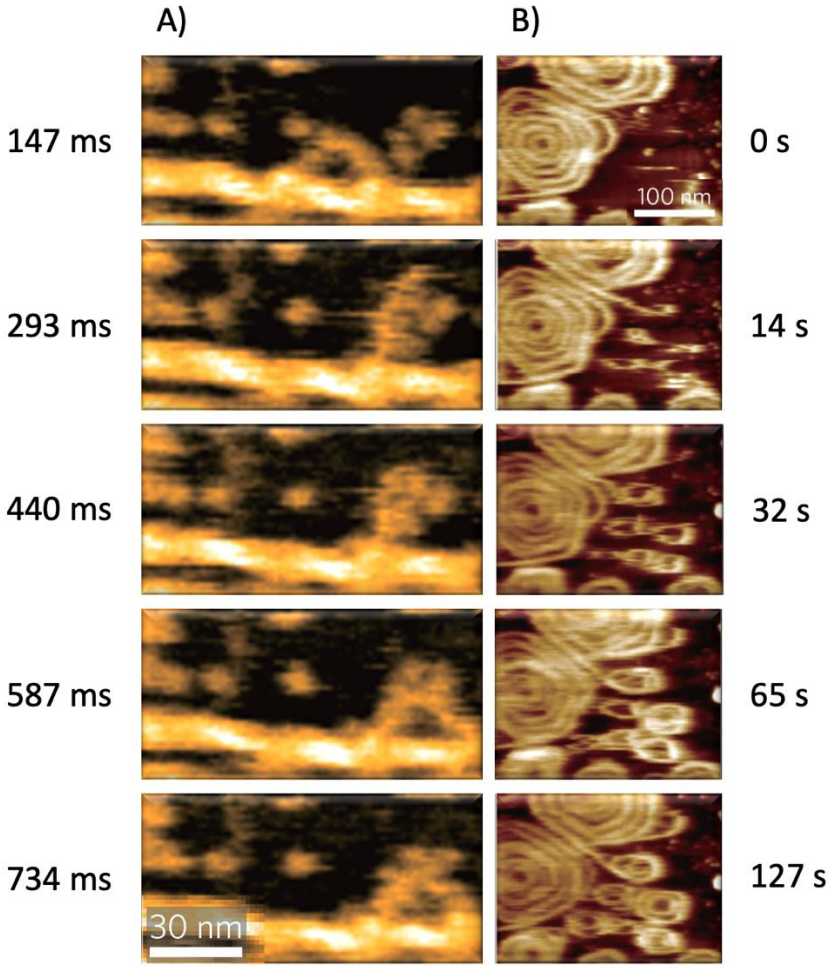

Figure 28: Examples of High-Speed AFM being used to study molecular processes. A) Myosin V walking unidirectionally along an actin filament, showing rotation of the leading lever-arm on trailing head detachment from actin (Kodera et al., 2010). B) Spiral filament formation by polymerization of the ESCRT-III protein Snf7 on a supported lipid membrane (Chiaruttini et al., 2015).

- Limitations for mechanical measurements

    - For most applications focused on the sample mechanical characterization, contact mode is required to obtain force-distance curves without artifacts that can be properly fit to the corresponding model. Moreover, when acquiring several force-distance curves on a sample, it is important to ensure that that the sequential measurements have not damaged the cell and altered its mechanical properties.

    - Acquiring AFM measurements in biological samples is a highly user intensive process when compared to other AFM applications, like silicon wafer quality control, where the whole process is highly automated. During an AFM experiment on a biological sample, the user must prepare the sample, calibrate the AFM probe (deflection sensitivity and spring constant), load the sample, approach to the sample surface, locate the region within the sample, acquire the measurement and repeat the process for several areas in the sample.

      During this process the user must also monitor the total photodiode sum, observe if there is any laser drift and correct it, while ensuring that no contamination adheres to the tip or cantilever of the probe. As a result, the throughput of these experiments is low, with ~20 (Lekka & Laidler, 2009; Marcotti et al., 2019) being the common number of regions measured on a sample. However, to determine the appropriate number of regions to measure, the stiffness variations in a single region and in the population must be taken into consideration. In the case of single cells, they can be considered as heterogeneous objects and take multiple indentations at different locations to then calculate Young's modulus for each cell separately (Lekka & Laidler, 2009).

    - When a new AFM probe is mounted both the deflection sensitivity and spring constant of the cantilever must be calibrated by the user. How these calibrations are performed directly affects the values measured, making them critical for comparing the mechanical measurements of different samples. Laser drift, contamination adhered to the probe and bubbles can cause

changes in the deflection sensitivity and spring constant during the experiment, making it impossible to aggregate or compare these values. Therefore, to ensure good-quality AFM data acquisition it is critical to monitor deflection sensitivity, spring constant and photodiode sum during the experiment, while being able to detect the presence of laser drift and correct it. As a result, AFM is a very protocol-dependent technique, making it challenging to compare measurements made by different users and different instruments. Calibration methods like the SNAP (Schillers et al., 2017), which rely on pre-calibrated probes, have improved the estimation of the deflection sensitivity, leading to reduced variability between measurements.

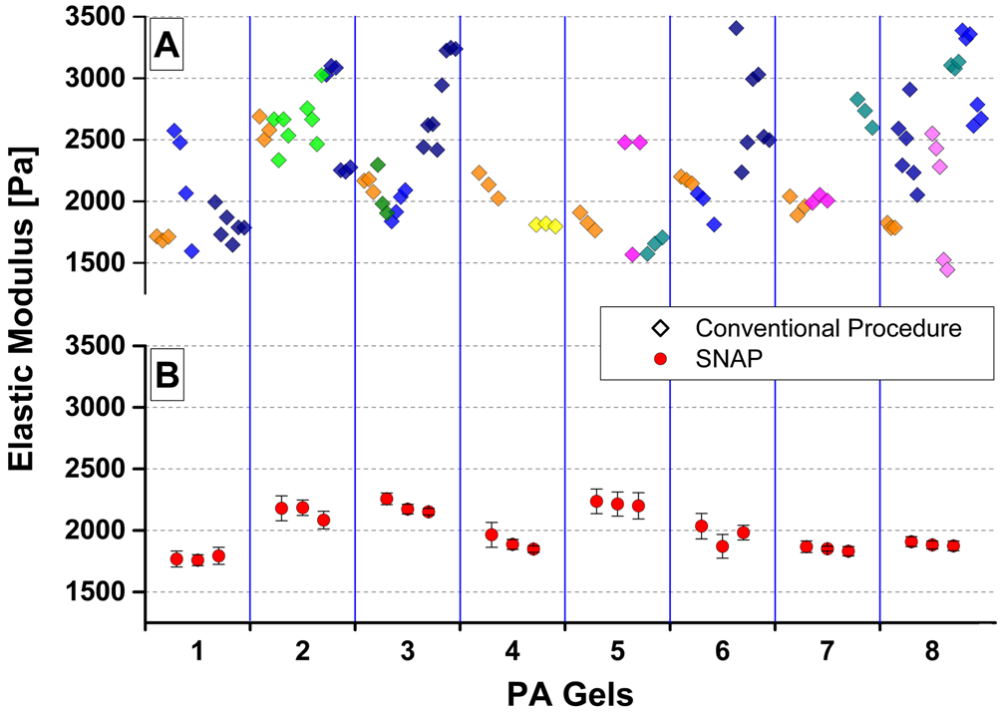

Figure 29: Comparison of the Elastic modulus measured on polyacrylamide (PA) gels by different labs and by different users on different instruments. The SNAP calibration method greatly reduces the variability between measurements when compared to the conventional calibration procedure. (Schillers et al. 2017)

- Changes to the geometry of the probe affect force-distance measurements, since most of the mechanical models used rely on a clearly defined shape and size of the AFM tip.

- The mechanical models currently used to characterize the mechanical properties of biological samples offer a good approximation. However, since many of the conditions assumed by the models are not met in an experimental setting, one cannot rely on the absolute values. Nevertheless, these results allow to compare between samples characterized in strictly similar experimental conditions.

1.4.8. Recent approaches to improve AFM throughput

Most diagnostic samples contain a large background of normal cells within which diseased cells represent a small minority. In this case, sufficient throughput is required to process enough cells to obtain statistically accurate results concerning the target cells of interest. During the past years three main approaches have been explored to increase AFM throughput for measuring biological samples properties:

1.4.8.1. Increasing scan speed

Compared to other microscopy techniques, like fluorescence, AFM is limited by its slow time resolution. Therefore, one way to potentially increase the throughput of AFM is to decrease the time that takes to measure a region of the sample. This approach has already been studied and explored in depth, with several laboratories specialized in this topic. Some of the developments in this field include new scan modes, High-Speed AFM (HS-AFM) (Ando, 2013) and new probe designs. At the moment, only the development of new modes and cantilevers have been applied to measurements of mammalian cells and tissue samples, as current HS-AFM setups are not yet compatible with these samples and are mostly used for imaging molecules and lipid membranes (Chiaruttini et al., 2015; Kodera et al., 2010; Watanabe-Nakayama et al., 2020).

To achieve higher scanning speeds, manufacturers like Bruker have developed new scanning modes that optimize the movement of the cantilever, while allowing to quantify the mechanical properties of the sample. As an example, the Quantitative Imaging (QI) mode, unlike other similar modes (e.g., Force Volume mode), is optimised for fast surface scanning (Chopinet, Formosa, et al., 2013; Chopinet, Roduit, et al., 2013). Figure 30 shows a diagram of the tip movement in QI mode. The green trace represents the vertical movement of the

lever, and the blue one symbolises the horizontal movement. The force curve is recorded when there is no movement (vertical and horizontal) of the tip. The algorithm that governs the tip movement minimises the lateral forces and controls the vertical forces. Using these curves, a whole range of information is available during the analysis (adhesion, elasticity topography, ...).

HS-AFM takes this approach to the limit, by acquiring multiple scans (frames) per second. Several advancements in many fronts were required to achieve these scanning speeds (Ando, 2013):

- As the cantilever is the slowest component of the AFM, cantilevers with higher resonance frequencies and small spring constants are required to not damage the sample and achieve higher imaging speeds. For this reason, HS-AFM uses miniaturized cantilevers (100–140nm thick, 2–5μm wide and 9–14μm long), one order of magnitude smaller than the ones used in conventional AFM (Figure 30).

- To achieve high imaging speeds, the X and Y scanners together with the Z piezo require a high bandwidth to move following the rapid changes in the sample topography.

- For HS-AFM imaging, sharp-tip cantilevers are normally used to achieve the highest resolution possible. Due to the fast-scanning speeds, several frames are acquired every second. Therefore, depending on the scan resolution, the tip interacts with the sample thousands of times per second. To minimize the invasiveness and damage to the sample, oscillating acquisition modes, like tapping mode, are normally used in HS-AFM.

- For controlling the multiple elements in the system, improvements in the electronics, feedback systems and software are needed to achieve video rate scanning speeds.

The combination of these developments has allowed to observe biological processes at the nanoscale in real-time, like the Myosin V walk (Kodera et al., 2010), and study their dynamics.

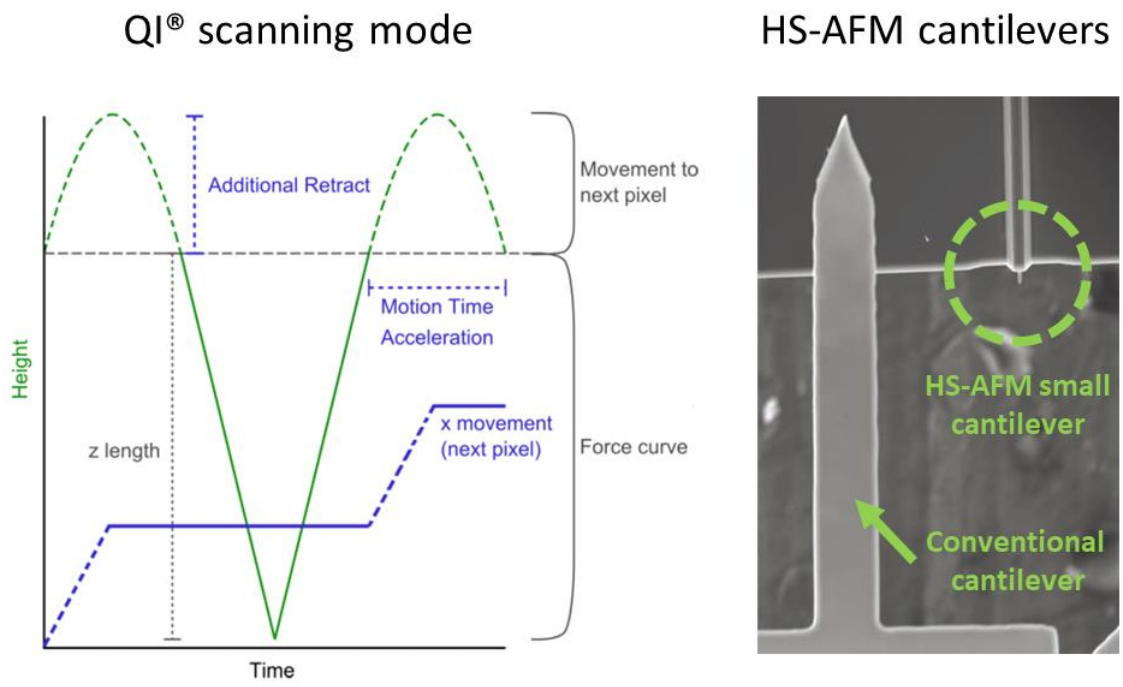

Figure 30: Examples of developments to increase AFM scan speed: Diagram depicting the optimized paths for the vertical (green trace) and horizontal (blue trace) of the cantilever in QI® mode. (Left) Size comparison between conventional cantilevers and small cantilevers used in HS-AFM (Right).

Although this approach has resulted in several landmark developments, it may face issues due to the physical limits of mechanical properties. At higher speeds, the hydrodynamic effects of the medium worsen, and they influence the measurements, making it necessary to use smaller cantilevers and apply corrections to the cantilever drift and data collected during analysis. Moreover, the viscoelastic properties of cells and tissues vary with speed and in some applications, like in force spectroscopy, a minimum contact time can be required to promote interactions. In conclusion, this approach may be incompatible for some applications and does not tackle other factors that severely hinder the higher throughput capabilities of AFM, like the high operator dependence.

1.4.8.2. Measurements in parallel

The main developments following this approach include cantilever arrays and miniaturized AFMs. Although this approach can increase throughput and cantilever arrays have been proven a successful approach in tissue samples (Weder & Favre, n.d.), there remain several challenges for ensuring registration between the array and the surface, to ensure that consistent indentations are made over all the cantilevers in the array. Moreover, this approach is primarily

suitable for measuring samples with a large area like tissue slices or cell monolayers, as the throughput in applications like single cell measurements is limited by the positioning of the cells within the sample. Therefore, micropatterning may be needed to ensure that multiple cells are indented on every measurement.

To overcome the tip-sample registration issue, some of these systems include Micro Electro-Mechanical Systems (MEMS) that provide control of the tip-sample interaction (Figure 31). These systems have been proven to be a successful approach in high-throughput characterization of silicon wafers by AFM for quality control. However, systems incorporating MEMS are not compatible with in-liquid measurements, limiting its application to cells and tissue samples (Sadeghian et al., 2017).

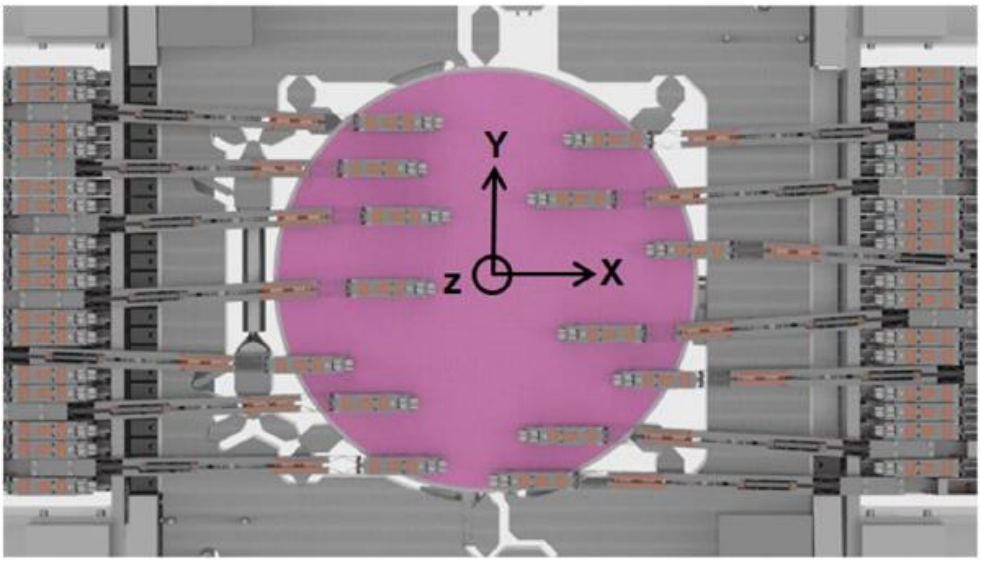

Figure 31: Miniaturized AFM (MAFM) setup used for silicon wafer quality control. Reproduced from (Sadeghian et al., 2017)

1.4.8.3. Automated measurements

The last approach is Automation, which has already proven to be successful for silicon wafer quality control using AFM and for biomedical applications using other microscopy techniques (e.g., automated image-based digital pathology scanners in hospitals). Due to the high dependence on the operator, one of the limiting factors for AFM throughput is the time availability of the operator. Consequently, automating the system and lowering the dependence of the operator would improve it's time of useful operation, thus increasing the overall number of measurements. However, scanning over such long periods of

time presents several challenges when working with biological samples, as suitable conditions to ensure cell survival must be maintained. Moreover, refined algorithms capable of detecting the regions of interest to measure must be developed to reduce the need for human intervention.

Automation is the approach that we have chosen for this work. As several authors have worked in the development of AFM automation for characterizing biological samples during the recent years, in the next section an overview of the state of the art of AFM automation in biological samples is provided.

1.4.9. State of the art of AFM Automation for characterizing biological samples

Automation in AFM has already been explored, and multi-sample highly automated commercial systems are already available in the market. However, most of these systems focus on the imaging and characterization of non-biological samples like silicon wafers. To date, the ForceRobot (Bruker) remains the only bio-focused fully automated system available on the market. Nevertheless, even though the ForceRobot is capable of automatic regulation of the experimental conditions and can acquire force curves over extended periods of time, it is uniquely focused on performing force spectroscopy experiments and is not suitable for imaging nor characterizing the mechanical properties of soft samples (i.e., cells, tissues, vesicles).

With no commercial option available, most of the development in AFM automation has been done by research groups aiming to achieve a higher throughput in their experiments and reduce the amount of manual labour. One of the first automated AFM setups was developed in 2012 by Wang and collaborators (Wang et al., 2012) to automatically characterize fixed round Raji cells. In this system, cells placed on a petri dish are detected from video images using a circle detection algorithm based on the Hough transform. After detecting the circles, the AFM is directed to the centre of each circle and a scan line is performed on each horizontal axis. From both scan lines the limits of the cells are detected, and assuming the cell is circular the centre point is then extrapolated (Figure 32).

With this approach it is possible to automatically detect cells and acquire force curves on each cell, taking an average of 3 seconds to acquire measurements for each cell, allowing to obtain higher operational speeds. From a point of view of increasing throughput, the major drawbacks of this system are:

- It relies on the circularity of the cells for both optical and AFM detection, limiting its applications.

- Does not address the multi-region and multi-sample issues, requiring the user to move from one region to another in the sample and change the sample.

- Requires that the cell's substrate is completely flat, and the agglomeration of cells has to be avoided, as the system is not able to recognize these regions as not valid.

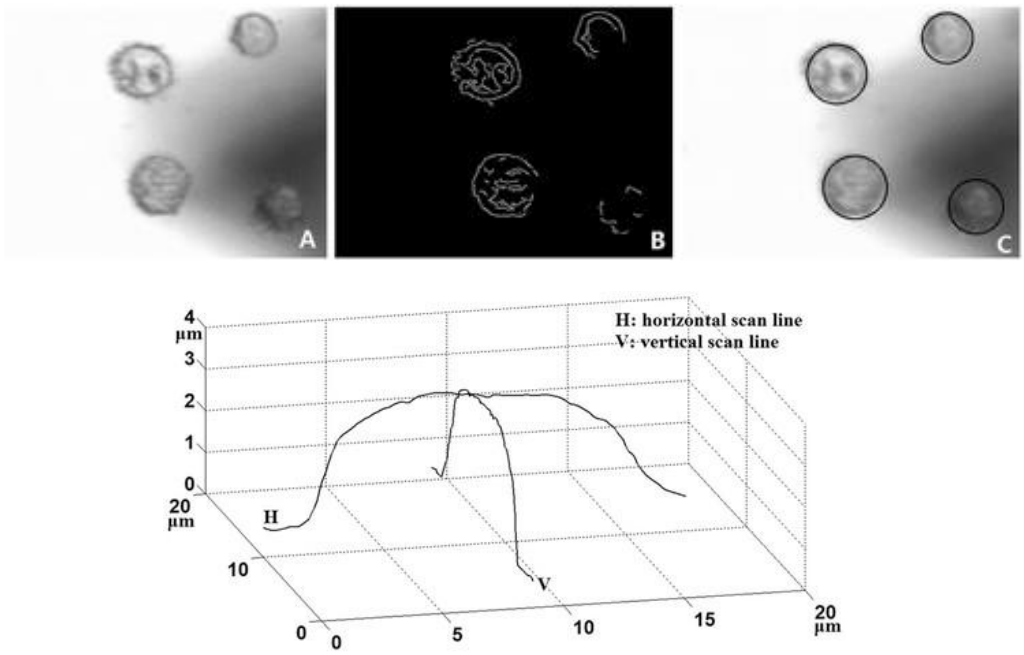

Figure 32: Top: Cell detection method on fixed Raji cells in the video image. A: original grey-scale image. B: edge detection. C: detected circles, overlaid. Bottom: Cell probing method on fixed Raji cells. The AFM is engaged on one of the cells detected and a scan line is taken along each axis to better localize the cell. Reproduced from (Wang et al., 2012)

The following year, Roy and collaborators (Roy et al., 2013) developed a semi-automated image-guided system, which allows for the automatic alignment of the AFM probe with the regions in the sample previously identified by a certified pathologist as regions of interest, from a digital stained image of the sample (Figure 33). On their work, they report that using this automated positioning system they were able to acquire 480 points in a region of

approximately 80µm × 150µm in about 80 minutes whereas if they were using manual positioning it would have taken them between 2-4 hours, depending on the expertise of the operator. However, the need for the previous time-consuming manual selection of the region of interest from an optical image together with the need of manually moving between the regions of the sample, makes it challenging to scale the throughput of this approach, especially for samples with multiple regions of interest.

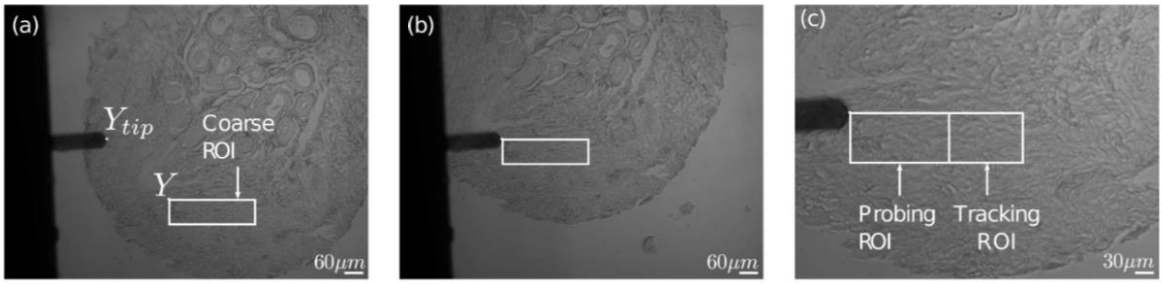

Figure 33: (a) - (c) Tracking protocol to position tissue underneath the AFM probe tip. A) The pathologist defines the ROI of interest in the sample. B) The system moves to the specified ROI and starts scanning C) within the ROI the system defines a region to measure (probing ROI) and a region to track (Tracking ROI) the position across multiple magnifications. Reproduced from (Roy et al. 2013).

In 2017 Peric and collaborators (Peric et al., 2017) developed a reusable microfluidic chip, manufactured from chemically inert materials, which allows for simultaneous fluorescence and atomic force microscopy. This system allows to trap cells, reverse the trapping, eject cells, and trap new cells for analysis, thus increasing the throughput of single-cell measurements (Figure 34). In their work the performance of their system is only demonstrated using rod-shaped bacteria; however, they state that this approach could be applicable to round-shaped cells.

Although this system reduces the time required for switching from one cell to another, the system still requires an operator to control the pump controller, manually move between wells and acquire the measurements via AFM. Moreover, expertise and specialized equipment are required to produce these chips.

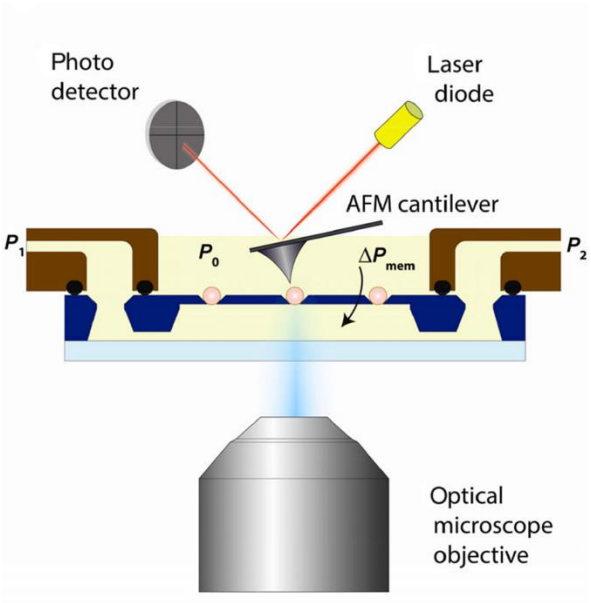

Figure 34: Measurement configuration for bacterial trapping in combined AFM/optical microscopy setup. A pressure difference ΔPmem is applied across the membrane containing the bacterial traps. The top side is exposed to atmospheric pressure P0, whereas the pressure in the channel is controlled through the input P1 and output P2. (Reproduced from Peric et al. 2017) (Peric et al., 2017)

Dujardin and collaborators (Dujardin et al., 2019) developed an automated system in 2019 that could be used for analysing cell's mechanical properties. This system includes a multiwell plate with multisample support, the ability of performing measurements both in-liquid and in-air, an automated system for detecting the regions of interest in the sample, tip and sample contamination detection, a cleaning procedure, bubble detection and tip quality control. Those capabilities make this system well suited for working with biological samples. On their work, they report that they were able to scan around 800 fixed *Yersinia pseudotuberculosis* bacteria in 8 hours.

For detecting cells in the sample, a large low-resolution survey scan (30 µm x30 µm) is performed. The regions corresponding to cells are then detected using a height threshold from this scan. Finally, the system moves to and acquires a higher resolution force map on each position (Figure 35).

Although this automated system works well with small cells like bacteria, it appeared to be suboptimal for working with mammalian cells. These cells are much larger than bacteria, and consequently, the previously described detection system is no longer suitable. Other cell detection methods based on image analysis could be implemented; however, the low-resolution optics coupled to the system highly limit this approach. Moreover, due to the limited x-y range of the AFM platform (30 µm x 30 µm) it is not possible to scan a whole

cell at once, and the limited Z range (3 µm) presents several issues, making it necessary to engage on specific regions of the cell with the piezo fully retracted or extended, requiring a more sophisticated detection system that would require better optics. These issues together with the inability to achieve proper temperature control across all wells, severely limited the application of this system to mammalian cells.

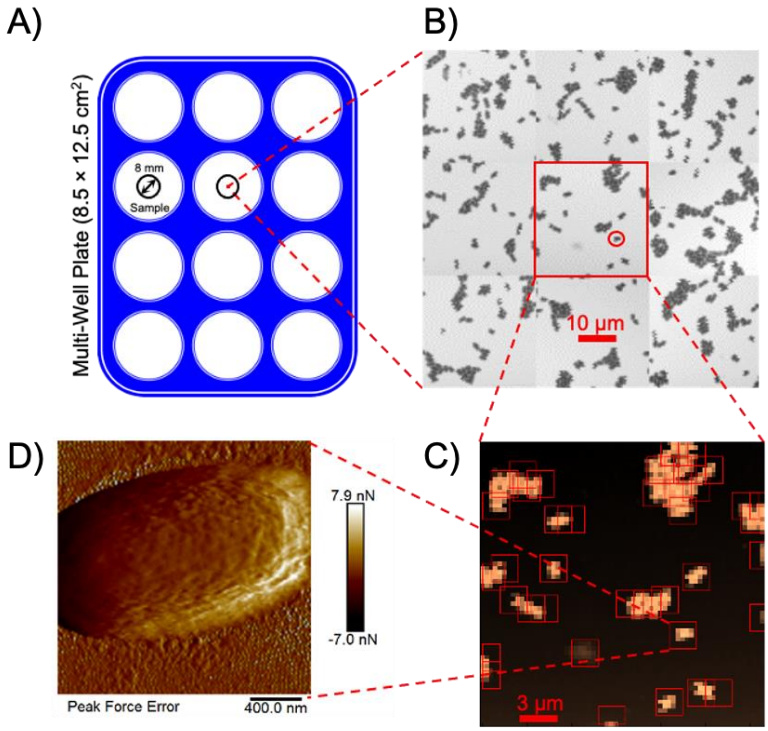

Figure 35: Illustration of the workflow of Yersinia pseudotuberculosis bacteria detection and scanning. (A) Schematic representation of the multi-well plate. (B) Image reconstructed from the 3-by-3 array of Force Volume capture survey scans taken in the control well. (C) One of the Force Volume height maps from [B], with detected areas of interest squared as detected automatically during the experiment. (D) Peak Force Error map of one of the bacteria in [C], taken automatically. (Reproduced from Dujardin et al. 2019) (Dujardin et al., 2019)

In the same year, Proa and collaborators (Proa-Coronado et al., 2019) developed an automated system based on the NanoWizard platform (Bruker), where cells are seeded onto the microwells of a microstructured polydimethylsiloxane (PDMS) stamp and then a Jython script is used to drive the AFM. The script directs the AFM tip to each well inside the piezo range (100 µm x100 µm) and acquires depending on the user input, force curves or force maps on each position. Once all the positions inside the piezo range have been measured, the motor stage automatically moves the tip to another area of the sample and the previous step is repeated (Figure 36). In their work, they report that using this approach, they were able to measure a population of 900 *Candida albicans* cells within 4 hours.

This approach significantly increases the throughput of AFM and could be applied to other cell types. However, as it requires the cells to be patterned, its throughput is highly dependent on the filling rate for the PDMS wells. To minimize this issue, checks are made based on the height measured on each well, to ensure that the well is not empty before each measurement is acquired. Although no correlative optical image is acquired for each position, AFM data can be used to ensure that the measurement corresponds to a single cell and not to imperfections of the PDMS stamp, cell debris or an agglomeration of cells. Finally, this system does not tackle the multi-sample issue and requires the user to manually change the sample.

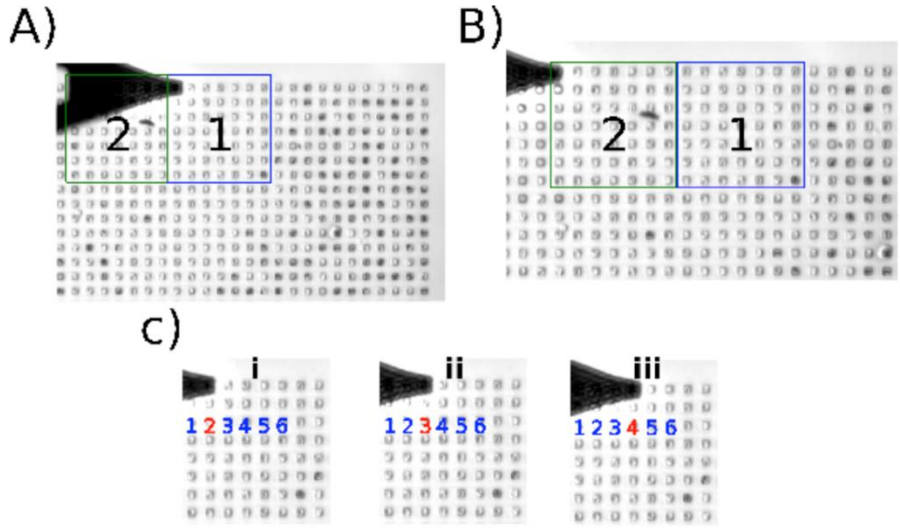

Figure 36: Automated AFM data acquisition system developed by Proa and collaborators. A: When the system finishes measuring all the microwells inside of a region (1), the algorithm moves automatically to the next region (2). B: Once the system moves to the next region (2), automated measurements are acquired inside the microwells of each region. C: Shows the data acquisition through different microwells (i-iii) in region 2. Reproduced from (Proa-Coronado et al., 2019).

Recently, in 2022 Rade and collaborators (Rade et al., 2022) developed an automated tip navigation algorithm based on deep-learning object detection using the YOLOv3 neural network (Figure 37). This approach allowed them to speed up the movement speed of the AFM cantilever probe to the desired cell shape up to 60 times. Moreover, this system allows to correlate each AFM measurement with an optical image of the cell. This enables the user to precisely know where each measurement was acquired and the state of the cell.

Although this system allows for a faster acquisition of AFM measurements, it relies on a neural network to detect the cells, and this approach may face issues with generalization for other types of samples and imaging conditions. Nevertheless, these new detection problems would be related to the original

purpose the neural network was trained for. Retraining the network using transfer learning (reusing a previously trained model) would allow the neural network to be used in these new experimental conditions (Yang et al., 2020).

However, even when using transfer learning, this would require the user to label new data and retrain the network, processes that is very time-consuming and requires an expert to label the images. To minimize this issue, Rade et al. utilized datasets acquired with different cameras and data augmentation to make the neural network more robust and tolerant to the high variety of cell shapes and orientations present in the sample. Finally, this system does not monitor the experimental conditions during the experiment and still requires the user to manually exchange samples during the experiment.

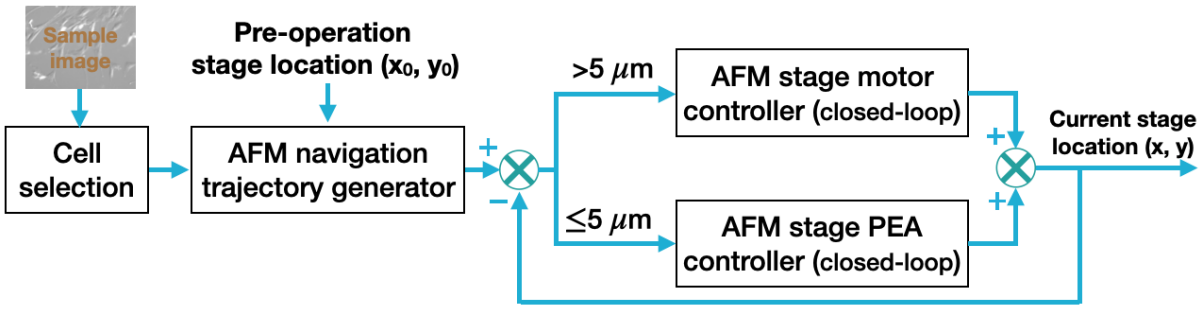

Figure 37: A schematic of the automatic AFM navigation closed-loop control (Rade et al., 2022).

In conclusion, although multiple developments have been done on AFM automation in the past years, there is still the need to develop an automated system compatible with mammalian cells and tissue samples capable of working with a wide range of samples, monitoring the experimental conditions to ensure the quality of the measurements and able to automatically handle sample exchange.

2. Results

2.1. Objectives

- Increase AFM throughput for characterizing biological samples commonly studied by AFM at different scales, focusing on nanovesicles, mammalian cells and tissue slides.

- Develop an automated AFM system focused on the nanomechanical characterization and imaging of mammalian cells and tissue samples. Incorporating optical detection for regions of interest within the sample and capable of being adapted to other types of samples and measurement modes (i.e., force spectroscopy, etc...).

- Develop the methodology and data analysis tools for measuring elasticity and viscoelasticity using the automated AFM system developed in this work.

2.2. AFM Automation

To enhance the throughput of AFM for characterizing single cells and tissue samples, various approaches have been explored, as explained in the introduction. However, these methods have their limitations, and there is still a need to develop a system that can handle a wide range of samples, instead of being restricted to a few specific applications. It also needs to be able to ensure data quality and deal with any possible complications that may arise during the experiment, such as laser drift or tip contamination.

The system developed in this study was designed to accommodate a diverse range of samples (nanovesicles, cells, tissues), and as such, requirements were carefully established to achieve this objective. A critical consideration was biocompatibility, with non-toxic materials and environment control being essential. Indeed, prolonged scanning of biological samples can result in the leaching of toxic compounds from system components, which can compromise cell viability.

Figure 38: Example of AFM coupled to an inverted microscope. The most common technique coupled to AFM is bright-field microscopy, which allows for cantilever laser alignment, sample morphology assessment, and the selection of regions of interest to measure. Fluorescence microscopy is another widely used technique in research that complements AFM, by allowing the monitoring of biochemical processes through the labeling of specific sample components.

From automation point of view, the system should be able to work with a wide range of samples of different scales, perform the instrument setup (mount the probe, align the laser and photodiode, calibrate the probe and approach the sample surface), move within different regions of the sample, detect the regions of interest to measure, perform the measurements, collect data about the experimental conditions (temperature, changes in the deflection sensitivity…), change the sample and handle the possible issues that may happen during the experiment (change the probe if its damaged, realign the photodiode…). Although automated data collection is the focus of this system, software capable of processing large volumes of data in a robust and reliable manner is crucial to obtain insights from this data and for the system to be successful.

Following the requirements listed above, the first approach was to continue the development of the previously developed automated AFM platform by Dujardin et al. in 2019. This system is based on the FastScan® (Bruker) commercial AFM platform, includes a multiwell plate and automated sample region change, sample change, photodiode alignment, tip state check, experimental conditions logging and region of interest (ROI) to be measured detection. However, as this system was developed primarily for the purpose of

imaging bacteria, some of the requirements for working with mammalian cells or tissue samples are not met.

The main limitations of this system include:

- The piezo range of the FastScan® (Bruker) is limited to 30 µm x 30 µm in X, Y and 3 µm in Z. Larger piezo ranges are necessary to work with rough samples like tissue or to measure mammalian cells, as their height can surpass 3 µm.

- The system lacks environment control, making it challenging to work with live cells for long periods of time. Previous attempts to incorporate heating to the titanium multiwell plate failed to achieve an homogeneous temperature among the wells.

- The ROI detection system consists of performing a large low-resolution AFM scan to find the positions of the cells (any point in the map exceeding a height threshold set by the user). This algorithm cannot discern between cells and debris, meaning that post processing is required to discard these areas. Moreover, the throughput of this approach is limited by how many cells can be found inside of the large scan, making it not suitable for larger cells.

- The optics coupled to the system consist of a 5-megapixel camera with digital zoom. Low resolution makes it challenging to obtain quality optical correlative images and implement computer vision ROI detection algorithms.

- Although the mounting system provides a secure and robust attachment of the glass coverslip to the multiwell plate. The procedure to attach the sample to the plate is complicated and can result in the coverslip breaking.

Faced with these limitations, another approach and a commercial AFM platform were selected for developing the system. To be compatible with a wide range of samples, it was decided to use the ROI detection method developed by Dujardin and collaborators (Dujardin et al., 2019) for small samples and situations where the resolution of the optics coupled to the system is not enough, and to develop a ROI detection method based on optical image analysis

for larger samples. The NanoWizard 3 (Bruker) platform was selected as the base to implement the automated system based on these criteria:

- Scan range of 100 µm x 100 µm in X, Y and 15 µm in Z. Suitable for working with large and rough samples.

- This platform is coupled to bright-field, confocal and stimulated emission depletion (STED) microscopy, providing a lot of versatility for developing optical-based ROI detection methods.

- Multiple features needed for automation are already available in the manufacturer's software.

- Possibility to work with petri dishes commercially available for cell culture, while being able to control the temperature of the medium in the petri.

The forthcoming sections of this chapter will delve into the specific features of the automated AFM system and outline the necessary developments that were made to enable its automation. In contrast to developing custom hardware, commercially available components were utilized for this project. As such, the focus was primarily on software development and experimental optimization (including sample preparation and AFM measurement parameters) to achieve AFM automation.

2.2.1. NanoWizard 3 List of the automated system hardware components

Below a list with all the commercial hardware used to develop the automated AFM system and perform the experiments in this work can be found:

- NanoWizard 3 AFM head (Bruker, Santa Barbara, CA, USA)
- Vortis-2 AFM controller (Bruker, Santa Barbara, CA, USA)
- Precision Motor Stage (Bruker, Santa Barbara, CA, USA)
- IX83 microscope (Olympus, Tokyo, Japan)
- STED-Confocal microscope (Abberior, Göttingen, Germany)
- Petri dish heater (Bruker, Santa Barbara, CA, USA)
- uEye CP colour camera (IDS, Obersulm, Germany)

Figure 39: Image of the hardware components used to develop the automated AFM system in this work.

2.2.2. NanoWizard 3 Platform automation software features

As previously stated, the NanoWizard 3 platform is well-suited for automation, thanks to a range of software features that enable its implementation. In the following section, we will examine the most significant features employed in the development of the automated AFM system.

JuniCam® module

The initial step in implementing a ROI detection system based on optical images is to acquire high-quality images. For this function, the NanoWizard 3 software incorporates the JuniCam® module, which enables the control of digital cameras connected to the platform directly from its graphical user interface (GUI). This module provides researchers with a live feed of the camera, enabling the acquisition of snapshots or videos, as well as adjustment of various image acquisition parameters such as contrast, brightness, etc.., without the need for additional software. However, it is important to note that the JuniCam® module only supports cameras from select manufacturers.

Direct Overlay® module

Once the ROIs have been detected in the optical image, it is necessary to correlate them with physical positions in the sample to be able to move the cantilever to each position and acquire the AFM scan. However, distortions in the images may arise from optical aberrations coming from the lenses and mirrors of the optical microscope. To achieve a proper correlation between the optical image and the AFM scan, distortions must be prevented, as this nonlinear stretching, rotating and offsetting will result in two images that won't precisely overlay.

The Direct Overlay® module allows to carry out an optical calibration to correctly perform the registration between optical images and AFM measurements. First the software moves the cantilever, forming a grid. At each point, an optical image is acquired automatically using the JuniCam® module and the position of the tip is automatically detected in each image without needing input on cantilever angle, shape or magnification. For the algorithm to work properly, the cantilever must be in focus with enough contrast between the cantilever and the sample. The algorithm then computes the factors that relate the distance travelled by the cantilever with the pixel positions of the cantilever on each image.

Once this optical calibration is performed, each time the user acquires an image, the algorithm performs a nonlinear conversion to correct the optical image for lens imperfections and transforms the image into a set of linearized AFM length coordinates. Finally, the calibrated optical image is transferred into the GUI, allowing the user to define AFM scan regions on any position of the optical image within the X and Y piezo range. If used in combination with the Precision motor stage, the user is no longer limited to the range of the X and Y piezo (100 µm x 100 µm) but to the range of the motor stage (20 mm x 20 mm). Thus, allowing the user to obtain cross-correlated mechanical measurements and a composite image covering the same range as the motor stage, by stitching multiple images together.

Calibration manager

To obtain quantitative data of the sample's mechanical properties, a calibration of the deflection sensitivity and spring constant of the cantilever is required.

The Calibration manager allows to automatically perform a non-contact calibration, by acquiring a thermal tune of the cantilever, from which the spring constant and deflection sensitivity of the cantilever are obtained by applying the Sader method (Sader et al., 2005).

Experiment Planner® module

Most commercial AFM platforms are closed systems with custom software and hardware, making it extremely challenging to implement custom software to control the instrument. For this reason, like in the work of Wang and collaborators (Wang et al., 2012) most automated AFM systems are developed in open custom AFMs or in collaboration with the AFM manufacturer.

The Experiment Planner® module provides a high-level programming interface, allowing the user to control different components of the instrument using Jython (Java implementation of the Python programming language) scripts. It thus allows the user to develop complex data acquisition routines, integrating the functionalities of the previously described modules, and log the experimental conditions. An example of the application of this module is the work of Proa and collaborators (Proa-Coronado et al., 2019), who utilized it to implement their automated AFM data acquisition routines.

2.2.3. Custom developments expanding the NanoWizard 3 software

Despite the NanoWizard 3 offering various functionalities as a foundation for automation, additional development was necessary to incorporate algorithms for ROI detection and experimental condition monitoring into the system. This section outlines the key software advancements required to establish our automated system, which are not present in commercially available NanoWizard 3 platforms.

Jython-CPython interface

Jython is the Java implementation of the Python programming language. This implementation allows Python to run on the Java Virtual Machine (JVM) and access to classes written in Java. These functionalities are ideal when implementing a high-level programming interface to drive an instrument

which its software is written in Java, like in the case of the NanoWizard 3 platform. Jython provides a simpler syntax than Java, making it more accessible for users to develop their custom scripts. In addition, since Jython can access classes written in Java, no major changes to the base code or the development workflow must be done by the company to implement this feature. Nevertheless, since the official and commonly used implementation of Python is based on C (CPython) and not Java, only the core CPython libraries and few libraries adapted are available in Jython. This results in tasks like image analysis or vector computations being more challenging than they normally are in CPython, due to the unavailability of several commonly used libraries like OpenCV, scikit-image or NumPy, since they have not been adapted to Jython.

To overcome this limitation, one option would have been to implement all the functionalities needed for image analysis (image loading, filters...), however this would have been very time consuming, and the resulting code would not have been as optimized as using the C based libraries, making it slow and complicated to use. Therefore, we decided to implement an interface which would allow the user to run CPython from within a Jython script, to overcome this issue and have as much flexibility as possible when developing the ROI detection routines.

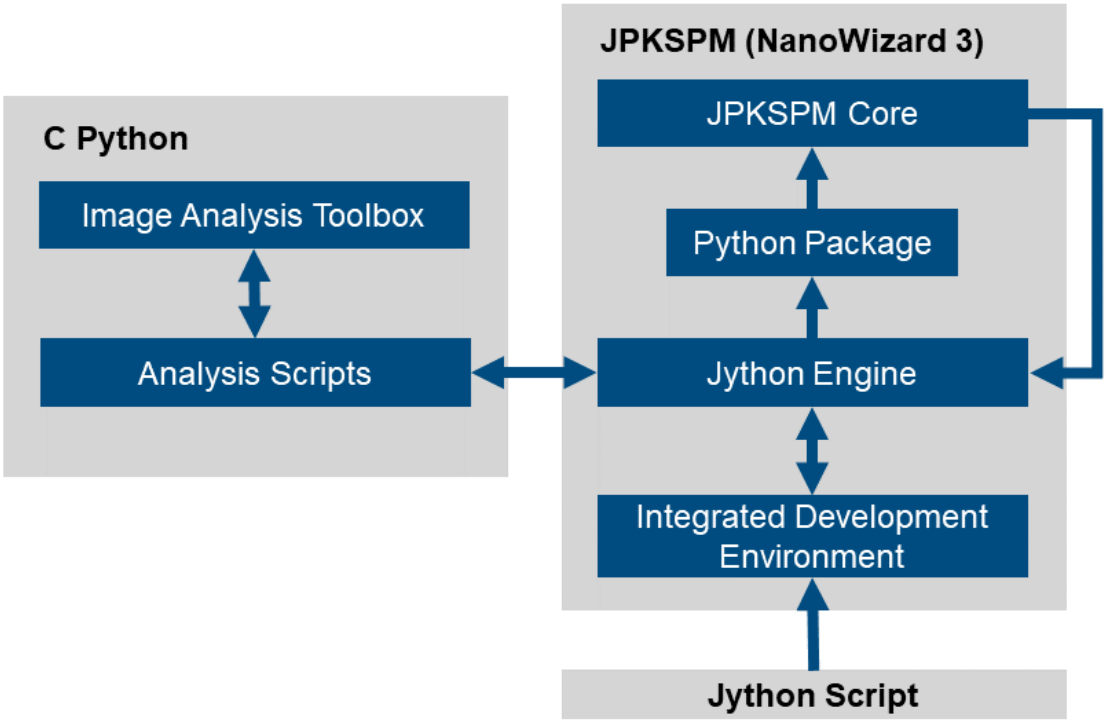

Figure 40: Diagram depicting the CPython – Jython interface developed which allows to call CPython scripts from Jython scripts while running an experiment loop in the Experiment Planner®

Automated cantilever calibration script

Ensuring that the deflection sensitivity and spring constant remain constant during the whole experiment is vital to be able to compare measurements through the experiment. Due to laser drift or contamination attaching to the tip, these values may shift. On a classical experiment, the user can observe the presence of drift or contamination, assess the situation and decide if an action is required (clean the tip, realign the laser, change the tip, etc.). In automated experiments it is necessary to monitor these values during the experiment to perform an automated assessment and decide on which action to take in case of an issue.

The calibration manager includes functions that can automatically retract the piezo, acquire a thermal tune and perform the Sader calibration for rectangular cantilevers. However, these functionalities cannot be accessed through the Experiment Planner Jython scripts by default. For this reason, a custom Jython script has been developed, with the help of the AFM manufacturer, to access these functionalities from other Jython scripts. This allows to perform automated non-contact calibrations through the experiment to monitor the changes in the deflection sensitivity.

Automated conversion of optical images into Direct Overlay® calibrated images

Once the ROIs have been detected in the optical image, it is necessary to transform the image pixel positions into physical positions in the sample for the motor stage to move to. The Direct Overlay® can be used to perform an optical calibration and obtain the factors needed to transform image coordinates into motor stage physical coordinates. Or, by default, this functionality cannot be accessed from the Experiment Planner Jython scripts. To overcome this issue, a custom method to perform this calibration could have developed instead of relying on the Direct Overlay® module. However, this option would have made the calibration process less user-friendly and tedious due to the lack of an integrated graphical user interface. Taking this into consideration, we decided to develop custom Jython scripts to access these functionalities from the Experiment Planner Jython scripts. It thus allows the system to automatically convert optical images into calibrated images and pixel positions into physical positions in the script, using the factors obtained by an optical calibration performed by the user before the experiment.

Access to AFM measurement data in real time

Some functionalities, such as ROI detection algorithms that rely on identifying features in the height data channel, or routines for assessing the quality of force curves during an experiment, require immediate access to the AFM data as it is being collected, for processing it and providing instructions to the main experiment loop.

This data could be accessed using custom scripts to load the AFM measurement files once they are saved. This approach is not ideal, as it must wait for the AFM file to be completely written into the disk, read the file and then process the file data. This approach is slow, especially when working with large files.

Another way is to read data directly from a memory buffer. As the data is being collected but before it is written onto the disk, the NanoWizard 3 software stores it in a memory buffer. By accessing the data directly from this buffer, it can be directly accessed without having to wait for the file to be written into the

disk. To implement this functionality, custom Jython scripts have been developed. This way, we can access the AFM data (height channel, individual force curves, etc.) as it is being collected from the Experiment Planner Jython scripts.

Confocal-STED image acquisition integration

Although a confocal-STED is coupled to the NanoWizard 3, its integration into the system is not as automated as bright-field image acquisition. By default, the confocal-STED and AFM can only communicate with each other by transistor-transistor logic (TTL) signals through the Jython scripts. The user can send a voltage pulse to trigger the confocal-STED image acquisition. This approach allows for the integration of automated image acquisition; however, the system does not register when the image acquisition has finished, and the image must be manually saved by the user. Making it impossible to implement fully automated routines based on detecting ROIs from confocal-STED images.

To overcome these limitations, custom scripts have been developed to communicate both instruments through the local network, allowing to trigger confocal-STED acquisition, save the images in a predefined folder and notify the automated routine when the image acquisition has been completed. As these routines required CPython libraries like NumPy to handle image data, these routines have been implemented in CPython and require the Jython-CPython interface to call them from the main Jython automation script.

The Abberior Inspector software, which is responsible of controlling the confocal-STED microscope, incorporates a Python interface named SpecPy. This interface allows to run a local environment, where CPython scripts can be used to drive the instrument. As the software that drives the NanoWizard 3 (JPK SPM) is only available in Linux and the software that drives the confocal-STED microscope is only available in Windows, it is necessary to use two computers to run each operating system and software.

By establishing a connection through the local network, the user can send signals from the computer connected to the AFM head (Client) to the computer connected to the confocal-STED (Server) through the experiment planner. Through this method the user can establish connection with the Abberior Imspector server and trigger the acquisition of an image with the current

configuration. Once the image has been completed, a signal is sent back to the experiment planner and the connection with the server is terminated. Finally, the image can be located in the folder selected to save the image and then converted to a calibration image by using the Direct Overlay® calibration factors.

2.2.4. Region of Interest (ROI) detection routines

A critical step for automation is the detection of the ROIs in the sample. The automated system has to be capable of mimicking the user and autonomously select the regions in the sample where to acquire measurements. If this system is not well-tuned, it will result in the system acquiring multiple non-valid measurements that will have to be discarded, hindering the overall throughput of the system.

As our goal was to develop a system capable of working with biological samples at different scales, two ROI detection routines have been implemented:

Method based on topographical features

For samples with a diameter smaller than 5 micrometres (i.e., nanovesicles, bacteria, etc.), the ROI detection system developed by Dujardin et al. was adapted into the system, as it suitable for samples in this size range. This system relies on detecting topographical features with a height above a predefined threshold in a low-resolution (2 µm – 20 µm distance between pixels) scan. The details of this algorithm implementation can be found in section 2.2.4.1.

This routine was implemented in CPython, as libraries based in C are faster and more efficient for loading and processing large amounts of data. Therefore, the CPython-Jython interface is required to use these routines from the Experiment Planner Jython scripts.

Method based on optical image analysis

The most common method used for detecting cells and tissue regions in biomedical and research applications is image analysis. Multiple tools allowing to segment cells and tissue regions from optical images have been developed in

the recent years (i.e., ImageJ, Imaris, etc.). Many of these tools are being used in multiple research fields daily to quantify the number of cells in a sample, describe their morphology or locate the presence of biomarkers. For this reason, routines based on image analysis have been included in the automated system to detect cells and tissue regions in the sample. Finally, for certain applications, like monitoring the mechanical properties of moving cells, it is crucial to be able to track objects during the experiment and to acquire measurements on the same cell sequentially. An object tracking algorithm based on the length of a line segment between two points (Euclidean distance) has been integrated in the system. The implementation details of these routines are described in sections 2.2.4.2, 2.2.4.3 and 2.2.4.4.

All the routines for image analysis have been implemented in CPython using the following libraries: Numpy (numeric computing), OpenCV (image processing), Pandas (data frame structures) and Scikit-Image (image processing). Therefore, in the same manner as the routine based on topographical features, the CPython-Jython interface is needed to use these routines from the Experiment Planner Scripts.

2.2.4.1. Height measured thresholding

The implementation of this method is based on the work of Dujardin et al. In their work, this method was used to detect the positions of bacteria in low-resolution survey scans (30 µm x 30 µm, 64 pixels x 64 pixels), by identifying the topographical features with a height above a predefined threshold. Once the bacteria positions were detected, a high-resolution scan was then acquired (500 nm x 500 nm, 256 x 256 pixels) on each position. This approach allowed to obtain topographical and mechanical data (elasticity and adhesion) from hundreds of bacteria on different samples in a completely automated way.

<u>Algorithm implementation:</u>

1. A low-resolution scan (2 µm – 20 µm distance between pixels) is acquired on a region of the sample.

2. The height channel data is flattened by fitting and subtracting a linear plane.

3. If the maximum height value in the survey scan is larger than the height threshold, a region with the shape and number of pixels for the zoom scan is defined around the position of the maximum height value.

4. To better centre the scan on the centre of detected object, the zoom scan region is thresholded again and the centre position of the region with height values above the height threshold is computed.

5. Steps 4 & 5 are repeated till the maximum value of the survey scan is below the height threshold.

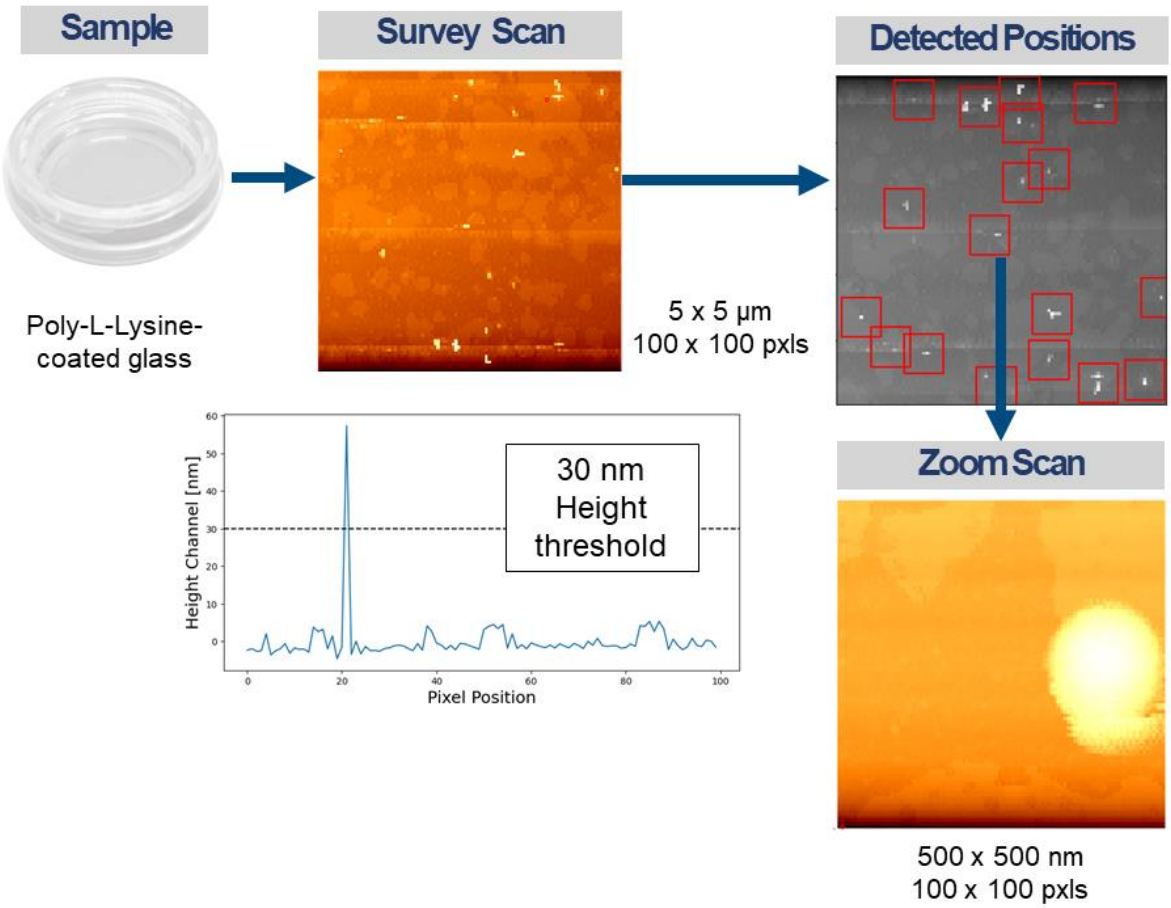

Figure 41: Diagram describing the height thresholding algorithm to detect ROIs. A survey scan is acquired, then the topographical data is flattened and thresholded to detect the ROI positions. The example data presented in this figure was acquired using Polystyrene beads.

<u>Strong points:</u>

- Easy to implement.

- Does not require sample labelling, allowing for high sample flexibility.

Limitations:

- Suitable only for small samples (< 5 μm in diameter), since the maximum scan size for the NanoWizard 3 is limited to 100 x 100μm^2 and larger samples would require larger survey scan sizes.

- This method relies on scanning a large area, meaning high scanning speeds (40 μm/s - 100 μm/s) have to be used to obtain a reasonable throughput (≥ 20 regions scanned/hour). Such high velocities increase the probability of damaging the tip and contamination attaching to the probe.

- Morphological parameters can be used to discern between the ROI and debris on the sample. Nevertheless, the low resolution of the survey scan makes it challenging to implement methods to discern between ROI and debris, making data postprocessing a critical step.

2.2.4.2. Bright Field Image Segmentation

The most ubiquitous form of microscopy coupled to AFM is bright-field. Bright-field microscopy is the simplest form of transmitted-light microscopy, allowing to observe transparent samples like cells and tissue slices without any labelling being required. Bright-field microscopy can therefore be considered as a low-invasive technique, with only intensive transmitted-light being able to damage the cell or affect its mechanical properties.

Algorithm implementation:

1. A bright-filed optical image is acquired on a region of the sample.

2. To correct for uneven illumination a flat-field correction is applied to image using the following formula:

$$\text{Corrected image} = \frac{i2}{Mean\ intensity\ of\ i2\ x\ (i2/i1)}$$

Where i_1 corresponds to the intensity values of the background image acquired using an empty petri dish / glass slide and i_2 to the intensity values of the bright-field image of the sample.

3. An entropy filter (Hamahashi, 2008) is then applied to the corrected image. This filter allows to detect subtle variations in the local grey level of an image. This method is used to detect texture and discern between the smooth glass (uniform distribution) and the rough sample (varying distribution). The result of this filter is an image where each pixel value represents the minimum number of bits needed to encode the local grey level distribution.

4. To segment the region corresponding to the sample from the background, triangle auto-thresholding is applied to the image resulting from applying the entropy filter.

5. The binary mask is cleaned by removing the objects on the border of the image and eliminating objects that are either too large or small.

6. The objects in the binary mask are then labelled by connecting neighbouring pixels with the same value.

7. The morphological parameters (area, circularity, perimeter, etc...) of each labelled region are calculated. Those regions with morphological parameters that met the limits set in the experiment configuration file are considered as valid.

8. The centroid of each valid region in the image is computed. The pixel coordinates are converted into physical coordinates using the calibration factors obtained using the DirectOverlay® module.

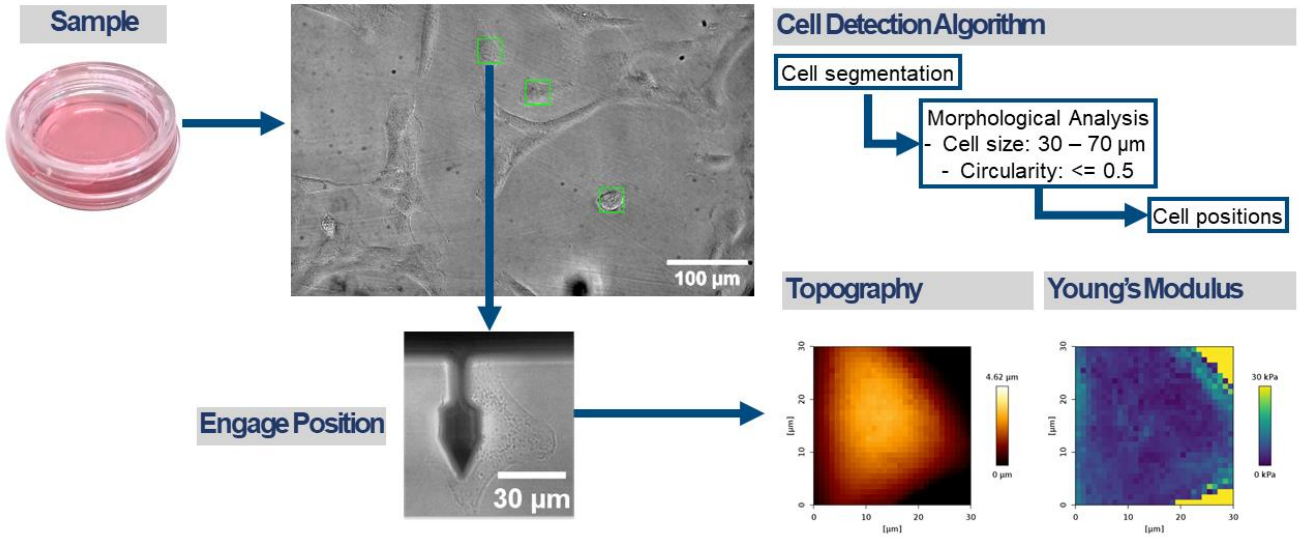

Figure 42: Diagram describing the ROI detection algorithm based on bright-field image segmentation. By applying a flat-field illumination correction and a variance filter, the ROIs corresponding to the cells are segmented from the glass. The data presented in this figure was acquired on hTERT-RPE-1cells seeded on glass-bottom petri dishes.

Strong points:

- Optical images of the sample are acquired, making it possible to observe where the sample was indented, if debris has attached to the AFM probe.

- Does not require sample labelling, allowing for high sample flexibility.

Limitations:

- Requires an optical calibration to properly transform pixel coordinates into physical coordinates.

- The performance of the algorithm relies on having similar illumination conditions in all acquired images.

- Due to the low contrast of bright-field microscopy, the algorithm may fail to segment the sample properly.

- Since the valid region selection relies on morphological parameters, if these settings are not properly defined debris may be confused for a ROI.

2.2.4.3. Confocal-STED Image Segmentation

AFM and Confocal-STED microscopy are complementary techniques. While AFM can be used to acquire high resolution topographic images and measure the mechanical properties of the sample, confocal and STED microscopy can be used to locate the presence of labelled molecules and/or monitor the dynamics of biological processes.

Algorithm implementation:

1. A Confocal-STED image is acquired on a region of the sample.

2. Otsu auto-thresholding (Otsu, 1979) is applied to the image, to segment the sample from the background.

3. The binary mask is cleaned by removing the objects on the border of the image and eliminating objects that are either too large or small.

4. The objects in the binary mask are then labelled, by connecting neighbouring pixels with the same value.

5. The morphological parameters (area, circularity, perimeter, etc...) of each labelled region are calculated. The regions with morphological parameters that meet the limits set in the experiment configuration file are marked as valid.

6. The centroid of each valid region in the image is computed. The pixel coordinates are converted into physical coordinates using the calibration factors obtained using the Direct Overlay© module.

Strong points:

- Confocal and STED provide high contrast images, facilitating the segmentation step.

- Information about the biochemical composition or dynamics of the sample can be obtained.

Limitations:

- The shutter and cooling fans of Confocal and STED microscopes are loud. Without the proper noise isolation, this vibration can affect AFM measurements.

- Labelling of the sample is required. Although a wide variety of labelling probes are available, controls must be performed to ensure that they do not affect the mechanical properties of the sample. As an example, in 2019 Flores et al. (Flores et al., 2019), observed that Lifeact-TagGFP2 alters F-actin organization, cellular morphology and biophysical behaviour of the cells.

- Prolonged exposition to the lasers used in confocal and STED microscopy may damage or kill the cell. Controls must be performed to ensure the viability of the sample during the measurements.

2.2.4.4. Object tracking

While studying cells that migrate during the experiment, to automate measurements on this samples it is necessary to track the position of the cells as they move. This allows to track over time the AFM measurements acquired on the same cell.

Algorithm implementation:

1. On the first image the centroids of each valid position are recorded, and a unique ID is assigned.

2. On the consecutive images, the Euclidian distance between the current centroids and the recorded centroids is measured. The positions with the lower Euclidian distance, below a maximum distance threshold that is defined in the experiment configuration, are paired together and the IDs assigned to the recorded centroids are assigned to the new matching centroids.

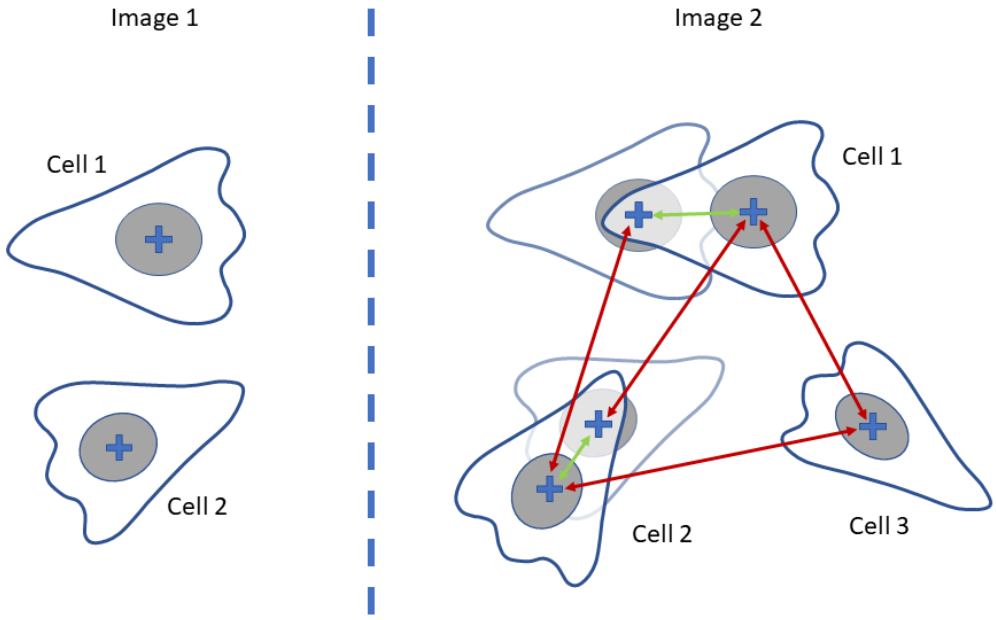

Figure 43: Diagram showing the implementation of the centroid-based object tracking. First the centroid of each cell (blue cross) in the image is detected and recorded, and a unique id number is given to each cell (left). On the following images the centroid of each cell is detected and recorded and recorded again. Then the Euclidian distance between the centroids detected on the previous image and the centroids detected on the current image (arrows) is computed for each combination of points. Finally, each cell is assigned the id of the cell with the shortest Euclidian distance (green arrow) from the previous image. If a new cell appears in the field of view, a new id is assigned to it.

Strong points:

- Easy to implement.

Limitations:

- Overlapping objects or with a large displacement between consecutive images may be assigned the wrong ID.

2.2.5. Experimental conditions monitoring

During an AFM experiment several issues may arise (i.e., laser drift, contamination getting attached to the tip, tip damage, etc.). In manually performed AFM, the user can identify these issues and perform the required action (i.e., re-align the photodiode, clean the tip, replace the tip, etc.). However, in automated experiments, the system must be capable of identifying these issues and triggering the right response.

When the experiment is initialized, and before each AFM measurement the system logs the medium temperature, horizontal deflection, vertical deflection and total photodiode sum. The initial values are used as references throughout the whole experiment. Large changes in the total photodiode sum, horizontal deflection or vertical deflection are an indicator of laser drift and/or tip contamination. The system considers that there is an issue when the horizontal and vertical deflection change more than 20 % from their corresponding initial value and when the total photodiode sum changes more than 10 % from its initial value. 20% was selected as the threshold for the horizontal and vertical deflection, as changes in this range indicate that the laser spot has moved outside of the central area of the photodiode, if the laser spot was originally placed in its centre. 10% was selected in the case of the total photodiode sum, as changes in this range correspond to shifts of the position of the laser in the cantilever, which result in large changes of the deflection sensitivity of the cantilever.

In addition to logging the experimental conditions before each measurement, the system acquires an optical image of the cantilever before and after each measurement. Thus, allowing the user to take note of the state of the cantilever between measurements.

Finally, the user can request the system to perform a periodic non-contact calibration of the cantilever through the experiment, by defining an interval. At each set interval a non-contact calibration routine is executed automatically. The cantilever retracts from the sample surface, a thermal tune is acquired, and the deflection sensitivity and spring constant are obtained via the Sader method. Currently this routine is only suitable for rectangular cantilevers, since it relies in the calibration manager developed by the instrument manufacturer.

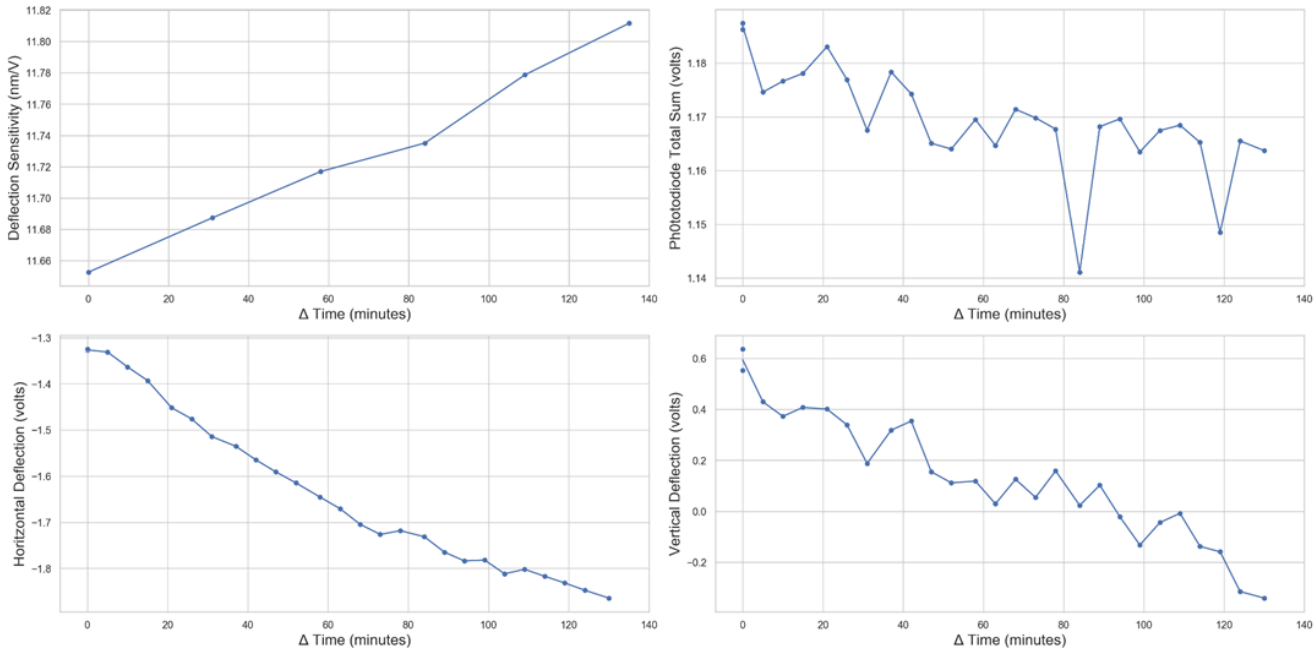

Figure 44: Example of experimental parameters recorded during an automated experiment.

Unlike other commercial AFM platforms (i.e., FastScan, etc.), the laser and photodiode are not motorized. It is then impossible to automatically realign the laser and photodiode. Moreover, the tip mounting mechanism does not allow for automatically switching the tip when it is damaged. Finally, as only one sample can be loaded at a time, the probe cannot be moved into another recipient containing a cleaning solution. These limitations make it impossible to implement many of the correction actions needed to address laser drift, tip contamination and tip damage. For this reason, in the current iteration of the system, when an issue in the experiment is detected, the experiment is halted, allowing the user to perform the required corrective action (i.e., clean the tip, change the tip, etc.) and then resume the experiment. Further developments in the hardware of the NanoWizard 3 platform are required to automatically perform these actions.

2.2.6. Force curve data quality checks

Even if the ROI detection system works properly and the experimental conditions are continuously monitored, some AFM measurements will include force curves not suitable for analysis. This is normally the result of the tip failing to properly engage on the sample or issues in the instrument setup (e.g., damaged tip, incorrect mounting of the tip in the holder, etc.). Optimizing the AFM acquisition parameters for each sample helps to minimize the number of

failed measurements. Nevertheless, during postprocessing the user still must manually discard these positions.

As this is a user intensive and long process, especially for large datasets, an automated analysis of the force curve is performed to assess their quality. Three criteria have been defined to classify a force curve as a failed measurement:

2.2.6.1. Number of points in the force curve

The initial check performed in the curves is to confirm that enough data points have been saved for the vertical deflection and height channel. In some measurements the instrument may fail to record enough data points for a position if it is not able to engage properly. Those force curves with less than 10 points in the vertical deflection and/or height channel can be easily discarded with this check.

2.2.6.2. Slope of the contact and baseline

Once the system has ensured that data has been collected for that position, the contact region and baseline of the force curve's approach segment are determined by calculating 4 points: first point of the curve, point at the 20% of the curve, point at the 80% of the curve and the last point of the curve. These point position have been selected assuming a classical force curve shape, where the contact part of the force curve has a larger slope than the baseline. A first-degree polynomial (line) is fit to each region to determine its slope. If the slope of the baseline is larger than 10% of the contact region slope, the curve is discarded.

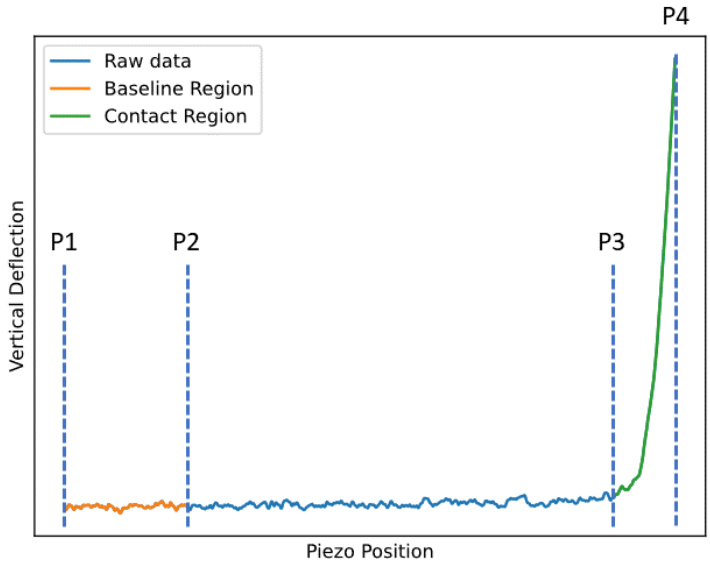

Figure 45: Diagram showing how the force curves are divided into contact and baseline regions for computing their corresponding slope.

2.2.6.3. Signal-to-noise ratio (SNR) in the baseline

Finally, the SNR of the baseline is computed using the following equation:

$$SNR = P_{signal}/P_{noise} = \mu/\sigma$$

Where P_{signal} denotes the signal's power (mean), P_{noise} denotes the power of noise (standard deviation), μ denotes the mean and σ denotes the standard deviation. Force curves with a SNR value larger than a threshold previously defined by the user are discarded.

2.2.7. Automated system workflow

Sections 2.2.1 to 2.2.6 have described in detail the different components and the motivations behind the development of this system. As the closing section of this chapter, here we will go over how the different components interact with each other and come together to form the automated system. An automated experiment using this system can be divided in 3 parts:

2.2.7.1. Experiment setup

In this iteration of the system the user is required to mount the cantilever, place the sample, calibrate the cantilever, perform the Direct Overlay® optical calibration and approach to the sample surface. In addition, the user has to define the parameters for the experiment in the experiment configuration file. The configuration file uses the JavaScript Object Notation Format (JSON). It is a standardized human-readable text-based format consisting of attribute-value pairs and can be easily edited. This file includes the following information which will be accessed depending on the type of experiment:

- Folder paths:
    - Base folder: Folder containing the folders for scripts, configs and experiments.
    - Scripts folder: Folder where the CPython scripts are located.
    - Configs folder: Folder where the configuration files are located.
    - Experiment folder: Folder the experiment data acquired will be saved to.

- Image acquisition parameters
    - Image X pixels: Optical image width in pixels.
    - Image Y pixels: Optical image height in pixels.
    - Pixel size (µm/pixel): Optical image pixel size.

- ROI detection parameters
    - Detection method: Which routine (listed in section 2.2.4.2, 2.2.4.3 and 2.2.4.4) was used for detecting ROIs.
    - Minimum size (µm): Minimum diameter for valid objects.
    - Maximum size (µm): Maximum diameter for valid objects.

- Tissue grid settings
    - Margin: Number of pixels to leave on each margin of the image when computing the positions for the grid of scans.
    - Point distance: Distance between scans in the grid.
    - Scan with no gaps: Flag whether to leave or not a distance between scans.
    - Skip rows: Flag to skip or not rows.
    - Number of rows: Number of rows to skip.
    - Skip columns: Flag to skip or not columns.
    - Number of columns: Number of columns to skip.

- AFM settings:
    - Acquisition mode: Which mode was used for acquiring AFM measurements (grid of single force curves, Quantitative Imaging® (QI) or force mapping.
    - Fast length (m): Fast length for single force curve grids.
    - Slow length (m): Slow length for single force curve grids.
    - Grid centre position (m): Offset for the grid centre position.
    - Number of fast points: Number of force curves in the fast axis of the single force curves grid.
    - Number of slow points: Number of force curves in the slow axis of the single force curves grid.
    - Scan angle: Rotation angle for the single force curve grid or scan.
    - Scan size (µm): X and Y scan size for force mapping and QI modes.
    - Number of pixels in scan: X and Y pixels for force mapping and QI modes.
    - Non-contact calibration interval: Interval of ROIs measured before a non-contact calibration is performed.

2.2.7.2. Data acquisition

The automated data acquisition is launched by executing the main Jython script in the Experiment Planner module. When the user runs the script, the main loop of the experiment starts. Then, depending on the experiment configuration, CPython routines will be called from the main loop to perform different actions.

This section will provide an overview of the steps performed during the main loop and the CPython routines. A more detailed explanation of how this system has been applied to automatically measure different types of samples is given in each section of chapter 2.3.

2.2.7.3. Jython environment (Main Loop)

1. When the main loop starts the experiment run is assigned a unique ID based on the current time stamp (i.e., 06-05-2022-13:43:05). Then a folder named after the experiment ID is created in the Experiment folder path in the configuration file.

2. Once the folder has been created, a copy of the configuration file and a text file containing the initial experimental values is saved.

3. At this point the motor stage moves to the first region of the sample and an optical image is acquired using the JuniCam® module. If the user has indicated in the configuration file a detection method based on fluorescence images, the CPython scripts to acquire and save confocal-STED images are called.

4. Once the optical image has been saved on the disk, the CPython routines to detect the ROIs are called. The scripts detect the suitable measurement positions based on the parameters stated in the configuration file.

5. Through the Jython-CPython interface the detected pixel coordinates are sent to the main loop. These coordinates are then transformed into linearized AFM coordinates using the DirectOverlay® calibration.

6. The motor stage moves to each position and the tip engages the sample. At this point the experimental conditions are logged, and an optical image is acquired, allowing the user to know the state of the tip before each measurement and the exact position of where the tip engaged the sample. If the user has specified an interval (N) to perform a non-contact calibration, every N ROIs measured, the non-contact calibration routine is triggered, and both the deflection sensitivity and spring constant are logged into a text file.

7. An AFM measurement is acquired based on the parameters in the experiment configuration file. Once the measurement has been completed; a second optical image is acquired, allowing the user to observe the state of the cantilever and the sample after the measurement.

8. Steps 6 and 7 are repeated till all the detected ROIs have been measured.

9. The motor stage then moves to the next region in the sample. Steps 3 – 9 are repeated till the maximum number of sample regions or experiment duration has been reached.

2.2.5.2.2. CPython environment (Auxiliary functions)

The CPython routines are called to perform two main functions: confocal-STED image acquisition and ROI detection. When each routine is called through the Jython-CPython interface, the code is executed in a Python 3 environment and data is transmitted in both directions. For the confocal-STED image acquisition routine, the system triggers the image acquisition by sending a signal through the local network to the SpecPy interface. The main loop then waits to receive the signal from SpecPy indicating that the fluorescent image has been acquired and saved into the disk. In the case of the ROI detection routines, the main loop sends information about the parameters to be used (i.e., detection method, minimum cell size, etc.) and location of the optical-image or topographical data to be processed. Only after the routine returns the detected ROI pixel coordinates, the main experiment loop can continue.

2.2.7.4. Data organization

All the data acquired by the automated routine is saved in the folder created automatically for each experiment. This folder contains the experiment logs, AFM data collected, raw optical images and images depicting the different stages of the ROI detection process.

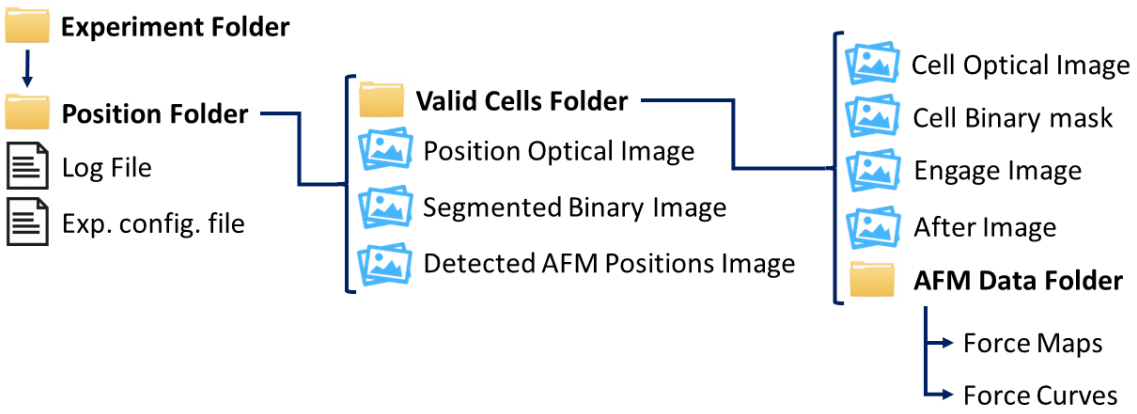

Figure 46: Diagram depicting how the data collected during an automated experiment is saved.

2.2.7.5. Data processing

The optical images are saved in TIFF format, allowing the user to open and process the images acquired in multiple tools (i.e ImageJ, Imaris, etc.). Logs are saved as human-readable text files. AFM data is saved in the proprietary format of the manufacturer. To process those files, the user can use the data processing software provided by the manufacturer or open-source software packages (i.e. AtomicJ, PyJibe, Gwyddion, etc.), including the open-source software package developed in this work, PyFM, which is described in detail in section 2.4.

2.3. AFM Automation Applications

As a result of the several developments in the field of biophysics over the last years, phenotyping of mechanical properties is now considered to have the potential to be used in the biomedical field in applications such as disease diagnosis and prognosis. AFM is one of the most well-established techniques for studying the mechanical properties of biological samples. However, much progress is still needed before this method can be applied in the clinical setting. Especially in standardization, increasing its throughput and making it more accessible.

The main objective of this work was to develop automation to increase the throughput of AFM when characterizing biological samples. In order to demonstrate the possible applications of the system developed in this project, three of the most relevant types of samples at different scales for the biomedical field have been characterised using this system: nanovesicles (artificial liposomes extruded at 30nm and 100nm), mammalian cells (hTERT-RPE-1and NIH 3T3) and tissue sections (rat bladder tissue).

2.3.1. Artificial Nanovesicles

Extracellular vesicles (EVs) are nanoparticles secreted by cells composed by one (unilamellar) or several (multilamellar) lipid bilayers enveloping a cargo (i.e., cytosolic proteins, micro-RNA, etc.). Their subpopulations are heterogeneous, differing in size, charge, biogenesis and number of layers (lamellarity).

EVs have been shown to play a key role in cell-to-cell communication and to be involved in a wide variety of physiological and pathological processes. For

example, recent studies have shown that EVs participate in the proliferation of diseases like Alzheimer, hepatitis and cancer. As EVs are readily available in multiple body fluids (i.e., blood, urine, etc.) and their number and characteristics change depending on the state of the cell, EVs show great potential as a new class of cell-free diagnostic tool.

Although most studies focus on the biochemical characterization of EVs, changes in the composition of their lipid bilayers have been shown to influence their mechanical properties and morphology. As EVs are a subject to a wide variety of mechanical stresses during their lifetime, studying the changes in their mechanical properties is fundamental for understanding their physiological and pathological role. For instance, studies have linked changes in the stiffness of these particles to alterations in their endocytic pathways, efficiency of uptake and circulation time in the blood.

As nanometric objects (100-1000nm) (Ståhl et al., 2019), few techniques are able to characterize the mechanical properties of EVs and thanks to its nanometric resolution, AFM is the most widely used technique. Different approaches have been developed to extract mechanical parameters from AFM data. They include: determination of linear stiffness, contact models to obtain the Young's modulus, applying thin-shell theory to obtain the bending modulus and an ad hoc model elaborated by Roos & Wuite's groups based on a modification of Calham-Helfrich theory (Canham, 1970; Helfrich, 1973; Vorselen et al., 2017), allowing to estimate the stiffness, osmotic pressure and bending modulus of the vesicle.

As a proof of concept, the system has been adapted to characterize the mechanical properties of synthetic vesicles. This allows to automatically map the mechanical properties of each vesicle, raising the throughput of vesicle measurements to hundreds per preparation. EVs with three different lipid bilayer compositions, extruded at two different sizes (30nm and 100nm) mimicking the size of EVs in vivo, have been used in this study. The goal was to compare different mechanical models to observe which better describes the mechanical properties of EVs, and establishing methodology that could ultimately be applied to cell-derived EVs in pathological and non-pathological conditions.

The lipid bilayer compositions chosen for the study are the following:

- DPPC (Dipalmitoylphosphatidylcholine): DPPC is a minimal component of cell membranes, where it can only be found in trace amounts. However, solid-like membranes composed by this phospholipid have been extensively used in the literature to model membranes. Since these systems have been extensively characterized by AFM, they have been included in this study.

- DPPC (Dipalmitoylphosphatidylcholine): CHOL (Cholesterol) (Ratio 1:1): Cholesterol has a profound effect on the physical properties of phospholipid bilayers by affecting their ordering, condensing and regulating their fluidity. By inducing a liquid-order phase, cholesterol also affects the phospholipid molecules by either increasing or decreasing the fluidity of their hydrocarbon chains when the temperature is below or above the gel to liquid-crystalline phase temperature respectively. The ratio of DPPC to CHOL used in this study produces vesicles with membranes displaying a solid-like behaviour at room temperature.

- DOPC (1,2-Dioleoyl-sn-glycero-3-phosphocholine): SM (Sphingomyelin) (Ratio 1:1): Ideally in the study we would have included vesicles with a membrane composition displaying liquid-like behaviour. However, we decided to include vesicles displaying both a liquid-like and solid-like phase as they proved easier to produce and measure. To achieve this two-phase behaviour at room temperature a mixture of DOPC (liquid-like) and SM 16:0 (solid-like) was used.

These conditions offer systems of controlled complexity and with expected properties that can be used to optimize experimental conditions.

2.3.1.1. Vesicle extrusion

1 mL of each lipid solution was extruded 31 times through a polycarbonate membrane with a pore size of 30nm or 100nm at 55 ºC with an Avanti Mini-Extruder (Avanti, Birmingham, AL, USA).

2.3.1.2. Sample preparation for AFM

35 mm diameter glass-bottom petri dishes (Willco, Amsterdam, NL) were used as a substrate. First, to functionalize the surface, the glass surface of the petri

dish was coated with Poly-L-Lysine (PLL) at a concentration of 0.1% and left to incubate for 3 minutes at room temperature. Then the surface was rinsed 5 times with Milli-Q water and coated with the nanovesicles mixture and left to incubate at room temperature for 30 minutes. Finally, the surface was rinsed with PBS (Phosphate Buffered Saline) buffer solution 5 times.

Different sample preparations on multiple substrates were tested before selecting this method. Mica and PLL-coated mica were the first choice for the substrate. However, they proved to not be good substrates for vesicle adsorption and were discarded. As a second approach ultra flat SiO_2 was tested. This substrate proved not to be suitable for all lipid compositions. Finally, PLL-coated glass was tested. Which proved to be a suitable substrate for all the experimental conditions.

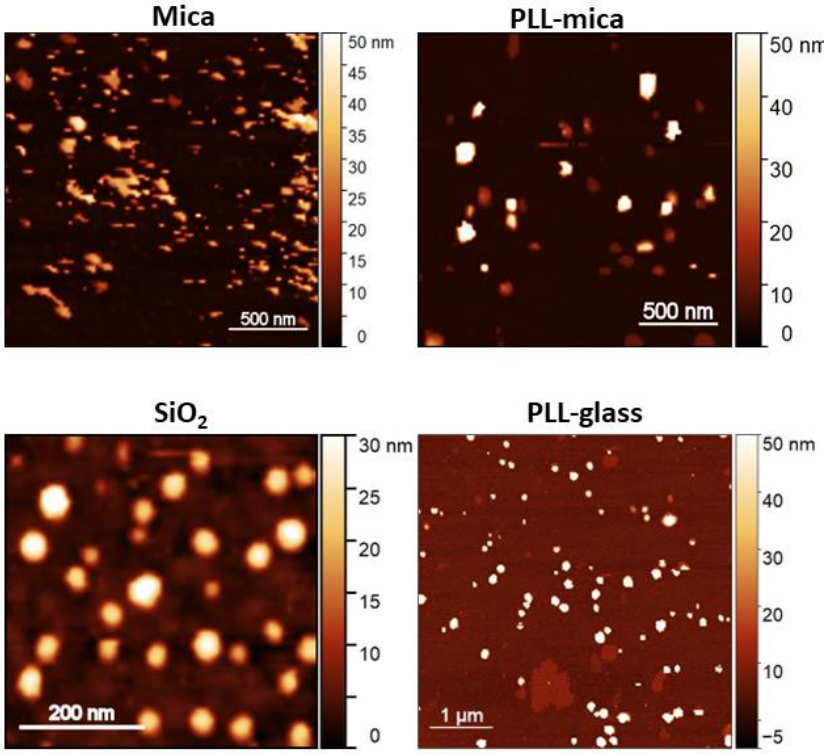

Figure 47: Different substrates tested. Mica and Poly-L-Lysine (PLL)-coated mica are not good substrates for vesicle adsorption. SiO2 and Poly-L-Lysine-coated glass are good substrates.

2.3.1.3. AFM measurement parameters

The AFM measurements were performed with an AC40 cantilever (pyramidal tip, 8 nm tip radius, 35° side angle and a spring constant of 0.101N/m) (Bruker, Santa Barbara, CA, USA). Quantitative Imaging (QI) was performed with a setpoint of 0.3nN, ramp size of 200nm at a ramp speed of 40µm/s, Figure 48

shows an example of force curves collected with these parameters. For the survey scans a scan size of 5 µm x 5µm and a resolution of 100 x100 pixels was used. The zoom scans were performed with the same parameters at a scan size of 500nm x 500nm.

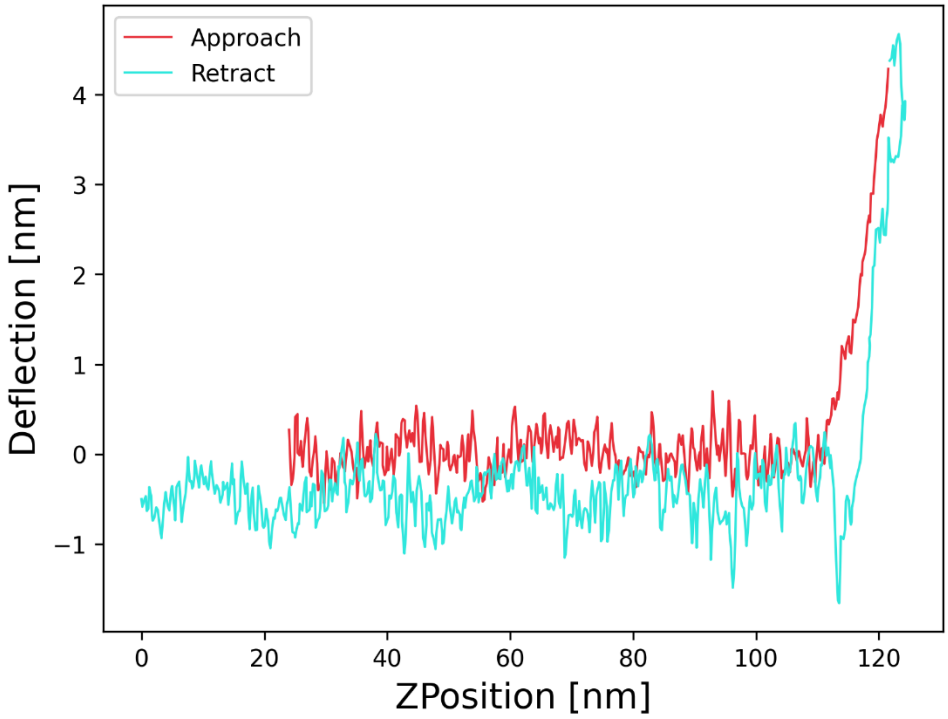

Figure 48: Example of force curve collected on DOPC:CHOL mixture vesicles extruded at 50nm. Due to the speed overshooting of the piezo is observed in the retract portion of the curve.

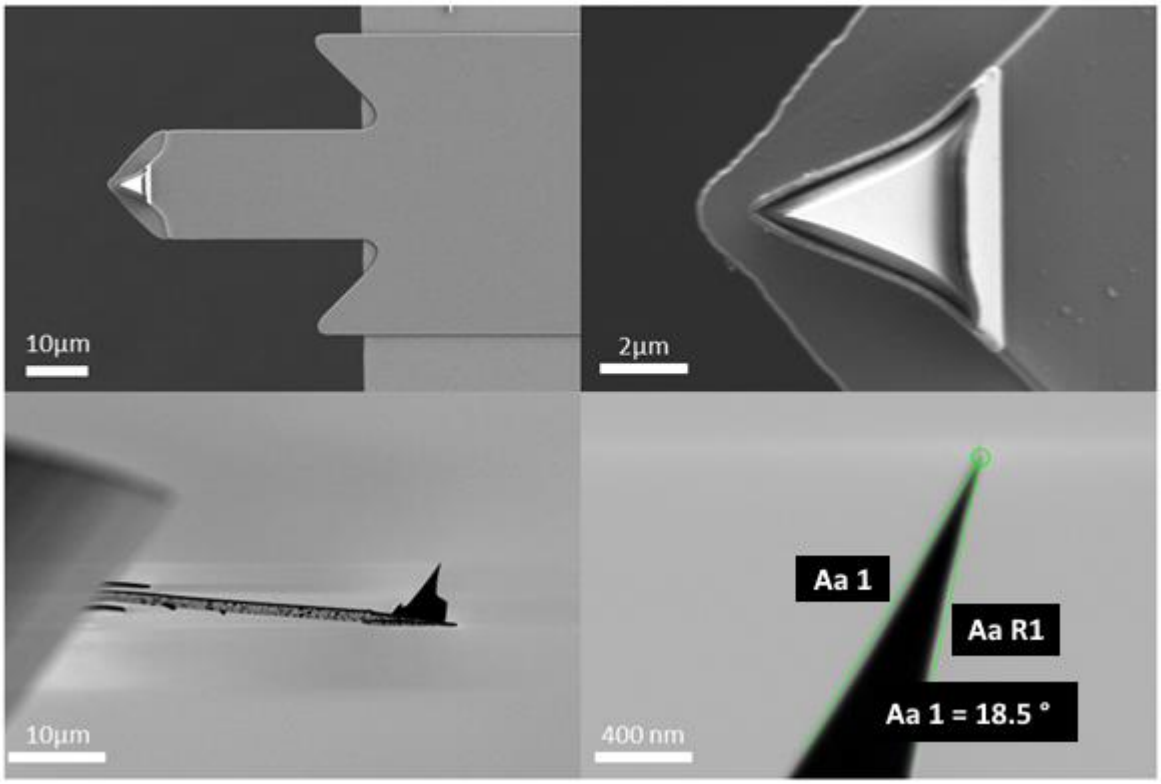

Figure 49: AC40 probe scanning electron microscopy image.

2.3.1.4. Nanovesicle detection

The algorithm to detect the nanovesicle positions has been adapted from the previous work of Dujardin et al. (Dujardin et al., 2019). For this application the detection algorithm has been implemented as described below:

1. A low-resolution scan of 5 x 5µm^2 and 100 x 100pxls^2 is acquired on a region of the sample.

2. The height channel data is flattened by fitting and subtracting a linear plane.

3. While the maximum height value in the survey scan is larger than the height threshold, a region of 500 x 500nm^2 is defined around the position of the maximum height value. Each time a region is delimited, the height values within that region are not considered in the following loop.

4. To better centre the scan on the centre of detected object, each 500 x 500 nm^2 scan region is thresholded again and the centre position of the region with height values above the height threshold is computed. Examples of these scans can be observed on Figure 50.

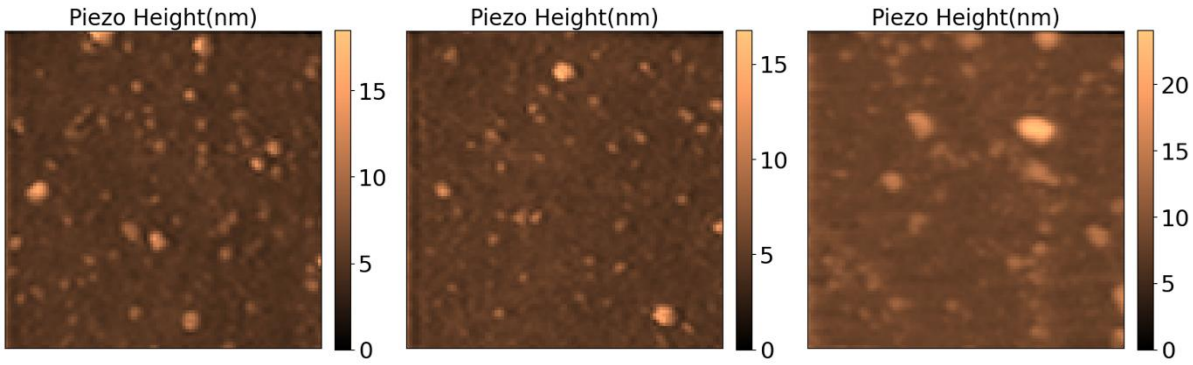

Figure 50: Examples of 500 x 500 nm^2 scan regions acquired on DPPC: CHOL nanovesicles extruded at 30nm.

2.3.1.5. AFM automation implementation

The automated data acquisition routines have been implemented on a NanoWizard III by relying on the Experiment Planner® module. Which provides a programming interface which allows to drive the instrument and monitor the experimental parameters from Jython (Java implementation of Python) scripts. Additionally, a custom Python library has been developed to access the height data channel of the measurements once they have been acquired.

2.3.1.6. AFM automated measurements workflow

Experiment Set-up

Before each experiment the user calibrates the instrument and places the sample on the sample holder.

Start-up

To start each automated run, the user inputs the parameters to use during the experiment (survey scan parameters, zoom scan parameters, etc.) and runs the script using the Experiment Planner® module. As the nanovesicles used for this

study present sizes inferior to 500nm the motor stage was not used and all measurements were acquired within the X and Y piezo maximum range (100 x 100μm^2).

Automated ROI detection

Once the script is executed survey scans are acquired sequentially within the X and Y piezo range. Every survey scan is processed using a custom Python library capable of reading the height channel data collected and processing it following the ROI detection routine described above to detect the nanovesicle positions within each map.

Scan

On each detected position a zoom scan is then collected using the parameters defined by the user. When a zoom scan has been collected on each detected position the system moves to the next area and acquires a new survey scan. The ROI detection and scan routines are executed in a loop, until the user stops the experiment or the whole piezo area (100 x 100μm^2) has been measured.

2.3.1.7. AFM data analysis

As we are interested in the mechanical and morphological properties of individual vesicles, an algorithm to segment the vesicle regions from the substrate on each map and group the force curves corresponding to each vesicle was developed. The algorithm performs the following operations:

1. A first-degree plane fit is performed to the sensor height channel data of each QI map.

2. Triangle thresholding is used to automatically segment the vesicle regions from the substrate and obtain a binary mask.

3. The region of each vesicle is then labelled by grouping neighbouring pixels with the same value.

4. The binary mask of each vesicle is processed to obtain its maximum Ferret diameter, area and circularity. The vesicles with a Ferret diameter

outside the range of +/- 20% the theoretical diameter (30nm or 100nm) are discarded.

5. The curve indices of the QI scan corresponding to each vesicle region are obtained.

6. This mask is used to segment the height channel data corresponding to each vesicle. Using the height profile of the vesicle the curvature radius is obtained.

Figure 51 provides a visual representation of this process:

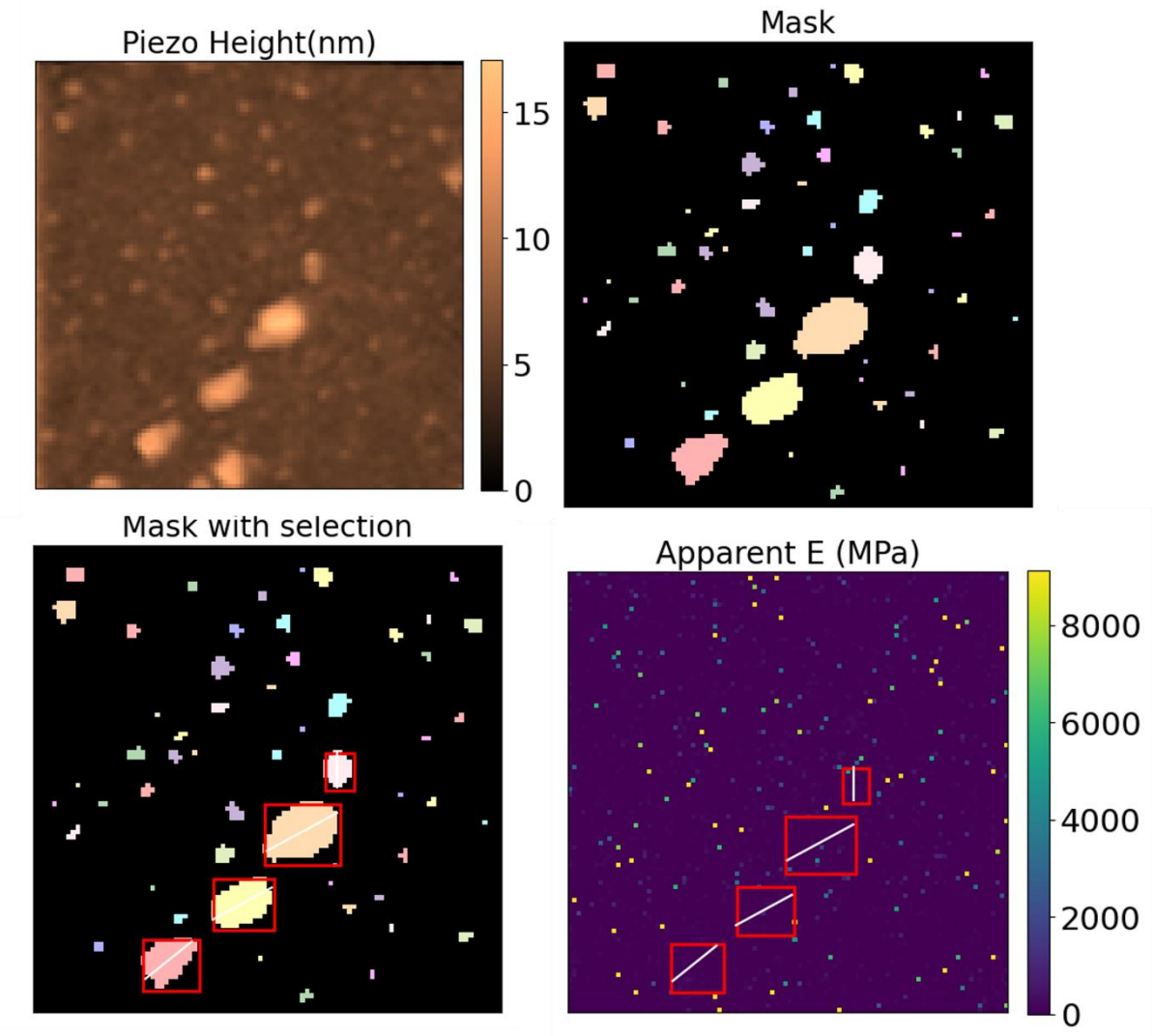

Figure 51 Example of AFM data analysis. First the piezo height data is flattened, triangle thresholding is used to segment the regions corresponding to the sample from the substrate. Then the areas corresponding to the nanovesicles (red bounding boxes) are determined using morphological parameters (maximum Ferret diameter [white line] and circularity). Finally, using this region definition the curves acquired on the nanovesicles are selected and parameters like the Apparent Young's modulus (E) are obtained.

Once the curve indices for each have been determined the force curves are processed to obtain three mechanical parameters:

2.3.1.7.1. Young's Modulus (E)

Although a Pyramidal probe was used to acquire the force-distance curves. At this scale the Paraboloidal model better characterizes the tip indenting the vesicle, as it can be observed in Figure 52. For this reason, the Hertz paraboloidal model was fit to the approach segment of each force curve to obtain E:

$$F(\delta) = \frac{4\sqrt{R}}{3(1-\nu^2)} E\delta^{3/2}$$

where R corresponds to the tip radius and ν to the Poisson's ratio.

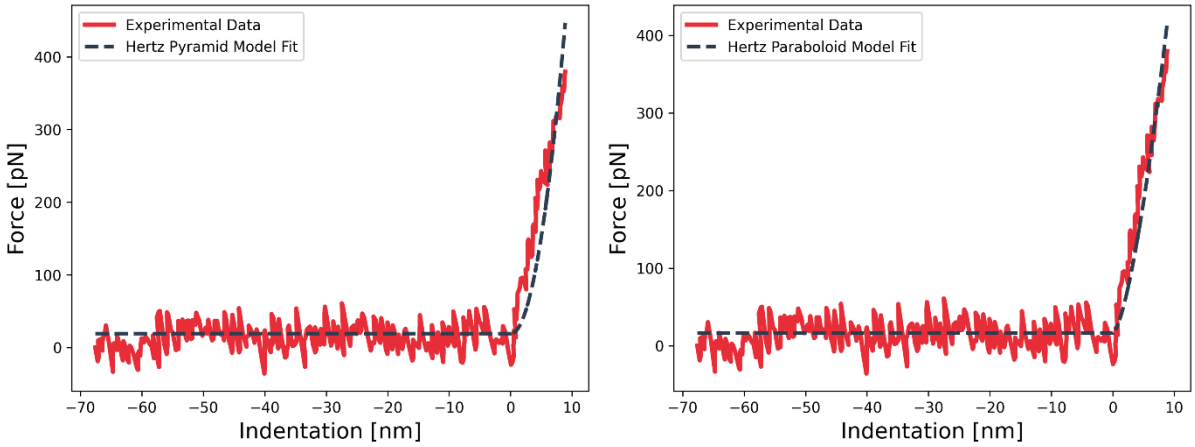

Figure 52: Comparison between pyramidal and paraboloidal model in Hertz fit on experimental data acquired on DOPC:CHOL mixture vesicles extruded at 50nm. As in small vesicles the surface is finite and curved, the Young's modulus value (E) will depend on the size of the vesicle. The paraboloidal model fits better the experimental data collected due to the geometry of the tip (blunted pyramidal tip with a spherical cap radius), for small indentations, like in this case, the paraboloidal model is the most suitable.

2.3.1.7.2. Bottom-Effect-Corrected Young's Modulus (E_{BEC})

Since the indentation values larger than 20% of their maximum height were observed in some vesicles, the E values obtained were bottom effect corrected using the model developed by Garcia & Garcia (Garcia & Garcia, 2018).

$$\mathrm{F}(\delta) = F_0(\delta)\left[\frac{1}{h^0} + \frac{1.133\sqrt{\delta R}}{h} + \frac{1.497\delta R}{h^2} + \frac{1.469\delta R\sqrt{\delta R}}{h^3} + \frac{0.755(\delta^2 R^2)}{h^4}\right]$$

$$F_0(\delta) = \frac{4\sqrt{R}}{3(1-\nu^2)} E\delta^{3/2}$$

Using the height value of every pixel corresponding to the vesicle (h), the correction factor was computed for each force curve. Then the E value obtained from fitting the paraboloidal model was multiplied by this factor to obtain E_{BEC}.

2.3.1.7.3. Thin Shell Theory Bending Modulus (k_v)

As an alternative parameter to the Young's Modulus the bending modulus was computed for each force curve. The Young's Modulus (E_{TST}) was obtained by fitting a first-degree polynomial to the contact part in the approach segment of each force distance curve to obtain the equivalent stiffness (Keq) and then applying the TST-based analytical solution. E_{TST} was then used to compute k_v using the Thin Shell Theory expression that relates both parameters:

$$kv = E_{TST} h^3 / 12(1-\nu),$$

Where k_v corresponds to the Thin Shell Theory Bending Modulus, E_{TST} to the Young's Modulus, h to the height of the bilayer (evaluated from AFM imaging experiments) and ν to the Poisson's ratio.

2.3.1.8. Mechanical properties of artificial vesicles

Three samples of each lipid composition and extrusion size were automatically measured. From the topographical data of the QI maps the area, maximum height (h_{max}), curvature radius (Cr) and flatness (h_{max} / Cr) were obtained for each vesicle. The mean values of each parameter for each group can be found in Table 2.

Extrusion Size	Lipid Composition	Number of vesicles	Area	Maximum height (hmax)	Curvature Radius (Cr)	Flatness (hmax / Cr)
30 nm	DPPC	94	2059.04 ± 170.58 nm^2	6.42 ± 0.49 nm	8.75 ± 0.64 nm	0.76 ± 0.03
	DPPC: CHOL	178	1930.34 ± 111.77 nm^2	7.10 ± 0.42 nm	8.72 ± 0.42 nm	0.86 ± 0.02
	DOPC:SM	72	1257.64 ± 126.92 nm^2	5.82 ± 0.57 nm	7.60 ± 0.56 nm	0.77 ± 0.03
50 nm	DPPC	100	5402.25 ± 448.71 nm^2	12.43 ± 1.50 nm	12.30 ± 1.10 nm	0.94 ± 0.03
	DPPC: CHOL	42	6063.10 ± 676.67 nm^2	12.55 ± 1.58 nm	13.99 ± 1.27 nm	0.85 ± 0.06
	DOPC:SM	139	7698.20 ± 441.62 nm^2	17.51 ± 1.13 nm	17.82 ± 1.10 nm	1.03 ± 0.03
100 nm	DPPC	126	37540.08 ± 1255.59 nm^2	76.46 ± 3.98 nm	59.66 ± 2.39 nm	1.24 ± 0.04
	DPPC: CHOL	69	21892.75 ± 1309.62 nm^2	47.49 ± 3.43 nm	41.70 ± 3.22 nm	1.16 ± 0.05
	DOPC:SM	110	24438.18 ± 1440.89 nm^2	33.88 ± 2.33 nm	35.98 ± 2.24 nm	1.00 ± 0.04

Table 2: Morphological values obtained for each lipid composition and extrusion size. Values are represented as the mean ± standard error.

Vesicles extruded using larger filter pore size presented larger values of area, maximum height and curvature radius. With a mean h_{max} / Cr ratio of 0.79 vesicles extruded with a pore size of 30nm were the most flattened vesicles.

In addition to the topographical data, QI scans also contain the force-distance curves acquired for each pixel. By fitting the paraboloidal Hertz model the median values for the Young's modulus were obtained for each vesicle. To avoid the effect of the substrate on the determination of the Young modulus and compare between different vesicle extrusion sizes, the force distance curves were fitted up to an indentation of 3nm and the values were bottom effect corrected. Figure 53 below shows the distribution of the median Young's Modulus (E) and Bottom Effect Corrected Young's Modulus (E_{BEC}) for each lipid composition and extrusion size:

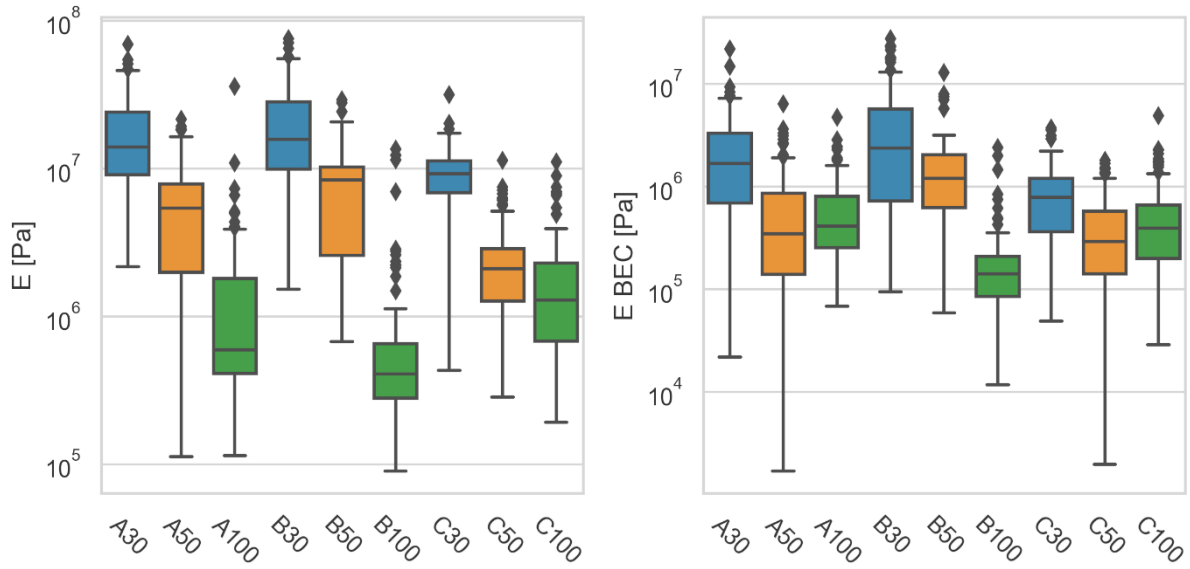

Figure 53: Obtained Young's modulus (E) (Left) and Bottom Effect Corrected Young's Modulus (EBEC) (Right) values for each vesicle of the lipid compositions (A: DPPC, B: DOPC:CHOL, C: DPPC:SM) extruded at different sizes (30nm, 50nm, 100nm). A corresponds to DPPC, B to DPPC: CHOL and C to DOPC:SM.

The values obtained for E by fitting the Hertz paraboloidal model showed changes of more than 1 order of magnitude for each extrusion size and same lipid composition. The bottom effect correction reduced the difference range between different extrusion sizes and same lipid composition.

Finally, from the force distance curves by applying Thin Shell Theory (TST) the Young's Modulus (E_{TST}) and Bending Modulus (k_V) are obtained. As the sample sizes of each group were different and the values of E_{TST} and k_V were not normally distributed, the significance of E_{TST} and k_V difference between lipid

compositions and extrusions sizes was assessed by applying the Kruskal-Wallis test (Kruskal & Wallis, 1952). When comparing conditions with different extrusion sizes but same lipid compositions no significant differences in the values of E_{TST} were found except when comparing between DOPC:SM 30nm - DOPC:SM 100nm (p value = 0.037) and DOPC:SM 50 nm - DOPC:SM100 nm (p value < 0.0001). On the other hand, when comparing E_{TST} values of conditions with different lipid composition but same extrusion size, significant differences were observed in all cases except when comparing DPPC and DOPC:SM extruded at 100nm. Figure 54 depicts the results of the statistical tests and the distributions of the median E_{TST} of each group. Regarding the values of k_V, no statistical difference was observed between groups. Figure 55 shows the results of the statistical tests and median k_V distribution for each test.

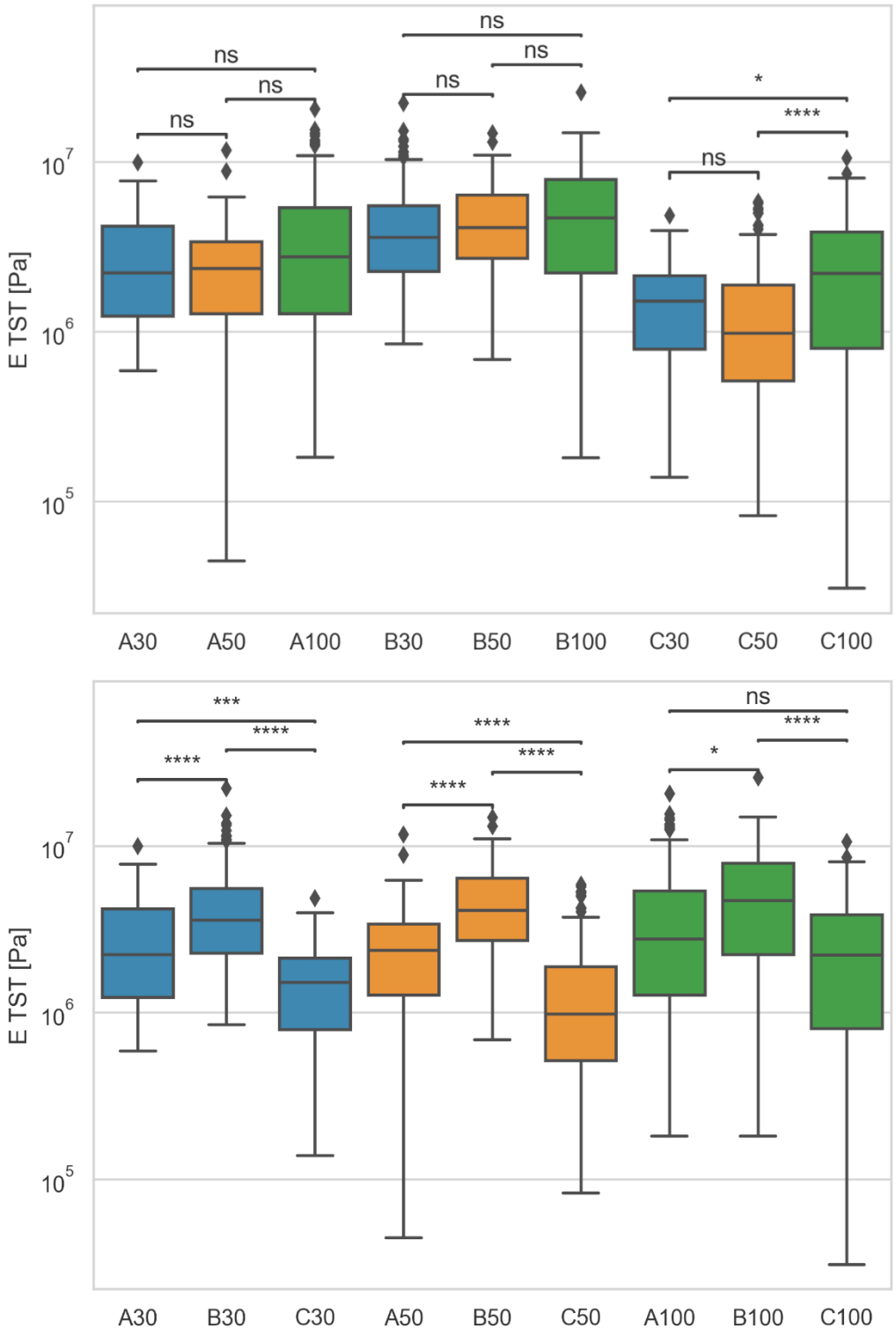

Figure 54: Obtained Young's modulus (ETST) by applying Thin Shell Theory for each vesicle of the lipid compositions (A: DPPC, B: DOPC:CHOL, C: DPPC:SM) extruded at different sizes (30nm, 50nm, 100nm). On the top the ETST values of conditions with the same lipid composition but extruded at different sizes are compared. Statistically significant differences are found only between C30 – C100 and C50 -C100. On the bottom the ETST values of conditions with different lipid compositions but same extrusion size are compared. Statistically significant differences are found with the same trend when the vesicles are extruded at 30 nm and 50nm. However, when extruded at 100 nm no statistically significant difference is observed between A100 and C100. **Kruskal-Wallis test** *p-value annotation legend: ns: 5.00e-02 < p <= 1.00e+00, *: 1.00e-02 < p <= 5.00e-02, **: 1.00e-03 < p <= 1.00e-02, ***: 1.00e-04 < p <= 1.00e-03, ****: p <= 1.00e-04.*

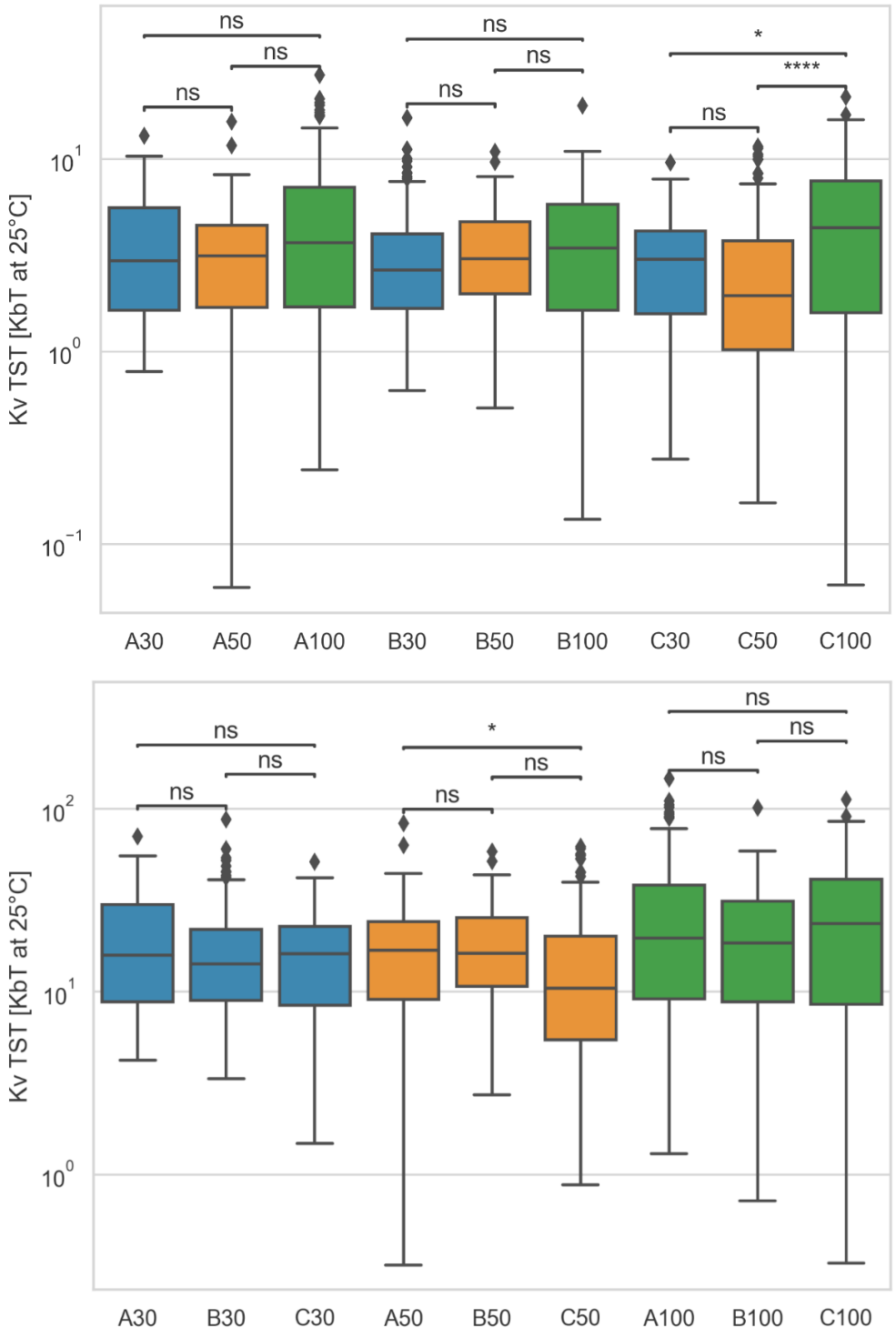

Figure 55: Obtained Bending Modulus (k_υ) at 25°C by applying Thin Shell Theory for each vesicle of the lipid compositions (A: DPPC, B: DOPC:CHOL, C: DPPC:SM) extruded at different sizes (30nm, 50nm, 100nm). On the top the kV values of conditions with the same lipid composition but extruded at different sizes are compared. Statistically significant differences are found only between C30 and C100. On the bottom the k_υ values of conditions with different lipid compositions but same extrusion size are compared. Statistically significant differences are found only between A50 and C50. Kruskal-Wallis test *p-value annotation legend: ns: 5.00e-02 < p <= 1.00e+00, *: 1.00e-02 < p <= 5.00e-02, **: 1.00e-03 < p <= 1.00e-02, ***: 1.00e-04 < p <= 1.00e-03, ****: p <= 1.00e-04.*

2.3.1.9. Discussion

In this study nanovesicles of three different lipid compositions and extruded at three different sizes were measured automatically by AFM in liquid using a custom system capable of detecting the ROIs to measure from a survey scan. An approach which was proven successful by Dujardin and collaborators (Dujardin et al., 2019) to automatically measure bacteria. Thanks to the automation of the system, we were able to characterize a total of 930 nanovesicles in 108 hours, only requiring the user to perform the setup of the instrument and exchange the samples.

The QI scans obtained for each nanovesicle allowed to characterize both its morphology and mechanical properties. As it can be observed in Table 2, nanovesicles of different lipid composition but extruded at the same size, presented similar morphological characteristics. With the area, maximum height and curvature radius being larger for those vesicles extruded at a larger size. Although, we expected smaller vesicles to retain their shape better when being deposited on the sample, vesicles extruded at 50nm and 100nm presented a higher maximum height / curvature radius ratio. Thus, preserving better their circular shape and being less absorbed into the surface. Why this is the case is not clear, but it could be related to the nanovesicles being unstable due to a bad extrusion step. As the vesicles were extruded by hand using a Hamilton syringe, too much pressure may have caused the vesicles to be less stable. Another option could be the destabilization of the nanovesicles during the shock freezing. More tests are required to understand why these vesicles retain their shape worse than the other conditions.

As a first approach to measure the mechanical properties of the nanovesicles, the hertz paraboloidal model was fit to the approach segment to each force curve acquired on the nanovesicle. Moreover, to reduce the effect of the substrate and be able to compare between vesicles extruded at different sizes, the model was fit until an indentation of 3nm and the resulting Young´s modulus values were corrected for bottom effect. Both the non-corrected and corrected values of the Young´s modulus presented variations of up to an order of magnitude between nanovesicles with the same lipid mixture composition but extruded at different sizes.

In addition to the Hertz model, we decided to measure the Young´s modulus by applying thin shell theory. The values obtained from the analysis showed no

statistical differences between groups of the same lipid composition but extruded at different sizes, except for DOPC:SM where statistically significant differences were observed both between vesicles extruded at 30nm – 100nm and 50nm – 100nm. In a similar way, when comparing the values of groups of different lipid mixture but extruded at the same size, the expected trend of DPPC: CHOL having the highest value, the being followed by DPPC and then finally DOPC:SM showing the lowest value is observed both in vesicles extruded at 30nm and 50nm. But in vesicles extruded at 100 nm the median of DOPC:SM is still lower than DPPC, but there are no statistically significant differences between both groups. This suggest that the sample preparation for DOPC:SM extruded at 100nm could have not been properly performed, as the values of Young´s modulus for this group are larger than the same lipid mixture extruded at 30nm and 50nm.

With the Thin Shell theory Young´s modulus values and the experimental values for bilayer thickness, the values of the bending modulus were computed. Unlike in the case of the Young´s modulus no statistical differences are observed between the groups. Moreover, the values obtained for the bending modulus are one order of magnitude lower than the values reported by other authors for DPPC (Delorme & Fery, 2006; Et-Thakafy et al., 2017; Ridolfi et al., 2021). This could be explained due to the tip choice, experimental parameters and lower indentation depths (3nm) used in this study.

2.3.1.10. Automated measurements protocol

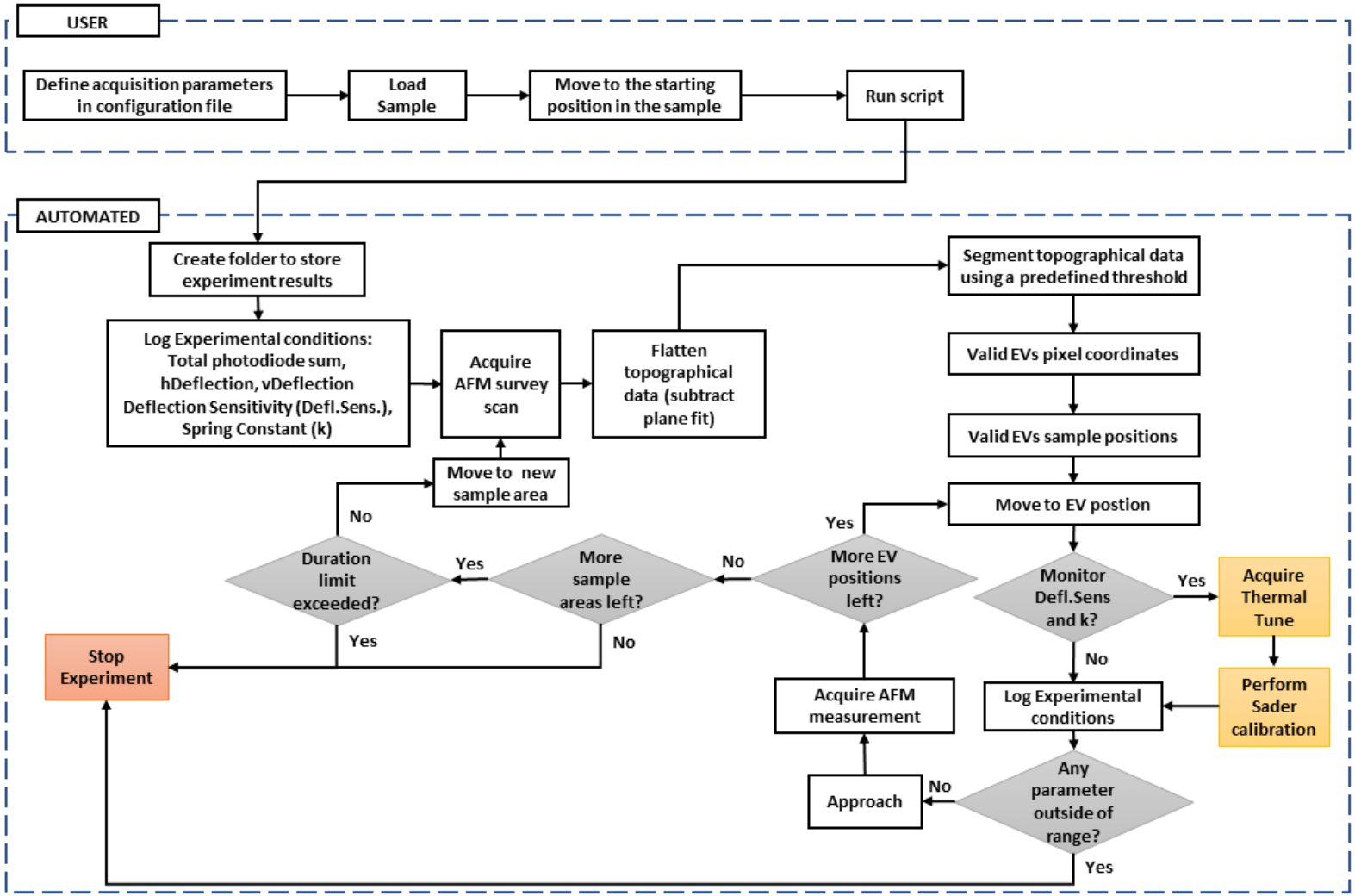

Figure 56: Diagram summarizing the automated AFM protocol used in the experiments performed on nanovesicles.

2.3.2. Mammalial epithelial cells (hTERT-RPE-1)

The hTERT-immortalized Retinal Pigment Epithelial (hTERT-RPE-1) cell line was derived from the RPE-340 human cell line through transfection with vectors encoding for the human telomerase reverse transcriptase (hTERT). The transfected cells present longer telomeres, divide faster and their in vitro cellular senescence is slower, allowing them to exceed the normal life-span of their original cell line (Bodnar et al., 1998; Hindul et al., 2022). Thanks to these characteristics, the hTERT-RPE-1 cell line is a widely spread model, used to study human physiological processes and in drug development research.

Several studies have characterized the effect of cytoskeleton disruptors on hTERT-RPE-1 cells (Flormann et al., 2021; Rigato et al., 2015). This cell line is commonly used in nano-mechanobiology to study how the disruption of the cell's cytoskeleton affects its mechanical properties. The aim of this section is to use Latrunculin-A to alter the mechanical properties of the cells and observe, if the same effect previously described by other authors can be measured from the results obtained in an automated way. Latrunculin-A blocks actin polymerization by binding to G-actin monomers (Morton et al., 2000). As a result of the actin networks disruption, it has been observed that Latrunculin-A treated hTERT-RPE-1 cells present a lower average apparent Young's modulus (E) when compared to non-treated cells (Flormann et al., 2021; Rigato et al., 2015). To validate the automated system, AFM measurements were acquired on hTERT-RPE-1cells randomly seeded on bare glass and micropatterned, treated with Latrunculin-A and DMSO (Control), solvent used to dissolve Latrunculin-A.

2.3.2.1. Cell culture

hTERT-RPE-1 cells (ATCC, Manassas, VA, USA) were cultured in DMEM/F12 (ThermoFischer, Waltham, MA, USA) containing 10% foetal bovine serum and 1% Penicillin/Streptomycin. Before performing the automated measurements, the cells were seeded at a density of 0.3×10^4 (8 cells / mm^2) in 35 mm diameter glass-bottom petri dishes (WillCo, Amsterdam, NL) or micropatterns produced using the protocol in section 2.3.2.2. Finally, the cells were incubated in the petri dish overnight at 37°C and 5% CO_2.

2.3.2.2. Micropattern preparation

Micropatterns were produced on glass using the protocol defined by Azioune et al. 2010 (Azioune et al., 2010), optimized for a UVO-Cleaner® model 30 (Jetlight, Irvine, CA, USA). A mask with crossbow and circle patterns was used to emulate cells in a polarized and non-polarized state respectively.

1. 30 mm diameter borosilicate glass coverslips (VWR, Radnor, PA, USA) are cleaned with acetone in an ultrasonic bath for 5 minutes.

2. After drying the coverslips, they are placed inside the UVO-Cleaner® and exposed to UV (λ = 253.7nm) for 5 minutes to make them more hydrophilic.

3. The hydrophilic side of the coverslip is covered with a solution of poly (L-lysine)-graft-poly ethylene glycol (PLL-g-PEG) (SuSoS, Dübendorf, CH) in purified water at a concentration of 0.1 mg/mL. The coverslips are incubated inside a wet chamber at room temperature for 1 hour.

4. The coverslips are then rinsed once with PBS and twice with purified water.

5. The low reflective chrome oxide coated side of the photomask is exposed to UV for 5 minutes to make it more hydrophilic.

6. The pegylated side of the coverslips is placed in contact with the not chrome-coated side of the photomask with a 7.5 µL drop of purified water. The capillary force keeps the coverslip attached to the photomask.

7. The photomask is then exposed to UV for 3 minutes with the high reflective chrome coated side towards the UV lamp. This step will allow enough UV light to pass through the mask micro-openings, degrading the PLL-g-PEG to create a well with the micropattern's shape.

8. To remove the coverslips from the mask without damaging the mask or the PLL-g-PEG coated surface, water is added around the coverslips. After they detach, they are removed using plastic tweezers without touching the mask.

9. The coverslips are then mounted into 35 mm diameter glass bottom petri dishes with a 22 mm diameter opening (WillCo, Amsterdam, NL) using double sided adhesive rings (3M, Maplewood, MN, USA).

10. A solution of fibronectin is added in the petri to fill the patterns, at a concentration of 0.1 mg/mL for 1h at room temperature.

11. The surface of the coverslip is then washed 5 times with PBS.

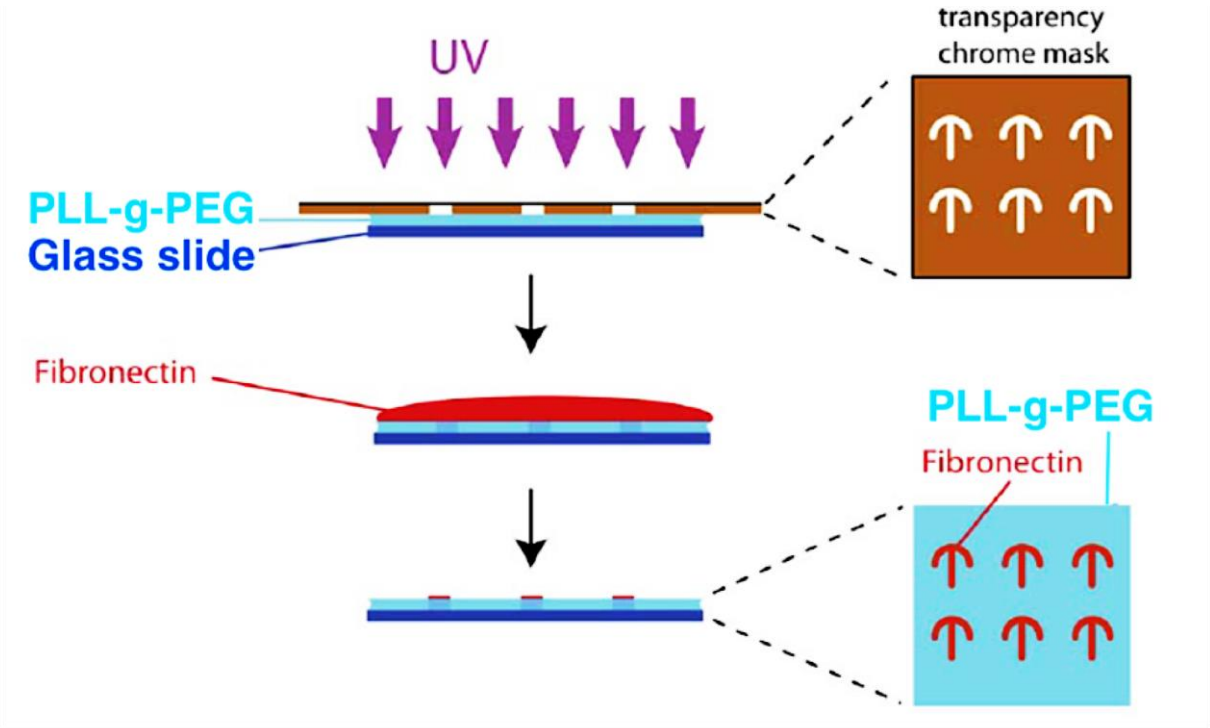

Figure 57: Photolithographic micropatterning on PLL-g-PEG using UV light and a chrome mask. (Reproduced from Wang et al. 2011)

2.3.2.3. Sample preparation for AFM

Before each automated AFM measurement, the medium inside of the petri dish was replaced by 1mL of medium containing 0.2 µM Latrunculin-A (Treatment) or 0.08% Dimethyl Sulfoxide (DMSO) (Control). As Latrunculin-A is dissolved in DMSO when added to the cell culture medium, DMSO was added to the control medium at the same concentration as when the Latrunculin-A treatment is applied to isolate the effect of Latrunculin-A from the DMSO. The exposition time for cells seeded on bare glass is 15 minutes. The exposition time was lowered to 12 minutes in the case of micropatterned cells to prevent cell detachment. After the exposition time had passed, the sample was washed 3

times with DMEM/F12 containing 1% Penicillin/Streptomycin and 20 mM HEPES to remove any traces of medium containing the drug. Since AFM measurements were performed outside of an incubator or chamber, with no CO_2 concentration control, HEPES buffer was added to preserve the pH equilibrium for longer despite the changes in CO_2 concentration. During the measurements, the medium was kept at 37°C using a petri dish heater (Bruker, Santa Barbara, CA, USA), pre-calibrated using a thermocouple.

2.3.2.4. AFM measurement parameters

Grids of single force curves (SFC) and Quantitative Imaging (QI) Scans were acquired on samples with cells seeded on bare glass whereas only grids of SFC were acquired on micropatterned cells. In both acquisition modes, the perinuclear region of the cell was targeted and the force setpoint was optimized to achieve a maximum indentation depth between 0.3 µm - 0.8 µm.

SFC grids were acquired with a MLCT-SPH-5UM-DC-D probe (paraboloidal tip, 5 µm radius, 0.4N/m spring constant) (Bruker, Santa Barbara, CA, USA) using the following parameters: 1nN force setpoint, 4µm ramp size, 30µm/s ramp speed, 20 x 20 μm^2 grid size and 4 x 4 points. QI mapping was performed with a PFQNM-LC-A-CAL probe (paraboloidal tip, 70nm radius, 0.094N/m spring constant) (Bruker, Santa Barbara, CA, USA) using the following parameters: 0.5 nN force setpoint, 4 µm ramp size, 30 µm/s ramp speed, 30 x 30 μm^2 scan size and 30 x 30 pixels.

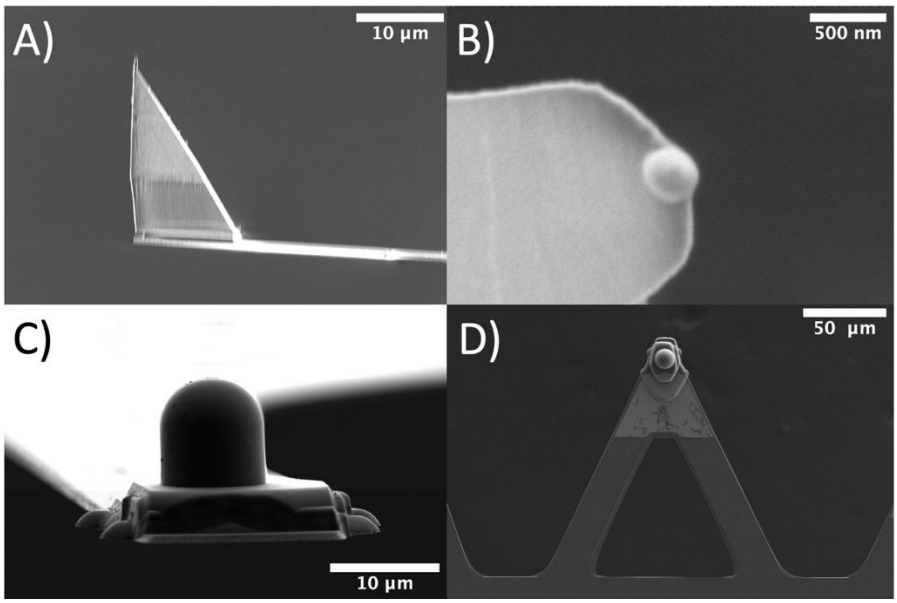

Figure 58: Side-view and top-view scanning electron microscopy images of a PFQNM-LC-A-CAL (A-B) and a MLCT-SPH-5UM-DC-D (C-D) probe.

2.3.2.5. Optical image acquisition and processing parameters

To detect the cells, bright-field images were acquired on each sample area, with a resolution of 1936 x 1216 pixels and a pixel size of 0.3µm/pixel. To detect the cell positions the bright-field image segmentation algorithm described in section 2.2.4.2 was used, with an entropy filter kernel size of 8 x 8 pixels. Only cells with a maximum Ferret diameter between 30-70µm and a circularity of <= 0.5 were selected to be measured

2.3.2.6. AFM data analysis

The criteria used to define force curves that must be rejected is described in section 2.2.6.

All QI scans with more than 30 % of bad force curves, where two or more cells are present or the cell occupies the 100 % (no substate) or less than 30% (failed to centre properly on the cell) of the scan, were discarded. The remaining scans were processed using the JPK data processing software (Bruker, Santa Barbara, CA, USA) by fitting the paraboloidal Hertz model to the approach segment of the force curves up to an indentation of 500nm, a tip radius of 70nm and a Poisson's ratio of 0.5. To account for the effect of the substrate on the thinner

parts of the cell, the E values were then corrected using the bottom effect correction (BEC) model developed by Garcia and Garcia (Garcia & Garcia, 2018) :

$$\mathrm{F}(\delta) = F_0(\delta)\left[\frac{1}{h^0} + \frac{1.133\sqrt{\delta R}}{h} + \frac{1.497\delta R}{h^2} + \frac{1.469\delta R\sqrt{\delta R}}{h^3} + \frac{0.755(\delta^2 R^2)}{h^4}\right]$$

$$F_0(\delta) = \frac{4\sqrt{R}}{3(1-\nu^2)} E\delta^{3/2}$$

where R is the tip radius, ν is the Poison's ratio and h is the sample height at each pixel.

Finally, the E values corresponding to the cell were selected by using the indentation as a mask assuming a minimum indentation threshold of 100nm.

From each SFC grid, bad curves were discarded. The remaining curves were processed using the JPK data processing software (Bruker, Santa Barbara, CA, USA) by fitting the paraboloidal Hertz model to the approach segment of the force curves up to an indentation of 500nm, a tip radius of 5µm and a Poisson's ratio of 0.5. Force curves with an indentation smaller than 300nm were discarded, with the objective of only selecting those curves in the perinuclear region of the cell. The median E of each cell was computed using the force curves remaining on each grid.

2.3.2.7. Measured effect of Latrunculin-A on hTERT-RPE-1 cells

Latrunculin A has been shown to reversibly disrupt the organization of cultured cells microfilaments when present in the medium at concentrations in the range of 0.1-1 µM, by inhibiting the polymerization of actin (Coué et al., 1987). In this section, the effects on the apparent Young's modulus (E) of hTERT-RPE-1 cells treated with Latrunculin A at a concentration of 0.2 µM, are compared to cells treated with 0.8% DMSO, the solvent used to dissolve Latrunculin A. DMSO is used as control, to ensure the changes in the mechanical properties of the cells are only due to the effect of Latrunculin A. As the medium containing Latrunculin A was replaced by fresh medium before AFM measurements (Rotsch & Radmacher, 2000), it is expected that during the experiment the effects of Latrunculin A will be reversed within 1h (Coué et al., 1987) and that cells measured at the beginning of the experiment will present a lower Young's modulus than the cells measured at the end (2h after rinsing).

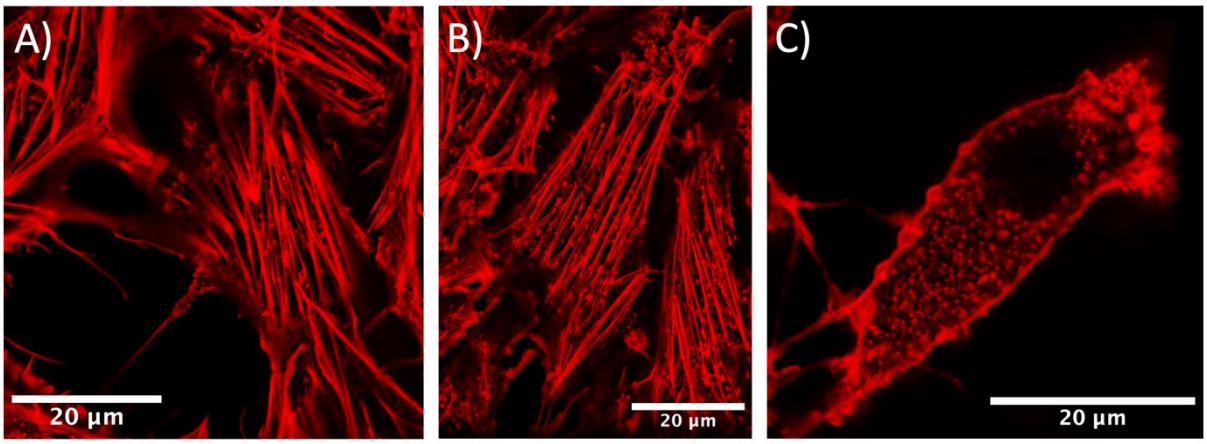

Figure 59: Confocal images of hTERT-RPE-1 cells with actin filaments stained using Phalloidin-Atto 647N. A) hTERT-RPE-1 cells with no treatment. B) hTERT-RPE-1 cells exposed to 0.8% DMSO for 15 minutes. C) hTERT-RPE-1 cells exposed to 0.2 µm Latrunculin-A for 15 minutes. Actin filaments can be observed in non-treated cells and DMSO-treated cells, whereas in Latrunculin-A treated cells actin fibbers have been disrupted and no fibbers can be observed.

To maximize the throughput of AFM, the first approach was to use a colloidal probe with a large contact area and perform a grid of force-distance curves in the centre of hTERT-RPE-1 cells seeded in random positions on a glass-bottom petri dish. Due to the low resolution of the measurements, this approach does not allow to study the distribution of the mechanical properties of the cell. However, it provides a good average fingerprint of the mechanical properties of the cell.

Three replicates were measured for each condition. Since the measurements were performed without environment control, each AFM experiment duration was limited to ~2 hours to ensure cell survivability and prevent sample contamination. The medium was kept at 37°C using a petri dish heater pre-calibrated using a thermocouple, HEPES buffer and antibiotics were added to the medium to maintain the pH and prevent bacterial growth.

The Young's modulus E is directly related to the indentation during the measurements. Then, to better compare between conditions, the approach segment of each force-distance curve was fit to the hertz paraboloidal model up to an indentation of 500nm. This indentation depth was selected to isolate the mechanical properties of the cytoskeleton components on the perinuclear area and minimize the effect of nucleus compression and the stiff substrate on which cells are seeded.

After postprocessing and discarding non-suitable curves, the data of 1154 cells (588 DMSO-treated, 566 Latrunculin-A-treated) was used for the analysis, yielding an average throughput of 118 cells per hour. The values measured for the median apparent Young's modulus are 212.13 Pa for DMSO-treated cells and 105.91 Pa for Latrunculin-A-treated cells. This shows that Latrunculin-A-treated cells are 2 times less elastic than DMSO-treated cells (Figure 60).

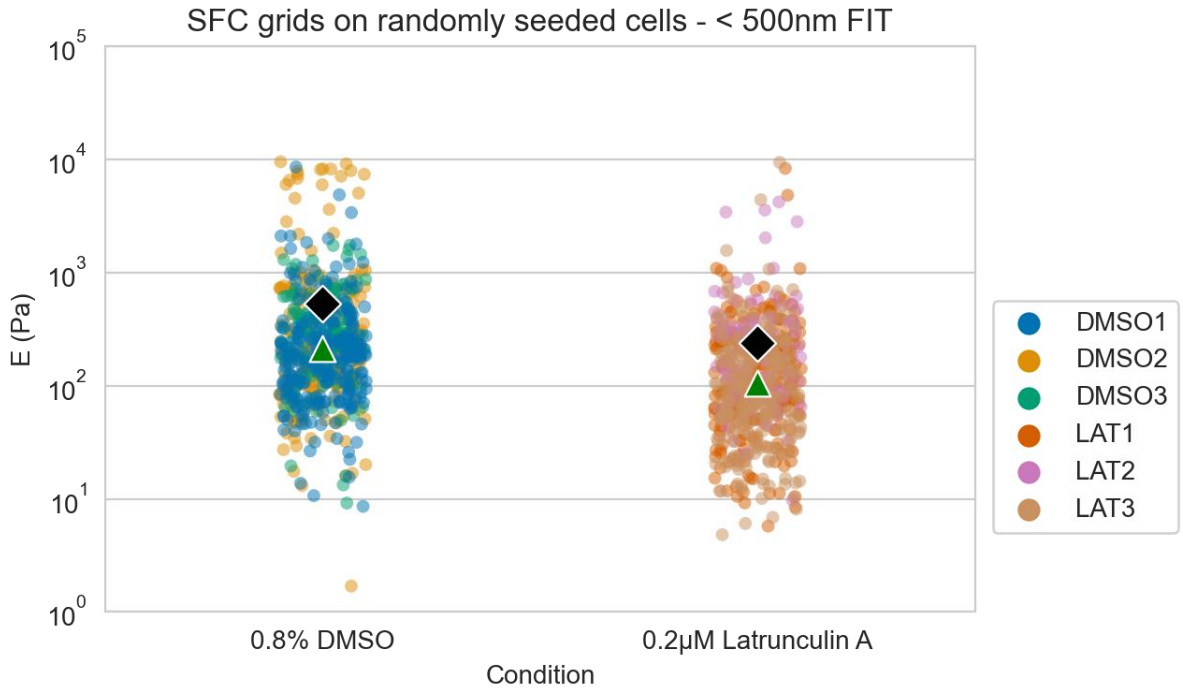

Figure 60: Apparent Young's modulus (E) of hTERT-RPE-1 cells seeded on glass-bottom petri dishes. Each point represents the median E of a 4 x 4 grid of single force curves acquired on the perinuclear region of the cell (0.8% DMSO N = 588, 0.2 µM Latrunculin-A N = 566). The black diamond represents the mean (536.93 Pa 0.8% DMSO, 240.90 Pa 0.2 µM Latrunculin A) and the green triangle represents the median (212.13 Pa 0.8% DMSO, 105.91 Pa 0.2 µM Latrunculin-A).

As a second approach the same measurements using the same parameters were performed on micropatterned hTERT-RPE-1 cells. Micropatterns enforce a defined morphology, similar adhesion profile and cytoskeleton conformation on cells. It makes the sample more homogeneous and decreases the dispersion of the mechanical properties of the population. Micropatterns also force single cells to distribute following an evenly spaced grid through the surface, making them interesting from the point of view of developing automation. Cells are then evenly distributed and it thus increases the number of single cells that can be measured on each field of view and minimizes the travel distance between cells. Similar cell morphology ensures that the measurement is performed on the same cell region each time. Nevertheless, micropatterning protocols require multiple steps and have to be optimized for each cell line. After

optimizing our protocol, we could achieve yields of 30 % - 40 % of populated micropatterns. The occupancy rate of the micropatterns could be increased by increasing the number of seeded cells; however, this would result in several micropatterns being occupied by multiple cells and not being suitable for measurement.

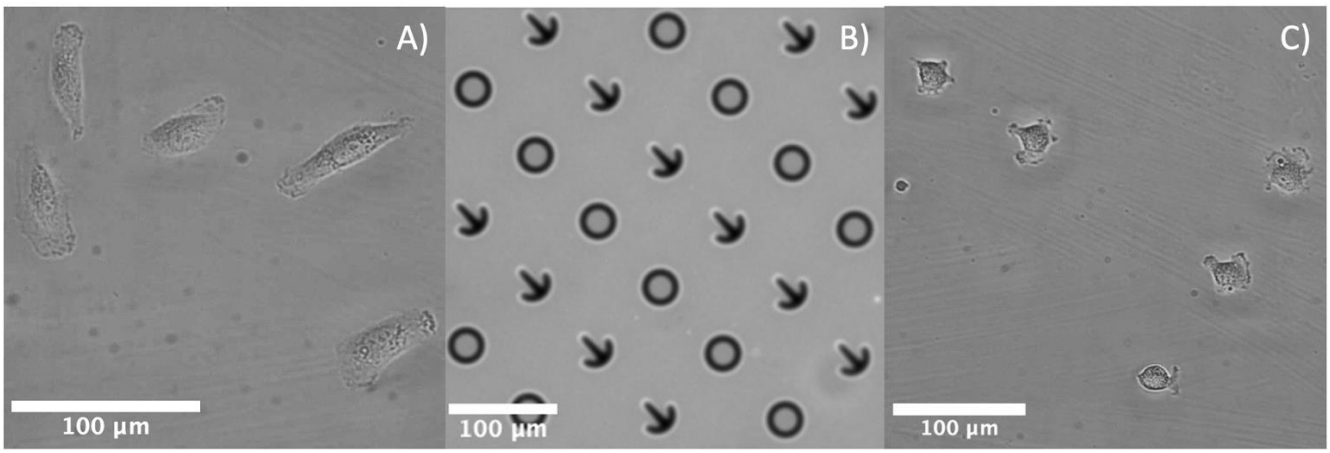

Figure 61: Sample preparations used. A) Bright-field image of hTERT-RPE-1 cells randomly seeded on bare glass. B) Fluorescent image of micropatterns containing fluorescent fibronectin. A photomask with ring-shaped and crossbow-shaped openings was used. C) Bright-field image of hTERT-RPE-1 cells seeded on micropatterns.

After postprocessing, the data of 1668 cells (834 DMSO-treated, 927 Latrunculin-A-treated) was used for the analysis, with an average of 132 cells measured per hour. The values measured for the median apparent Young's modulus are 102.47 Pa for DMSO-treated and 43.64 Pa for Latrunculin-A-treated cells. Such a difference indicates that Latrunculin-A-treated cells 2.35 times less elastic than DMSO-treated cells (Figure 62).

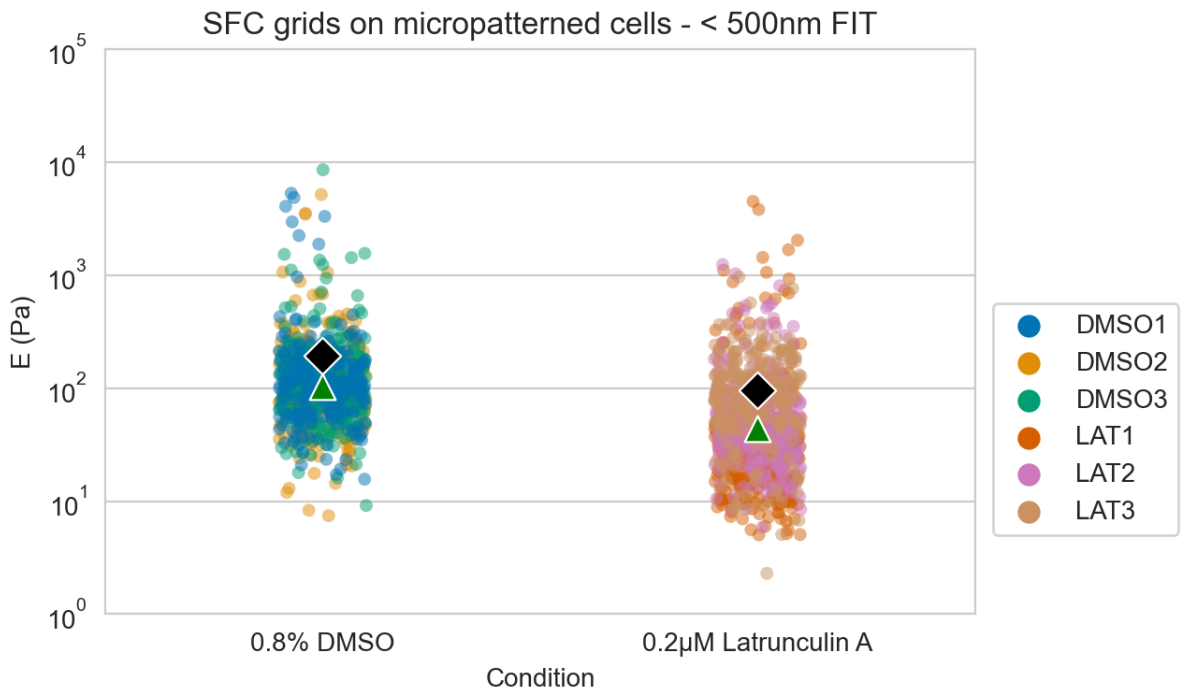

Figure 62: Apparent Young's modulus (E) of hTERT-RPE-1 cells seeded on micropatterns. Each point represents the median E of a 4x4 grid of single force curves acquired on the perinuclear region of the cell (0.8% DMSO N = 834, 0.2µM Latrunculin-A N = 927). The black diamond represents the mean (193.38 Pa 0.8% DMSO, 96.22 Pa 0.2µM Latrunculin-A) and the green triangle represents the median (102.47 Pa 0.8% DMSO, 43.64 Pa 0.2µM Latrunculin-A)

Finally, as a third experiment, quantitative imaging was performed on hTERT-RPE-1 cells randomly seeded on glass-bottom petri dishes. The throughput of these measurements was severely limited due to the long acquisition time for each scan (4 minutes and 29 seconds per scan) when compared to the acquisition time for each grid of single force curves (16 seconds per grid). However, higher resolution measurements allow to observe the heterogenicity on the distribution of the mechanical properties depending on the cell region.

Maps showing artifacts or multiple cells were discarded manually. After postprocessing, the data of 112 cells (54 DMSO-treated, 58 Latrunculin-A-treated) was used for the analysis. Yielding an average of 9 cells measured per hour. The median apparent Young's modulus measured were 4120.99 Pa for DMSO-treated cells and 2619.45 Pa for Latrunculin-A-treated cells. Resulting on Latrunculin-A-treated cells 1.57 times less elastic than DMSO-treated cells (Figure 63).

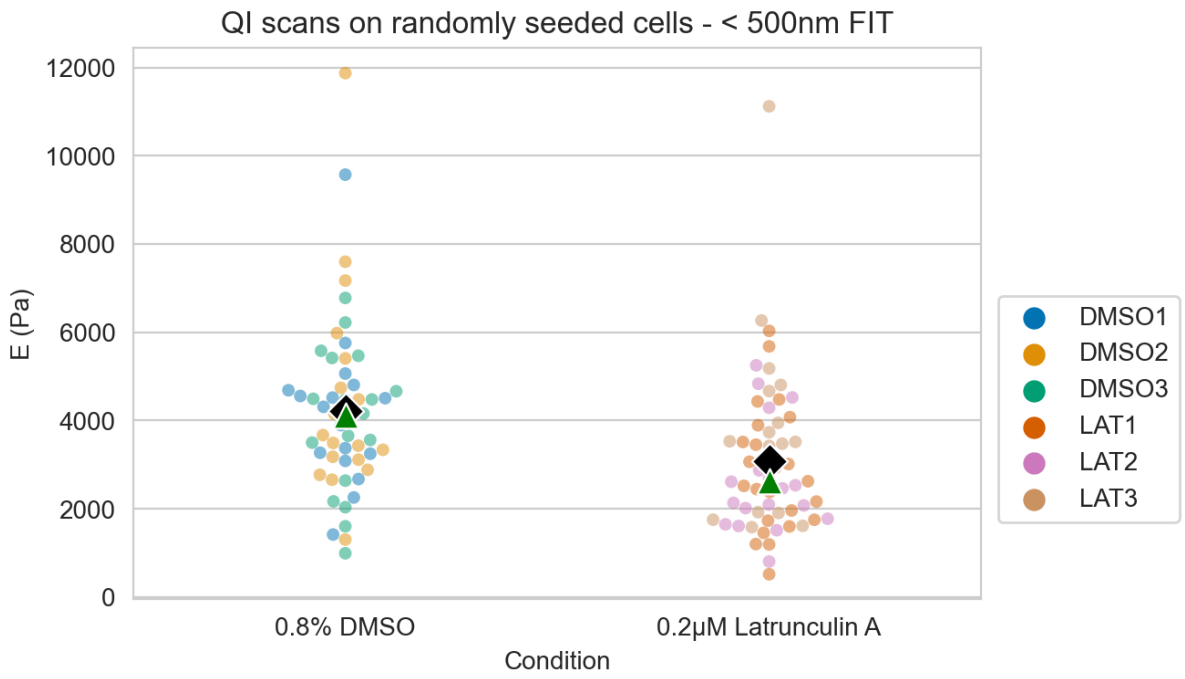

Figure 63: Apparent Young's modulus (E) of hTERT-RPE-1 cells seeded on glass-bottom petri dishes. Each point represents the median E of a 30x30 QI scan acquired on the perinuclear region of the cell (0.8% DMSO N = 54, 0.2µM Latrunculin-A N = 58). The black diamond represents the mean (4226.04 Pa 0.8% DMSO, 3074.23 Pa 0.2µM Latrunculin-A) and the green triangle represents the median (4120.99 Pa 0.8% DMSO, 2619.45 Pa 0.2µM Latrunculin-A)

To account for the effect of the stiff substrate, the apparent Young's modulus values were corrected using the bottom effect correction model (Figure 64) proposed by Garcia and Garcia in 2018 for a paraboloidal indenter.

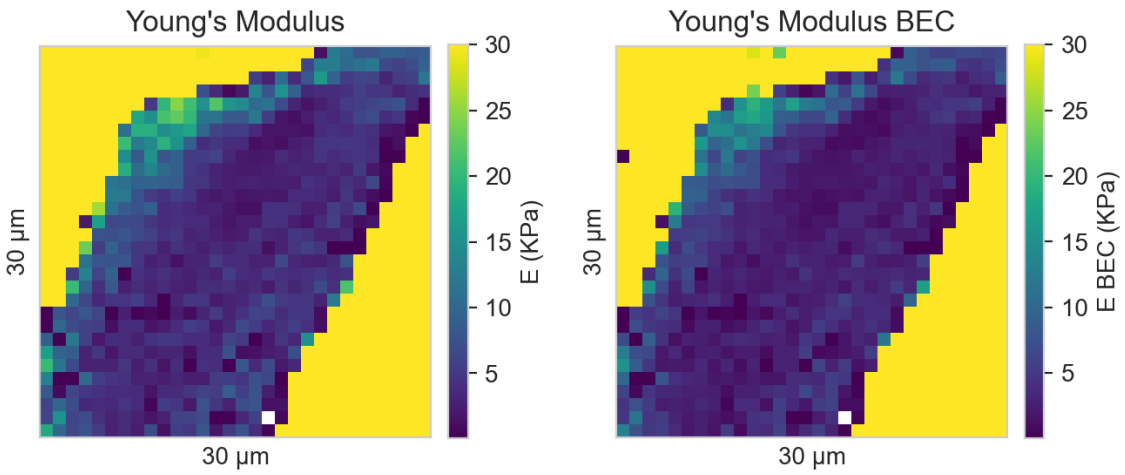

Figure 64: Young's modulus and Bottom Effect Corrected Young's modulus of a hTERT-RPE-1 cell.

The corrected values for the median apparent Young's modulus measured are 3457.68 Pa for DMSO-treated cells and 2401.30 Pa for Latrunculin-A-treated cells. Resulting on Latrunculin-A-treated cells 1.44 times less elastic than DMSO-treated cells (Figure 65).

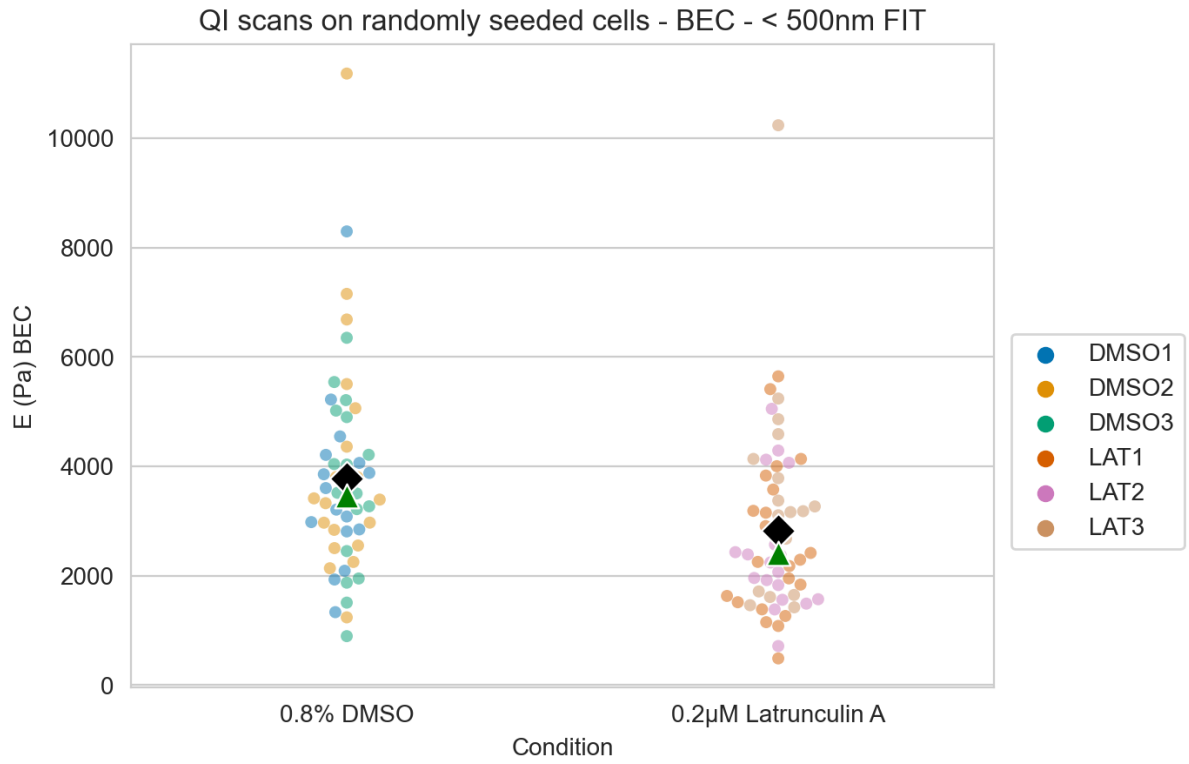

Figure 65: Bottom effect corrected Apparent Young's modulus (EBEC) of hTERT-RPE-1 cells seeded on glass-bottom petri dishes. Each point represents the median E of a 30 x 30 QI scan acquired on the perinuclear region of the cell (0.8 % DMSO N = 54, 0.2 µM Latrunculin-A N = 58). The black diamond represents the mean (3769.37 Pa 0.8% DMSO, 2819.97 Pa 0.2 µM Latrunculin-A) and the green triangle represents the median (3457.69 Pa 0.8% DMSO, 2401.30 Pa 0.2 µM Latrunculin-A)

2.3.2.8. Discussion

To assess the effect of Latrunculin-A on the mechanical properties of hTERT-RPE-1 cells, the apparent Young's modulus (E) of cells exposed to Latrunculin-A and DMSO was measured in three different experiments. On the first experiment hTERT-RPE-1 cells were seeded on bare glass and grids of 4x4 force curves and a dimension of 20µmx20µm were acquired on each cell. For the second experiment the hTERT-RPE-1 cells were micropatterned in patterns shaped as crossbows (polarized) and rings (non-polarized), as it can be observed in Figure 61. Micropatterning allowed to make the sample more homogeneous and increase the density of single cells in the sample. Finally, Quantitative Imaging (QI) scans were acquired on cells seeded on bare glass. For each experiment three replicated were measured for each condition and the perinuclear region of the cell was targeted.

The goal of the force curve grids was to measure a few points on each cell to maximize the throughput. For this application colloidal probe with a radius of 5µm was used, to achieve a large contact area on each indentation and obtain a mechanical fingerprint of the whole cell. A decrease of the median E was observed both in cells seeded on bare glass (212.13 Pa for DMSO-treated, 105.91 Pa for Latrunculin-A-treated) and micropatterned (102.47 Pa for DMSO-treated, 43.64 Pa for Latrunculin-A-treated). The throughput achieved in both preparations with automation was an order of magnitude larger than the throughput of doing the experiments by hand (20 cells/hour) using the same parameters. This increase was thanks to the automated routines to automatically detect suitable cells and move to position. A throughput of 118 cells/hour was achieved for cells seeded on bare glass. And micropatterns helped to increase the throughput to 132 cells/hour. Although a higher throughput was achieved on micropatterned cells, the sample preparation requires more steps and is longer than for seeding cells on bare glass. Moreover, the micropatterning protocol must be optimized for each cell line and yields of $\leq 50\%$ are expected.

Although hTERT-RPE-1 cells were seeded on micropatterns of two different shapes. The results from both shapes were aggregated together, as no statistically significant differences were observed in cells treated with DMSO (Figure 66).

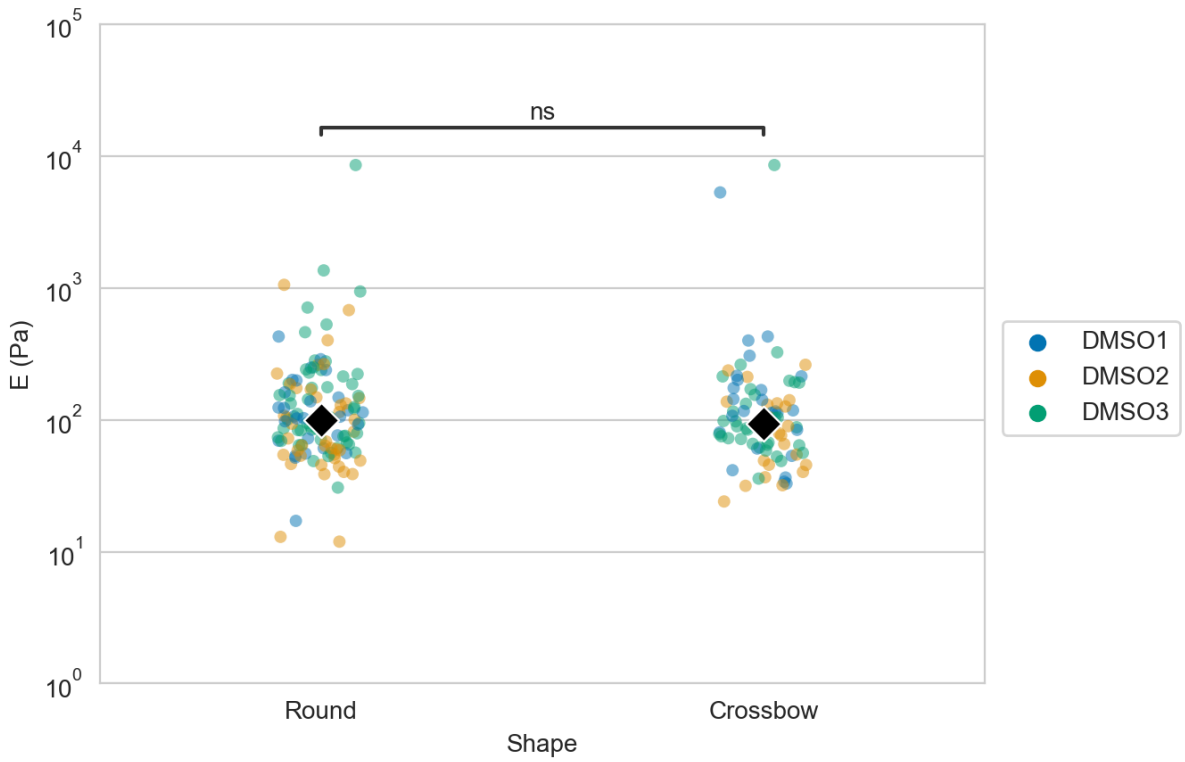

Figure 66: Apparent Young's modulus (E) of RPE1 cells seeded on micropatterns. To compare the effect of the pattern shape on the value of E a sample of 25% of the total number of DMSO treated cells (N = 208 cells) was randomly selected. As the shape classification was performed manually using the images acquired before each measurement, only DMSO treated cells were selected for this test as it was easier to visually classify the shape of the cell. Each point represents the median E of a 4x4 grid of single force curves acquired on the perinuclear region of the cell (Round N = 124, Crossbow N = 84). The black diamond represents the median (100.20 Pa Round, 93.30 Pa Crossbow) ns: 5.00e-02 < p (Wilcoxon–Mann–Whitney test).

Cells are heterogeneous, different parts of the cell present different mechanical properties. By acquiring higher resolution maps the mechanical heterogenicity of the cell can be captured and analysed. To extend the applications of the automated system and provide more flexibility to the user, QI was included into the system. Scans of 30x30 force curves with a dimension of 30µmx30µm were acquired on cells seeded on bare glass. For this application a paraboloidal probe with a radius of 70nm was used, to have a contact area that would allow for higher resolution measurements. Like in the previous conditions, a decrease in the median E was observed (4120.99 Pa for DMSO-treated, 2619.45 Pa for Latrunculin-A-treated).

The decrease of the median E in cells treated with Latrunculin-A was observed in all three conditions and is in agreement with the behaviour overserved in other studies (Flormann et al., 2021; Rigato et al., 2015) for the same cell line and different cell lines.

Values measured in QI are between 1-2 orders of magnitude larger than those measured by acquiring single force curve grids. Although all force curves were fit up to 500nm of indentation, QI scans included more measurements on the peripheries of the cell, which have been shown to be stiffer, therefore making the median apparent Young's modulus values larger, when compared to single force curve grids measurements, where force curves were mostly localized on the perinuclear region. This difference could also be attributed to the influence of the tip geometry on the apparent young's modulus measured, which has been reported on previous studies. Where tips with a smaller contact area consistently measured larger E values (Nguyen & Chung, 2019). To minimize the effect of the substrate on the values measured on the cell periphery, E were corrected. After the correction the median E values were still 1-2 orders of magnitude larger (3457.68 Pa for DMSO-treated, 2401.30 Pa for Latrunculin-A-treated).

To ensure that the values from the start of the experiment could be compared with those at the end. During each replicate the deflection sensitivity, total photodiode sum, vertical and horizontal deflection were measured. No large fluctuations were observed in these parameters. However, a progressive decrease of the photodiode sum, accompanied by an increase of the deflection sensitivity was consistently observed.

Sample preparation	Acquisition mode	Drug treatment	Replicate	N Cells	Experiment Duration	N Cells / Hour	Theoretical Maximum N Cells	Average E (Pa)	Median E (Pa)
Cells seeded on bare glass	Single force curve grids	0.8% DMSO	1	257	2 h 02 min	126.39	457	339.47	179.43
			2	216	2 h 01 min	107.11	453	859.88	211.28
			3	132	1 h 17 min	102.86	288	392.91	284.91
		0.2µM Latrunculin A	1	250	2 h 00 min	125.00	450	221.64	107.82
			2	104	0 h 48 min	130.00	180	390.72	192.81
			3	232	1 h 59 min	116.98	446	194.50	80.32
	Quantitative Imaging	0.8% DMSO	1	17	1 h 59 min	8.57	27	4176.52	4310.21
			2	19	2 h 07 min	8.98	29	4490.80	3670.03
			3	18	1 h 54 min	9.47	26	3993.35	4313.79
		0.2µM Latrunculin A	1	23	2 h 10 min	10.62	30	2834.35	2519.78
			2	18	1 h 53 min	9.56	26	2652.15	2298.54
			3	17	1 h 57 min	8.72	27	3845.67	3515.47
Cells seeded on micropatterns	Single force curve grids	0.8% DMSO	1	246	1 h 55 min	128.35	431	222.77	106.93
			2	270	2 h 16 min	119.12	510	179.96	97.33
			3	320	2 h 19 min	138.13	521	182.11	102.90
		0.2µM Latrunculin A	1	341	2 h 20 min	146.14	525	103.84	27.20
			2	342	2 h 31 min	135.89	566	77.56	42.35
			3	250	2 h 00 min	125.00	450	111.35	86.28

Table 3: Summary table containing all the results obtained for hTERT-RPE-1 cells. The theoretical maximum N cells is computed as the duration of acquisition of a single scan or grid times the experiment duration.

2.3.2.9. Automated measurements protocol

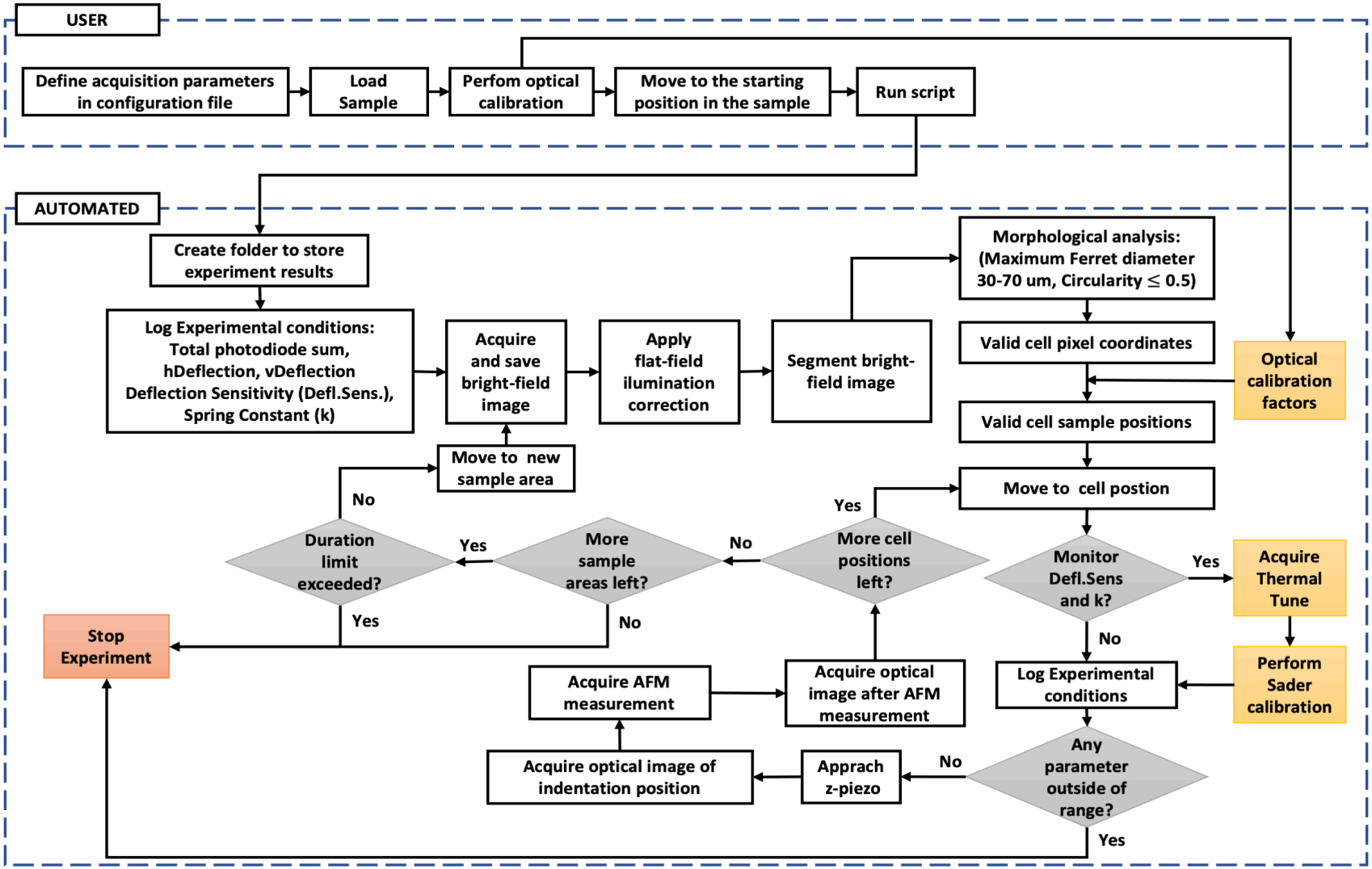

Figure 67: Diagram summarizing the automated protocol used on the experiments performed on hTERT-RPE-1 cells.

2.3.3. Migratting cells (NIH3T3)

Despite the limitation of 2D systems to study cell migration, they have been extensively applied to uncover fundamental principles of this process. In this context, atomic force microscopy (AFM) reveals itself as a fine technique to study the elastic and viscous characteristics of single cells and their subcellular compartments. Different approaches have been used to study the mechanical properties of motile cells in different stages of their movement by means of AFM (Rotsch et al., 1999; Laurent et al., 2005; Rianna et al., 2020). However, these studies focused on studying specific areas of the cell over-time, primarily the lamellipodia.

Here, we developed a platform based on automated AFM measurements coupled to optical microscopy (OM) to track mechanical changes over time of single cells migrating in 2D substrates. In our experiments, OM images are continuously acquired to estimate the centroid of single cells. This centroid position is used to establish the location in the corresponding AFM measurement. QI scans are automatically acquired for each cell and time-point, this is an array of force-distance curves which generates spatially resolved mechanical maps of cells. Ultimately, cell migration speed and direction can be correlated with the ability of the cell to redistribute its local mechanical properties.

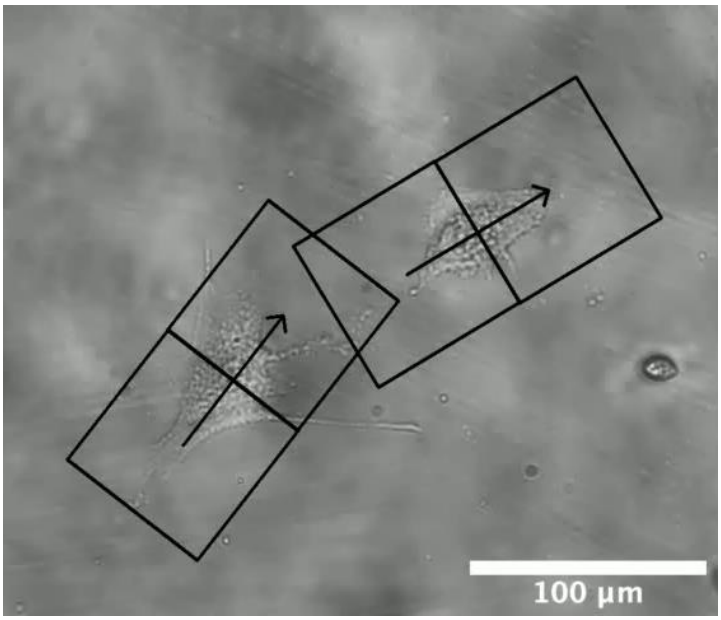

Figure 68:Bright field image of NIH3T3 cells migrating on glass. The black arrow represents the migrating direction of each cell and the black squares (70x70µm) represent the positions to acquire AFM maps.

2.3.3.1. Cell culture

NIH 3T3 cells (ATCC, Manassas, VA, USA) were cultured in DMEM (ThermoFischer, Waltham, MA, USA) containing 10% foetal bovine serum and 1% Penicillin/Streptomycin. The cells were then seeded in 35mm diameter glass bottom petri dishes (WillCo, Amsterdam, NL). All samples were incubated over night at 37°C and 5% CO2.

2.3.3.2. Sample preparation for AFM

As AFM experiments were performed outside of an incubator or chamber with environment control. Before measuring each sample, the medium is replaced by medium containing 20mM HEPES, to maintain pH equilibrium during the experiment duration. During the measurements, the medium temperature was kept at 37°C using a petri dish heater, pre calibrated with a thermocouple.

2.3.3.3. AFM measurement parameters

QI was the acquisition mode used for all measurements. To study the mechanical properties of whole cells two scans, one on the front and one on the back, of 32x32 pixels and 70µmx70µm were acquired on each cell sequentially. To lower the acquisition time and study the mechanical properties of the leading and retracting edge of each cell, in another set of experiments, two scans of 32x16 pixels and 70µmx35µm were acquired instead. Scans were acquired using a PFQNM-LC-A-CAL probe (paraboloidal tip, 70nm radius, 0.105N/m spring constant) (Bruker, Santa Barbara, CA, USA) using the following parameters: 0.5nN force setpoint, 4µm ramp size and 150µm/s ramp speed.

All scans were acquired using a scan direction perpendicular to the migration angle of each cell in order to prevent artifacts caused by the cell movement during the scan. Although the maximum scan size of the NanoWizard 3 platform is 100µm x 100µm. Scan size was limited to a maximum of 70µm x 70µm to allow a free 180° rotation of the scan position.

2.3.3.4. AFM Data analysis

The bad curves of each QI scan were discarded based on the criteria stated in section 2.2.6 Scans with more than 30% of bad curves were discarded from the analysis. The remaining scans were processed using the JPK data processing software. The hertz model for a paraboloid indenter was fit to the extend segment of each force-distance curve to obtain the apparent Young's Modulus (E). Using the sensor height data and the Garcias' bottom effect correction the E values were corrected (E_{BEC}). Finally, for the analysis the values corresponding to the cell were separated from the values in the substrate by thresholding considering a minimum indentation of 50nm.

To compute the E front to back ratio, a profile was drawn along the migrating axis of the cell. E_{BEC} values along this axis were separated between the front and back of the cell using the centroid of the cell as reference point. The ratio was then computed using the median E_{BEC} of each region.

Using the bright-field images acquired during the experiment the travelled distance and migrating speed of each cell was obtained using the Manual Tracking plugin in Fiji.

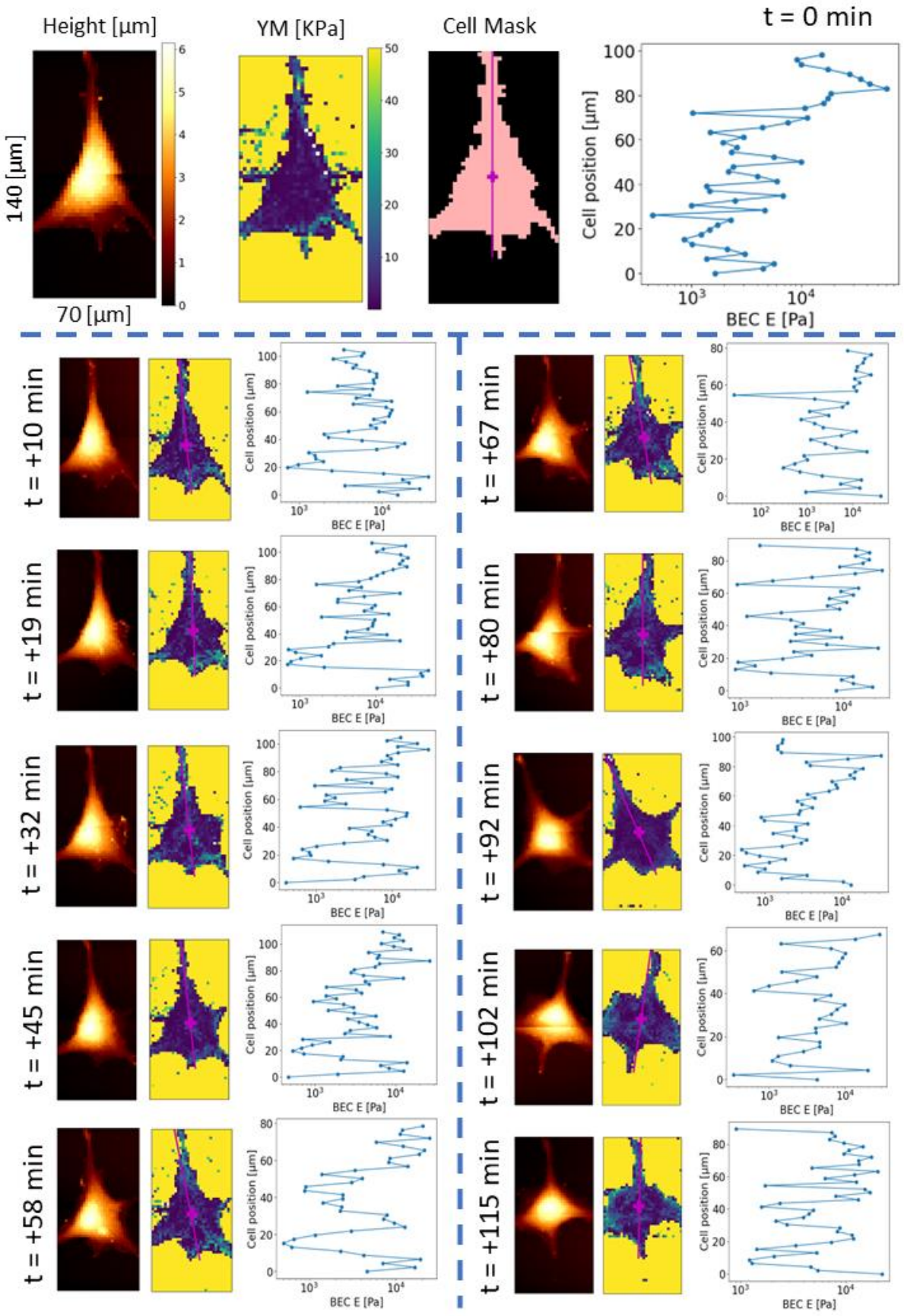

Figure 69: Time lapse of the mechanical properties of a migrating NIH3T3 cell.

2.3.3.5. Cell migration control experiments

Every time a force-distance curve is acquired the AFM tip contacts and indents the cell. To ensure that the interaction of the tip did not influence the cell migration on the glass substrate, before performing the AFM experiments, the basal migrating behaviour of NIH3T3 cells was characterized.

To obtain the average migration speed, cells were seeded on glass bottom petri dishes and bright-field images were acquired on three different samples every 5 minutes for 2 hours. These measurements were performed mimicking the conditions of the AFM experiment. CO2 concentration in the environment was not controlled, HEPES was used to maintain a stable pH during the measurements and the medium was kept at 37ºC using a petri dish heater. Then the Manual Tracking plugin in Fiji was used to process the optical images and obtain the migrating speed of each cell. The data of 138 cells was used in the analysis, yielding an average migration speed of 12.26μm/hour (Figure 65). The value is in the range of the average migration speed reported for NIH3T3 in other studies (Munevar et al., 2001; Schneider et al., 2008; Tremel et al., 2009).

2.3.3.6. Mechanical properties dynamics of migrating NIH3T3 cells

Using the described routine NIH3T3 fibroblasts were measured as they migrated on a glass surface. Sequential QI scans of 46 cells over a period of 2 hours were acquired, together with correlated bright field optical images of each cell at each time point.

To assess if the continuous acquisition of AFM scans on the cells influenced their migrating speed, 138 NIH3T3 cells were followed during 2 hours without performing any AFM measurements on them. The migrating distance, speed and angle of the 138 cells where no AFM was performed and the 46 cells where AFM was performed was measured manually using the Manual Tracking Fiji macro. With a median migrating speed of 11.36μm/hour for cells where no AFM was performed and 13.69μm/hour for cells where AFM was performed, no statistically significant differences were observed (Figure 70).

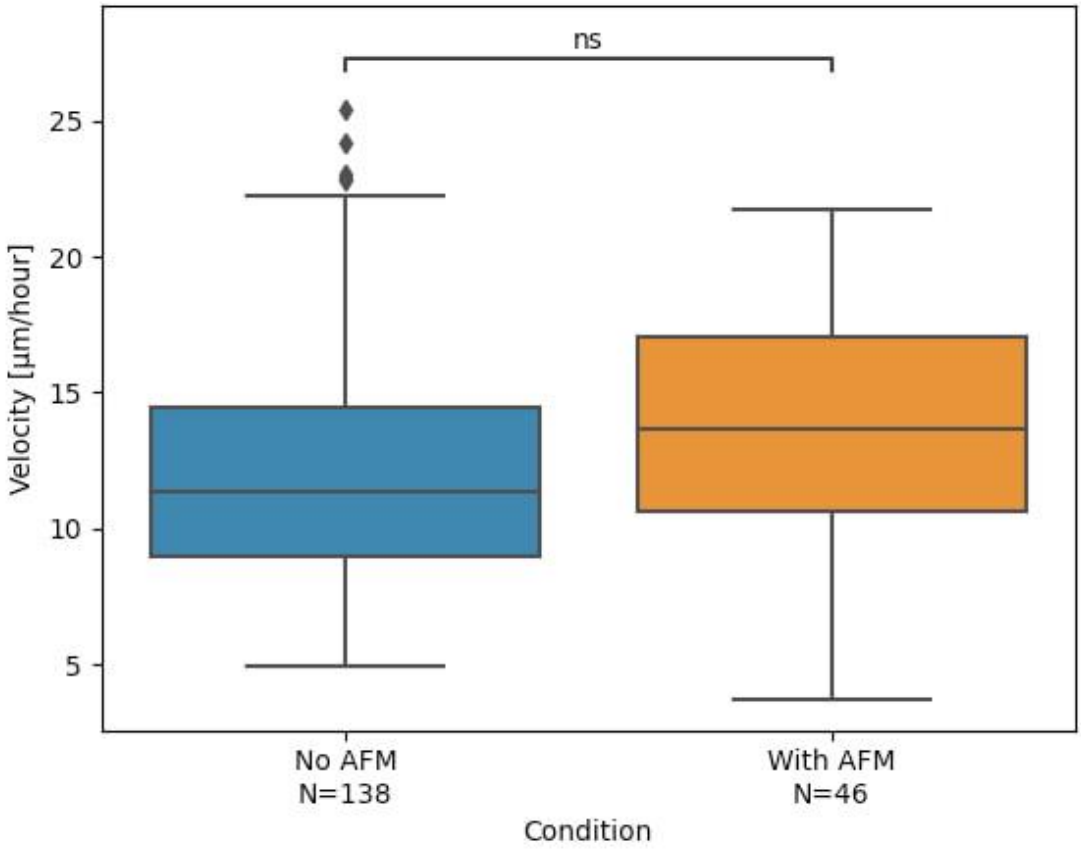

Figure 70: Boxplot showing the median migrating velocity of cells where No AFM was performed, and cells where AFM was performed. No statistically significant differences were observed between either group. T-test *p-value annotation legend: ns: 5.00e-02 < p <= 1.00e+00, *: 1.00e-02 < p <= 5.00e-02, **: 1.00e-03 < p <= 1.00e-02, ***: 1.00e-04 < p <= 1.00e-03, ****: p <= 1.00e-04.*

From the QI scans the aspect ratio, bottom effect corrected (BEC) Young's modulus front-to-back and BEC Young's modulus leading edge (aligned towards the migrating direction) / following edge ratios were obtained (Figure 69).

The correlation between the parameters extracted was quantified using the Kendal rank correlation coefficient (Kendall, 1938). Where 1 indicates a strong positive correlation, 0 indicates no correlation and -1 indicates string negative correlation.

The results show a strong correlation between the median BEC Young's modulus of the leading edge and the mean (0.701) and median (0.770) BEC Young's modulus of the whole cell.

The BEC Young's Modulus front-to-back ratio showed a weak correlation (0.119) with the migrating speed (Table 4) and no correlation with the distance travelled, cell aspect ratio migrating angle and delta migrating angle. On the

other hand, the BEC Young's modulus Ratio between the leading edge and the following edge showed a weak negative correlation (-0.127) with the migrating speed (Table 4) and no correlation with the distance travelled, cell aspect ratio, migrating angle and delta migrating angle.

	Distance Travelled	Migrating Speed	Cell Aspect Ratio	Migrating Angle	Δ Migrating angle
BEC Young's modulus front-to-back ratio	0.056	0.119	0.003	0.021	-0.006
BEC Young's modulus leading edge / following edge ratio	-0.032	-0.127	-0.011	-0.012	0.003

Table 4: Kendal rank correlation coefficients for NIH3T3 cells.

2.3.3.7. Discussion

The algorithm developed in this work allowed to monitor the mechanical properties of 46 cells during 2hours while they migrated on a glass substrate automatically. As correlated optical images together with QI scans were obtained for each cell at each time point, this allowed to correlate the morphology and migrating behaviour with the changes in the mechanical properties of the cell.

In 2022 Seifert et al. (Seifert et al., 2022) measured the mechanical properties of migrating and cytochalasin-D treated platelets by SICM. In this work they observed that migrating palettes exhibited a higher stiffening rate at the leading edge of the cell. In a similar way, in our results we have observed that the leading edge of the cell presents a higher median BEC Young's Modulus than

the rest of the cell. With the median BEC Young's Modulus of the whole cell and the leading edge being strongly correlated (0.770).

Both the BEC Young's Modulus front-to-back ratio and leading edge / following edge ratio were found to be weakly correlated tot the migrating speed, 0.119 and -0.127 respectively, but not to the migrating angle or changes in the migrating angle of the cell. Suggesting that even if the cell is moving on a direction, it is constantly probing for other routes, and this is reflected in changes in its mechanical properties.

2.3.3.8. Automated measurements protocol

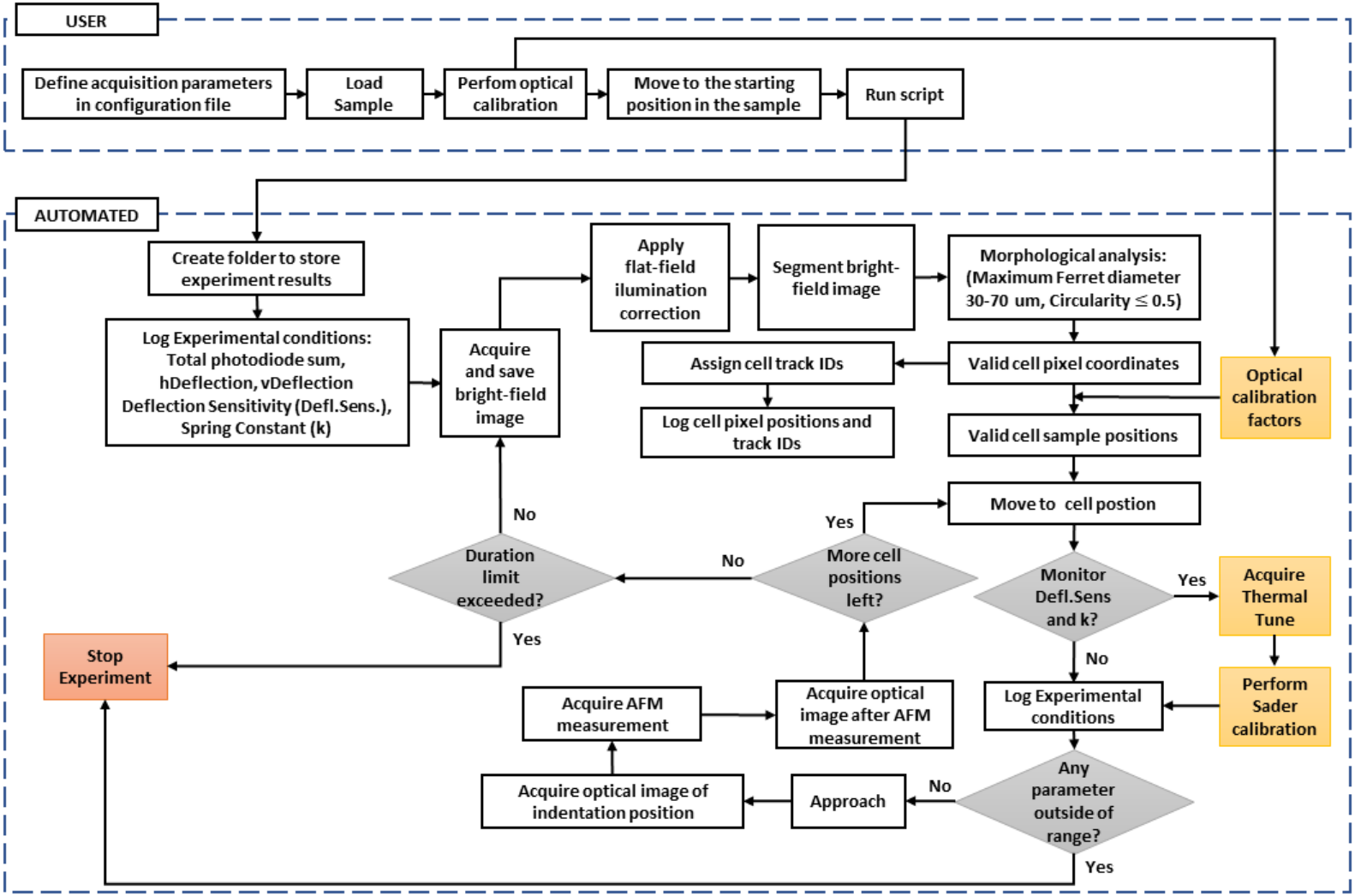

Figure 71: Diagram summarizing the automated protocol used on the experiments performed on NIH3T3 cells.

2.3.3. Tissue sections

The mechanical properties of soft tissues, such as their elasticity and viscosity, are fundamental characteristics that play a critical role in defining cell and tissue functions, tissue development, disease progression, and tissue homeostasis (B et al., 2019; Burdick & García, 2020; Shivashankar et al., 2015). Each organ has specific mechanical properties that are altered when homeostasis is disrupted. Leading to tissue ageing and the development of various diseases such as cancer, fibrosis, cardiovascular diseases, and diabetes (Chang et al., 2021; Hajjarian et al., 2021; Kaushik et al., 2016; Martinez-Vidal et al., 2021, 2023; Paszek et al., 2005).

The bladder is a hollow organ that undergoes stretching and contraction during filling and voiding respectively, which are achieved through cycles of mechanical relaxation and contractility. The histological structure of the bladder is optimized to resist these morphological changes and resist the mechanical stresses in different directions while performing its function. Microscopically it is composed by the following layers from inside out:

Lining epithelium

The urinary bladder is lined with a specialized stratified epithelium known as the urothelium. This type of epithelium is exclusive to urinary structures such as the ureter, urinary bladder, and proximal urethra. The urothelium is composed of three histological layers: the apical layer, the intermediate layer, and the basal layer (Bolla et al., 2022). The innermost layer, the apical layer, forms a barrier between the bladder lumen (where the urine is stored) and underlying tissue. It is composed of a single layer of umbrella-shaped cells that are frequently binucleated. The intermediate layer is formed from two to three layers of polygonal cells, while the basal layer is formed from two to three layers of small cuboidal cells.

When the bladder is relaxed, the urothelium is thick with five to seven structural layers. However, as the bladder wall stretches to accommodate increased volume when the bladder fills with urine, the urothelium reorganizes into two or three layers without structural damage (Bolla et al., 2022).

Lamina propria

The lamina propria is the sub-urothelial layer separating the urothelium and underlying muscularis propria. The overlying urothelium is separated from the lamina propria by a basement membrane, consisting of a heterogenous network of structural proteins and cells. This network is composed of an extracellular matrix with elastic fibbers, capillaries, lymphatics, immune cells, afferent and efferent nerve endings, fibroblasts, myofibroblasts, adipocytes, interstitial cells of Cajal or telocytes, indistinct smooth muscle cells, and the muscularis mucosae (Bolla et al., 2022).

The interstitial cells of Cajal, which form a syncytium with smooth muscle cells and nerve endings, are also located in the lamina propria. They are known to function as pacemaker cells in the gut, urethra, and prostate (Bolla et al., 2022). In the bladder they act as nerve signal transducers to the bladder's smooth muscle cells.

Muscularis propria

The muscularis propria or detrusor muscle is composed of three sublayers: the inner longitudinal, middle circular, and outer longitudinal. These sublayers are well-defined around the neck of the bladder but are randomly aligned with the rest of the bladder wall. The bladder's body has a higher smooth muscle content than the trigone, reflecting a well-developed network of myofibroblasts of the lamina propria and muscularis mucosae in the body (Bolla et al., 2022).

Serosa / Adventitia

The serosa is a thin connective tissue layer that covers the bladder dome and is continuous with the peritoneal layer of the abdominal wall. It contains blood vessels of various sizes. The adventitia is a loose connective tissue layer that serves as the outer layer of the bladder in areas where there is no serosa.

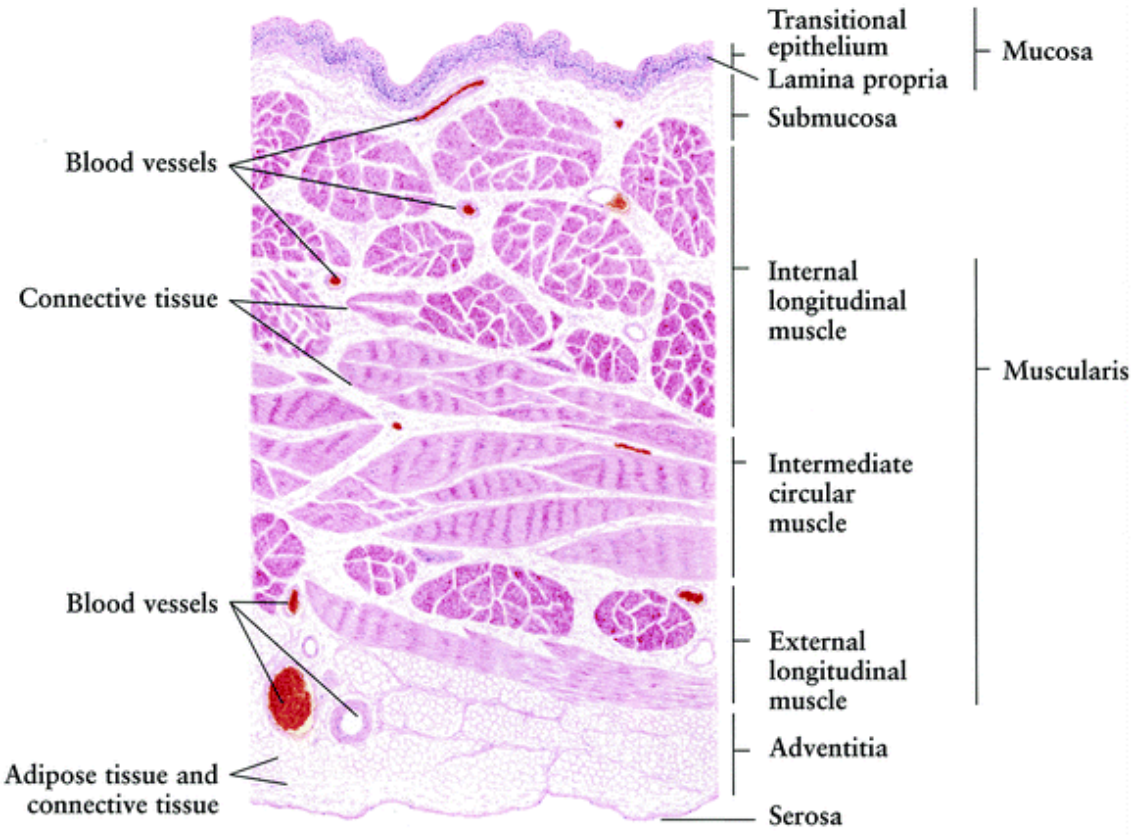

Figure 72: Diagram depicting the histology of human bladder tissue.
(Mak, R.H., Viswanathan, A.N., Shipley, W.U. 2014)

The mechanical properties of the bladder have been investigated at a macroscopic level, including the characterization of different macroscopic areas. As observed in various benign bladder pathologies that progress from a stiffer matrix to a more compliant structure, alterations of the mechanical properties of the bladder can lead to dysfunction of its physiological role. Moreover, malignant bladder diseases have been found to be associated with a high content of collagen fibbers in the extracellular matrix (ECM), resulting in further stiffening of the bladder, particularly in patients with relapsing tumours. While clinical studies that investigate the mechanical properties of the bladder offer valuable insights, they provide a snapshot of the clinical situation and focus uniquely on macroscopic measurements (Dahms et al., 1998; Korossis et al., 2009). Therefore, future studies could benefit from exploring the molecular and cellular mechanisms underlying the changes in bladder mechanical properties to gain a deeper understanding of the complex relationship between the mechanical properties of the bladder and the development of bladder diseases.

AFM nanoindentation is seen as one of the most suitable techniques to determine the nanomechanical properties of bladder tissue, thanks to its ability to be coupled with brightfield and epifluorescence microscopy and its ability to provide mechanical measurements with a high lateral resolution. However, due to bladder tissue samples being large and heterogeneous, several maps on multiple regions are needed to properly characterize the nanomechanical properties of a single sample (Martinez-Vidal et al., 2023). Determining and acquiring the number of maps needed to correctly characterize the mechanical properties of the tissue sample is a lengthy and user intensive process. To facilitate data acquisition of several maps, some commercial instruments allow to define positions to scan sequentially. However, the user is still required to draw each one of the map positions and move from one region of the tissue to another.

To tackle this limitation of AFM, in this section we describe an automated workflow that has been developed to measure the mechanical properties of tissue in an automated way. Where the user is only required to define the measurement parameters, loading the sample and calibrating the instrument, while the automated system goes over the sample and acquires AFM measurements on several regions of the tissue.

For testing the feasibility of this system, the algorithm has been tested on healthy rat bladder tissue slides provided by the Ospedale San Raffaele (OSR) (Milan, Italy).

2.3.3.1. Cryosection preparation

The samples were provided by the Ospedale San Raffaele (OSR) (Milan, Italy). After the healthy rats were sacrificed, cryoprotectant O.C.T compound was instilled in the bladder and used to freeze the organ on dry ice and ethanol. 50µm thick cryosections are then prepared on polarized glass slides and stored at -80°C.

2.3.3.2. Automated AFM workflow

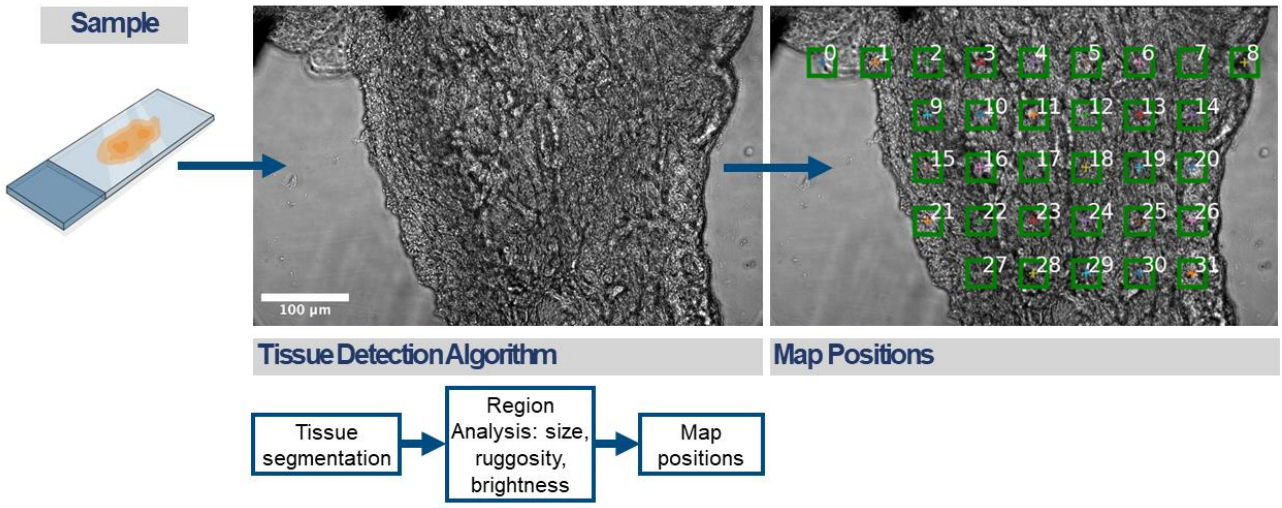

Figure 73: Diagram summarizing the automated protocol for measuring tissue slices.

2.3.3.3. AFM Sample preparation

The samples were prepared for AFM measurements following the protocol developed by Laura Martinez Vidal from OSR (Martinez-Vidal et al. 2022).

1. The frozen rat tissue sections are thawed at room temperature for 10 minutes.

2. Right before the AFM measurements the OCT is washed away from the tissue section by washing the glass slide in PBS for 10 minutes. This step is repeated twice.

3. A circle is drawn around the tissue section with a hydrophobic pen and 200uL of PBS are added.

4. At this point samples are ready to perform AFM in liquid at room temperature.

2.3.3.4. AFM measurements parameters

All AFM measurements were performed with a MLCT-SPH-5UM-F probe (paraboloidal tip, 5µm radius, 0.899N/m spring constant). Using a ramp size of 8µm and a ramp speed of 20µm/s. The system was configured to acquire maps of 30µm x 30µm with a resolution of 6 x 6 force curves. This approached allowed to characterize in detail small regions of the tissue sample (500µm^2).

2.3.3.5. AFM data analysis

The bad curves of each QI scan were discarded based on the criteria stated in section 2.2.6. Scans with more than 30% of bad curves were discarded from the analysis. The remaining scans were processed using the open-source software PyFM. This tool is described in detail in section 2.4. The hertz model for a paraboloid indenter was fit to the extend segment of each force-distance curve to obtain the apparent Young's Modulus.

2.3.3.6. Mechanical measurements of rat bladder tissue

Sequential maps of 30µm x 30µm and 6 x 6 pixels were acquired arranged as a grid, with a spacing of 30µm between scans in x and y. To prevent detachment and contamination of the tissue sample, the experiment duration was limited to 2 h. This approach allowed to automatically obtain 57 maps and characterize a total area of 51.3mm^2 of the sample.

The bladder wall was found to have varying mechanical properties, with Young's modulus values ranging from a few kPa to several hundred kPa in different regions. The YM of the urothelium was found to be the lowest at 12 kPa, while the lamina propria, which is the second layer of the bladder tissue, exhibited a gradual increase in YM to 90 kPa, indicating an increase in stiffness. However, the outer muscle tissue layer showed a transient decrease in YM to 50 kPa.

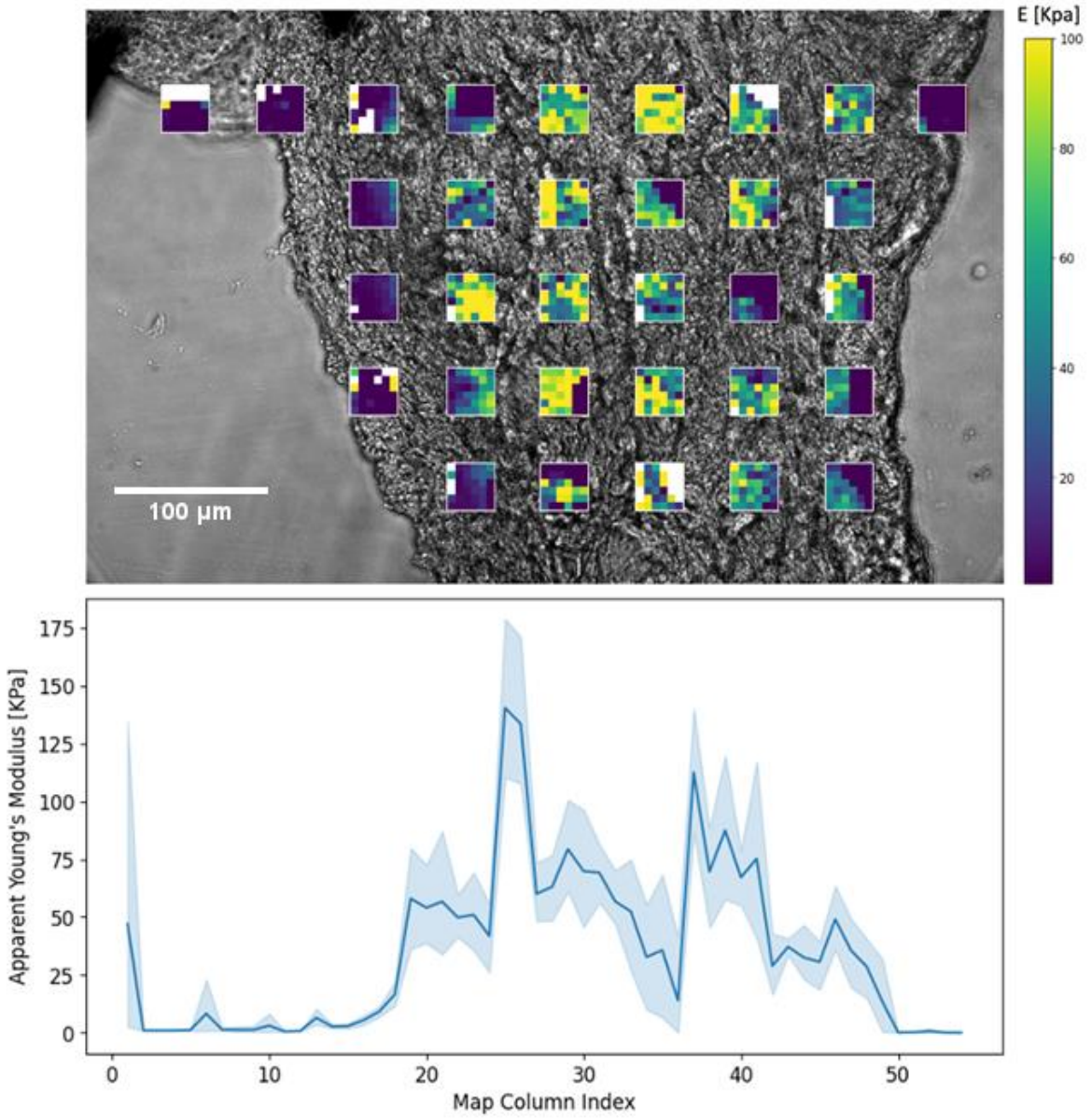

Figure 74: 30 µm x30µm mechanical maps acquired on rat bladder tissue. Where each white pixel represents a bad force curve (Top). Profile of the apparent Young's modulus across the bladder tissue section (Bottom).

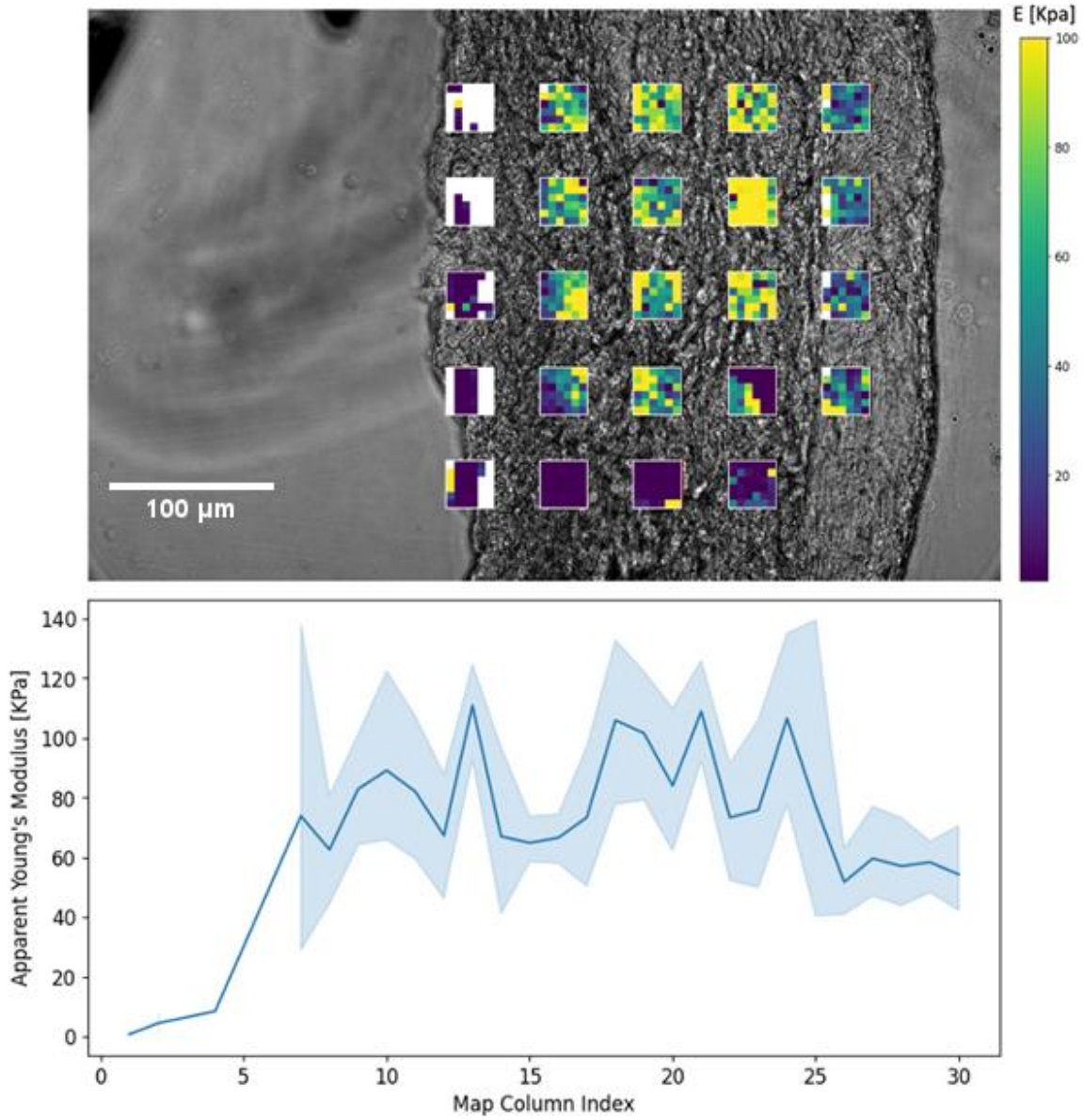

Figure 75: 30µm x30µm mechanical maps acquired on rat bladder tissue. Where each white pixel represents a bad force curve (Top). Profile of the apparent Young's modulus across the bladder tissue section (Bottom).

2.3.3.7. Discussion

Bladder wall tissue is highly heterogeneous and presents a complex histological structure, with distinct layers presenting different cell composition and organization. As a result, to correctly characterize the nanomechanical properties and capture this heterogeneity multiple measurements across the sample are required. Making it a time-consuming and user intensive process when performed by hand. To address this issue and allow to better characterize the mechanical properties of tissue samples, we have developed an automated

system capable of moving across the tissue sample and acquiring the measurements without the need of a user. Moreover, as the ROIs detection algorithm relies on optical images, all mechanical maps acquired with this system are correlated to a bright-field image. Thus, allowing the user to identify where every measurement has been taken on the sample.

As a proof of concept, the mechanical properties of a rat bladder tissue section were automatically characterized using the automated AFM system developed in this work. The spatially resolved AFM scans obtained display a gradient of elasticity across the bladder wall. The median Young's Modulus measurements revealed that the urothelium had the lowest value at 12 kPa, while the lamina propria, which constitutes the second layer of bladder tissue, demonstrated an incremental increase in stiffness to reach 90 kPa. Interestingly, the outer muscle tissue layer showed a drop in the median Young' Modulus to 50 kPa. In order to ensure the tissue sample remained attached and uncontaminated, the experiment was limited to a duration of 2 hours. Despite this constraint, the experiment successfully yielded 57 maps and enabled the characterization of a total area of 51.3mm2 of the sample in an automated manner.

Recently Maritnez-Vidal and collaborators (Martinez-Vidal et al., 2023) performed a similar study where they measured the Young's moduls of healthy and tumoral rat bladder tissue using both AFM and a nanoindenter. Both methodologies yielded results displaying the same trend to the one observed in this work. Thus, validating the results obtained using the automated routine.

Although this system has been showed to be a viable approach for the automatic mechanical characterization of tissue sections. As the current system can only define a single force setpoint for all indentation. In heterogeneous samples with a gradient of stiffness as the rat bladder tissue studied in this work, in some regions of the tissue is not possible to indent properly the sample. Resulting in a failed measurement. This can be observed in Figures 74 and 75, where the setpoint used was suitable for indenting stiffer regions like the lamina propria and the muscle layer, but in softer regions like the urothelium the parameters used resulted in several failed measurements (white squares). This issue can also be observed in the measurements performed by Martinez-Vidal et al., where most failed measurements are located on the urothelium. In future iterations of the system, using and indentation setpoint instead of a force setpoint would help mitigate this issue.

2.3.3.8. Automated measurements protocol

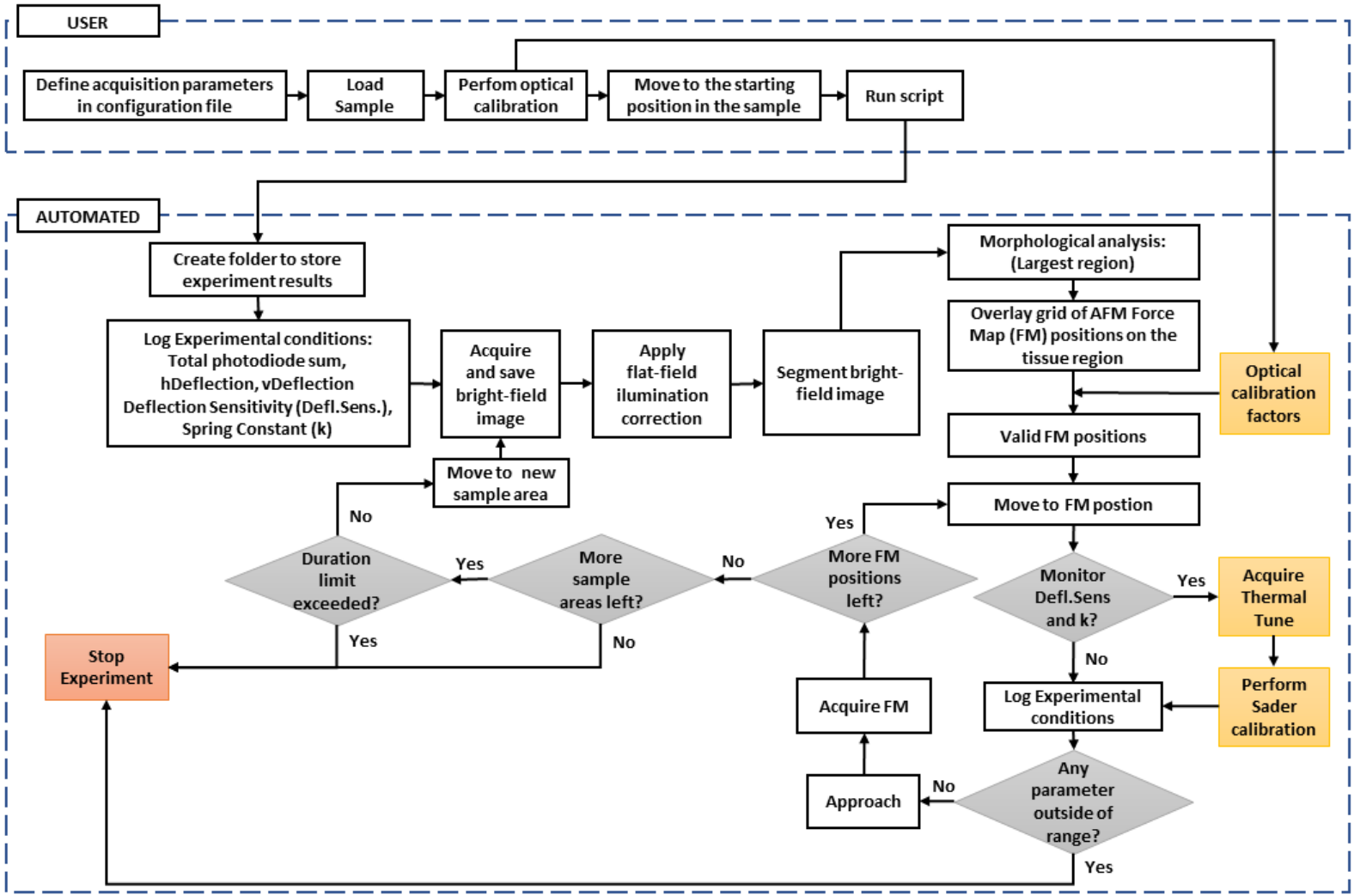

Figure 76: Diagram summarizing the automated protocol used on the experiments performed on rat bladder tissue sections.

2.4. PyFM: Open-source data analysis software

In recent years, the study of cellular and extracellular matrix (ECM) mechanics has increased considerably due to the realisation of its fundamental role in several physiological and pathological processes like cell division, migration, differentiation and malignancy (Engler et al., 2006; Rianna et al., 2020). Amongst other techniques, atomic force microscopy (AFM) has proven to be a powerful tool to characterise the mechanical properties of living cells and ECM (Lekka et al., 2023a, 2023b) and it is considered as a standard tool in the field. Despite its popularity, standardisation of sample preparation, measurement and data analysis protocols are still lacking.

Moreover, in the context of AFM automation, standardized automated data processing routines enhance efficiency by handling the high volume of data acquired during each experiment. They ensure consistency and precision, reducing human errors in data analysis. Thus, improving reproducibility, vital in scientific research and quality control. Addressing the handling of high AFM data throughput, increases experiment productivity and reliability, collectively empowering researchers to extract accurate, reliable insights from their studies.

To overcome some of these limitations, several efforts have been initiated towards AFM probe calibration procedures (Sader et al., 2016; Schillers et al., 2017), and open source or free AFM data analysis tools like Gwyddion (Nečas & Klapetek, 2012), TopoStats (Beton et al., 2021), AtomicJ (Hermanowicz et al., 2014), PyJibe (Müller et al., 2019), ViscoIndent (Efremov et al., 2020) and Rheos (Kaplan et al., 2019).

The analysis of AFM force measurements is generally carried out using either home-made (Domke & Radmacher, 1998; Lekka et al., 1999; Carl & Schillers, 2008; S. W. Chen et al., 2022; Kontomaris et al., 2023) or instrument-associated commercial software. Although these tools allow to extract the topographical and mechanical properties of the sample, most of these packages are either not open source, limited to the most standard models, not compatible with other manufacturers data formats, do not allow obtaining viscoelastic parameters or do not support microrheology data.

The most common approach to determine the elasticity of soft biological samples is the acquisition of AFM force-distance curves (FDCs), to then fit an elastic contact model, usually to the approach segment of the curve, and obtain the apparent Young's modulus (E). For determining the viscoelasticity of the sample, two main approaches are possible:

- FDC (time-domain method): where a viscoelastic model is fitted to the full FDC (approach and retract) (Brückner et al., 2017; Efremov et al., 2020; Sanchez et al., 2021) or to certain segments (approach, pause, steps (Yango et al., 2016)).

- Microrheology (frequency-domain method): consisting in the force response analysis of small amplitude z oscillations at different frequencies to determine the complex shear modulus (Alcaraz et al., 2003).

Most available AFM open-source and commercial software tools allow to compute E from FDCs but not viscoelastic parameters. Amongst open-source tools, only VisconIndent natively supports rheology data, but even that is limited to time domain analysis, which requires a priori knowledge regarding the constitutive behaviour of the sample under test. A turn-key solution that encompassess both time and frequency domain viscoelastic analysis, as well as microrheology related signal correction procedures is still missing. Making this type of analysis more accessible is important, as recent works have shown the time dependent response of ECM plays a crucial role in tissue organisation (Elosegui-Artola et al., 2023). PyFM has been developed with these needs in mind.

2.4.1 Software architecture

The software functionalities were splitted into different self-contained libraries to help organise the code while making it more readable, maintainable, testable and reusable. Similarly to the AFM data analysis PyJibe developed by Paul Muller (Müller et al., 2019), the functionalities of PyFM are split on three main Python libraries organized in a hierarchical manner:

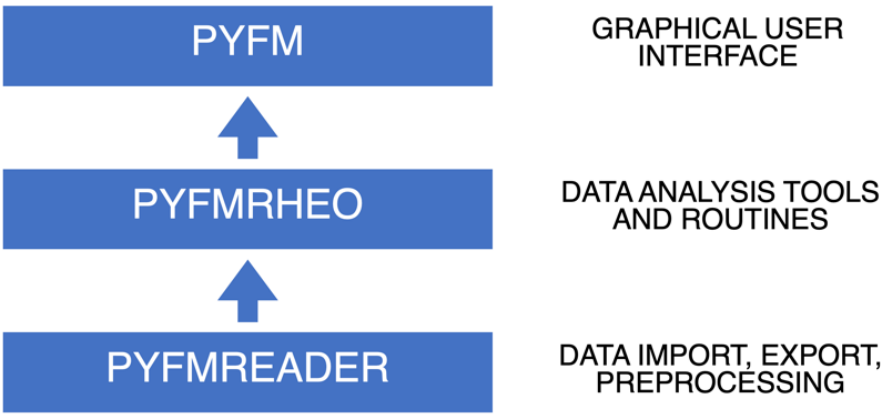

Figure 77: Diagram representing how the libraries composing PyFM are organized.

2.4.1.1. PyFMReader

Source code : https://github.com/jlopezalo/PyFMReader

This library includes methods to load and pre-process data from different AFM manufacturer files, making FDCs, topography data and metadata accessible to the user. At the core of this library, is the unified file format (UFF) object (manuscript in preparation). The files from different instruments are parsed and the metadata, force curve and image data are loaded into the UFF object. To allow flexibility in implementing functionalities, each force curve and segment are stored as an object. This implementation results in a hierarchical data organisation (Figure 78) where AFM file objects point to the different force curve objects and each force curve object points to distinct segment objects for the approach, pause, modulation and retract segments. The name of the file is used as the id to relate all data objects from each file.

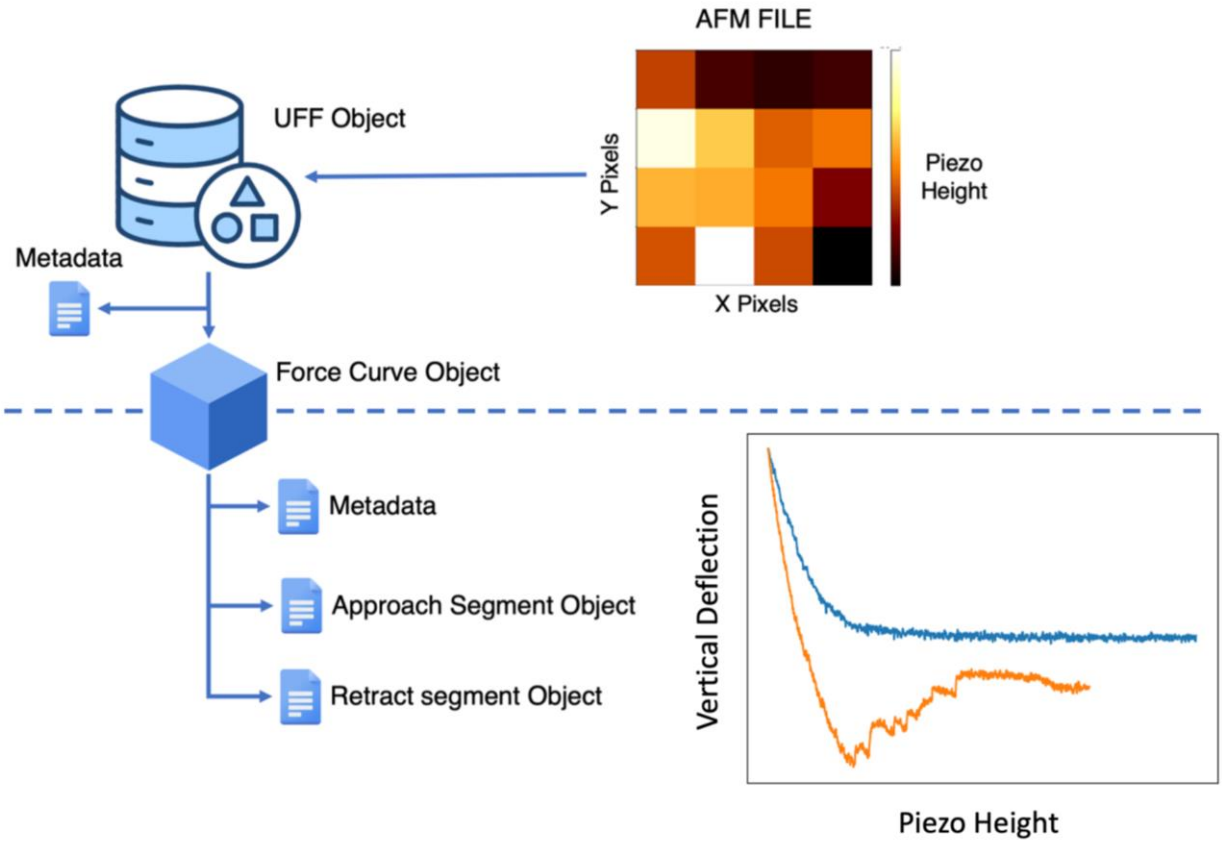

Figure 78: Hierarchical data organisation used in PyFM.

PyFMReader can be used as a stand-alone library to load data acquired by Bruker® instruments running JPK SPM software v4.2 - v7.0 (.jpk-force, .jpk-force-map, .jpk-qi-data) or Nanoscope software v7.0 - v9.0 (.spm, .pfc). PyFMReader allows exporting to UFF txt data files. Interactive Jupyter notebooks are provided with examples on how to load files and access loaded data.

2.4.1.2. PyFMRheo

Source code : https://github.com/jlopezalo/PyFMRheo

As the main building block of PyFM, this library includes a wide variety of models and predefined routines for the nanomechanical characterization of biological samples, correction for hydrodynamic drag, calibration of the z-piezo for oscillatory measurements and non-contact calibration of AFM probes. As PyFMReader and PyFMRheo have been developed with the intention of

being used together, the predefined routines available in PyFMRheo expect input FDCs and thermals as objects defined by PyFMReader. Nevertheless, this library can be used on its own, with the user being able to decide which library to use to load their data, which allows it to be used for the analysis of any data acquired on lab made or other commercial instruments. All models and tools required for processing AFM force curves and thermal tunes are fully accessible, allowing the users to compose their own custom data processing scripts. Examples on how to use each of the predefined routines are provided as interactive Jupyter notebooks.

Elastic Models

Contact models describing the force (F) versus indentation (δ) relationship allowing to obtain the Young's modulus (E) from the approach segment of FDC for several AFM tip geometries have been included:

Tip geometry	Formula	Reference
Paraboloidal	$\mathrm{F}(\delta) = \frac{4\sqrt{R}}{3(1-\nu^2)} E\delta^{\frac{3}{2}}$	(Hertz, 1882)
Conical	$\mathrm{F}(\delta) = \frac{2\ tan\ \theta}{\pi(1-\nu^2)} E\delta^2$	(LOVE, 1939; Sneddon, 1965)
4-sided regular pyramid	$\mathrm{F}(\delta) = \frac{tan\ \theta}{\sqrt{2}(1-\nu^2)} E\delta^2$	(Barber & Billings, 1990; Bilodeau, 1992)

Table 5: Implemented elastic models.

Where R corresponds to the tip radius, ν to the Poisson's ratio and θ to the semi-opening angle of the cone or the pyramid face angle.

Additionally, the library includes a model considering the finite thickness of the sample developed by Garcia & Garcia (Garcia & Garcia, 2018), where the thickness of the sample is considered when determining the Young's modulus.

Tip geometry	Formula	Reference
Paraboloidal	$\mathrm{F}(\delta) = F_0(\delta)\left[\frac{1}{h^0} + \frac{1.133\sqrt{\delta R}}{h} + \frac{1.497\delta R}{h^2} + \frac{1.469\delta R\sqrt{\delta R}}{h^3} + \frac{0.755(\delta^2 R^2)}{h^4}\right]$ $F_0(\delta) = \frac{4\sqrt{R}}{3(1-\nu^2)} E\delta^{\frac{3}{2}}$	(Garcia & Garcia, 2018)
Conical	$\mathrm{F}(\delta) = F_0(\delta)\left[\frac{1}{h^0} + \frac{0.721\delta\ tan\ tan\ \theta}{h} + \frac{0.650\delta^2(tan\ tan\ \theta)^2}{h^2} + \frac{0.491\delta^3(tan\ tan\ \theta)^3}{h^3} + \frac{0.225\delta^4(tan\ tan\ \theta)^4}{h^4}\right]$ $F_0(\delta) = \frac{2\ tan\ tan\ \theta}{\pi(1-\nu^2)} E\delta^2$	
4-sided regular pyramid	$\mathrm{F}(\delta) = F_0(\delta)\left[\frac{1}{h^0} + \frac{0.721\delta\ tan\ tan\ \theta}{h} + \frac{0.650\delta^2(tan\ tan\ \theta)^2}{h^2} + \frac{0.491\delta^3(tan\ tan\ \theta)^3}{h^3} + \frac{0.225\delta^4(tan\ tan\ \theta)^4}{h^4}\right]$ $F_0(\delta) = \frac{tan\ \theta}{\sqrt{2}(1-\nu^2)} E\delta^2$	

Table 6: Implemented bottom effect corrected elastic models.

Due to the complexity of automatically determining the thickness of the sample at each pixel, in particular for force maps, the models incorporating Garcia & Garcia bottom effect correction are implemented in the PyFMRheo analysis library but are not accessible through the Graphical User Interface (GUI).

Default routine implementation

1. The raw data of the curve is pre-processed to obtain the tip position (δ) by subtracting the cantilever vertical deflection (d) to the piezo position (z).

2. An estimate of the point of contact (PoC) is computed using the ratio of variances (RoV) method based on (Gavara, 2016).

3. The spring constant and initial estimation of the PoC are used to obtain the force (F) vs indentation (δ) curve.

4. Using the parameters defined by the user, the corresponding model is fitted to the force vs indentation curve to obtain the refined PoC and the Young's modulus (E).

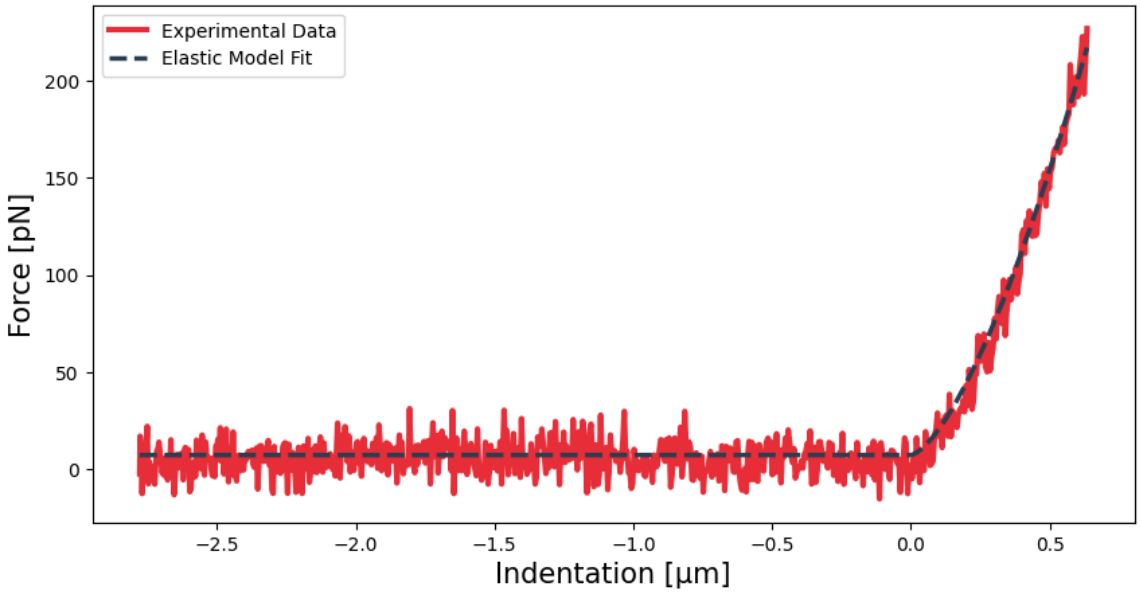

Figure 79: Approach segment of a force vs indentation curve acquired on a HeLa cell fitted to a Hertz paraboloidal elastic model, with an apparent Young's modulus equal to 886 Pa.

Viscoelastic models

Several models have been proposed to determine the viscoelastic force-indentation relationship of a sample. Most of these models are numerical (Efremov et al., 2017) or analytical (Brückner et al., 2017; D. Garcia et al., 2020) solutions based on the seminal works by Lee and Radock (Lee & Radok, 1960), Graham (Graham, 1967) and Ting (Ting, 1966, 1968). The selection and implementation of the models were performed focusing on the determination of the mechanical properties of living mammalian cells and extracellular matrices. Such samples which have been shown to exhibit a power law response both at low and high frequencies (Balland et al., 2006; Fabry et al., 2001; Jorba et al., 2017, 2019; Rigato et al., 2017). PyFMRheo includes both numerical and analytical models for a power law response material.

Tip geometry	FDC Segment	Equation	Reference
Paraboloidal	Approach	$F(t,\delta(t)) = \frac{4\sqrt{R}}{3(1-\nu^2)}\int_0^t E(t-\xi)\frac{\partial\delta^{\frac{3}{2}}}{\partial\xi}d\xi$	(Efremov et al., 2017)
	Retract	$F(t,\delta(t)) = \frac{4\sqrt{R}}{3(1-\nu^2)}\int_0^{t_1(t)} E(t-\xi)\frac{\partial\delta^{\frac{3}{2}}}{\partial\xi}d\xi$	
Conical	Approach	$F(t,\delta(t)) = \frac{2\tan\theta}{\pi(1-\nu^2)}\int_0^t E(t-\xi)\frac{\partial\delta^2}{\partial\xi}d\xi$	
	Retract	$F(t,\delta(t)) = \frac{2\tan\theta}{\pi(1-\nu^2)}\int_0^{t_1(t)} E(t-\xi)\frac{\partial\delta^2}{\partial\xi}d\xi$	
4-sided regular pyramid	Approach	$F(t,\delta(t)) = \frac{\tan\theta}{\sqrt{2}(1-\nu^2)}\int_0^t E(t-\xi)\frac{\partial\delta^2}{\partial\xi}d\xi$	
	Retract	$F(t,\delta(t)) = \frac{\tan\theta}{\sqrt{2}(1-\nu^2)}\int_0^{t_1(t)} E(t-\xi)\frac{\partial\delta^2}{\partial\xi}d\xi$	

Table 7: Implemented viscoelastic numerical models.

Where F is the force acting on the cantilever tip, δ is the indentation, t is the time, t_1 is the auxiliary function determined by:

$$\int_{t_1(t)}^{t} E(t-\xi)\frac{\partial\delta}{\partial\xi}d\xi = 0,$$

ξ is the dummy time variable required for the integration, E(t) is the Young's relaxation modulus described by a power-law rheology (PLR) model:

$$E(t) = E_0\left(\frac{t}{t_0}\right)^{-\beta},$$

where E_0 is the instantaneous elastic modulus, t_0 an arbitrary time scale assumed to be 1s, and β is the power-law exponent (β = 0 for material with solid-like behaviour, α = 1 for material with fluid-like behaviour).

Tip geometry	FDC Segment	Formula	Reference
Paraboloidal	Approach	$\mathrm{F}(t) = \frac{v_a^{\frac{3}{2}}}{\widetilde{C}} E_0 \frac{{t_0}^{\beta} 3\sqrt{\pi}\Gamma(1-\beta)}{4\Gamma\left(\frac{5}{2}-\beta\right)} t^{\frac{3}{2}-\beta}$	Based on (Brückner et al., 2017)
	Retract	$\mathrm{F}(t) = \frac{1}{\widetilde{C}} E_0 v_a^{\frac{3}{2}} \left(\frac{t}{t_0}\right)^{-\beta} t_1^{\frac{3}{2}} 2F1\left(\frac{3}{2}, \beta; \frac{5}{2}; \frac{t_1}{t}\right)$	
Conical / 4-sided regular pyramid	Approach	$\mathrm{F}(t) = 2\frac{{v_a}^2}{\widetilde{C}} E_0 \frac{{t_0}^{\beta}\Gamma[2]\Gamma[1-\beta]}{\Gamma[3-\beta]} t^{2-\beta}$	
	Retract	$\mathrm{F}(t) = 2\frac{v_r^2 E_0 t_0^{\beta}}{\widetilde{C}\,(2-3\beta+\beta^2)}\left[t^{2-\beta} + (t-t_1)^{1-\beta}(t_1 + (1+\beta)t)\right]$	

Table 8: Implemented viscoelastic analytical models.

Where F is the force acting on the cantilever tip, δ is the indentation, t is the time, t_1 is the auxiliary function determined by:

$$t_1 = t - \left(1 + \frac{v_r}{v_a}\right)^{\frac{1}{1-\beta}} (t - t_m),$$

where v_a is the constant approach velocity, v_r is the constant retract velocity. E(t) is the Young's relaxation modulus described by a power-law rheology (PLR) model:

$$E(t) = E_0 \left(\frac{t}{t_0}\right)^{-\beta},$$

$\widetilde{C}$ is the geometry dependent coefficient:

Tip geometry	Coefficient
Paraboloid	$\widetilde{C} = 3(1-\nu^2) / \left(4\sqrt{R}\right)$
Cone	$\widetilde{C} = \pi(1-\nu^2) / \left(2\,tan\,\theta\right)$
4-sided regular pyramid	$\widetilde{C} = 1.342(1-\nu^2) /\ tan\,\theta$

Table 9: Geometry coefficients used in the implemented viscoelastic analytical models (Table 8)

Default viscoelastic routine implementation

1. The raw data of the curve is pre-processed to obtain the tip position (δ) by subtracting the cantilever vertical deflection (d) to the piezo position (z).

2. An estimate of the point of contact (PoC) is computed using the ratio of variances (RoV) method based on Gavara, 2016.

3. The spring constant and initial PoC estimation are used to obtain the force (F) vs. indentation (δ) curve.

4. The elastic model corresponding to the AFM tip geometry is fitted to the approach segment of the force vs. indentation curve to obtain an estimation of the Young's modulus and a better estimation of the PoC.

5. The corresponding viscoelastic model is then fitted to the full approach-retract cycle of the force vs indentation curve to obtain the power-law fluidity exponent (β), the instantaneous apparent Young's modulus (E_0) and the PoC. The viscous drag force (force felt by the cantilever due to the viscosity of the medium) can be corrected, from the correction factor specified by the user and the respective approach and retract velocities.

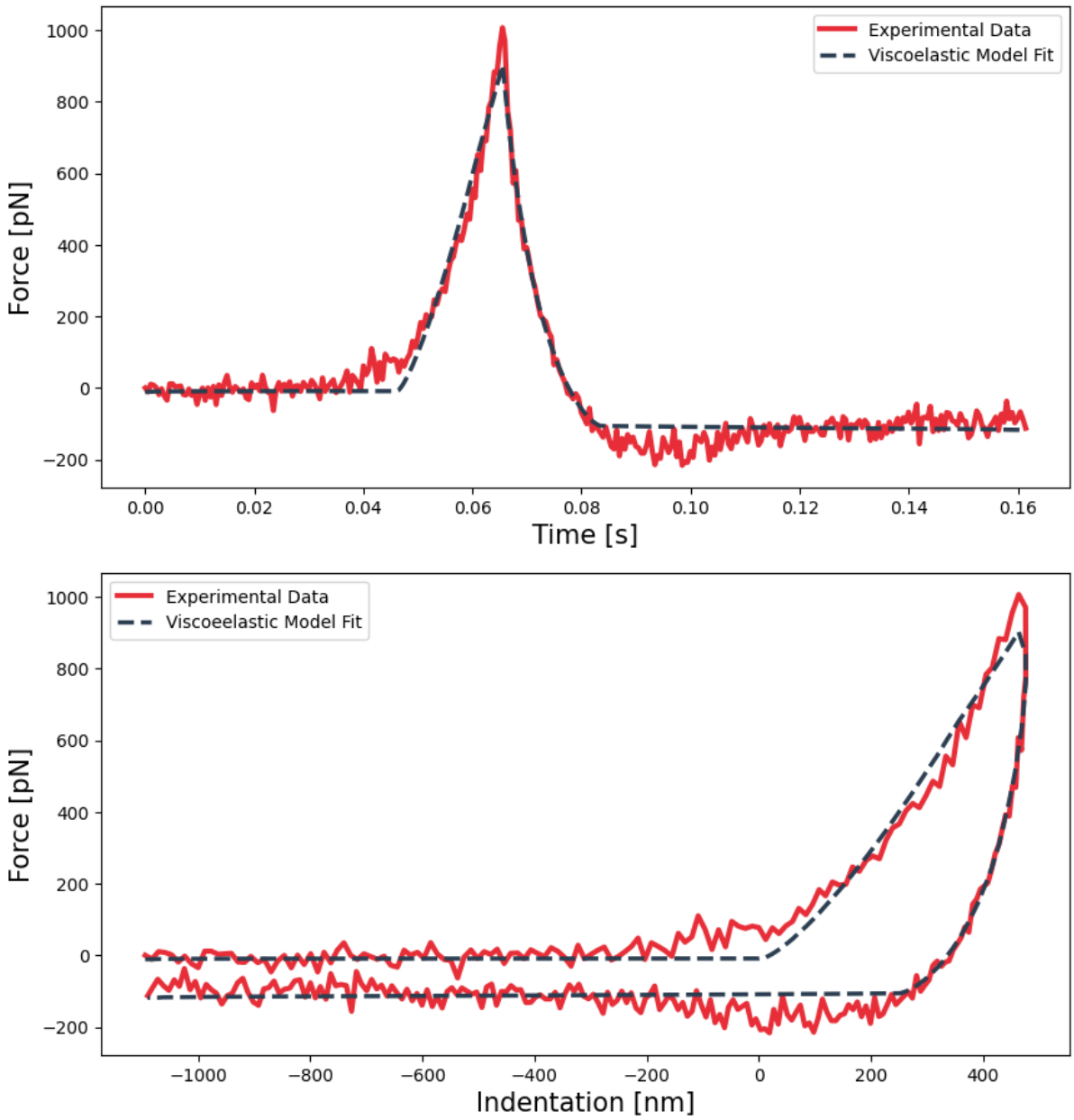

Figure 80: Force indentation curve acquired on a HeLa cell fitted to an analytic paraboloidal viscoelastic model, with an instantaneous apparent Young's Modulus (E0) and fluidity exponent of 334 Pa and 0.17 respectively. The fit is done on the force vs time curve (top) and can then be displayed on the force vs. indentation curve (bottom), allowing a direct comparison with the elastic fit shown on Figure 79.

Determination of the complex shear modulus from active microrheology measurements

Dynamic mechanical analysis (DMA), or microrheology measurements, consist on applying deformations in a cyclical manner to a material in the following manner:

1. The cantilever approaches and indents the sample.

2. The cantilever oscillates at a single frequency. This step is repeated in order to measure all the desired frequencies.

3. The cantilever is retracted from the sample.

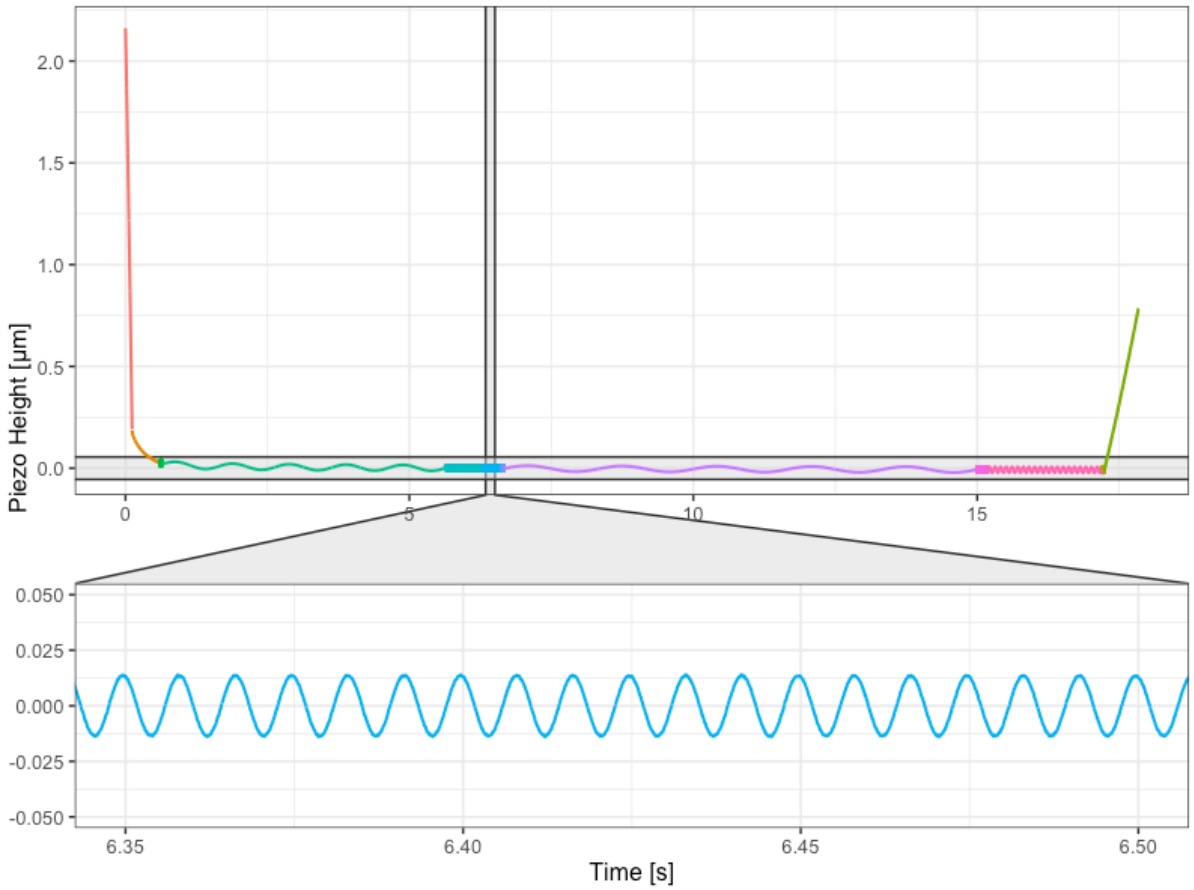

Figure 81: Microrheology data acquired on a HeLa cell. The cantilever is brought to contact with the sample up to reach the working indentation (red portion of the curve) and then oscillated at different frequencies (depicted in different colours, green, blue, violet, rose portions of the curve) before to be retracted from the sample (green portion of the curve). The inset shows the sinusoidal oscillations of the cantilever at a single frequency.

These cyclic forces result in variable deformations. As the stress (force applied to an area of the material) or strain (material deformation) applied is oscillatory (sinusoidal), the response of the sample is also sinusoidal. If a material is purely elastic, the strain and stress will be perfectly synchronous, at all times, meaning that, when the force is applied, the material will deform, and when the force stops being applied, the sample will recover its original shape. If the material is purely viscous, an applied stress will induce a strain response that is both delayed in time and not recovered once the application of stress ceases. Generally a material will exhibit both elastic and viscous behaviours, resulting in a strain response that will lag (phase angle 0 – 90°) behind the applied stress. From DMA, the following frequency dependent parameters can be obtained:

- Complex modulus ($G*$): Overall resistance of the material to deformation including a real part (elastic, G') and an imaginary part (viscous, G'').

- Storage modulus (G'): Elasticity of the materials and its ability to store energy.

- Loss modulus ($G"$): Viscosity of the material and its ability to dissipate energy.

- Loss tangent (η): Degree of solid- or liquid-like mechanical behaviour of the material.

Purely elastic material	Purely viscous material
$G'(\omega) = \frac{E}{2(1+\nu)}$ $G"(\omega) = 0$ $\eta(\omega) = 0$	$G' = 0$ $G"(\omega) = \mu\omega$ $\eta(\omega) \to \infty$

Table 10: Values of the storage modulus, loss modulus and loss tangent for purely elastic and viscous materials.

Where E is the Young's modulus, ν is the Poisson's ratio and ω is the angular frequency.

Mammalian cells and extracellular matrices (ECM) are viscoelastic materials, with both an elastic and viscous component. In 2003 Alcaraz et al. defined a methodology for the microrheological characterization of biological samples with AFM. When a sample is cyclically indented in AFM, a certain stress is applied to the sample, causing it to deform. Both the stress and the deformation of the sample can be measured through force-indentation curves, where the force can be used to monitor the stress applied, and the indentation signal can be used to monitor the corresponding deformation of the sample.

Models for two AFM tip geometries have been implemented:

Geometry	Function	Reference
Paraboloidal	$G*(\omega) = \frac{1-\nu}{4(R\delta_0)^{\frac{1}{2}}}\frac{F(\omega)}{\delta(\omega)}$	(Rico et al., 2005)
Pyramidal	$G*(\omega) = \frac{1-\nu}{3\delta_0 tan\,\theta}\frac{F(\omega)}{\delta(\omega)}$	(Alcaraz et al., 2003)

Table 11: Implemented frequency domain rheological models.

Where δ_0 corresponds to the working indentation at which small amplitude oscillations are applied.

The default routine expects data which has been acquired by indenting the sample and applying single frequency oscillations at different segments. As it can be observed in Figure 81.

Default rheology routine implementation

1. The force curve is pre-processed to obtain the piezo position (z) vs tip position (δ).

2. An estimate of the point of contact (PoC) is computed from the approach segment using the ratio of variances (RoV) method based on (Gavara, 2016). This allows determining the value of the working indentation.

3. If the user provides piezo calibration data and selects the option, the amplitude and phase of the z-piezo signal are corrected.

4. Both signals are then detrended by subtracting the rolling average of the signal with a window size equal to the number of points of each period.

5. The transfer function (H_d) is computed considering the small amplitude indentation ($\delta(\omega)$) as the input signal and the measured force ($F(\omega)$) as the output signal.

$$H_d = \frac{F(\omega)}{\delta(\omega)}$$

6. If the user provides a value for the drag force at contact, the transfer function values are corrected accordingly.

7. $G^*(\omega)$ is computed using the corresponding frequency domain rheological model. From the values of $G^*(\omega)$, $\eta(\omega)$ is computed.

Z-Piezo characterization

When characterising the microrheological properties of cells or ECM, any delay between the force and indentation signals inherent to the instrument will result in an over- or underestimation of the viscoelastic properties of the sample. By acquiring oscillatory measurements in a non-deformable substrate, like glass, the inherent phase angle (ϕ_{PZT}) between the deflection and z movement signals of the instrument can be measured and used to correct the measurements acquired on the sample.

$$G^*_{corr} = G^* \, e^{-i\phi_{PZT}}$$

In addition to the previous correction, in this routine, the ratio between the vertical deflection and the z-piezo signals is computed. This value can then later be used to correct the z-piezo signal acquired on the sample.

$$z_{corr} = z\, A_{corr}$$

Default z-piezo characterization routine implementation

1. Both the z-piezo displacement (z) and the vertical deflection of the cantilever are detrended (d) by subtracting the rolling average of the signal with a window size equal to the number of points of each period.

2. The transfer function is computed considering Z_{PZT} as the input signal and d_v as the output signal.
$$H_d = d/z$$

3. From the transfer function, the phase between z and d signals at each applied frequency are obtained.

4. Finally, the signal amplitude quotient between z and d signals is computed.
$$A_{corr} = \frac{A_d}{A_Z}$$

Determination of viscous drag coefficient

To minimise the noise in the measurements and to provide a suitable environment when working with living cells, most AFM microrheological measurements are performed in liquid. Therefore, when the cantilever oscillates, the surrounding fluid applies force on the cantilever by adding resistance to the motion (hydrodynamic drag). In the same manner as the piezo lag, the hydrodynamic drag results in an overestimation of the viscous properties of the measured sample. To account for this effect, Alcaraz and collaborators (Alcaraz et al., 2002) proposed a correction applicable to AFM measurements on soft samples in liquid at low Reynold numbers (Re < 1). They approached this problem by modelling the AFM cantilever as a sphere close to a rigid wall. The characterization of the hydrodynamic on a spherical body close to a rigid wall has been addressed by multiple authors (Brenner, 1961; R. G. Cox & Brenner, 1967). Based on these works, Alcaraz and collaborators estimate the drag force $b(h)$ when approaching the sample to be:

$$b(h) = \frac{6\pi\eta {a_{eff}}^2}{\left(h + h_{eff}\right)}$$

Where η is the viscosity of the fluid, a_{eff} is the effective radius of the cantilever, h_{eff} is the effective height of the tip and h is the distance between the tip and the sample.

Using this scaled spherical model, the drag force at contact ($b(0)$) can be estimated by measuring the drag force $b(h)$ at different cantilever-sample separations and extrapolating the data to $h = 0$.

To compute $b(h)$ the default routine expects data acquired with a specific protocol:

1. The AFM tip approaches and indents the sample (cell, tissue, gel, etc.).

2. The cantilever retracts a certain distance defined by the user.

3. The cantilever is oscillated at a single frequency defined by the user.

4. Steps 2 and 3 are repeated until the maximum desired distance from the sample has been reached.

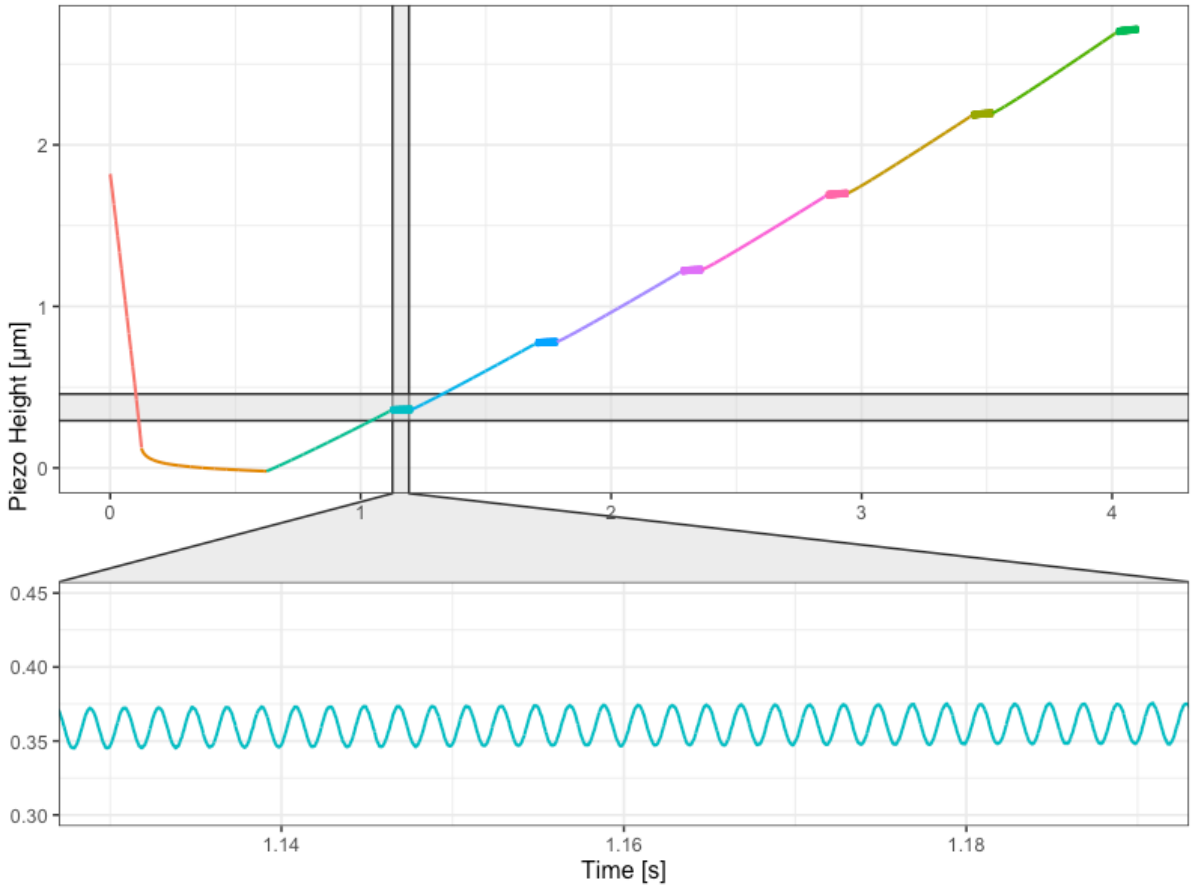

Figure 82: Data acquired on HeLa cells, using a SAA-SPH-5UM AFM paraboloidal probe (Bruker, Santa Barbara, CA, USA), to determine the viscous drag. The cantilever is brought into contact with the sample (h = 0 µm, orange portion of the curve) and retracted 6 times (segments depicted in 6 different colours) until the maximum tip-sample distance of 2.75 µm is reached. After every retract, the cantilever is oscillated at the same frequency. This modulation step is shown in the inset.

Default viscous drag routine implementation

1. If the user provides piezo calibration data and selects the option to correct the amplitude of the z-piezo, the signal is corrected.

2. The transfer function (H_d) is computed considering the indentation (δ) as the input signal and the measured force (F) as the output signal.

$$H_d = \frac{F(\omega)}{\delta(\omega)}$$

3. If the user provides piezo calibration data, the transfer function values are corrected using the piezo amplitude and lag.

4. $b(h)$ is then computed using the following expression:

$$b(h) = \frac{H_d}{(2\pi\omega)}$$

Non-contact cantilever calibration

Many indirect calibration methods have been developed, with the Sader method being the most widely used, thanks to its ease of use and applicability to different cantilever geometries (rectangular, V-shaped) (Sader et al., 1999, 2005, 2012). This method relies on measuring the quality factor (Q) and resonant frequency (ω_R) from the thermal spectrum of the cantilever to estimate the spring constant (k) by relying on hydrodynamic theory. When the cantilever oscillates, the surrounding fluid (air, water, etc.) applies force on the cantilever in two ways: by adding resistance to the motion (hydrodynamic drag) and by adding mass to the cantilever. By relating the measured ω_R and Q factor of the cantilever oscillating in a fluid to the values of the cantilever oscillating in vacuum, an analytical model to determine the spring constant of the cantilever for the first eigenmode (k_1) can be derived, by taking into consideration the geometry of the cantilever together with the density and viscosity of the fluid (Sader et al., 2005). The spring constant of a rectangular cantilever can be determined applying the following formula:

$$k = 0.1906\, \rho\, b^2\, L\, \Gamma_i(\omega_R)\, {\omega_R}^2\, Q$$

Where ρ is the density of the medium, b is the thickness of the cantilever, L is the length of the cantilever, Γ_i are the imaginary components of the hydrodynamic function, ω_R is the resonance frequency of the cantilever and Q is the quality factor of the cantilever. Although this expression is limited to rectangular cantilevers, the Sader method was later extended to cantilevers of arbitrary shape (Sader et al., 2012)

With the goal of allowing to calibrate the spring constant of cantilevers with a reference standard, Sader et al. developed a virtual instrument (https://sadermethod.org/) that allows the user to obtain the spring constant of a cantilever regardless of its shape by measuring ω_R and Q. This method is referred to as the global calibration initiative (GCI) (Sader et al., 2012, 2016).

In 2006, Higgins et al. proposed a non-contact method to obtain the optical lever sensitivity (or deflection sensitivity) from the thermal spectrum of the cantilever, assuming that the spring constant remains unchanged in air and liquid. This approach requires a previous calibration of the spring constant in air with the Sader or other method (Higgins et al., 2006). As this method yields a deflection sensitivity different to the one obtained by contact-based methods, the result is then multiplied by a correction factor to obtain the correct value.

Although the Sader and GCI methods enhance the precision of nanomechanical measurements when compared to conventional contact-based approaches (Sader et al., 2012, 2016), they both assume cantilevers with a high Q value, which is not always the case for most cantilevers in liquid. For this reason, in 2020, Sumbul and collaborators (Sumbul et al., 2020) assessed the accuracy and precision of these methods. In this study, they observed that using the single harmonic oscillator (SHO) model to fit the thermal spectra together with the GCI method was less prone to systematic uncertainties and provided higher accuracy in the determination of k and the deflection sensitivity (Sumbul et al., 2020). The implementation of the calibration routine in this package has been based on these findings.

Default spring constant calibration routine implementation

1. The SHO model is fit to the first eigenmode peak of the thermal tune data to obtain the white noise of the signal (A_{white}), the amplitude of the peak (B), the resonance frequency (f_R) and Q factor of the cantilever.

$$S_{SHO}(f) = A_{white}^2 + \frac{B^2 f_R^4}{Q^2}\left[(f^2 - f_R^2)^2 + \frac{f^2 f_R^2}{Q^2}\right]^{-1}$$

2. From these values the spring constant can be computed using the general Sader method. This step is only valid for rectangular and V-shaped cantilevers.

3. If the user provides thermal data acquired in air, their username and password for the Global Calibration Initiative (GCI) web application, the software will get the GCI spring constant through the application programming interface of the GCI web application.

4. The deflection sensitivity (or inverse of the optical lever sensitivity, invOLS) is computed using the method proposed by Higgins et al. and Sumbul et al. The user can specify the factors to correct for the static versus dynamic deflection (sometimes referred as χ) and the fundamental oscillation mode (sometimes referred as β) of the cantilever (Chighizola et al., 2023). If no correction factor is specified, the default values ($sqrt(\beta)/\chi$) of 0.90 (rectangular) and 0.87 (V-shaped) are used (Pirzer & Hugel, 2009; Stark et al., 2001; Sumbul et al., 2020).

2.4.1.3. PyFMGui

Source code: https://github.com/jlopezalo/PyFMGUI

To make the software more accessible to the end user, a graphical user interface (GUI) has been developed. This GUI allows the user to load, visualise and process data using the methods from the PyAFMReader and PyAFMRheo libraries. Multiprocessing has been implemented to speed up loading and processing of large files.

2.4.1.4. PyFM Dependencies

Library name	Description	References
Numpy	Numerical computation and N-dimensional arrays.	(Harris et al., 2020)
Pandas	Data manipulation and DataFrame data structures.	(McKinney, 2010)
SciPy	Algorithms for scientific computing.	(Virtanen et al., 2020)
Lmfit	Non-Linear least-squares minimization and curve-fitting.	(Newville et al., 2023)
PyQT 5	Graphical user interface framework.	https://github.com/PyQt5
PyQTGraph	User interface graphics.	https://github.com/pyqtgraph
PyInstaller	Freezing PyFM code for distribution.	https://github.com/pyinstaller

Table 12: Open source Python libraries used by PyFM.

2.4.2. Software Validation

2.4.2.1. Cell culture

HeLa cells (ATCC, Manassas, VA, USA) were cultured in MEM (ThermoFischer, Waltham, MA, USA) containing 10% foetal bovine serum, 10% L-Glutamine and 1% Penicillin/Streptomycin. Cells were then seeded in 35 mm diameter glass-bottom Petri dishes (WillCo, Amsterdam, NL) and incubated overnight at 37°C and 5% CO_2.

2.4.2.2. AFM measurements

For measuring the mechanical properties of cells, maps of force curves, with a size of 30 µm x 30 µm and a resolution of 4 x 4 pixels, were acquired on the nucleus area of 20 cells using a NanoWizard III (Bruker, Santa Barbara, CA, USA). The maps were acquired using a SAA-SPH-5UM probe (hemispherical tip, 5 µm radius, 0.192N/m spring constant) (Bruker, Camarillo, CA, USA) using the

following parameters: 1nN force setpoint, 4µm ramp size and 20µm/s ramp speed. During all measurements, indentations ~500nm were targeted to avoid the bottom effect of the substrate.

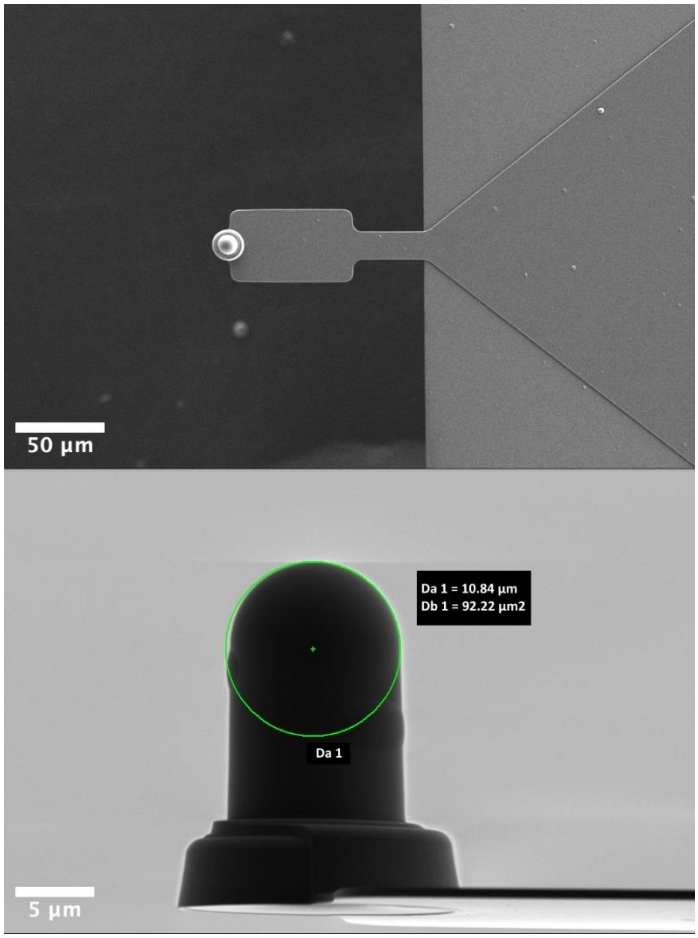

Figure 83: Scanning electron microscopy images of the SAA-SPH-5UM AFM probe (Bruker, Santa Barbara, CA, USA). Top view (top) Side view (bottom).

We acquired two datasets. The first dataset (A) involved approaching and retracting the tip at a constant speed to collect data for analysis using elastic and viscoelastic models. The second dataset (B) involved oscillating the tip in contact with the sample to collect data for analysis using complex shear modulus models. In this latter case, sinusoidal oscillations of 0.6 Hz, 1 Hz, 10 Hz, 60 Hz, 120 Hz and 200 Hz were applied during the z-piezo characterization and microrheological measurements on cells. To compute the drag force at contact, the cantilever was oscillated at 500 Hz at tip-sample distances between 500nm and 3µm.

2.4.2.3. AFM data processing

All data was processed using three software packages:

- PyFM: The software package developed in this work.

- MATLAB Routines: Custom routines developed in MATLAB and applied before for elastic (Rico et al., 2005) and viscoelastic (Gerum et al., 2022) FDCs data processing.

- JPK DP (v.7.1.23): Commercial software developed and provided by Bruker, used to visualise and process data acquired with the NanoWizard AFM platform.

2.4.2.3.1. Determination of the Young's modulus of living HeLa cells

The Young's modulus (E) of 20 HeLa cells was measured, as shown in Figure 79, by fitting the paraboloidal Hertz's contact model (Table 5) to the approach segment of each force-distance curve of the dataset A. All three software packages were used for this analysis.

2.4.2.3.2. Determination of the viscoelasticity of living HeLa cells

The same dataset A was used to compute the power-law fluidity exponent by fitting the analytical model developed by (Brückner et al., 2017) for a paraboloidal tip (Table 8), as shown in Figure 80.

Only the MATLAB routines and PyFM were used for this analysis.

2.4.2.3.3. Microrheological measurements on HeLa cells

For this analysis, the dataset B acquired on 20 HeLa cells was used to compute the power-law parameters (scaling factor G_0 and fluidity exponent β). To minimise the effect of the viscous drag and Z-piezo artefacts, the phase lag and amplitude quotient of the Z-piezo, together with the drag force at contact, were determined using PyFM (Figure 84).

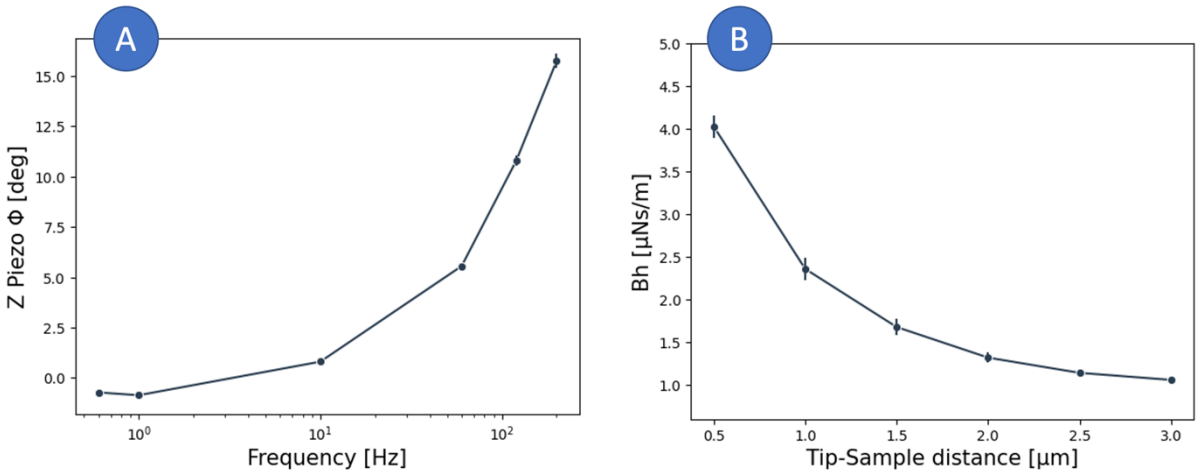

Figure 84: A) Z-piezo phase lag measured on a NanoWizard III for each frequency. B) Drag force measured at different cantilever-sample separations while applying 500 Hz oscillations. The data shown on each plot corresponds to the mean ± SE of three 4x4 force curves maps.

The geometric mean of the $G^*(f)$ for each cell was then fitted to a double power law:

$$G'(f) = A\ cos\ cos\ (\pi\alpha/2)\ f^{\alpha} + B\ cos\ cos\ (\pi\beta/2)\ f^{\beta}$$

$$G''(f) = A\ sin\ sin\ (\pi\alpha/2)\ f^{\alpha} + B\ sin\ sin\ (\pi\beta/2)\ f^{\beta}$$

By least squares minimization using the Lmfit (Newville et al., 2023) Python 3 library, leaving the four parameters A, B, β free. Microrheology measurements were only processed using PyFM.

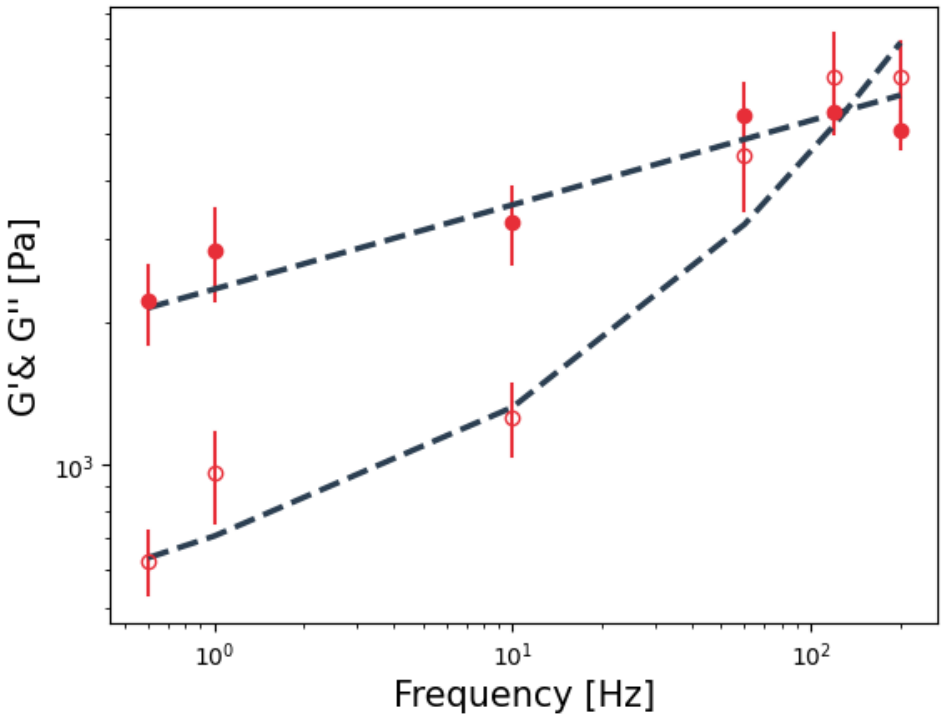

Figure 85: Experimental G'(f) (filled symbols) and G"(f) (hollow symbols) data of a cell fitted to a double power law. Each point shows the geometric mean ± SE of three 4x4 force curves map. The dashed line is a fit to the double power law with fitted parameters A, B, β equal to 2663 Pa, 38 Pa, 0.17 and 0.99, respectively.

2.4.2.4. Results

2.4.2.4.1. Comparison between apparent Young's modulus values

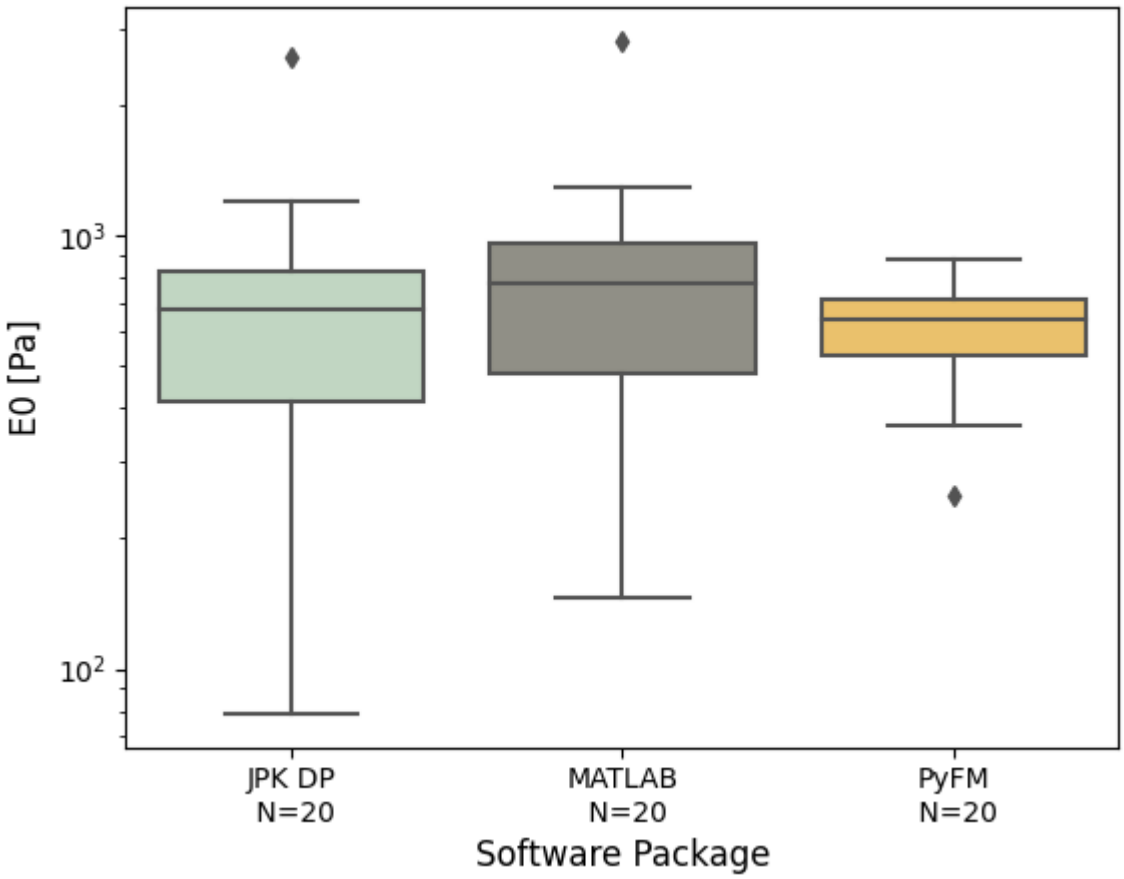

Figure 86: Median apparent Young's modulus (E) of individual HeLa cells (N=20 cells, with 16 measurements per cell) measured by different software packages. Centre line in the box plots represents the median value, top and bottom limits of the box represent the first and third quartiles (25% and 75%) of the data. Whiskers represent minimum and maximum values; diamonds represent the outliers (points outside 1.5 times the interquartile range).

To validate the elastic model fit of PyFM, a dataset comprising measurements of 20 HeLa cells was analysed using three different software packages. From the analysis the following results were obtained: JPK DP E0 = 676 Pa $\pm$ 93 Pa (median $\pm$ SE), MATLAB routines E0 = 776 Pa $\pm$ 110 Pa and PyFM E0 = 641 Pa $\pm$ 32 Pa. Where SE refers to the standard error, computed through bootstrapping (10000 resamples) . All values are in agreement with each other and vary in a range of 4-17%, with the MATLAB routines and PyFM showing the greatest difference (135 Pa). PyFM allows more robust determination of the contact point thanks to the RoV method (Gavara, 2016). This ensures less dispersion of the E0 results, whereas the fit errors were wider for the previous methods.

2.4.2.4.2. Comparisons between power-law fluidity exponent values obtained

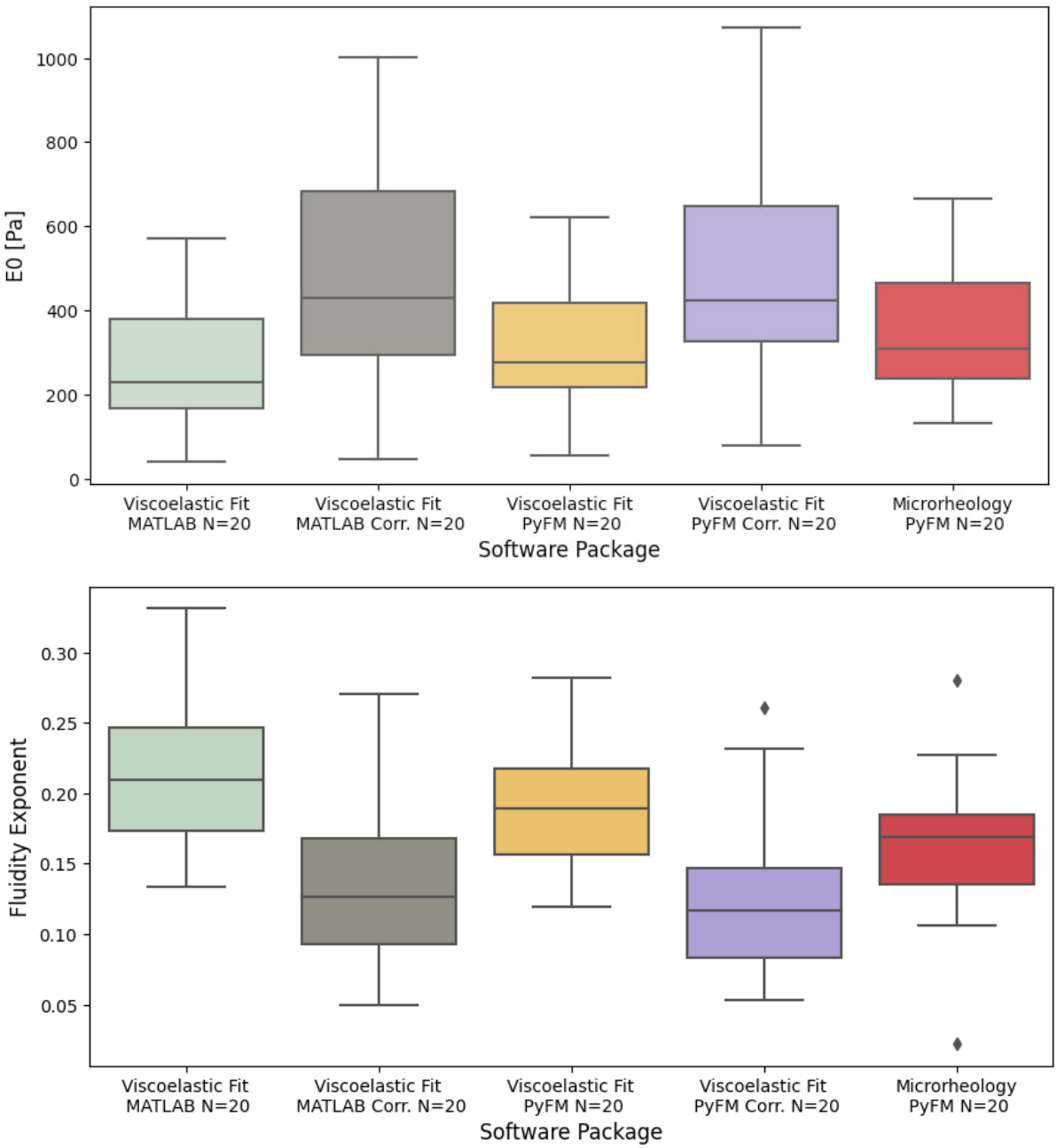

Figure 87: Instantaneous elastic modulus (E0) (Top) and Power-law fluidity exponent (α) (Bottom) of individual HeLa cells (N=20 cells, 16 measurements per cell) measured by different software packages. The values obtained from fitting the viscoelastic model represent the median E0 and α with and without correcting for the viscous drag assuming a viscous drag of 0.003 pN nm-1 s-1. The values reported obtained from the microrheology measurements represent the α obtained by fitting the geometric mean for each cell. G^* (f) was corrected for the z-piezo phase lag, signal amplitude and hydrodynamic drag (b (0) = 0.005 pN s nm-1). Centre line in the box plots represents the median value, top and bottom limits of the box represent Q1 and Q3 of the data. Whiskers represent minimum and maximum value; diamonds represent the outliers (points outside 1.5 times the interquartile range).

The power-law fluidity exponent was measured on HeLa cells through both a time-domain and a frequency-domain method.

For the time-domain method, the dataset A was used to fit the viscoelastic model developed by Brückner et al. (Brückner et al., 2017) to the full approach-retract cycle (as shown on Figure 80). The model was fitted using both the MATLAB routines and PyFM. As the measurements were performed in liquid, the data was corrected assuming a viscous drag factor of 0.003 pN nm^{-1} s^{-1}. The following values were obtained from the analysis: Viscoelastic Fit MATLAB α = 0.21 $\pm$ 0.018 (median $\pm$ SE), Viscoelastic Fit MATLAB Corrected α = 0.13 $\pm$ 0.018, Viscoelastic Fit PyFM α = 0.18 $\pm$ 0.014, Viscoelastic Fit PyFM Corrected α = 0.12 $\pm$ 0.013. Where SE refers to the standard error, computed through bootstrapping (10000 resamples). As expected, the values corrected for the viscous drag were lower for fluidity exponent and higher for E_0 than the non-corrected ones. Nevertheless, the values obtained from both routines are in agreement and in the range of α values that other authors have reported for cells (Brückner et al., 2017; Efremov et al., 2017; Flormann et al., 2021).

For the frequency-domain method, the dataset B, acquired on 20 other HeLa cells, was used. During the analysis, the measurements were corrected for the z-piezo phase lag, amplitude quotient and hydrodynamic drag (b(0) = 0.005 $pNsnm^{-1}$). A α of 0.17 $\pm$ 0.013 (median $\pm$ SE) was measured. These values are within the range of values that other authors have reported for HeLa cells (Flormann et al., 2021; Rother et al., 2014) and are similar to the values obtained from the viscoelastic fits. This trend was previously observed by other authors (Efremov et al., 2017).

2.4.3. Discussion

In this work, an open-source software package has been developed allowing us to measure the elastic and viscoelastic properties of soft samples from FDCs and microrheological measurements. The modularity of PyFM provides a user the possibility to use the package as a turn-key solution or to implement their custom features.

To validate the implemented algorithms, experimental data acquired on living HeLa cells was processed using three different software packages: commercial JPK DP, custom MATLAB routines and PyFM. The median apparent Young's modulus (E) of 20 cells was obtained using all three software packages. All

results obtained are in agreement with each other and differ in a range of 4 – 17%.

The viscoelastic properties of HeLa cells were characterised by both fitting a viscoelastic model to the approach-retract cycle (time-domain method) and by performing microrheological measurements (frequency-domain method). The viscoelastic model developed by Brücker et al. (Brückner et al., 2017) was fitted to the approach-retract cycle of the FDCs to determine E_0 and the fluidity exponent using both the MATLAB routines and PyFM on the same dataset. Microrheology data was processed using PyFM. Values obtained for E_0 and the power-law fluidity exponent were in agreement both between software packages and methodologies. This opens the way to characterising the rheological behaviour of samples directly from datasets consisting of regular approach-retract force curves, for example, for high resolution mechanical maps. Thus, speeding data acquisition and analysis when compared to DMA experiments.

Although version 1.0 of PyFM includes the most widely used models and functionalities needed for mechanically characterising biological samples, further improvements could be performed in the determination of the point of contact in the microrheology routine and other models to describe G* could be implemented. A separation dependent viscous drag correction may be also added to the FDC based approach. Furthermore, implementation of thickness determination from AFM mechanical maps will allow accurate correction of the bottom effect across the cell surface. We expect that PyFM will become a standard in the field, given its versatility, open-source nature, modularity and robustness.

3. Conclusions and future work

This work is aimed at developing AFM automation for studying the mechanical properties of biological samples at different scales. The results presented in this study indicate that this platform is suitable for automatically measuring the mechanical properties of biological samples at different scales. Thanks to the modularity of our system, we were able to successfully adapt our system to acquire data automatically on a wide range of samples by incorporating different acquisition routines for each application. We placed great focus on the experiment quality by continuously monitoring the experimental parameters (i.e., deflection sensitivity, photodiode sum, temperature, ...) and assessing the quality of the force curves as they are being acquired.

Although several authors have previously developed automated AFM systems, these were normally focused on a specific application / sample and did not incorporate neither data quality checks of the data collected nor monitoring of experimental parameters, such as the deflection sensitivity. In this work we decided to take a general approach and built a platform that could accommodate different data acquisition routines and that could be easily adapted to work with a wide range of samples. To validate our system, we studied the mechanical properties of 4 different samples.

First, we measured artificial nanovesicles (NVs) extruded from three different lipid mixtures—Dipalmitoyl phosphatidylcholine (DPPC) alone, DPPC mixed with Cholesterol (CHOL), and 1,2-Dioleoyl-sn-glycero-3-phosphocholine (DOPC) mixed with Sphingomyelin (SM)—at diameters of 30nm, 50nm, and 100nm. For performing these experiments, it was necessary to implement a ROI detection system suitable for these samples. We decided to incorporate the algorithm developed by Dujardin and collaborators (Dujardin et al., 2019), which had already proven to work with bacteria. With the data collected, we compared different mechanical models to determine which one better describes the mechanical properties of the NVs. We concluded that the Thin Shell theory provides a better description, as it is less influenced by the size of the NVs when compared to the application of the Hertz Model. Although the differences in the mechanical properties between the three different lipid mixtures were not as perceivable as we expected, the development of this automated data acquisition and analysis protocol, paves the way for the

establishment of a methodology that can be applied to cell-derived extracellular vesicles (EVs) under both pathological and non-pathological conditions.

As a second application, we treated Telomerase Reverse Transcriptase immortalized Retinal Pigment Epithelial (hTERT-RPE-1) cells, which had diameters ranging from 30µm to 70µm, with Latrunculin-A. This substance inhibits actin polymerization and has been reported in the literature to cause a decrease in the apparent Young's modulus (E) of hTERT-RPE-1 cells (Flormann et al., 2021; Rigato et al., 2015). For performing these experiments, it was necessary to develop an algorithm capable of detecting cells from bright-field images and selecting cells with a similar morphology. Our automated experiments confirmed a decrease in E compared to non-treated cells, thus validating the application of our system to mammalian cells.

Furthermore, by integrating a tracking algorithm into the automated system, we were able to monitor the mechanical properties of NIH3T3 fibroblasts as they migrated on glass. The data collected allowed us to obtain and correlate the morphological and mechanical properties of the cells at different time points. We observed that both the front-to-back ratio of the BEC Young's Modulus and the leading edge/following edge ratio of migrating NIH3T3 cells exhibited a weak correlation with the migration speed but not with the migration angle or changes in the migration angle of the cell. This suggests that even when cells are moving in a particular direction, they are constantly exploring alternative paths. In future studies, the system could be applied to provide more insights on the mechanisms of chemotaxis and chemotaxis, by studying how the mechanical properties of cells change on substrates of different stiffness or when exposed to certain chemical stimuli.

Finally, we adapted the system to work with 50µm thick rat bladder tissue, a highly heterogeneous tissue consisting of three distinct zones with different mechanical properties. Our automated experiments successfully captured the mechanical fingerprint of the tissue samples, revealing the three distinct regions and obtaining values consistent with previous studies (Martinez-Vidal et al., 2023). This demonstration highlights the applicability of our system to tissue samples. Future work could incorporate thresholding based on indentation rather than a force setpoint, to reduce the number of failed measurements when measuring tissues with mechanically different regions.

A major limitation of this system is that it is only capable of working with a single sample (petri dish, glass slide) at a time, severely hindering its throughput. Future iterations of this system could incorporate support for a multiwell plate or microscopy chambers of different geometries (Figure 88). However, modifications to the Precision Motor Stage and the glass cantilever holder would be necessary. Multi-sample support would reduce the requirement of a user to change the sample each time, thus reducing its reliance on the user, and would allow us to implement tip cleaning procedures by including a well with a cleaning solution. In a similar manner as Dujardin and collaborators implemented it on their platform.

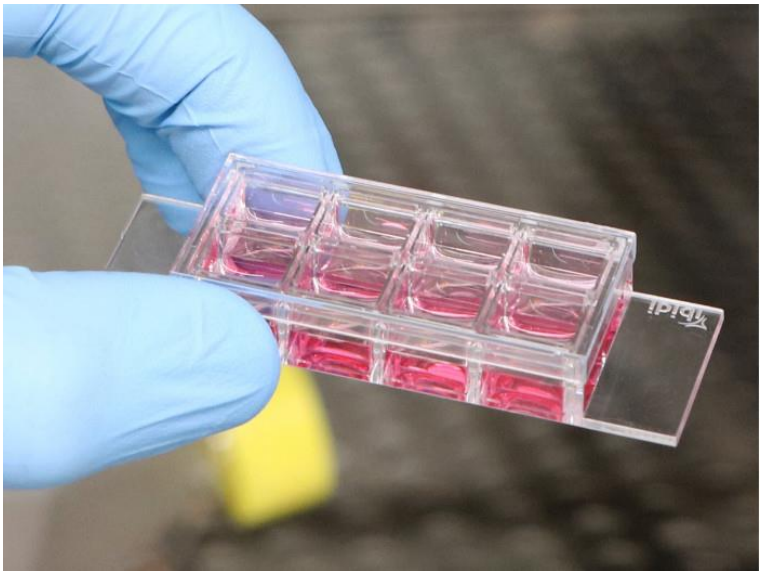

Figure 88: Ibidi® µ-Slide 8 Well high Glass Bottom microscopy chamber. (Ibidi®)

Moreover, the lack of CO2 control and a sterile enclosure made performing experiments on live-cells for a prolonged period (8-24h) impossible. As the medium would become contaminated and the cells would start to die. To minimize these issues, we used a silicone membrane to cover the petri dish to prevent medium evaporation and used a medium containing antibiotics and HEPES buffer. The incorporation of a sterile enclosure with temperature, humidity and CO2 control would significantly increase the duration of the experiments.

Tip exchanging algorithms could also increase the duration of the experiments and further reduce the reliance on the operator. In the current iteration, if the system encounters an issue (i.e., large change in the photodiode sum due to contamination getting stuck on the tip) the experiment is halted and the user is

informed. If the system could handle these issues by attempting to clean the tip or changing the tip, the experiment could be resumed without the need of an operator.

In addition to the automated AFM system, we have developed an open-source software package that allows for the measurement of elastic and viscoelastic properties of soft samples using force-distance curves (time-domain) and microrheological measurements (frequency-domain). We have validated this software against in-house MATLAB scripts and the JPK Data Processing commercial software. Future improvements could include the implementation of more mechanical models and tools to import data formats from other manufacturers.

In conclusion, this work has successfully produced an automated AFM system capable of studying the mechanical properties of biological samples at different scales and ready to be used and improved upon in a lab setting. By incorporating different acquisition routines and continuously monitoring experimental parameters, we have achieved high-quality data collection. The platform has been validated through the study of various samples, including nanovesicles, mammalian cells, migrating fibroblasts, and tissue samples. Our system's versatility and adaptability pave the way for broader applications in studying extracellular vesicles, cell mechanics, and tissue mechanical characterization. While the system has limitations in terms of throughput and experimental duration, future iterations can address these issues by incorporating multi-sample support, sterile enclosures, and tip exchanging algorithms. Additionally, we have developed an open-source software package that incorporates standardized automated routines for the measurement of elastic and viscoelastic properties. Thus, allowing to process high volumes of data in a robust and reproducible way. Overall, our work contributes to the advancement of automated AFM technology for comprehensive biomechanical studies.

4. References

Aharon, A., Spector, P., Ahmad, R. S., Horrany, N., Sabbach, A., Brenner, B., & Aharon-Peretz, J. (2020). Extracellular Vesicles of Alzheimer's Disease Patients as a Biomarker for Disease Progression. *Molecular Neurobiology*, *57*(10), 4156–4169. https://doi.org/10.1007/s12035-020-02013-1

Alcaraz, J., Buscemi, L., Grabulosa, M., Trepat, X., Fabry, B., Farré, R., & Navajas, D. (2003). Microrheology of human lung epithelial cells measured by atomic force microscopy. *Biophysical Journal*, *84*(3), 2071–2079. https://doi.org/10.1016/S0006-3495(03)75014-0

Alcaraz, J., Buscemi, L., Puig-de-Morales, M., Colchero, J., Baró, A., & Navajas, D. (2002). Correction of Microrheological Measurements of Soft Samples with Atomic Force Microscopy for the Hydrodynamic Drag on the Cantilever. *Langmuir*, *18*(3), 716–721. https://doi.org/10.1021/la0110850

Ando, T. (2013). High-speed atomic force microscopy. *Journal of Electron Microscopy*, *62*. https://doi.org/10.1093/jmicro/dfs093

Anselmo, A. C., Zhang, M., Kumar, S., Vogus, D. R., Menegatti, S., Helgeson, M. E., & Mitragotri, S. (2015). Elasticity of Nanoparticles Influences Their Blood Circulation, Phagocytosis, Endocytosis, and Targeting. *ACS Nano*, *9*(3), 3169–3177. https://doi.org/10.1021/acsnano.5b00147

Ashrafuzzaman, M., & Tuszynski, J. (2013a). Lipids in Membranes. In M. Ashrafuzzaman & J. Tuszynski (Eds.), *Membrane Biophysics* (pp. 31–49). Springer. https://doi.org/10.1007/978-3-642-16105-6_3

Ashrafuzzaman, M., & Tuszynski, J. (2013b). Structure of Membranes. In M. Ashrafuzzaman & J. Tuszynski (Eds.), *Membrane Biophysics* (pp. 9–30). Springer. https://doi.org/10.1007/978-3-642-16105-6_2

Ashrafuzzaman, M., & Tuszynski, J. (2013c). The Membrane as a Transporter, Ion Channels and Membrane Pumps. In M. Ashrafuzzaman & J. Tuszynski (Eds.), *Membrane Biophysics* (pp. 51–74). Springer. https://doi.org/10.1007/978-3-642-16105-6_4

Aumailley, M. (2013). The laminin family. *Cell Adhesion & Migration*, *7*(1), 48–55. https://doi.org/10.4161/cam.22826

Azioune, A., Carpi, N., Tseng, Q., Théry, M., & Piel, M. (2010). Protein micropatterns: A direct printing protocol using deep UVs. *Methods in Cell Biology*, *97*, 133–146. https://doi.org/10.1016/S0091-679X(10)97008-8

B, A., Rao, S., & Pandya, H. J. (2019). Engineering approaches for characterizing soft tissue mechanical properties: A review. *Clinical Biomechanics*, *69*, 127–140. https://doi.org/10.1016/j.clinbiomech.2019.07.016

Balland, M., Desprat, N., Icard, D., Féréol, S., Asnacios, A., Browaeys, J., Hénon, S., & Gallet, F. (2006). Power laws in microrheology experiments on living cells: Comparative analysis and modeling. *Physical Review E*, *74*(2), 021911. https://doi.org/10.1103/PhysRevE.74.021911

Banquy, X., Suarez, F., Argaw, A., Rabanel, J.-M., Grutter, P., Bouchard, J.-F., Hildgen, P., & Giasson, S. (2009). Effect of mechanical properties of hydrogel nanoparticles on macrophage cell uptake. *Soft Matter*, *5*(20), 3984–3991. https://doi.org/10.1039/B821583A

Barber, J. R., & Billings, D. A. (1990). An approximate solution for the contact area and elastic compliance of a smooth punch of arbitrary shape. *International Journal of Mechanical Sciences*, *32*(12), 991–997. https://doi.org/10.1016/0020-7403(90)90003-2

Barros, C. S., Franco, S. J., & Müller, U. (2011). Extracellular Matrix: Functions in the Nervous System. *Cold Spring Harbor Perspectives in Biology*, *3*(1), a005108. https://doi.org/10.1101/cshperspect.a005108

Bearer, E. L. (1993). Role of Actin Polymerization in Cell Locomotion: Molecules and Models. *American Journal of Respiratory Cell and Molecular Biology*, *8*(6), 582–591. https://doi.org/10.1165/ajrcmb/8.6.582

Belotti, Y., Tolomeo, S., Conneely, M. J., Huang, T., McKenna, S. J., Nabi, G., & McGloin, D. (2019). High-Throughput, Time-Resolved Mechanical Phenotyping of Prostate Cancer Cells. *Scientific Reports*, *9*(1), Article 1. https://doi.org/10.1038/s41598-019-42008-0

Berardi, M., Bielawski, K., Rijnveld, N., Gruca, G., Aardema, H., van Tol, L., Wuite, G., & Akca, B. I. (2021). Optical interferometry based micropipette aspiration provides real-time sub-nanometer spatial resolution. *Communications Biology*, *4*(1), Article 1. https://doi.org/10.1038/s42003-021-02121-1

Beton, J. G., Moorehead, R., Helfmann, L., Gray, R., Hoogenboom, B. W., Joseph, A. P., Topf, M., & Pyne, A. L. B. (2021). TopoStats – A program for automated tracing of biomolecules from AFM images. *Methods*, *193*, 68–79. https://doi.org/10.1016/j.ymeth.2021.01.008

Bilodeau, G. G. (1992). Regular Pyramid Punch Problem. *Journal of Applied Mechanics*, *59*(3), 519–523. https://doi.org/10.1115/1.2893754

Binnig, G., Quate, C. F., & Gerber, Ch. (1986). Atomic Force Microscope. *Physical Review Letters*, *56*(9), 930–933. https://doi.org/10.1103/PhysRevLett.56.930

Binnig, G., & Rohrer, H. (1983). Scanning tunneling microscopy. *Surface Science*, *126*(1), 236–244. https://doi.org/10.1016/0039-6028(83)90716-1

Binnig, G., Rohrer, H., Gerber, Ch., & Weibel, E. (1983). 7 × 7 Reconstruction on Si(111) Resolved in Real Space. *Physical Review Letters*, *50*(2), 120–123. https://doi.org/10.1103/PhysRevLett.50.120

Bodnar, A. G., Ouellette, M., Frolkis, M., Holt, S. E., Chiu, C.-P., Morin, G. B., Harley, C. B., Shay, J. W., Lichtsteiner, S., & Wright, W. E. (1998). Extension of Life-Span by Introduction of Telomerase into Normal Human Cells. *Science*, *279*(5349), 349–352. https://doi.org/10.1126/science.279.5349.349

Bolla, S. R., Odeluga, N., & Jetti, R. (2022). Histology, Bladder. In *StatPearls*. StatPearls Publishing. http://www.ncbi.nlm.nih.gov/books/NBK540963/

Brandl, F., Sommer, F., & Goepferich, A. (2007). Rational design of hydrogels for tissue engineering: Impact of physical factors on cell behavior. *Biomaterials*, *28*(2), 134–146. https://doi.org/10.1016/j.biomaterials.2006.09.017

Brenner, H. (1961). The slow motion of a sphere through a viscous fluid towards a plane surface. *Chemical Engineering Science*, *16*(3), 242–251. https://doi.org/10.1016/0009-2509(61)80035-3

Brückner, B. R., Nöding, H., & Janshoff, A. (2017). Viscoelastic Properties of Confluent MDCK II Cells Obtained from Force Cycle Experiments. *Biophysical Journal*, *112*(4), 724–735. https://doi.org/10.1016/j.bpj.2016.12.032

Bueno, C. C., Garcia, P. S., Steffens, C., Deda, D. K., & de Lima Leite, F. (2017). 5—Nanosensors. In A. L. Da Róz, M. Ferreira, F. de Lima Leite, & O. N. Oliveira (Eds.), *Nanoscience and its Applications* (pp. 121–153). William Andrew Publishing. https://doi.org/10.1016/B978-0-323-49780-0.00005-3

Burdick, J. A., & García, A. J. (2020). Special Issue: Biomaterials in Mechanobiology. *Advanced Healthcare Materials*, *9*(8), 2000412. https://doi.org/10.1002/adhm.202000412

Bussmann, J., & Raz, E. (2015). Chemokine-guided cell migration and motility in zebrafish development. *The EMBO Journal*, *34*(10), 1309–1318. https://doi.org/10.15252/embj.201490105

Butin-Israeli, V., Adam, S. A., Goldman, A. E., & Goldman, R. D. (2012). Nuclear lamin functions and disease. *Trends in Genetics*, *28*(9), 464–471. https://doi.org/10.1016/j.tig.2012.06.001

Caille, N., Thoumine, O., Tardy, Y., & Meister, J.-J. (2002). Contribution of the nucleus to the mechanical properties of endothelial cells. *Journal of Biomechanics*, *35*(2), 177–187. https://doi.org/10.1016/S0021-9290(01)00201-9

Camussi, G., Deregibus, M. C., Bruno, S., Cantaluppi, V., & Biancone, L. (2010). Exosomes/microvesicles as a mechanism of cell-to-cell communication. *Kidney International*, *78*(9), 838–848. https://doi.org/10.1038/ki.2010.278

Canham, P. B. (1970). The minimum energy of bending as a possible explanation of the biconcave shape of the human red blood cell. *Journal of Theoretical Biology*, *26*(1), 61–81. https://doi.org/10.1016/S0022-5193(70)80032-7

Carl, P., & Schillers, H. (2008). Elasticity measurement of living cells with an atomic force microscope: Data acquisition and processing. *Pflugers Archiv: European Journal of Physiology*, *457*(2), 551–559. https://doi.org/10.1007/s00424-008-0524-3

Causes de décès—Inserm-CépiDc. (2020). https://opendata-cepidc.inserm.fr/

Chang, W.-H., Cerione, R. A., & Antonyak, M. A. (2021). Extracellular Vesicles and Their Roles in Cancer Progression. *Methods in Molecular Biology (Clifton, N.J.)*, *2174*, 143–170. https://doi.org/10.1007/978-1-0716-0759-6_10

Chen, S. W., Teulon, J.-M., Kaur, H., Godon, C., & Pellequer, J.-L. (2022). Nano-structural stiffness measure for soft biomaterials of heterogeneous elasticity. *Nanoscale Horizons*, *8*(1), 75–82. https://doi.org/10.1039/D2NH00390B

Chen, Y., Ju, L., Rushdi, M., Ge, C., & Zhu, C. (2017). Receptor-mediated cell mechanosensing. *Molecular Biology of the Cell*, *28*(23), 3134–3155. https://doi.org/10.1091/mbc.E17-04-0228

Chiaruttini, N., Redondo-Morata, L., Colom, A., Humbert, F., Lenz, M., Scheuring, S., & Roux, A. (2015). Relaxation of Loaded ESCRT-III Spiral Springs Drives Membrane Deformation. *Cell*, *163*(4), 866–879. https://doi.org/10.1016/j.cell.2015.10.017

Chighizola, M., Dini, T., Marcotti, S., D'Urso, M., Piazzoni, C., Borghi, F., Previdi, A., Ceriani, L., Folliero, C., Stramer, B., Lenardi, C., Milani, P., Podestà, A., & Schulte, C. (2022). The glycocalyx affects the mechanotransductive perception of the topographical microenvironment. *Journal of Nanobiotechnology*, *20*(1), 418. https://doi.org/10.1186/s12951-022-01585-5

Chighizola, M., Rodriguez-Ramos, J., Rico, F., Radmacher, M., & Podestà, A. (2023). 3.1.3 AFM Calibration Issues. In *3.1.3 AFM Calibration Issues* (pp. 105–128). De Gruyter. https://doi.org/10.1515/9783110640632-007

Chopinet, L., Formosa, C., Rols, M. P., Duval, R. E., & Dague, E. (2013). Imaging living cells surface and quantifying its properties at high resolution using AFM in QI™ mode. *Micron*, *48*, 26–33. https://doi.org/10.1016/j.micron.2013.02.003

Chopinet, L., Roduit, C., Rols, M.-P., & Dague, E. (2013). Destabilization induced by electropermeabilization analyzed by atomic force microscopy. *Biochimica et Biophysica Acta (BBA) - Biomembranes*, *1828*(9), 2223–2229. https://doi.org/10.1016/j.bbamem.2013.05.035

Ciczora, Y., Janel, S., Soyer, M., Popoff, M., Werkmeister, E., & Lafont, F. (2019). Blocking bacterial entry at the adhesion step reveals dynamic recruitment of membrane and cytosolic probes. *Biology of the Cell*, *111*(3), 67–77. https://doi.org/10.1111/boc.201800070

Cortese, B., Gigli, G., & Riehle, M. (2009). Mechanical Gradient Cues for Guided Cell Motility and Control of Cell Behavior on Uniform Substrates. *Advanced Functional Materials*, *19*(18), 2961–2968. https://doi.org/10.1002/adfm.200900918

Coué, M., Brenner, S. L., Spector, I., & Korn, E. D. (1987). Inhibition of actin polymerization by latrunculin A. *FEBS Letters*, *213*(2), 316–318. https://doi.org/10.1016/0014-5793(87)81513-2

Cox, R. G., & Brenner, H. (1967). The slow motion of a sphere through a viscous fluid towards a plane surface—II Small gap widths, including inertial effects. *Chemical Engineering Science*, *22*(12), 1753–1777. https://doi.org/10.1016/0009-2509(67)80208-2

Cox, T. R., & Erler, J. T. (2011). Remodeling and homeostasis of the extracellular matrix: Implications for fibrotic diseases and cancer. *Disease Models & Mechanisms*, *4*(2), 165–178. https://doi.org/10.1242/dmm.004077

Dahms, Piechota, Dahiya, Lue, & Tanagho. (1998). Composition and biomechanical properties of the bladder acellular matrix graft: Comparative analysis in rat, pig and human. *British Journal of Urology*, *82*(3), 411–419. https://doi.org/10.1046/j.1464-410X.1998.00748.x

Darling, E. M., & Di Carlo, D. (2015). High-Throughput Assessment of Cellular Mechanical Properties. *Annual Review of Biomedical Engineering*, *17*(1), 35–62. https://doi.org/10.1146/annurev-bioeng-071114-040545

Das, M., Ithychanda, S., Qin, J., & Plow, E. F. (2014). Mechanisms of talin-dependent integrin signaling and crosstalk. *Biochimica et Biophysica Acta*, *1838*(2), 10.1016/j.bbamem.2013.07.017. https://doi.org/10.1016/j.bbamem.2013.07.017

Dechat, T., Pfleghaar, K., Sengupta, K., Shimi, T., Shumaker, D. K., Solimando, L., & Goldman, R. D. (2008). Nuclear lamins: Major factors in the structural organization and function of the nucleus and chromatin. *Genes & Development*, *22*(7), 832–853. https://doi.org/10.1101/gad.1652708

Delorme, N., & Fery, A. (2006). Direct method to study membrane rigidity of small vesicles based on atomic force microscope force spectroscopy. *Physical Review E*, *74*(3), 030901. https://doi.org/10.1103/PhysRevE.74.030901

Deng, X., Xiong, F., Li, X., Xiang, B., Li, Z., Wu, X., Guo, C., Li, X., Li, Y., Li, G., Xiong, W., & Zeng, Z. (2018). Application of atomic force microscopy in cancer research. *Journal of Nanobiotechnology*, *16*(1), 102. https://doi.org/10.1186/s12951-018-0428-0

Derjaguin, B. V., Muller, V. M., & Toporov, Yu. P. (1975). Effect of contact deformations on the adhesion of particles. *Journal of Colloid and Interface Science*, *53*(2), 314–326. https://doi.org/10.1016/0021-9797(75)90018-1

D. Garcia, P., R. Guerrero, C., & Garcia, R. (2020). Nanorheology of living cells measured by AFM-based force–distance curves. *Nanoscale*, *12*(16), 9133–9143. https://doi.org/10.1039/C9NR10316C

Dias, M. V. S., Costa, C. S., & daSilva, L. L. P. (2018). The Ambiguous Roles of Extracellular Vesicles in HIV Replication and Pathogenesis. *Frontiers in Microbiology*, *9*, 2411. https://doi.org/10.3389/fmicb.2018.02411

Domke, J., & Radmacher, M. (1998). Measuring the Elastic Properties of Thin Polymer Films with the Atomic Force Microscope. *Langmuir*, *14*(12), 3320–3325. https://doi.org/10.1021/la9713006

Dudani, J. S., Gossett, D. R., Tse, H. T. K., & Carlo, D. D. (2013). Pinched-flow hydrodynamic stretching of single-cells. *Lab on a Chip*, *13*(18), 3728–3734. https://doi.org/10.1039/C3LC50649E

Dufrêne, Y. F., Ando, T., Garcia, R., Alsteens, D., Martinez-Martin, D., Engel, A., Gerber, C., & Müller, D. J. (2017). Imaging modes of atomic force microscopy for application in molecular and cell biology. *Nature Nanotechnology*, 12(4), Article 4. https://doi.org/10.1038/nnano.2017.45

Dujardin, A., Wolf, P. D., Lafont, F., & Dupres, V. (2019). Automated multi-sample acquisition and analysis using atomic force microscopy for biomedical applications. *PLOS ONE*, 14(3), e0213853. https://doi.org/10.1371/journal.pone.0213853

Efremov, Y. M., Kotova, S. L., & Timashev, P. S. (2020). Viscoelasticity in simple indentation-cycle experiments: A computational study. *Scientific Reports*, 10(1), Article 1. https://doi.org/10.1038/s41598-020-70361-y

Efremov, Y. M., Okajima, T., & Raman, A. (2019). Measuring viscoelasticity of soft biological samples using atomic force microscopy. *Soft Matter*, *16*(1), 64–81. https://doi.org/10.1039/C9SM01020C

Efremov, Y. M., Wang, W.-H., Hardy, S. D., Geahlen, R. L., & Raman, A. (2017). Measuring nanoscale viscoelastic parameters of cells directly from AFM force-displacement curves. *Scientific Reports*, 7(1), Article 1. https://doi.org/10.1038/s41598-017-01784-3

Elosegui-Artola, A., Gupta, A., Najibi, A. J., Seo, B. R., Garry, R., Tringides, C. M., de Lázaro, I., Darnell, M., Gu, W., Zhou, Q., Weitz, D. A., Mahadevan, L., & Mooney, D. J. (2023). Matrix viscoelasticity controls spatiotemporal tissue organization. *Nature Materials*, 22(1), Article 1. https://doi.org/10.1038/s41563-022-01400-4

Engler, A. J., Sen, S., Sweeney, H. L., & Discher, D. E. (2006). Matrix Elasticity Directs Stem Cell Lineage Specification. *Cell*, *126*(4), 677–689. https://doi.org/10.1016/j.cell.2006.06.044

Et-Thakafy, O., Delorme, N., Gaillard, C., Mériadec, C., Artzner, F., Lopez, C., & Guyomarc'h, F. (2017). Mechanical Properties of Membranes Composed of Gel-Phase or Fluid-Phase Phospholipids Probed on Liposomes by Atomic Force Spectroscopy. *Langmuir*, 33(21), 5117–5126. https://doi.org/10.1021/acs.langmuir.7b00363

Fabry, B., Maksym, G. N., Butler, J. P., Glogauer, M., Navajas, D., & Fredberg, J. J. (2001). Scaling the Microrheology of Living Cells. *Physical Review Letters*, 87(14), 148102. https://doi.org/10.1103/PhysRevLett.87.148102

Flores, L. R., Keeling, M. C., Zhang, X., Sliogeryte, K., & Gavara, N. (2019). Lifeact-TagGFP2 alters F-actin organization, cellular morphology and biophysical behaviour. *Scientific Reports*, 9(1), 3241. https://doi.org/10.1038/s41598-019-40092-w

Flormann, D. A. D., Anton, C., Pohland, M. O., Bautz, Y., Kaub, K., Terriac, E., Schäffer, T. E., Rheinlaender, J., Janshoff, A., Ott, A., & Lautenschläger, F. (2021). Oscillatory Microrheology, Creep Compliance and Stress Relaxation of Biological Cells Reveal Strong Correlations as Probed by Atomic Force Microscopy. *Frontiers in Physics*, 9. https://www.frontiersin.org/article/10.3389/fphy.2021.711860

Garcia, P. D., & Garcia, R. (2018). Determination of the Elastic Moduli of a Single Cell Cultured on a Rigid Support by Force Microscopy. *Biophysical Journal*, 114(12), Article 12. https://doi.org/10.1016/j.bpj.2018.05.012

Gavara, N. (2016). Combined strategies for optimal detection of the contact point in AFM force-indentation curves obtained on thin samples and adherent cells. *Scientific Reports*, *6*(1), Article 1. https://doi.org/10.1038/srep21267

Gavara, N. (2017). A beginner's guide to atomic force microscopy probing for cell mechanics. *Microscopy Research and Technique*, 80(1), Article 1. https://doi.org/10.1002/jemt.22776

Gerum, R., Mirzahossein, E., Eroles, M., Elsterer, J., Mainka, A., Bauer, A., Sonntag, S., Winterl, A., Bartl, J., Fischer, L., Abuhattum, S., Goswami, R., Girardo, S., Guck, J., Schrüfer, S., Ströhlein, N., Nosratlo, M., Herrmann, H., Schultheis, D., … Fabry, B. (2022). Viscoelastic properties of suspended cells measured with shear flow deformation cytometry. *eLife*, 11, e78823. https://doi.org/10.7554/eLife.78823

Gnanachandran, K., Kędracka-Krok, S., Pabijan, J., & Lekka, M. (2022). *Nanomechanical and microrheological properties of bladder cancer cells at cellular and spheroid levels* (p. 2022.03.21.485153). bioRxiv. https://doi.org/10.1101/2022.03.21.485153

Graham, G. A. C. (1967). The contact problem in the linear theory of viscoelasticity when the time dependent contact area has any number of maxima and minima. *International Journal of Engineering Science*, 5(6), 495–514. https://doi.org/10.1016/0020-7225(67)90037-7

Gray, D. S., Tien, J., & Chen, C. S. (2003). Repositioning of cells by mechanotaxis on surfaces with micropatterned Young's modulus. *Journal of Biomedical Materials Research Part A*, *66*A(3), 605–614. https://doi.org/10.1002/jbm.a.10585

Guck, J., Ananthakrishnan, R., Mahmood, H., Moon, T. J., Cunningham, C. C., & Käs, J. (2001). The Optical Stretcher: A Novel Laser Tool to Micromanipulate Cells. *Biophysical Journal*, *81*(2), 767–784. https://doi.org/10.1016/S0006-3495(01)75740-2

Gurung, S., Perocheau, D., Touramanidou, L., & Baruteau, J. (2021). The exosome journey: From biogenesis to uptake and intracellular signalling. *Cell Communication and Signaling*, *19*(1), 47. https://doi.org/10.1186/s12964-021-00730-1

Hajjarian, Z., Brachtel, E. F., Tshikudi, D. M., & Nadkarni, S. K. (2021). Mapping mechanical properties of the tumor microenvironment by laser speckle rheological microscopy. *Cancer Research*, *81*(18), 4874–4885. https://doi.org/10.1158/0008-5472.CAN-20-3898

Hamahashi, S. (2008). *Entropy filter, and area extracting method using the filter* (Patent US 7.460,702 B2).

Hansma, P. K., Drake, B., Marti, O., Gould, S. A. C., & Prater, C. B. (1989). The Scanning Ion-Conductance Microscope. *Science*, *243*(4891), 641–643. https://doi.org/10.1126/science.2464851

Harris, C. R., Millman, K. J., van der Walt, S. J., Gommers, R., Virtanen, P., Cournapeau, D., Wieser, E., Taylor, J., Berg, S., Smith, N. J., Kern, R., Picus, M., Hoyer, S., van Kerkwijk, M. H., Brett, M., Haldane, A., del Río, J. F., Wiebe, M., Peterson, P., … Oliphant, T. E. (2020). Array programming with NumPy. *Nature*, *585*(7825), Article 7825. https://doi.org/10.1038/s41586-020-2649-2

Helfrich, W. (1973). Elastic Properties of Lipid Bilayers: Theory and Possible Experiments. *Zeitschrift Für Naturforschung C*, *28*(11–12), 693–703. https://doi.org/10.1515/znc-1973-11-1209

Hermanowicz, P., Sarna, M., Burda, K., & Gabryś, H. (2014). AtomicJ: An open source software for analysis of force curves. *Review of Scientific Instruments*, *85*(6), 063703. https://doi.org/10.1063/1.4881683

Herrmann, H., Bär, H., Kreplak, L., Strelkov, S. V., & Aebi, U. (2007). Intermediate filaments: From cell architecture to nanomechanics. *Nature Reviews Molecular Cell Biology*, *8*(7), Article 7. https://doi.org/10.1038/nrm2197

Hertz, H. (1882). Ueber die Berührung fester elastischer Körper. In A. L. Crelle, C. W. Borchardt, & Schellbach (Eds.), *Band 92* (pp. 156–171). De Gruyter. https://doi.org/doi:10.1515/9783112342404-004

Higgins, M. J., Proksch, R., Sader, J. E., Polcik, M., Mc Endoo, S., Cleveland, J. P., & Jarvis, S. P. (2006). Noninvasive determination of optical lever sensitivity in atomic force microscopy. *Review of Scientific Instruments*, *77*(1), 013701. https://doi.org/10.1063/1.2162455

Hindul, N. L., Jhita, A., Oprea, D. G., Hussain, T. A., Gonchar, O., Campillo, M. A. M., O'Regan, L., Kanemaki, M. T., Fry, A. M., Hirota, K., & Tanaka, K. (2022). Construction of a human hTERT RPE-1 cell line with inducible Cre for editing of endogenous genes. *Biology Open*, *11*(2), bio059056. https://doi.org/10.1242/bio.059056

Holuigue, H., Nacci, L., Chiaro, P. D., Chighizola, M., Locatelli, I., Schulte, C., Alfano, M., Diaferia, G. R., & Podestà, A. (2023). *Native extracellular matrix probes to target patient- and tissue- specific cell-microenvironment interactions by force spectroscopy* (p. 2022.12.02.518867). bioRxiv. https://doi.org/10.1101/2022.12.02.518867

Johnson, K. L., Kendall, K., & Roberts, A. D. (1971). Surface Energy and Contact of Elastic Solids. *Proceedings of The Royal Society A: Mathematical, Physical and Engineering Sciences*, *324*, 301–313. https://doi.org/10.1098/rspa.1971.0141

Johnson, S. M., Banyard, A., Smith, C., Mironov, A., & McCabe, M. G. (2020). Large Extracellular Vesicles Can be Characterised by Multiplex Labelling Using Imaging Flow Cytometry. *International Journal of Molecular Sciences*, *21*(22), Article 22. https://doi.org/10.3390/ijms21228723

Jorba, I., Beltrán, G., Falcones, B., Suki, B., Farré, R., García-Aznar, J. M., & Navajas, D. (2019). Nonlinear elasticity of the lung extracellular microenvironment is regulated by macroscale tissue strain. *Acta Biomaterialia*, *92*, 265–276. https://doi.org/10.1016/j.actbio.2019.05.023

Jorba, I., Uriarte, J. J., Campillo, N., Farré, R., & Navajas, D. (2017). Probing Micromechanical Properties of the Extracellular Matrix of Soft Tissues by Atomic Force Microscopy. *Journal of Cellular Physiology*, *232*(1), 19–26. https://doi.org/10.1002/jcp.25420

Júnior, C., Ulldemolins, A., Narciso, M., Almendros, I., Farré, R., Navajas, D., López, J., Eroles, M., Rico, F., & Gavara, N. (2023). Multi-Step Extracellular Matrix Remodelling and Stiffening in the Development of Idiopathic Pulmonary Fibrosis. *International Journal of Molecular Sciences*, *24*(2), Article 2. https://doi.org/10.3390/ijms24021708

Kaplan, J. L., Bonfanti, A., & Kabla, A. J. (2019). RHEOS.jl—A Julia Package for Rheology Data Analysis. *Journal of Open Source Software*, *4*(41), 1700. https://doi.org/10.21105/joss.01700

Kaushik, S., Pickup, M. W., & Weaver, V. M. (2016). From transformation to metastasis: Deconstructing the extracellular matrix in breast cancer. *Cancer Metastasis Reviews*, *35*(4), 655–667. https://doi.org/10.1007/s10555-016-9650-0

Kendall, M. G. (1938). A new measure of rank correlation. *Biometrika*, *30*(1–2), 81–93. https://doi.org/10.1093/biomet/30.1-2.81

Klapholz, B., & Brown, N. H. (2017). Talin – the master of integrin adhesions. *Journal of Cell Science*, *130*(15), Article 15. https://doi.org/10.1242/jcs.190991

Kodera, N., Yamamoto, D., Ishikawa, R., & Ando, T. (2010). Video imaging of walking myosin V by high-speed atomic force microscopy. *Nature*, *468*(7320), 72–76. https://doi.org/10.1038/nature09450

Kol, N., Shi, Y., Tsvitov, M., Barlam, D., Shneck, R. Z., Kay, M. S., & Rousso, I. (2007). A Stiffness Switch in Human Immunodeficiency Virus. *Biophysical Journal*, *92*(5), 1777–1783. https://doi.org/10.1529/biophysj.106.093914

Kontomaris, S. V., Stylianou, A., Chliveros, G., & Malamou, A. (2023). Determining Spatial Variability of Elastic Properties for Biological Samples Using AFM. *Micromachines*, *14*(1), Article 1. https://doi.org/10.3390/mi14010182

Korchev, Y. E., Bashford, C. L., Milovanovic, M., Vodyanoy, I., & Lab, M. J. (1997). Scanning ion conductance microscopy of living cells. *Biophysical Journal*, *73*(2), 653–658. https://doi.org/10.1016/S0006-3495(97)78100-1

Korossis, S., Bolland, F., Southgate, J., Ingham, E., & Fisher, J. (2009). Regional biomechanical and histological characterisation of the passive porcine urinary bladder: Implications for augmentation and tissue engineering strategies. *Biomaterials*, *30*(2), 266–275. https://doi.org/10.1016/j.biomaterials.2008.09.034

Kreplak, L., Bär, H., Leterrier, J. F., Herrmann, H., & Aebi, U. (2005). Exploring the Mechanical Behavior of Single Intermediate Filaments. *Journal of Molecular Biology*, *354*(3), 569–577. https://doi.org/10.1016/j.jmb.2005.09.092

Kruskal, W. H., & Wallis, W. A. (1952). Use of Ranks in One-Criterion Variance Analysis. *Journal of the American Statistical Association*, *47*(260), 583–621. https://doi.org/10.1080/01621459.1952.10483441

Kular, J. K., Basu, S., & Sharma, R. I. (2014). The extracellular matrix: Structure, composition, age-related differences, tools for analysis and applications for tissue engineering. *Journal of Tissue Engineering*, *5*, 2041731414557112. https://doi.org/10.1177/2041731414557112

Lammerding, J. (2011). Mechanics of the Nucleus. In *Comprehensive Physiology* (pp. 783–807). John Wiley & Sons, Ltd. https://doi.org/10.1002/cphy.c100038

Laurent, V. M., Kasas, S., Yersin, A., Schäffer, T. E., Catsicas, S., Dietler, G., Verkhovsky, A. B., & Meister, J.-J. (2005). Gradient of rigidity in the lamellipodia of migrating cells revealed by atomic force microscopy. *Biophysical Journal*, *89*(1), 667–675. https://doi.org/10.1529/biophysj.104.052316

Lee, E. H., & Radok, J. R. M. (1960). The Contact Problem for Viscoelastic Bodies. *Journal of Applied Mechanics*, *27*(3), 438–444. https://doi.org/10.1115/1.3644020

Leipzig, N. D., & Shoichet, M. S. (2009). The effect of substrate stiffness on adult neural stem cell behavior. *Biomaterials*, *30*(36), 6867–6878. https://doi.org/10.1016/j.biomaterials.2009.09.002

Lekka, M. (2016). Discrimination Between Normal and Cancerous Cells Using AFM. *BioNanoScience*, *6*(1), 65–80. https://doi.org/10.1007/s12668-016-0191-3

Lekka, M., Gil, D., Pogoda, K., Dulińska-Litewka, J., Jach, R., Gostek, J., Klymenko, O., Prauzner-Bechcicki, S., Stachura, Z., Wiltowska-Zuber, J., Okoń, K., & Laidler, P. (2012). Cancer cell detection in tissue sections using AFM. *Archives of Biochemistry and Biophysics*, *518*(2), 151–156. https://doi.org/10.1016/j.abb.2011.12.013

Lekka, M., & Laidler, P. (2009). Applicability of AFM in cancer detection. *Nature Nanotechnology*, *4*(2), Article 2. https://doi.org/10.1038/nnano.2009.004

Lekka, M., Laidler, P., Gil, D., Lekki, J., Stachura, Z., & Hrynkiewicz, A. Z. (1999). Elasticity of normal and cancerous human bladder cells studied by scanning force microscopy. *European Biophysics Journal: EBJ*, *28*(4), 312–316. https://doi.org/10.1007/s002490050213

Lekka, M., Navajas, D., Radmacher, M., & Podestà, A. (Eds.). (2023a). *Volume 1 Biomedical Methods*. De Gruyter. https://doi.org/doi:10.1515/9783110640632

Lekka, M., Navajas, D., Radmacher, M., & Podestà, A. (Eds.). (2023b). *Volume 2 Biomedical Applications*. De Gruyter. https://doi.org/doi:10.1515/9783110989380

Li, M., Xi, N., Wang, Y., & Liu, L. (2021). Atomic force microscopy for revealing micro/nanoscale mechanics in tumor metastasis: From single cells to microenvironmental cues. *Acta Pharmacologica Sinica*, *42*(3), Article 3. https://doi.org/10.1038/s41401-020-0494-3

Liu, Y., Cui, M., Huang, J., Sun, M., Zhao, X., & Zhao, Q. (2019). Robotic Micropipette Aspiration for Multiple Cells. *Micromachines*, *10*(5), Article 5. https://doi.org/10.3390/mi10050348

LOVE, A. E. H. (1939). BOUSSINESQ'S PROBLEM FOR A RIGID CONE. *The Quarterly Journal of Mathematics*, *os-10*(1), 161–175. https://doi.org/10.1093/qmath/os-10.1.161

Maître, J.-L., & Heisenberg, C.-P. (2013). Three Functions of Cadherins in Cell Adhesion. *Current Biology*, *23*(14), R626–R633. https://doi.org/10.1016/j.cub.2013.06.019

Marcotti, S., Reilly, G. C., & Lacroix, D. (2019). Effect of cell sample size in atomic force microscopy nanoindentation. *Journal of the Mechanical Behavior of Biomedical Materials*, *94*, 259–266. https://doi.org/10.1016/j.jmbbm.2019.03.018

Martinez-Vidal, L., Chighizola, M., Berardi, M., Alchera, E., Locatelli, I., Pederzoli, F., Venegoni, C., Lucianò, R., Milani, P., Bielawski, K., Salonia, A., Podestà, A., & Alfano, M. (2023). Micro-mechanical fingerprints of the rat bladder change in actinic cystitis and tumor presence. *Communications Biology*, *6*(1), Article 1. https://doi.org/10.1038/s42003-023-04572-0

Martinez-Vidal, L., Murdica, V., Venegoni, C., Pederzoli, F., Bandini, M., Necchi, A., Salonia, A., & Alfano, M. (2021). Causal contributors to tissue stiffness and clinical relevance in urology. *Communications Biology*, *4*, 1011. https://doi.org/10.1038/s42003-021-02539-7

Maugis, D. (1992). Adhesion of spheres: The JKR-DMT transition using a dugdale model. *Journal of Colloid and Interface Science*, *150*(1), 243–269. https://doi.org/10.1016/0021-9797(92)90285-T

McKee, T. J., Perlman, G., Morris, M., & Komarova, S. V. (2019). Extracellular matrix composition of connective tissues: A systematic review and meta-analysis. *Scientific Reports*, *9*(1), Article 1. https://doi.org/10.1038/s41598-019-46896-0

McKinney, W. (2010). Data Structures for Statistical Computing in Python. In S. van der Walt & J. Millman (Eds.), *Proceedings of the 9th Python in Science Conference* (pp. 56–61). https://doi.org/10.25080/Majora-92bf1922-00a

Meister, A., Gabi, M., Behr, P., Studer, P., Vörös, J., Niedermann, P., Bitterli, J., Polesel-Maris, J., Liley, M., Heinzelmann, H., & Zambelli, T. (2009). FluidFM: Combining Atomic Force Microscopy and Nanofluidics in a Universal Liquid Delivery System for Single Cell Applications and Beyond. *Nano Letters*, *9*(6), 2501–2507. https://doi.org/10.1021/nl901384x

Morton, W. M., Ayscough, K. R., & McLaughlin, P. J. (2000). Latrunculin alters the actin-monomer subunit interface to prevent polymerization. *Nature Cell Biology*, *2*(6), 376–378. https://doi.org/10.1038/35014075

Mulcahy, L. A., Pink, R. C., & Carter, D. R. F. (2014). Routes and mechanisms of extracellular vesicle uptake. *Journal of Extracellular Vesicles*, *3*, 10.3402/jev.v3.24641. https://doi.org/10.3402/jev.v3.24641

Müller, P., Abuhattum, S., Möllmert, S., Ulbricht, E., Taubenberger, A. V., & Guck, J. (2019). nanite: Using machine learning to assess the quality of atomic force microscopy-enabled nano-indentation data. *BMC Bioinformatics*, *20*(1), 465. https://doi.org/10.1186/s12859-019-3010-3

Munevar, S., Wang, Y., & Dembo, M. (2001). Traction Force Microscopy of Migrating Normal and H-ras Transformed 3T3 Fibroblasts. *Biophysical Journal*, *80*(4), 1744–1757. https://doi.org/10.1016/S0006-3495(01)76145-0

Myers, J. P., Santiago-Medina, M., & Gomez, T. M. (2011). Regulation of axonal outgrowth and pathfinding by integrin-ECM interactions. *Developmental Neurobiology*, *71*(11), 901–923. https://doi.org/10.1002/dneu.20931

Nečas, D., & Klapetek, P. (2012). Gwyddion: An open-source software for SPM data analysis. *Open Physics*, *10*(1), 181–188. https://doi.org/10.2478/s11534-011-0096-2

Newville, M., Otten, R., Nelson, A., Stensitzki, T., Ingargiola, A., Allan, D., Fox, A., Carter, F., Michał, Osborn, R., Pustakhod, D., lneuhaus, Weigand, S., Aristov, A., Glenn, Deil, C., mgunyho, Mark, Hansen, A. L. R., … Caldwell, S. (2023). *lmfit/lmfit-py: 1.2.0* [Computer software]. Zenodo. https://doi.org/10.5281/zenodo.7810964

Nguyen, Q. D., & Chung, K.-H. (2019). Effect of tip shape on nanomechanical properties measurements using AFM. *Ultramicroscopy*, *202*, 1–9. https://doi.org/10.1016/j.ultramic.2019.03.012

Otsu, N. (1979). A Threshold Selection Method from Gray-Level Histograms. *IEEE Transactions on Systems, Man, and Cybernetics*, *9*(1), 62–66. https://doi.org/10.1109/TSMC.1979.4310076

Paszek, M. J., Zahir, N., Johnson, K. R., Lakins, J. N., Rozenberg, G. I., Gefen, A., Reinhart-King, C. A., Margulies, S. S., Dembo, M., Boettiger, D., Hammer, D. A., & Weaver, V. M. (2005). Tensional homeostasis and the malignant phenotype. *Cancer Cell*, *8*(3), 241–254. https://doi.org/10.1016/j.ccr.2005.08.010

Pearlstein, E., Gold, L. I., & Garcia-Pardo, A. (1980). Fibronectin: A review of its structure and biological activity. *Molecular and Cellular Biochemistry*, *29*(2), 103–128. https://doi.org/10.1007/BF00220304

Peric, O., Hannebelle, M., Adams, J. D., & Fantner, G. E. (2017). Microfluidic bacterial traps for simultaneous fluorescence and atomic force microscopy. *Nano Research*, *10*(11), 3896–3908. https://doi.org/10.1007/s12274-017-1604-5

Pirzer, T., & Hugel, T. (2009). Atomic force microscopy spring constant determination in viscous liquids. *Review of Scientific Instruments*, *80*(3), 035110. https://doi.org/10.1063/1.3100258

Plodinec, M., Loparic, M., Monnier, C. A., Obermann, E. C., Zanetti-Dallenbach, R., Oertle, P., Hyotyla, J. T., Aebi, U., Bentires-Alj, M., Lim, R. Y. H., & Schoenenberger, C.-A. (2012). The nanomechanical signature of breast cancer. *Nature Nanotechnology*, *7*(11), Article 11. https://doi.org/10.1038/nnano.2012.167

Pogoda, K., Byfield, F., Deptuła, P., Cieśluk, M., Suprewicz, Ł., Skłodowski, K., Shivers, J. L., van Oosten, A., Cruz, K., Tarasovetc, E., Grishchuk, E. L., Mackintosh, F. C., Bucki, R., Patteson, A. E., & Janmey, P. A. (2022). Unique Role of Vimentin Networks in Compression Stiffening of Cells and Protection of Nuclei from Compressive Stress. *Nano Letters*, *22*(12), 4725–4732. https://doi.org/10.1021/acs.nanolett.2c00736

Prat-Vidal, C., Rodríguez-Gómez, L., Aylagas, M., Nieto-Nicolau, N., Gastelurrutia, P., Agustí, E., Gálvez-Montón, C., Jorba, I., Teis, A., Monguió-Tortajada, M., Roura, S., Vives, J., Torrents-Zapata, S., Coca, M. I., Reales, L., Cámara-Rosell, M. L., Cediel, G., Coll, R., Farré, R., … Bayes-Genis, A. (2020). First-in-human PeriCord cardiac bioimplant: Scalability and GMP manufacturing of an allogeneic engineered tissue graft. *eBioMedicine*, *54*. https://doi.org/10.1016/j.ebiom.2020.102729

Proa-Coronado, S., Séverac, C., Martinez-Rivas, A., & Dague, E. (2019). Beyond the paradigm of nanomechanical measurements on cells using AFM: An automated methodology to rapidly analyse thousands of cells. *Nanoscale Horizons*, *5*(1), 131–138. https://doi.org/10.1039/C9NH00438F

Rade, J., Zhang, J., Sarkar, S., Krishnamurthy, A., Ren, J., & Sarkar, A. (2022). Deep Learning for Live Cell Shape Detection and Automated AFM Navigation. *Bioengineering*, *9*(10), Article 10. https://doi.org/10.3390/bioengineering9100522

Rebelo, L. M., de Sousa, J. S., Mendes Filho, J., & Radmacher, M. (2013). Comparison of the viscoelastic properties of cells from different kidney cancer phenotypes measured with atomic force microscopy. *Nanotechnology*, *24*(5), 055102. https://doi.org/10.1088/0957-4484/24/5/055102

Rheinlaender, J., & Schäffer, T. E. (2013). Mapping the mechanical stiffness of live cells with the scanning ion conductance microscope. *Soft Matter*, *9*(12), 3230–3236. https://doi.org/10.1039/C2SM27412D

Rianna, C., Radmacher, M., & Kumar, S. (2020). Direct evidence that tumor cells soften when navigating confined spaces. *Molecular Biology of the Cell*, *31*(16), 1726–1734. https://doi.org/10.1091/mbc.E19-10-0588

Ricard-Blum, S. (2011). The Collagen Family. *Cold Spring Harbor Perspectives in Biology*, *3*(1), a004978. https://doi.org/10.1101/cshperspect.a004978

Rico, F., Roca-Cusachs, P., Gavara, N., Farré, R., Rotger, M., & Navajas, D. (2005). Probing mechanical properties of living cells by atomic force microscopy with blunted pyramidal cantilever tips. *Physical Review E*, *72*(2), 021914. https://doi.org/10.1103/PhysRevE.72.021914

Ridolfi, A., Caselli, L., Baldoni, M., Montis, C., Mercuri, F., Berti, D., Valle, F., & Brucale, M. (2021). Stiffness of Fluid and Gel Phase Lipid Nanovesicles: Weighting the Contributions of Membrane Bending Modulus and Luminal Pressurization. *Langmuir*, *37*(41), Article 41. https://doi.org/10.1021/acs.langmuir.1c01660

Rigato, A., Miyagi, A., Scheuring, S., & Rico, F. (2017). High-frequency microrheology reveals cytoskeleton dynamics in living cells. *Nature Physics*, *13*(8), Article 8. https://doi.org/10.1038/nphys4104

Rigato, A., Rico, F., Eghiaian, F., Piel, M., & Scheuring, S. (2015). Atomic Force Microscopy Mechanical Mapping of Micropatterned Cells Shows Adhesion Geometry-Dependent Mechanical Response on Local and Global Scales. *ACS Nano*, *9*(6), 5846–5856. https://doi.org/10.1021/acsnano.5b00430

Roca-Cusachs, P., Almendros, I., Sunyer, R., Gavara, N., Farré, R., & Navajas, D. (2006). Rheology of Passive and Adhesion-Activated Neutrophils Probed by Atomic Force Microscopy. *Biophysical Journal*, *91*(9), Article 9. https://doi.org/10.1529/biophysj.106.088831

Ross, M. H., & Pawlina, W. (2016a). Chapter 4: Tissues: Concept and Classification. In *Histology: A Text and Atlas with Correlated Cell and Molecular Biology: Vol. Chapter 4: Tissues: Concept and Classification* (7th ed.).

Ross, M. H., & Pawlina, W. (2016b). Chapter 5: Epithelial Tissue. In *Histology: A Text and Atlas with Correlated Cell and Molecular Biology: Vol. Chapter 5: Epithelial Tissue* (7th ed.).

Ross, M. H., & Pawlina, W. (2016c). Chapter 6: Connective Tissue. In *Histology: A Text and Atlas with Correlated Cell and Molecular Biology: Vol. Chapter 6: Connective Tissue* (7th ed.).

Ross, M. H., & Pawlina, W. (2016d). Chapter 11: Muscle Tissue. In *Histology: A Text and Atlas with Correlated Cell and Molecular Biology: Vol. Chapter 11: Muscle Tissue* (7th ed.).

Ross, M. H., & Pawlina, W. (2016e). Chapter 12: Nerve Tissue. In *Histology: A Text and Atlas with Correlated Cell and Molecular Biology: Vol. Chapter 12: Nerve Tissue* (7th ed.).

Rother, J., Nöding, H., Mey, I., & Janshoff, A. (2014). Atomic force microscopy-based microrheology reveals significant differences in the viscoelastic response between malign and benign cell lines. *Open Biology*, *4*(5), 140046. https://doi.org/10.1098/rsob.140046

Rotsch, C., Jacobson, K., & Radmacher, M. (1999). Dimensional and mechanical dynamics of active and stable edges in motile fibroblasts investigated by using atomic force microscopy. *Proceedings of the National Academy of Sciences*, *96*(3), 921–926. https://doi.org/10.1073/pnas.96.3.921

Rotsch, C., & Radmacher, M. (2000). Drug-Induced Changes of Cytoskeletal Structure and Mechanics in Fibroblasts: An Atomic Force Microscopy Study. *Biophysical Journal*, *78*(1), Article 1. https://doi.org/10.1016/S0006-3495(00)76614-8

Roy, R., Chen, W., Cong, L., Goodell, L. A., Foran, D. J., & Desai, J. P. (2013). A Semi-Automated Positioning System for Contact-Mode Atomic Force Microscopy (AFM). *IEEE Transactions on Automation Science and Engineering*, *10*(2), 462–465. https://doi.org/10.1109/TASE.2012.2226154

Sadeghian, H., Herfst, R., Dekker, B., Winters, J., Bijnagte, T., & Rijnbeek, R. (2017). High-throughput atomic force microscopes operating in parallel. *Review of Scientific Instruments*, *88*(3), 033703. https://doi.org/10.1063/1.4978285

Sader, J. E., Borgani, R., Gibson, C. T., Haviland, D. B., Higgins, M. J., Kilpatrick, J. I., Lu, J., Mulvaney, P., Shearer, C. J., Slattery, A. D., Thorén, P.-A., Tran, J., Zhang, H., Zhang, H., & Zheng, T. (2016). A virtual instrument to standardise the calibration of atomic force microscope cantilevers. *The Review of Scientific Instruments*, *87*(9), 093711. https://doi.org/10.1063/1.4962866

Sader, J. E., Chon, J. W. M., & Mulvaney, P. (1999). Calibration of rectangular atomic force microscope cantilevers. *Review of Scientific Instruments*, *70*(10), 3967–3969. https://doi.org/10.1063/1.1150021

Sader, J. E., Pacifico, J., Green, C. P., & Mulvaney, P. (2005). General scaling law for stiffness measurement of small bodies with applications to the atomic force microscope. *Journal of Applied Physics*, *97*(12), 124903. https://doi.org/10.1063/1.1935133

Sader, J. E., Sanelli, J. A., Adamson, B. D., Monty, J. P., Wei, X., Crawford, S. A., Friend, J. R., Marusic, I., Mulvaney, P., & Bieske, E. J. (2012). Spring constant calibration of atomic force microscope cantilevers of arbitrary shape. *Review of Scientific Instruments*, *83*(10), 103705. https://doi.org/10.1063/1.4757398

Sanchez, J. G., Espinosa, F. M., Miguez, R., & Garcia, R. (2021). The viscoelasticity of adherent cells follows a single power-law with distinct local variations within a single cell and across cell lines. *Nanoscale*, *13*(38), 16339–16348. https://doi.org/10.1039/D1NR03894J

Sancho, A., Vandersmissen, I., Craps, S., Luttun, A., & Groll, J. (2017). A new strategy to measure intercellular adhesion forces in mature cell-cell contacts. *Scientific Reports*, *7*(1), Article 1. https://doi.org/10.1038/srep46152

Schächtele, M., Hänel, E., & Schäffer, T. E. (2018). Resonance compensating chirp mode for mapping the rheology of live cells by high-speed atomic force microscopy. *Applied Physics Letters*, *113*(9), Article 9. https://doi.org/10.1063/1.5039911

Schillers, H., Rianna, C., Schäpe, J., Luque, T., Doschke, H., Wälte, M., Uriarte, J. J., Campillo, N., Michanetzis, G. P. A., Bobrowska, J., Dumitru, A., Herruzo, E. T., Bovio, S., Parot, P., Galluzzi, M., Podestà, A., Puricelli, L., Scheuring, S., Missirlis, Y., … Radmacher, M. (2017). Standardized Nanomechanical Atomic Force Microscopy Procedure (SNAP) for Measuring Soft and Biological Samples. *Scientific Reports*, *7*(1), Article 1. https://doi.org/10.1038/s41598-017-05383-0

Schneider, L., Klausen, T. K., Stock, C., Mally, S., Christensen, S. T., Pedersen, S. F., Hoffmann, E. K., & Schwab, A. (2008). H-ras transformation sensitizes volume-activated anion channels and increases migratory activity of NIH3T3 fibroblasts. *Pflügers Archiv - European Journal of Physiology*, *455*(6), 1055–1062. https://doi.org/10.1007/s00424-007-0367-3

Seifert, J., Rheinlaender, J., Eysmondt, H. von, & Schäffer, T. E. (2022). Mechanics of migrating platelets investigated with scanning ion conductance microscopy. *Nanoscale*, *14*(22), 8192–8199. https://doi.org/10.1039/D2NR01187E

Shivashankar, G. V., Sheetz, M., & Matsudaira, P. (2015). Mechanobiology. *Integrative Biology*, *7*(10), 1091–1092. https://doi.org/10.1039/c5ib90040a

Sicard, D., Haak, A. J., Choi, K. M., Craig, A. R., Fredenburgh, L. E., & Tschumperlin, D. J. (2018). Aging and anatomical variations in lung tissue stiffness. *American Journal of Physiology-Lung Cellular and Molecular Physiology*, *314*(6), L946–L955. https://doi.org/10.1152/ajplung.00415.2017

Silver, F. H., Kelkar, N., & Deshmukh, T. (2021). Molecular Basis for Mechanical Properties of ECMs: Proposed Role of Fibrillar Collagen and Proteoglycans in Tissue Biomechanics. *Biomolecules*, *11*(7), 1018. https://doi.org/10.3390/biom11071018

Sneddon, I. N. (1965). The relation between load and penetration in the axisymmetric boussinesq problem for a punch of arbitrary profile. *International Journal of Engineering Science*, *3*(1), 47–57. https://doi.org/10.1016/0020-7225(65)90019-4

Ståhl, A., Johansson, K., Mossberg, M., Kahn, R., & Karpman, D. (2019). Exosomes and microvesicles in normal physiology, pathophysiology, and renal diseases. *Pediatric Nephrology (Berlin, Germany)*, *34*(1), 11–30. https://doi.org/10.1007/s00467-017-3816-z

Stark, R. W., Drobek, T., & Heckl, W. M. (2001). Thermomechanical noise of a free v-shaped cantilever for atomic-force microscopy. *Ultramicroscopy*, *86*(1), 207–215. https://doi.org/10.1016/S0304-3991(00)00077-2

Sumbul, F., Hassanpour, N., Rodriguez-Ramos, J., & Rico, F. (2020). One-Step Calibration of AFM in Liquid. *Frontiers in Physics*, *8*. https://www.frontiersin.org/articles/10.3389/fphy.2020.00301

Takada, Y., Ye, X., & Simon, S. (2007). The integrins. *Genome Biology*, *8*(5), 215. https://doi.org/10.1186/gb-2007-8-5-215

Takayama, Y., Perret, G., Kumemura, M., Ataka, M., Meignan, S., Karsten, S. L., Fujita, H., Collard, D., Lagadec, C., & Tarhan, M. C. (2018). Developing a MEMS Device with Built-in Microfluidics for Biophysical Single Cell Characterization. *Micromachines*, *9*(6), Article 6. https://doi.org/10.3390/mi9060275

Teckchandani, A., & Cooper, J. A. (2022). The ubiquitin-proteasome system regulates focal adhesions at the leading edge of migrating cells. *eLife*, *5*, e17440. https://doi.org/10.7554/eLife.17440

Ting, T. C. T. (1966). The Contact Stresses Between a Rigid Indenter and a Viscoelastic Half-Space. *Journal of Applied Mechanics*, *33*(4), 845–854. https://doi.org/10.1115/1.3625192

Ting, T. C. T. (1968). Contact Problems in the Linear Theory of Viscoelasticity. *Journal of Applied Mechanics*, *35*(2), 248–254. https://doi.org/10.1115/1.3601188

Tremel, A., Cai, A., Tirtaatmadja, N., Hughes, B. D., Stevens, G. W., Landman, K. A., & O'Connor, A. J. (2009). Cell migration and proliferation during monolayer formation and wound healing. *Chemical Engineering Science*, *64*(2), 247–253. https://doi.org/10.1016/j.ces.2008.10.008

Trepat, X., Chen, Z., & Jacobson, K. (2012). Cell Migration. In *Comprehensive Physiology* (pp. 2369–2392). John Wiley & Sons, Ltd. https://doi.org/10.1002/cphy.c110012

Virtanen, P., Gommers, R., Oliphant, T. E., Haberland, M., Reddy, T., Cournapeau, D., Burovski, E., Peterson, P., Weckesser, W., Bright, J., van der Walt, S. J., Brett, M., Wilson, J., Millman, K. J., Mayorov, N., Nelson, A. R. J., Jones, E., Kern, R., Larson, E., … van Mulbregt, P. (2020). SciPy 1.0: Fundamental algorithms for scientific computing in Python. *Nature Methods*, *17*(3), Article 3. https://doi.org/10.1038/s41592-019-0686-2

Von der mark, K. (2006). CHAPTER 1—Structure, Biosynthesis and Gene Regulation of Collagens in Cartilage and Bone. In M. J. Seibel, S. P. Robins, & J. P. Bilezikian (Eds.), *Dynamics of Bone and Cartilage Metabolism (Second Edition)* (pp. 3–40). Academic Press. https://doi.org/10.1016/B978-012088562-6/50002-9

Vorselen, D., MacKintosh, F. C., Roos, W. H., & Wuite, G. J. L. (2017). Competition between Bending and Internal Pressure Governs the Mechanics of Fluid Nanovesicles. *ACS Nano*, *11*(3), 2628–2636. https://doi.org/10.1021/acsnano.6b07302

Wang, Z., Liu, L., Wang, Y., Xi, N., Dong, Z., Li, M., & Yuan, S. (2012). A Fully Automated System for Measuring Cellular Mechanical Properties. *Journal of Laboratory Automation*, 17(6), 443–448. https://doi.org/10.1177/2211068212460236

Watanabe-Nakayama, T., Sahoo, B. R., Ramamoorthy, A., & Ono, K. (2020). High-Speed Atomic Force Microscopy Reveals the Structural Dynamics of the Amyloid-β and Amylin Aggregation Pathways. *International Journal of Molecular Sciences*, 21(12), Article 12. https://doi.org/10.3390/ijms21124287

Weder, G., & Favre, M. (n.d.). *Parallel Atomic Force Microscopy for Rapid Nanomechanical Tissue Diagnostics*. 1.

Wen, J. H., Choi, O., Taylor-Weiner, H., Fuhrmann, A., Karpiak, J. V., Almutairi, A., & Engler, A. J. (2015). Haptotaxis is cell type specific and limited by substrate adhesiveness. *Cellular and Molecular Bioengineering*, 8(4), 530–542. https://doi.org/10.1007/s12195-015-0398-3

Xu, W., Mezencev, R., Kim, B., Wang, L., McDonald, J., & Sulchek, T. (2012). Cell Stiffness Is a Biomarker of the Metastatic Potential of Ovarian Cancer Cells. *PLOS ONE*, 7(10), e46609. https://doi.org/10.1371/journal.pone.0046609

Yang, F., Zhang, W., Tao, L., & Ma, J. (2020). Transfer Learning Strategies for Deep Learning-based PHM Algorithms. *Applied Sciences*, 10(7), Article 7. https://doi.org/10.3390/app10072361

Yango, A., Schäpe, J., Rianna, C., Doschke, H., & Radmacher, M. (2016). Measuring the viscoelastic creep of soft samples by step response AFM. *Soft Matter*, 12(40), 8297–8306. https://doi.org/10.1039/C6SM00801A

Yeung, T., Georges, P. C., Flanagan, L. A., Marg, B., Ortiz, M., Funaki, M., Zahir, N., Ming, W., Weaver, V., & Janmey, P. A. (2005). Effects of substrate stiffness on cell morphology, cytoskeletal structure, and adhesion. *Cell Motility and the Cytoskeleton*, 60(1), 24–34. https://doi.org/10.1002/cm.20041

Zahn, J. T., Louban, I., Jungbauer, S., Bissinger, M., Kaufmann, D., Kemkemer, R., & Spatz, J. P. (2011). Age-Dependent Changes in Microscale Stiffness and Mechanoresponses of Cells. *Small*, 7(10), 1480–1487. https://doi.org/10.1002/smll.201100146

5. List of figures

6. List of tables

ANNEX I

1. Software widgets and functionality

In a similar manner to the JPK Data Processing software, the main window of PyFM consists of a multiple document interface where the functionality has been split into different widgets and menus that the user can open, close and reorganize. In this section each of these components of the PyFM GUI will be described.

1.1. File menu

This drop-down menu allows the user to load single files or folders containing several files. The software will automatically load any valid JPK (.jpk-force, .jpk-force-map, .jpk-qi-data), Bruker (.spm, .pfc) or UFF (.uff) file. This menu also allows the user to open the Export Results widget and to delete all current session loaded files and results.

1.2. View menu

This drop-down menu allows the user to automatically reorganize the widgets currently open in the multiple document interface and enter/exit full screen mode.

1.3. Tool bar

The tool bar allows to open or maximize the different widgets.

1.4. Data Viewer widget

When data is loaded into the session it can be observed in the Data Viewer widget. Clicking on the file id tree (A) will display the selected file. If the file is a force map the user can choose the curve to view by clicking on each pixel in D. Pannel B shows the metadata of the file. Pannel E shows the force curve data. The data displayed on E can be changed using panel C.

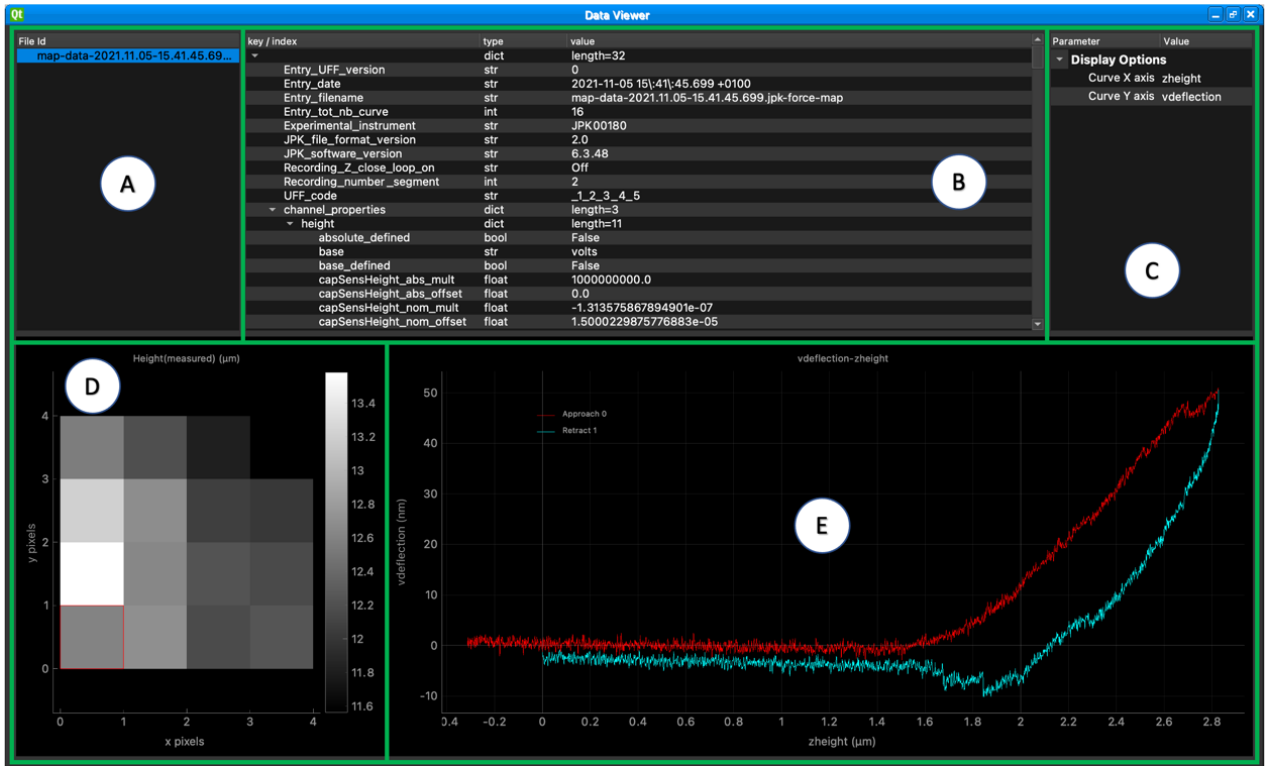

1.5. Thermal Tune widget

The determination of the cantilever's deflection sensitivity and spring constant is a critical step for AFM data processing.

1.6. 5Elasticity Fit widget

In this widget the user can analyse force curves by fitting the different elastic models implemented in PyFM. Panel A allows the user to select the file to analyse, the parameters for the analysis and to run the analysis for just one file or all the files loaded in the PyFM session. In the same manner as in the data viewer widget, if the selected file is a force map, the user can click on the pixels of panel B to select the different curves of the map. Panel C shows the raw data, pre-processed data, fit result and residuals.

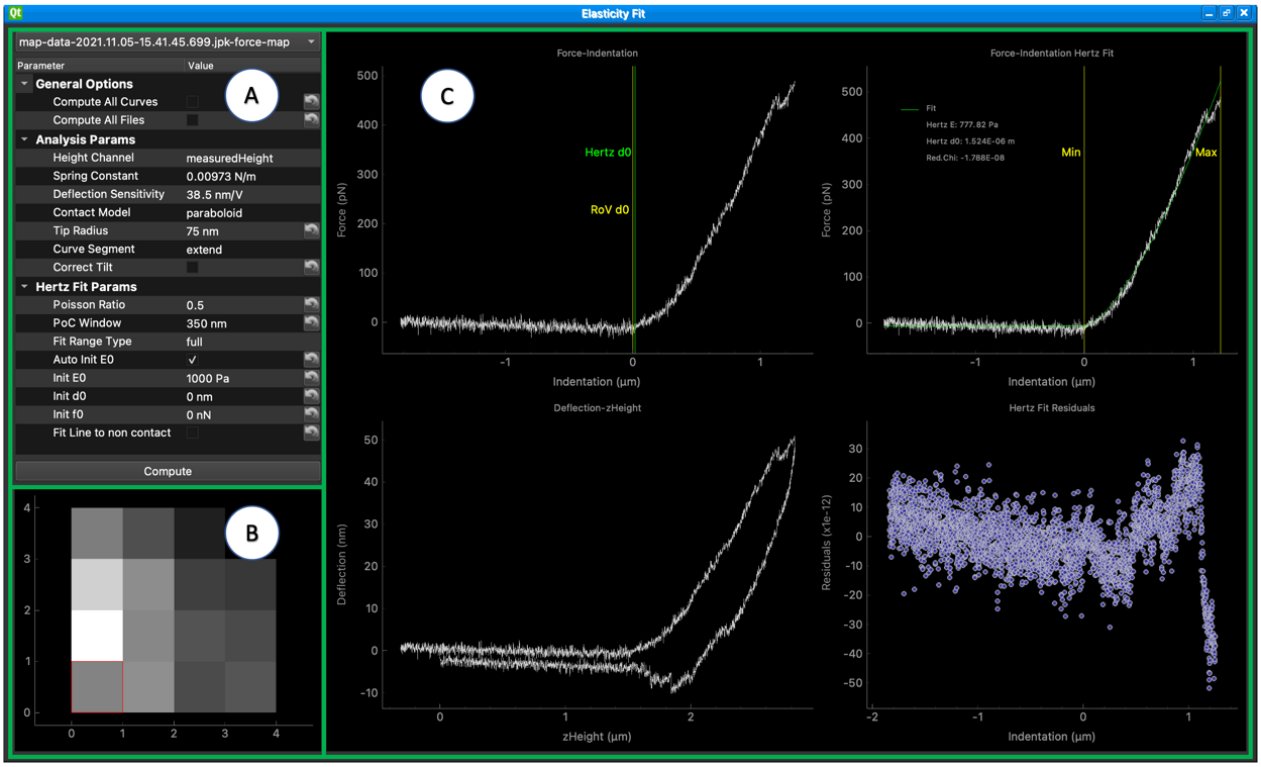

1.7. Viscoelasticity Fit widget

This widget follows the same structure as the Elasticity Fit widget but incorporating the viscoelastic model fit.

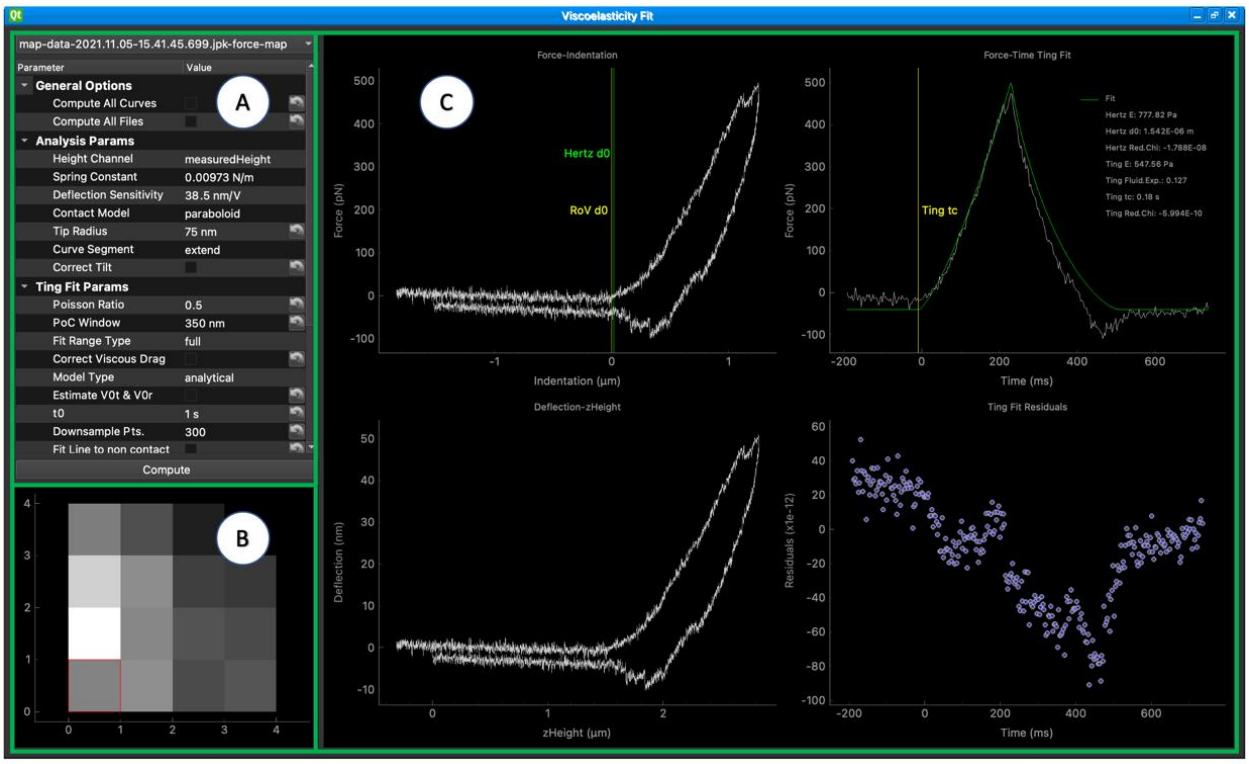

1.8. Microrheology widgets

Rheology related widgets, like the Piezo Characterization widget below, follow a similar layout. With the only difference being the display of the Fourier transform of each modulation segment.

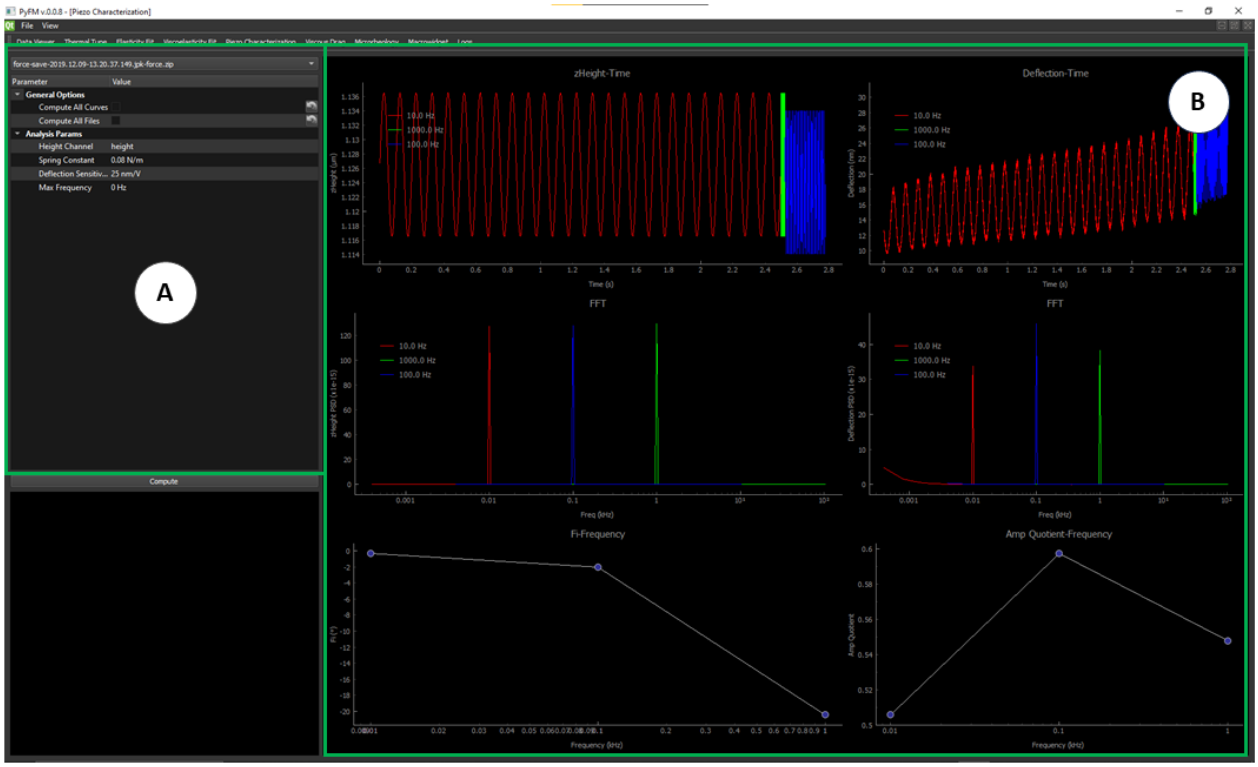

1.9. Macro widget

In the macro widget the user can write or load Python 3 scripts and execute them. These scripts have access to the data loaded in the software and the results obtained from the different analysis routines.

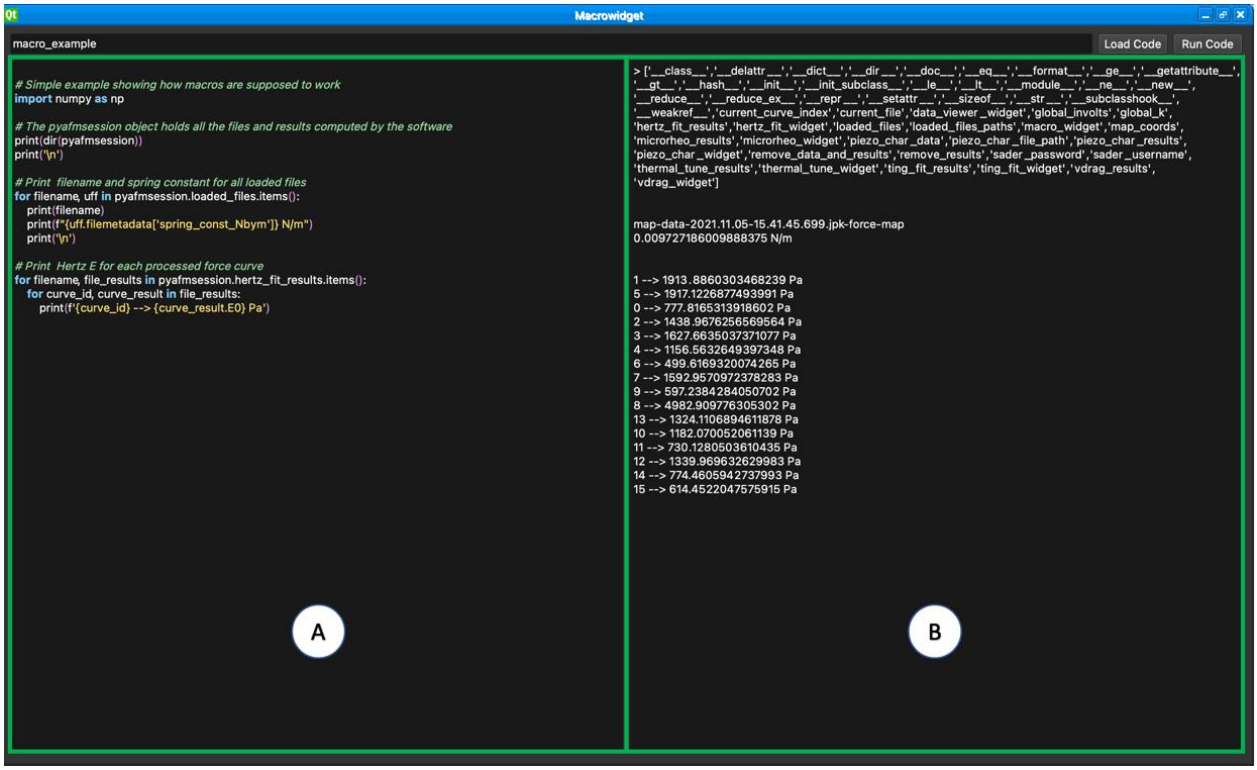

1.10. Export Data widget

This widget allows the user to view a summary of the results and export them as a txt file to the location of their choice.

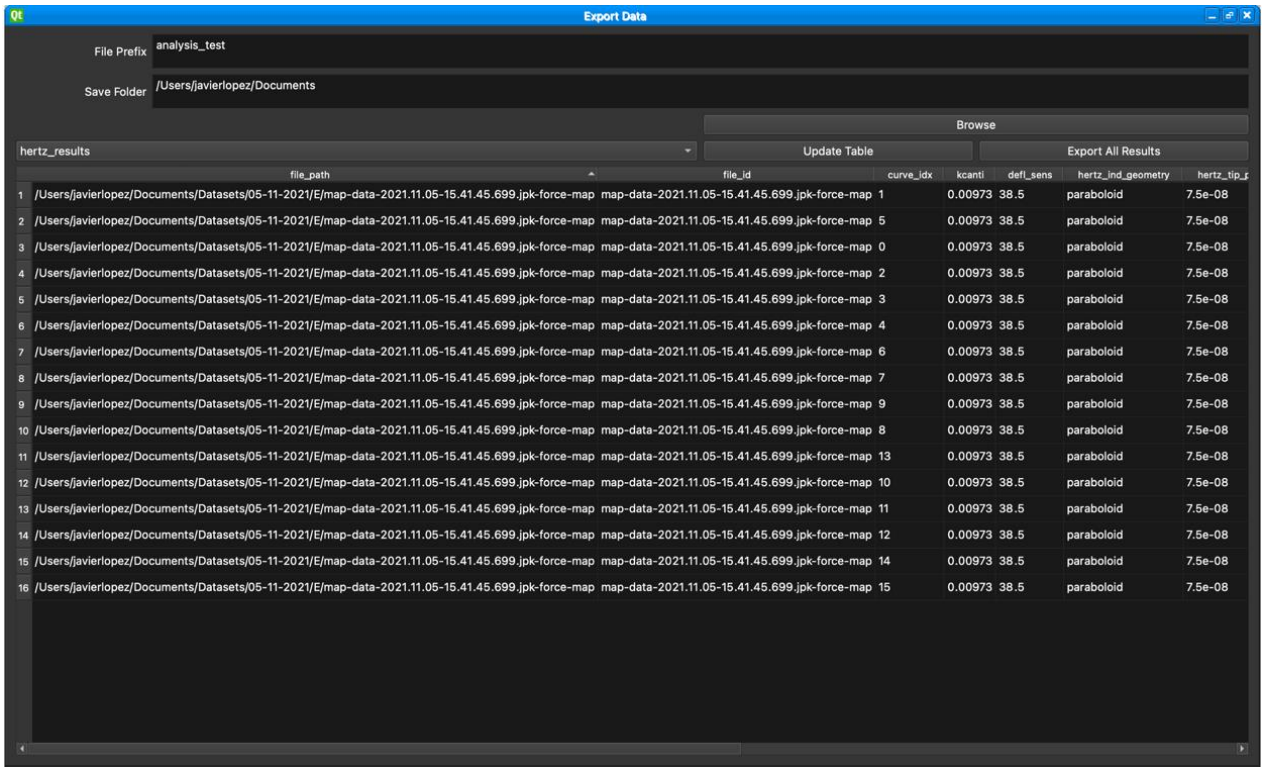

	file_path	file_id	curve_idx	kcanti	defl_sens	hertz_ind_geometry	hertz_tip_r
1	/Users/javierlopez/Documents/Datasets/05-11-2021/E/map-data-2021.11.05-15.41.45.699.jpk-force-map	map-data-2021.11.05-15.41.45.699.jpk-force-map	1	0.00973	38.5	paraboloid	7.5e-08
2	/Users/javierlopez/Documents/Datasets/05-11-2021/E/map-data-2021.11.05-15.41.45.699.jpk-force-map	map-data-2021.11.05-15.41.45.699.jpk-force-map	5	0.00973	38.5	paraboloid	7.5e-08
3	/Users/javierlopez/Documents/Datasets/05-11-2021/E/map-data-2021.11.05-15.41.45.699.jpk-force-map	map-data-2021.11.05-15.41.45.699.jpk-force-map	0	0.00973	38.5	paraboloid	7.5e-08
4	/Users/javierlopez/Documents/Datasets/05-11-2021/E/map-data-2021.11.05-15.41.45.699.jpk-force-map	map-data-2021.11.05-15.41.45.699.jpk-force-map	2	0.00973	38.5	paraboloid	7.5e-08
5	/Users/javierlopez/Documents/Datasets/05-11-2021/E/map-data-2021.11.05-15.41.45.699.jpk-force-map	map-data-2021.11.05-15.41.45.699.jpk-force-map	3	0.00973	38.5	paraboloid	7.5e-08
6	/Users/javierlopez/Documents/Datasets/05-11-2021/E/map-data-2021.11.05-15.41.45.699.jpk-force-map	map-data-2021.11.05-15.41.45.699.jpk-force-map	4	0.00973	38.5	paraboloid	7.5e-08
7	/Users/javierlopez/Documents/Datasets/05-11-2021/E/map-data-2021.11.05-15.41.45.699.jpk-force-map	map-data-2021.11.05-15.41.45.699.jpk-force-map	6	0.00973	38.5	paraboloid	7.5e-08
8	/Users/javierlopez/Documents/Datasets/05-11-2021/E/map-data-2021.11.05-15.41.45.699.jpk-force-map	map-data-2021.11.05-15.41.45.699.jpk-force-map	7	0.00973	38.5	paraboloid	7.5e-08
9	/Users/javierlopez/Documents/Datasets/05-11-2021/E/map-data-2021.11.05-15.41.45.699.jpk-force-map	map-data-2021.11.05-15.41.45.699.jpk-force-map	9	0.00973	38.5	paraboloid	7.5e-08
10	/Users/javierlopez/Documents/Datasets/05-11-2021/E/map-data-2021.11.05-15.41.45.699.jpk-force-map	map-data-2021.11.05-15.41.45.699.jpk-force-map	8	0.00973	38.5	paraboloid	7.5e-08
11	/Users/javierlopez/Documents/Datasets/05-11-2021/E/map-data-2021.11.05-15.41.45.699.jpk-force-map	map-data-2021.11.05-15.41.45.699.jpk-force-map	13	0.00973	38.5	paraboloid	7.5e-08
12	/Users/javierlopez/Documents/Datasets/05-11-2021/E/map-data-2021.11.05-15.41.45.699.jpk-force-map	map-data-2021.11.05-15.41.45.699.jpk-force-map	10	0.00973	38.5	paraboloid	7.5e-08
13	/Users/javierlopez/Documents/Datasets/05-11-2021/E/map-data-2021.11.05-15.41.45.699.jpk-force-map	map-data-2021.11.05-15.41.45.699.jpk-force-map	11	0.00973	38.5	paraboloid	7.5e-08
14	/Users/javierlopez/Documents/Datasets/05-11-2021/E/map-data-2021.11.05-15.41.45.699.jpk-force-map	map-data-2021.11.05-15.41.45.699.jpk-force-map	12	0.00973	38.5	paraboloid	7.5e-08
15	/Users/javierlopez/Documents/Datasets/05-11-2021/E/map-data-2021.11.05-15.41.45.699.jpk-force-map	map-data-2021.11.05-15.41.45.699.jpk-force-map	14	0.00973	38.5	paraboloid	7.5e-08
16	/Users/javierlopez/Documents/Datasets/05-11-2021/E/map-data-2021.11.05-15.41.45.699.jpk-force-map	map-data-2021.11.05-15.41.45.699.jpk-force-map	15	0.00973	38.5	paraboloid	7.5e-08